

Contributions to the development of oxygen-transporting materials as ceramic membranes for gas separation

Von der Naturwissenschaftlichen Fakultät
der Gottfried Wilhelm Leibniz Universität Hannover
zur Erlangung des Grades

Doktor der Naturwissenschaften
- Dr. rer. nat. -

genehmigte Dissertation

von

Dipl. Chem. Tobias Klande

geboren am 21.01.1983 in Celle

2013

Referent: Prof. Dr. Armin Feldhoff
Korreferent: Prof. Dr. Klaus-Dieter Becker
Tag der Promotion: 14.03.2013

Preface

The following thesis presents the results that I achieved in the past three years during my work as a scientific assistant at the Institute of Physical Chemistry and Electrochemistry at the Gottfried Wilhelm Leibniz Universität Hannover. The financial support was granted by the State of Lower Saxony (Germany, NTH bottom-up project, No. 21-71023-25-7/09), the Chinese-German Centre for Science (CDZ, Grant GZ676) and the Deutsche Forschungsgemeinschaft (DFG, Grant FE 928/4-1) under the guidance of Prof. Dr. Armin Feldhoff and Prof. Dr. Jürgen Caro.

Seven selected research articles are presented within this thesis and I am the first author in four of them. The following statement will point out my contributions to these articles. I would like to acknowledge the beneficial encouragement during the preparation of the manuscripts from all of my co-authors, but particularly by Prof. Dr. Klaus-Dieter Becker and Prof. Dr. Armin Feldhoff.

The first article, *Effect of doping, microstructure and CO₂ on La₂NiO_{4+δ}-based oxygen-transporting materials*, deals with investigations of the Ruddlesden-Popper phase La₂NiO_{4+δ} and was written by me. I carried out the synthesis and performed the X-ray diffraction (XRD) analysis, scanning electron microscopy (SEM), transmission electron microscopy (TEM), oxygen permeation measurements, and data interpretation. The Mössbauer measurements by Dr. Salvatore Cusenza and the interpretation by Prof. Dr. Klaus-Dieter Becker are kindly appreciated.

In the second article, *In-situ Mössbauer studies of ⁵⁷Fe-doped Ruddlesden-Popper type lanthanum nickel oxides*, further investigations of the iron-doped La₂NiO_{4+δ} and La₄Ni₃O_{10-δ} Ruddlesden-Popper phases, which are based on results of the first article, were conducted. The article was written by me. I synthesized the materials and performed the XRD analysis, SEM, TEM, oxygen permeation measurements, and data interpretation. Dr. Salvatore Cusenza and Dr. Piotr Gaczyński carried out the Mössbauer investigations, Prof. Dr. Klaus-Dieter Becker helped with interpretation of the Mössbauer results, and Dr. Lars Dörrer performed the conductivity measurements. I acknowledge the fruitful discussions with all co-authors during preparation of the manuscript, particularly with Prof. Dr. Klaus-Dieter Becker and Prof. Dr. Armin Feldhoff.

The third article, *Rapid glycine-nitrate combustion synthesis of the CO₂-stable dual phase membrane 40Mn_{1.5}Co_{1.5}O_{4-δ}-60Ce_{0.9}Pr_{0.1}O_{2-δ} for CO₂ capture via an oxy-fuel process*, was written by Dr. Huixia Luo and me in equal shares. I performed the in-situ XRD measurements and helped with data interpretation.

The fourth article, *Effect of A-site lanthanum doping on the CO₂ tolerance of SrCo_{0.8}Fe_{0.2}O_{3-δ} oxygen-transporting membranes*, deals with investigations of partially substituting the alkaline-earth element strontium by the rare-earth element lanthanum to obtain CO₂-tolerant materials. The manuscript was written by me

and I performed all experimental techniques and data interpretation. I thank Dipl.-Chem. Olga Ravkina for help during powder synthesis, membrane fabrication and oxygen permeation measurements. Furthermore, I thank Prof. Dr. Armin Feldhoff, who performed the energy-loss spectroscopy measurements in the TEM and supported me during manuscript preparation.

The fifth article, *Ca-containing CO₂-tolerant perovskite materials for oxygen separation*, studies the application of the alkaline-earth element calcium in CO₂-tolerant membrane materials. The article was written by Dr. Konstantin Efimov. I helped with membrane fabrication, oxygen permeation flux measurements and provided data interpretation and manuscript preparation support.

The sixth article, *Effect of microstructure on oxygen permeation of Ba_{0.5}Sr_{0.5}Co_{0.8}Fe_{0.2}O_{3-δ} and SrCo_{0.8}Fe_{0.2}O_{3-δ} membranes*, investigated the grain size distribution of these two oxide systems for different dwell times. The article was written by me and I performed the TEM investigations. All other measurements in the article were conducted by Dipl.-Chem. Olga Ravkina under my supervision.

The seventh article, *Investigation of Zr-doped BSCF perovskite membrane for oxygen separation in the intermediate temperature range*, examines the effect of zirconium substitution on the long-term phase stability of Ba_{0.5}Sr_{0.5}Co_{0.8}Fe_{0.2}O_{3-δ} (BSCF) membranes and was written by Dipl.-Chem. Olga Ravkina and me in equal shares. I provided support in data interpretation. All measurements in this article were conducted by Dipl.-Chem. Olga Ravkina during her diploma thesis under my supervision.

Acknowledgement

I enjoyed the last three years working in the field of inorganic membranes and materials science and I would like to thank each and everyone who supported me during my research work. I learned a lot of new techniques and I am especially grateful to all the people, who shared their knowledge with me.

First of all, I would like to deeply thank my supervisor Prof. Dr. Armin Feldhoff for his excellent support during the entire thesis and giving me the possibility of working in the field of materials science. He provided me with detailed knowledge of scanning and transmission electron microscopy and showed me how to perform excellent scientific work. He always inspired me and supported my work with many fruitful discussions. Furthermore, he assisted me in the preparation of my manuscripts and conference contributions.

I also thank Prof. Dr. Klaus-Dieter Becker from the Institut für Physikalische und Theoretische Chemie of the Technische Universität Braunschweig for helping me with the preparation of manuscripts, sharing his knowledge, and his willingness to be the second examiner of my doctoral thesis.

Furthermore, I would like to thank Prof. Dr. Carla Vogt from the Institut of Anorganische Chemie of the Leibniz Universität Hannover for supervising my diploma thesis in the year 2009 and for her readiness as the third examiner of my doctoral thesis.

I would like to extend my gratitude to Prof. Dr. Jürgen Caro, who gave me the possibility to work in his group and for the excellent working conditions during my thesis.

My special gratitude goes to Dr. Konstantin Efimov, who showed me all relevant techniques during the start of my Ph.D. and for his willingness to share his expertise with me. Special thanks go to him, Dr. Oliver Merka, and Dr. Monir Sharifi for sharing the same office with me, a lot of discussions and having a good time.

I would like to express my gratitude to all members of the Institute of Physical Chemistry and Electrochemistry, but especially to Zhengwen Cao, Fangyi Liang, Huixia Luo, Kaveh Partovi, Olga Ravkina, and Frank Steinbach. I greatly acknowledge the kind atmosphere in the group.

I would like to thank Yvonne Gabbey-Uebe and Kerstin Janze for administrative support. Special thanks to Wilfried Ribbe. I also thank Wilfried Becker, Markus Köhler, Peter Mühr, and Wolfgang Rogge from the mechanical and electrical workshops.

I kindly acknowledge my great parents Udo and Claudia, my brother Rouven and my beloved family for supporting me during my whole life and giving me the opportunity to finally reach this important stage of my life. Very special thanks go to my partner in life Kristina for her love, understanding and endless support. I would like to thank all of my friends, but especially Nils, Sarah, René, Anne, Alex, Guido, Maxi, and Steffen for having a great time.

Abstract

The world heavily relies on fossil fuels as energy source. The increasing demand of electricity is creating new worldwide challenges. With the emission of carbon dioxide (CO₂) and other greenhouse gases the global mean temperature rises, which results in severe environmental damage. The oxy-fuel process provides the possibility to sequester the formed CO₂. The required pure oxygen can be produced using mixed ionic electronic conducting materials, which offer the advantage to exclude nitrogen before combustion. This thesis presents seven original research articles, in which the stability of oxygen-transporting materials was investigated in two different contexts. The second and third chapter describe investigations to increase the chemical stability towards carbonate formation by avoiding or partially substituting alkaline-earth elements. In the fourth chapter the influence of the microstructure on oxygen permeation performance and the effect of B-site zirconium substitution on the long-term phase stability of Ba_{0.5}Sr_{0.5}Co_{0.8}Fe_{0.2}O_{3-δ} were examined.

In chapter 2 the alkaline-earth free Ruddlesden-Popper phases La₂NiO_{4+δ}, La₄Ni₃O_{10-δ} as well as a new dual phase material were investigated. The CO₂ tolerance of La₂NiO_{4+δ} was confirmed by *in-situ* X-ray diffraction (XRD) and long-term permeation experiments. The effect of B-site substitution with different valent cations on oxygen permeation was examined. Detailed transmission electron microscopy (TEM) and oxygen partial pressure and temperature dependent Mössbauer investigations reveal that the La₂Ni_{0.9}Fe_{0.1}O_{4+δ} system consists of a phase mixture of La₂Ni_{0.95}Fe_{0.05}O_{4+δ} and La₄Ni_{2.1}Fe_{0.9}O_{10-δ}, whereby La₂Ni_{0.98}Fe_{0.02}O_{4+δ} is a single-phase material. The new dual-phase material 40 Mn_{1.5}Co_{1.5}O_{4-δ} - 60Ce_{0.9}Pr_{0.1}O_{2-δ} was synthesized by a rapid combustion sol-gel route and exhibits a good tolerance towards CO₂ as well as long-term stability.

In chapter 3 the partial substitution of alkaline-earth elements with rare-earth elements based on thermodynamic considerations via an Ellingham diagram was examined. The SrCo_{0.8}Fe_{0.2}O_{3-δ} material offers high oxygen permeation flux but poor CO₂ tolerance. By increasing the lanthanum content up to 60 wt.% a CO₂-tolerant membrane material with the nominal composition La_{0.6}Sr_{0.4}Co_{0.8}Fe_{0.2}O_{3-δ} was obtained as proven by *in-situ* XRD and TEM investigations. The verification of this thermodynamic approach was further supported by the studies of La_{0.6}Ca_{0.4}Co_{0.8}Fe_{0.2}O_{3-δ} and La_{0.6}Sr_{0.4}FeO_{3-δ}.

In chapter 4 the effect of the microstructure on permeation performance of SrCo_{0.8}Fe_{0.2}O_{3-δ} and Ba_{0.5}Sr_{0.5}Co_{0.8}Fe_{0.2}O_{3-δ} materials was investigated. It was found that in case of SrCo_{0.8}Fe_{0.2}O_{3-δ} the membranes with larger grain sizes exhibited a smaller oxygen permeation flux. In case of Ba_{0.5}Sr_{0.5}Co_{0.8}Fe_{0.2}O_{3-δ} the membranes with small grains exhibited a lower oxygen permeation flux. This increased with larger grains, whereby the oxygen permeation flux was found to be nearly independent of grain size in the regime of 24 to 42 μm average grain diameter. Furthermore, the long-term phase stability of Ba_{0.5}Sr_{0.5}Co_{0.8}Fe_{0.2}O_{3-δ} was investigated with regards to the partial substitution of B-site cations by zirconium.

Keywords: mixed ionic electronic conductors, oxygen-transporting materials,
carbon dioxide

Zusammenfassung

Die Welt ist stark von fossilen Brennstoffen als Energiequelle abhängig. Durch den steigenden Bedarf an Elektrizität werden neue weltweite Herausforderungen auf uns zukommen. Die globale Durchschnittstemperatur stieg im Verlauf der letzten Jahrzehnte stetig durch die Emission von Kohlenstoffdioxid (CO_2) und anderen Treibhausgasen an und wird zu schwerwiegenden Umweltschädigungen führen. Das Oxy-Fuel-Verfahren bietet die Möglichkeit, das entstehende CO_2 abzutrennen. Der für die Verbrennung benötigte reine Sauerstoff kann durch eine Membrangestützte Denitrogenierung erhalten werden, wozu gemischt ionisch-elektrisch leitende Materialien dienen. Diese Doktorarbeit stellt sieben originale Forschungsartikel vor, in denen die Stabilität von sauerstofftransportierenden Materialien untersucht wurde. Das zweite und dritte Kapitel behandeln eine erhöhte Toleranz gegen Karbonatbildung durch Verzicht auf oder partielle Substitution der Erdalkalielemente. Im vierten Kapitel wurde der Einfluss der Mikrostruktur auf den Sauerstofffluss und der Effekt von einer partiellen Substitution des B-Gitterplatzes von $\text{Ba}_{0.5}\text{Sr}_{0.5}\text{Co}_{0.8}\text{Fe}_{0.2}\text{O}_{3-\delta}$ durch Zirkon auf die Langzeitphasenstabilität untersucht.

In Kapitel 2 werden die erdalkalifreien Ruddlesden-Popper Phasen $\text{La}_2\text{NiO}_{4+\delta}$, $\text{La}_4\text{Ni}_3\text{O}_{10-\delta}$ sowie ein neues Zweiphasenmaterial vorgestellt. Die CO_2 -Toleranz von $\text{La}_2\text{NiO}_{4+\delta}$ wurde mittels *in-situ* Röntgendiffraktometrie (XRD) und Langzeitpermeationsexperimenten bestätigt. Der Effekt einer Substitution mit verschiedenvalenten Kationen auf den Sauerstofffluss wurde untersucht. Detaillierte Transmissionselektronenmikroskopie (TEM) und Mössbauerexperimente zeigten, dass die Verbindung $\text{La}_2\text{Ni}_{0.9}\text{Fe}_{0.1}\text{O}_{4+\delta}$ aus einem Phasengemisch von $\text{La}_2\text{Ni}_{0.95}\text{Fe}_{0.05}\text{O}_{4+\delta}$ und $\text{La}_4\text{Ni}_{2.1}\text{Fe}_{0.9}\text{O}_{10-\delta}$ besteht, während die Verbindung $\text{La}_2\text{Ni}_{0.98}\text{Fe}_{0.02}\text{O}_{4+\delta}$ reinphasig vorliegt. Das neue Zweiphasenmaterial $40 \text{ Mn}_{1.5}\text{Co}_{1.5}\text{O}_{4-\delta} - 60 \text{ Ce}_{0.9}\text{Pr}_{0.1}\text{O}_{2-\delta}$ zeigt eine gute CO_2 -Toleranz und Langzeitstabilität.

In Kapitel 3 wurde die partielle Substitution von Erdalkalielelementen mit Seltenen Erden auf Grundlage von thermodynamischen Überlegungen mittels eines Ellinghamdiagramms untersucht. Das $\text{SrCo}_{0.8}\text{Fe}_{0.2}\text{O}_{3-\delta}$ -Material bietet eine hohe Sauerstoffleitfähigkeit, aber nur eine schlechte CO_2 -Toleranz. Durch Erhöhung des Lanthangehaltes auf 60 Gew.-% konnte eine CO_2 -tolerante Membran erhalten werden. Dies wurde mittels *in-situ* XRD und TEM nachgewiesen. Die Gültigkeit des thermodynamischen Ansatzes konnte weiterhin durch Untersuchungen von $\text{La}_{0.6}\text{Ca}_{0.4}\text{Co}_{0.8}\text{Fe}_{0.2}\text{O}_{3-\delta}$ und $\text{La}_{0.6}\text{Ca}_{0.4}\text{FeO}_{3-\delta}$ bestätigt werden.

Im letzten Kapitel 4 wurde der Einfluss der Mikrostruktur auf den Sauerstofffluss von $\text{SrCo}_{0.8}\text{Fe}_{0.2}\text{O}_{3-\delta}$ und $\text{Ba}_{0.5}\text{Sr}_{0.5}\text{Co}_{0.8}\text{Fe}_{0.2}\text{O}_{3-\delta}$ untersucht. Es wurde herausgefunden, dass für $\text{SrCo}_{0.8}\text{Fe}_{0.2}\text{O}_{3-\delta}$ größere Körner einen verringerten Sauerstofffluss aufwiesen. Für $\text{Ba}_{0.5}\text{Sr}_{0.5}\text{Co}_{0.8}\text{Fe}_{0.2}\text{O}_{3-\delta}$ wiesen Membranen mit kleineren Körnern einen kleineren Sauerstofffluss auf. Dieser stieg mit größeren Körnern an und blieb im Bereich von 24 bis 42 μm nahezu konstant. Des Weiteren wurde der Effekt von Zirkon, welches auf den B-Gitterplatz von $\text{Ba}_{0.5}\text{Sr}_{0.5}\text{Co}_{0.8}\text{Fe}_{0.2}\text{O}_{3-\delta}$ eingebracht wurde, auf die Langzeitphasenstabilität untersucht.

Stichwörter: gemischte Ionen- und Elektronenleiter, sauerstofftransportierende Materialien, Kohlenstoffdioxid

Contents

Preface	i
Acknowledgement	iii
Abstract	v
Zusammenfassung	vii
1 Introduction	1
1.1 Motivation	1
1.2 Perovskites and related structures	4
1.2.1 Cubic perovskite structure ABO_3	4
1.2.2 Perovskite-related Ruddlesden-Popper phases $A_{n+1}B_nO_{3n+1}$	6
1.3 Preparation of oxygen-transporting materials	8
1.3.1 Sol-gel process	8
1.3.2 Preparation of dense oxygen-transporting membranes	9
1.4 Mixed ionic electronic conductors	10
1.4.1 Defect chemistry and ionic conductivity	10
1.4.2 Electrical conductivity	13
1.4.3 Oxygen transport through dense oxide membranes	15
1.5 Integration of OTMs into fossil-fuel power plants	17
1.5.1 Four-end process: requirement for CO_2 -tolerant membranes	17
1.5.2 Three-end process: requirement for high-flux and long-term stable membranes	20
1.6 Bibliography	21
2 CO_2-tolerant alkaline-earth free membrane materials	33
2.1 Summary	33
2.2 Effect of doping, microstructure and CO_2 on $La_2NiO_{4+\delta}$ -based oxygen-transporting materials	34
2.3 In-situ Mössbauer studies of ^{57}Fe -doped Ruddlesden-Popper type lanthanum nickel oxides	44
2.4 Rapid glycine-nitrate combustion synthesis of the CO_2 -stable dual-phase membrane $40Mn_{1.5}Co_{1.5}O_{4-\delta}$ - $60Ce_{0.9}Pr_{0.1}O_{2-\delta}$ for CO_2 capture via an oxy-fuel process	54
3 CO_2-tolerant alkaline-earth containing membrane materials	65
3.1 Summary	65
3.2 Effect of A-site lanthanum doping on the CO_2 tolerance of $SrCo_{0.8}Fe_{0.2}O_{3-\delta}$ oxygen-transporting membranes	66

3.3	Ca-containing CO ₂ -tolerant perovskite materials for oxygen separation	76
4	Studies of microstructure and phase stability of perovskites	89
4.1	Summary	89
4.2	Effect of microstructure on oxygen permeation of Ba _{0.5} Sr _{0.5} Co _{0.8} Fe _{0.2} -O _{3-δ} and SrCo _{0.8} Fe _{0.2} O _{3-δ} membranes	90
4.3	Investigation of Zr-doped BSCF perovskite membrane for oxygen separation in the intermediate temperature range	100
	Abbreviations	I
	List of Figures	III
	Publications included in this thesis	IV
	Publications not included in this thesis	V
	Contributions to conferences	VI
	Curriculum Vitae	VIII
	Erklärung zu dieser Dissertation	IX

1

Chapter 1

Introduction

1.1 Motivation

With the growing world population and the economic growth of developing countries comes an increasing demand for electricity, which is today mainly produced by fossil-fuel power plants [1]. In fact about 81 % of the world's energy is generated from this source, 13 % comes from renewable energies, and 6 % from nuclear power plants [2]. The worldwide contribution of fossil fuels is assessed to remain at this high level up to the year 2050 [3]. For Germany, predictions and calculations performed by the Sachverständigenrat für Umweltfragen (SRU) conclude that it is possible to obtain a fossil-fuel free electricity generation for this period of time [4]. The major problem is that the operation of fossil-fuel power plants is not sustainable. This is not only in means of depletion of natural resources, but although by production of greenhouse gases, which are released into the atmosphere and contribute to global warming. The biggest player in this connection is carbon dioxide (CO_2) with a total estimated emission of 32 billion tonnes over the period from the year 1751 to 2008 [5]. More than 40 % of the anthropogenic CO_2 emissions are released by conventional fossil-fuel power plants [6]. The problem has been realized in politics already in 1997 as the United Nations framework convention on climate change (UNFCCC) initiated the Kyoto Protocol to contain greenhouse gas emissions and global warming. Until now 191 states have signed and ratified the treaty [7]. To reduce the green house gas emissions, it is not only necessary to promote the use of renewable energies, but also to improve existing technologies to work in a more sustainable way. The challenge of “green” materials science in this context is therefore to develop new techniques, processes, or materials, which can enhance the energy efficiency or lead to a drastic reduction of CO_2 emissions.

The mixed ionic electronic conducting (MIEC) materials with perovskite or

perovskite-related structures offer a promising way to encounter the problem of CO₂ emissions of fossil-fuel power plants in the near future. The possibility to tailor-make materials for specific applications provides hundreds of opportunities for materials design. A lot of research was already conducted in the last decades [8, 9]. By using MIEC materials as dense oxygen-transporting membranes (OTMs), which allow to separate oxygen from gas mixtures¹ with unrivalled selectivity for oxygen, a wide number of industrial processes, where the supply or removal of oxygen is required, can be optimized [11, 12]. In Fig. 1.1 the principle of operation of an OTM is schematically illustrated and some important applications are displayed, which will be discussed briefly on the following pages.

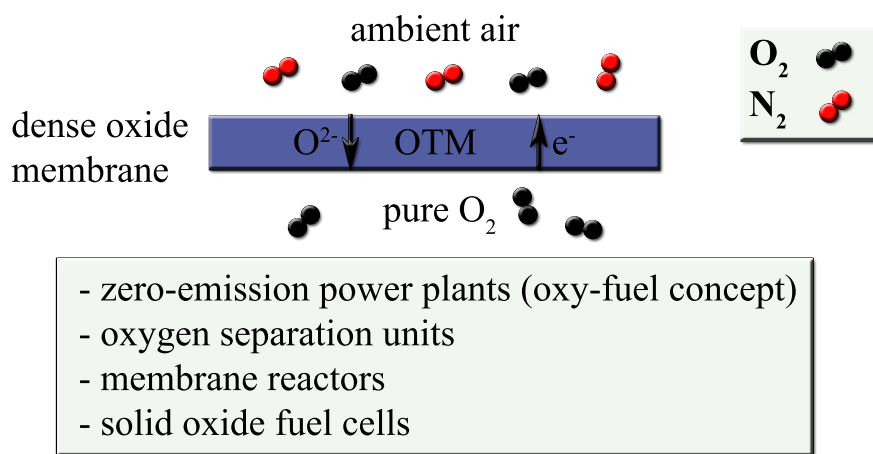


Figure 1.1: Possible applications of oxygen-transporting membranes (OTMs).

A recent hot topic in research is the concept of carbon capture and storage (CCS) technologies [13–17]. A possible way to combine fossil-fuel power plants with CCS is the concept of oxy-fuel combustion with the aim to reduce the CO₂ emission from fossil-fuel power plants leading to near zero emission [18, 19]. In this process the fuel is directly combusted with pure oxygen. The nitrogen is excluded at the beginning and does not need to be removed as nitrogen oxides by a complicated operation after the combustion. The reaction products, mainly CO₂ gas and water vapor, can then easily be separated by condensation of the water. The sequestered CO₂ can be readily stored [20]. Final storage can be in underground formations such as depleted mines or offshore in the oceans [21–24].

Another possible application, which should be only mentioned in passing here,

¹ This is in most applications ambient air, which is a mixture of approximately 78 vol.% N₂, 21 vol.% O₂, and 1 vol. % minor components [10].

is the use of MIEC materials in membrane reactors and catalysis. This sophisticated concept allows the coupling of a chemical reaction and product separation. It has been demonstrated for important petrochemical catalytic processes such as the oxidative coupling of methane to ethylene or ethane (OCM) [25], the partial oxidation of methane to syngas (POM) [26], or direct decomposition of nitrous oxide to nitrogen by oxygen removal [27].

The use of MIEC materials in solid oxide fuel cells (SOFCs) is another very important application [28]. The main advantage is the possibility to directly convert chemical energy into electrical energy with higher overall efficiencies compared to heat engines. The maximum system efficiency may be even higher than 80% [29]. For ceramic SOFCs, which have to be operated at elevated temperatures to attain a sufficient ionic and electronic conductivity, a variety of fuels such as hydrogen, natural gas or hydrocarbons can be used [30]. The main features to have are catalytic activity for oxygen reduction and high electrical conductivity of the cathode materials. This predestines certain MIEC materials for the use in SOFCs.

In the 1980's the group around Yasutake Teraoka discovered the MIEC properties of $\text{La}_{1-x}\text{Sr}_x\text{Co}_{0.4}\text{Fe}_{0.6}\text{O}_{3-\delta}$ perovskites [31]. They were also the first who investigated the effect of A-site and B-site doping on the properties of the lanthanum cobalt perovskites and gave birth to a whole new field of materials design [32]. However, the major problem of these perovskites is the high thermal expansion, which leads to low compatibility with other membrane reactor components. The resulting mechanical stress may lead to cracks or problems with the sealing, which compromise gas tightness of membranes. Another problem was the instability under large partial pressure gradients. The cubic structure of the known high-flux material $\text{SrCo}_{0.8}\text{Fe}_{0.2}\text{O}_{3-\delta}$ tends to collapse into the oxygen-ordered Brownmillerite phase in reducing atmospheres [33–35]. In 2000, Shao discovered that by partial substitution of strontium with 50 mol% of the larger barium cation a stabilization of the cubic perovskite structure occurs. He showed that it significantly improves the stability in low and high oxygen partial pressure [36–38]. However, another problem still prevails. For applications in highly CO_2 -exposed environments these alkaline-earth elements containing high-flux membranes are not suitable due to their tendency to form carbonates [39, 40]. It is possible to increase the CO_2 tolerance by avoiding the alkaline-earth elements. However, it is a thin line to find the optimum perovskite composition in matters of highest possible oxygen permeation flux and sufficient stability towards CO_2 . A possible solution to this problem is the use of materials such

as the Ruddlesden-Popper phases $\text{La}_{n+1}\text{Ni}_n\text{O}_{3n+1}$ ($n = 1, 2, \text{ and } 3$) [41, 42] or development of new dual-phase materials such as 40wt.% NiFe_2O_4 -60wt.% $\text{Ce}_{0.9}\text{Gd}_{0.1}\text{O}_{2-\delta}$ [43]. In the dual-phase membrane concept an ion and an electron conductor form interpenetrating, percolating networks, which lead to the MIEC properties.

In the presented thesis, MIEC materials were investigated regarding their tolerance towards CO_2 , the influence of microstructure on oxygen flux and the stabilization of known high-flux materials by selective substitution on the B site. Chapter 2 presents the perovskite related Ruddlesden-Popper phases $\text{La}_{n+1}\text{Ni}_n\text{O}_{3n+1}$ ($n = 1, 2, \text{ and } 3$) with high tolerance against CO_2 by avoiding alkaline-earth elements. In Chapter 3 rare-earth containing perovskite and dual-phase materials were partially doped with alkaline-earth elements (calcium, strontium) and the threshold value for obtaining CO_2 -tolerant materials was identified, which is not more than 40 mol% of alkaline-earth elements on the A site. Chapter 4 is dedicated to microstructure analysis and the impact on oxygen permeation flux. Furthermore, the stabilization of the cubic perovskite $\text{Ba}_{0.5}\text{Sr}_{0.5}\text{Co}_{0.8}\text{Fe}_{0.2}\text{O}_{3-\delta}$ (BSCF) structure in the intermediate temperature range (700-850 °C) by zirconium doping was investigated.

1.2 Perovskites and related structures

1.2.1 Cubic perovskite structure ABO_3

In the year 1829, Alexander von Humboldt led his second great expedition into the Ural Mountains [44]. The mineralogist Gustav Rose went with him and several years later, in 1839, Oberbergmeister Kämmerer delivered an unknown mineral from Achmatowsk in the Ural Mountains to Rose in Berlin. Rose investigated the new mineral and he and Kämmerer decided to name it perovskite after Count Lev Alexeyevich Perovsky to recognize his affords in the field of mineralogy [45]. Some confusion is caused by the fact that the name perovskite denotes an entire class of compounds and the particular composition CaTiO_3 , which was discovered in 1839. Speaking of perovskite structure typically implies cubic $Pm\bar{3}m$ (s.g. 221) structure, whereby the original CaTiO_3 exhibits orthorhombic $Pbnm$ (s.g. 62) structure with lattice parameters $a = 5.39 \text{ \AA}$, $b = 5.45 \text{ \AA}$, and $c = 7.65 \text{ \AA}$, and number of formula units per unit cell $Z = 4$ [46]. The prototype of the ideal cubic perovskite structure therefore is SrTiO_3 with $a = 3.905 \text{ \AA}$; $Z = 1$ [47], as defined by Megaw [48]. The atomic parameters as fractions of the unit cell are for the A-site cation

0, 0, 0 (Wyckoff position 1a), for the B-site cation $\frac{1}{2}, \frac{1}{2}, \frac{1}{2}$ (Wyckoff position 1b), and for the oxygen anion $\frac{1}{2}, \frac{1}{2}, 0$; $\frac{1}{2}, 0, \frac{1}{2}$; $0, \frac{1}{2}, \frac{1}{2}$ (Wyckoff position 3c) [49]. The ideal perovskite prototype is ABO_3 . It is formed of large cations on the A site (alkaline, alkaline-earth, or rare-earth cations), which are located in the middle of the cubic unit cell, smaller cations on the B site (preferentially transition metal cations), which are located at the corners of the cube, and oxygen anions, which are located at the edges. Six oxygen atoms form a perfect octahedron around the smaller B-site cations with an angle of 90° and equidistant B-O bonds (Fig. 1.2a). The corner-sharing octahedra form a three dimensional network, in which the larger A-site cations are placed inside the cavities and are coordinated by 12 oxygen atoms (Fig 1.2b). Alternatively, the structure can be described as face-centered cubic (fcc) sub lattice of the closed-packed A-site cations and oxygen anions stacked along the cubic [111] direction. Every fourth octahedral hole, which is exclusively surrounded by oxygen, is then occupied by a B-site cation.

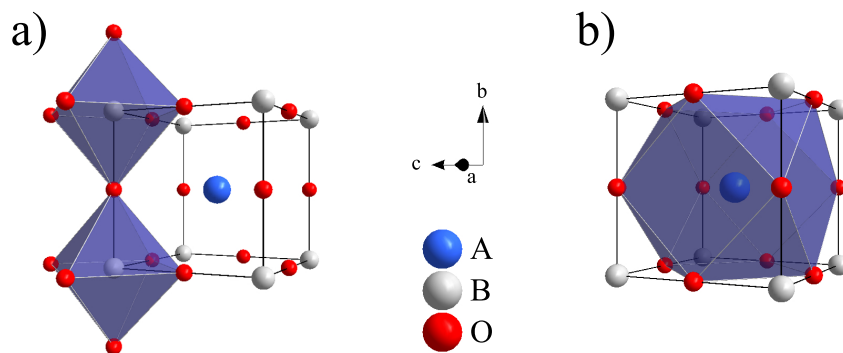


Figure 1.2: Unit cell of the ABO_3 perovskite with a) octahedral coordination of B-site cations and b) dodecahedral coordination of A-site cations (atomic radii are not drawn to scale).

It was Goldschmidt, who discovered in 1926, a simple but efficient way to predict the formation of perovskite structure [50]. By assuming a close-packing of hard spheres, he found that the ionic radii of the involved ions are fundamental. The ratio of the atomic radii defines the polyhedron formed and the packing of these polyhedra follows simple rules, as later attested by Pauling [51]. For the ideal cubic perovskite the A-site cations should have nearly the same size as the anions to fit in the 12 fold coordinated dodecahedra. The face diagonals can be described in terms of ionic radii as $2r_a + 2r_O$ and the edges as $2r_b + 2r_O$. By applying the Pythagorean

theorem the following equation with Goldschmidt's tolerance factor t can be derived:

$$t = \frac{r_A + r_O}{\sqrt{2}(r_B + r_O)} \quad (1.1)$$

Per definition, the ideal cubic perovskite structure² exhibits a tolerance factor of $t = 1$. It was found that ABO_3 compounds with t between 0.9 and 1.05 may crystallize in the cubic perovskite structure. However, the tolerance factor only offers a rough approximation, if the ABO_3 compound forms perovskite structure and which ionic radii are tolerated by the perovskite structure³. The concept of Goldschmidt's crystal chemistry led to intelligent material design and to hundreds of new phases just by estimation of the ionic radii. Today perovskites are known for their versatility reaching from $YBa_2Cu_3O_{7-\delta}$ (superconductivity) [52], $SrTiO_3$ (photo catalysts) [53], $BaTiO_3$ (capacitors) [54], $Pb(Zr_{0.52}Ti_{0.48})O_3$ (piezoelectrics) [55], $Co/PbZr_{0.2}Ti_{0.8}O_3/La_{0.7}Sr_{0.3}MnO_3$ (multiferroics) [56] and $Ba_{0.5}Sr_{0.5}Co_{0.8}Fe_{0.2}O_{3-\delta}$ (mixed-ionic electronic conductors) [36] to name only a few.

1.2.2 Perovskite-related Ruddlesden-Popper phases

$A_{n+1}B_nO_{3n+1}$

In 1955, Balz and Plieth discovered an unknown phase which was obtained as single crystals from melts of KF and NiF_2 [56]. These single crystals with the K_2NiF_4 structure were characterized by X-ray diffraction (XRD). Later, in 1957, Ruddlesden and Popper synthesized new compounds with the K_2NiF_4 structure by a solid state route [57]. They showed that Sr_2TiO_4 , Ca_2MnO_4 , and $SrLaAlO_4$ exhibited the tetragonal K_2NiF_4 structure discovered by Balz and Plieth. In their honor the new phases were named Ruddlesden-Popper phases. These phases show a strong relationship to the perovskites as they are constituted by an arrangement of ABO_3 perovskite and A_2O_2 rock salt-type layers along the crystallographic c -axis. Depending on the number of perovskite layers different members of the $A_{n+1}B_nO_{3n+1}$ structure with $n = 1, 2,$ and 3 are possible. A_2BO_4 ($n = 1$) consists of alternating perovskite and rock-salt layers (Fig. 1.3a). By increasing the number of perovskite layers ($n = 2$ or $n = 3$), the higher order Ruddlesden-Popper phases $A_3B_2O_7$ (Fig 1.3b) and $A_4B_3O_{10}$ (Fig. 1.3c) are formed. An infinite number of perovskite layers

² The prototype of the ideal cubic perovskite structure is $SrTiO_3$ with $t = 1$ [48].

³ After Goldschmidt the perovskite structure forms for $0.8 < t < 1$ [50].

forms the known ideal ABO_3 perovskite structure (Fig 1.3d). Promising OTM mate-

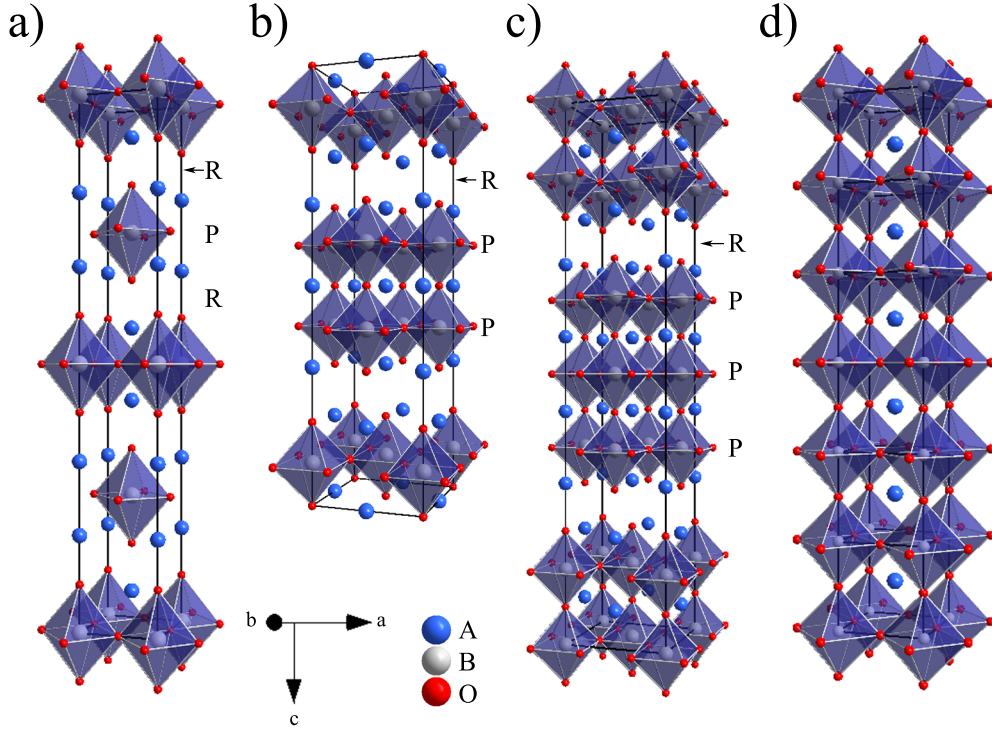


Figure 1.3: Presentation of the different Ruddlesden-Popper phases with octahedrally coordinated B-site cations. The rock-salt layers (R) and the perovskite layers (P) are indicated. a) super cell of A_2BO_4 b) unit cell of $A_3B_2O_7$ c) unit cell of $A_4B_3O_{10}$ d) super cell of ABO_3 .

materials with the Ruddlesden-Popper structure are the lanthanum nickelate phases (see chapter 2) and especially the $La_2NiO_{4+\delta}$ compound. It is an orthorhombically distorted polymorph of the tetragonal K_2NiF_4 structure due to the mismatch of lattice parameters of the two layers. This is minimized by a compression of the perovskite layers by slight tilting of the NiO_6 octahedra and an expansion of the rock-salt layers most probably aided by the insertion of excess oxygen ions [58]. Upon heating the structure adopts tetragonal structure at high temperatures, which is metastable at cooling to room-temperature [59]. The atomic parameters as fractions of the unit cell are for the lanthanum cation 0, 0, 0.3625 (Wyckoff position 4e), for the nickel cation 0, 0, 0 (Wyckoff position 2a), for the oxygen O1 anion $0, \frac{1}{2}, 0$ (Wyckoff position 4c), and for the oxygen O2 anion 0, 0, 0.1797 (Wyckoff position 4e) [60]. The structure is prominent for the ability to accommodate interstitial oxygen O3 (Fig 1.4), which is then located at $\frac{1}{4}, \frac{1}{4}, \frac{1}{4}$ (Wyckoff position 8e) [61]. The $La_2NiO_{4+\delta}$

system can take up excess oxygen ranging from $0 \leq \delta \leq 0.25$ at the interstitial positions [62]. This excess oxygen is responsible for the good ionic conductivity of the materials.

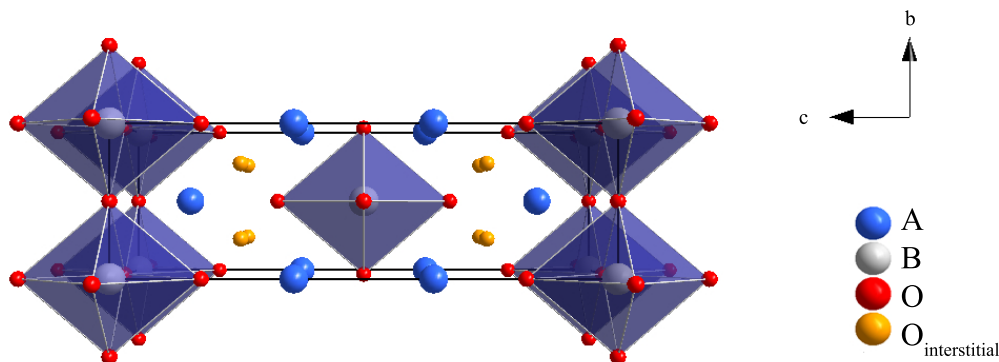


Figure 1.4: Perspective view of tetragonal $\text{La}_2\text{NiO}_{4+\delta}$ viewed along $[100]$ axis showing the interstitial oxygen position at $\frac{1}{4}, \frac{1}{4}, \frac{1}{4}$ (Wyckoff position 8e) [61].

1.3 Preparation of oxygen-transporting materials

1.3.1 Sol-gel process

There are several methods to produce oxide powders such as solid state reaction, co-precipitation, spray pyrolysis, hydrothermal synthesis, and sol-gel synthesis [63]. The sol-gel technique offers a simple and fast way to obtain high purity and well homogeneous powders, especially if complex stoichiometries are involved [64]. All of the materials in this thesis were produced by a modified Ethylenediaminetetraacetic acid (EDTA) and Citric acid (CA) sol-gel synthesis approach. The combination of EDTA and CA offers very effective chelating agents, which form complexes with a large variety of metal cations [65]. Fig. 1.6 displays the sol-gel route as it was used throughout the thesis [66, 67].

First of all calculated amounts of EDTA and CA were added to water. The pH value was adjusted to be around 9 to allow complete dissolution of the precursor powders. Then stoichiometric amounts of metal-salt precursor solutions were added. By monitoring the pH value the degree of polymerization could be roughly controlled

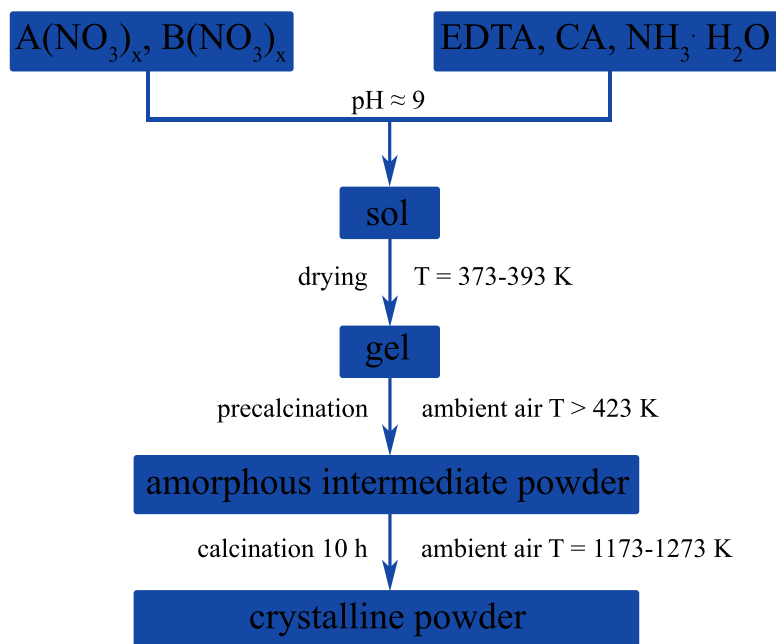


Figure 1.5: Flowchart of the used sol-gel route.

[68]. The solution was stirred over night at 373-393 K to evaporate most of the water. After that a highly viscous gel was formed, which was a three-dimensional, metal-organic polymer network. The metal precursors were homogenously distributed in the gel. This accounts for a major-time saving compared to other preparations methods such as solid state reaction. The obtained gel was then precombusted in a heating mantle in ambient air starting at 423 K. The temperature increased during the process to around 773 K due to initiated self combustion. Most of the organic residues were burned out as CO, CO₂, and nitrogen oxides. After that a fine nano-scaled amorphous intermediate powder precursor was obtained, which consists mainly of metal oxides and carbonates [69]. In a subsequent sintering step at 1173-1273 K the desired crystalline powder was formed by solid state reaction of the amorphous components [67, 70].

1.3.2 Preparation of dense oxygen-transporting membranes

An important step to characterize the oxygen permeation flux of the powders was the preparation of dense ceramic membranes. The powders, which were obtained by

the sol-gel synthesis, have to be pressed and sintered. Depending on the treatment of the green membrane bodies different microstructures can be archived, which can influence the membrane properties. In the sintering step the material will be heated just below the melting point. The surface free energy will be reduced, which results in a decrease of free energy of the system and finally in a densification of the sample [71]. This comes together with mass transport by diffusion of atoms and ions inside the sample by defects. These defects are imperfections of the crystal which form depending on temperature and surrounding gas pressure (see chapter 1.4.1). The absolute rates of sintering or grain growth are controlled by defect concentration, because they control the rate at which matter is transported [71]. The microstructure, the density, and the grain size are not only controlled by the maximum sintering temperature, but also by holding time at that temperature and heating and cooling rates. A crucial step is to find the optimum sintering conditions for each composition. In this thesis the green membrane bodies were uniaxially pressed with diameter of 16 or 18 mm and approximately 1 mm thickness. The green bodies were then sintered according to the empirically found optimum sintering conditions.

1.4 Mixed ionic electronic conductors

1.4.1 Defect chemistry and ionic conductivity

The ionic conductivity of many oxide compounds adheres closely to their defect chemistry. The perfect crystal at zero Kelvin and in vacuum is free of defects, but with rising temperature and interaction with the gas atmosphere, which in the case of oxides is related to the oxygen partial pressure, defects are formed as an energetic relation between Gibbs free energy, enthalpy and entropy. By the formation of defects the entropy increases, which lead to a minimum of the Gibbs free energy. This is defined by the following relation [72, 73].

$$\Delta G = \Delta H - T\Delta S \quad (1.2)$$

In the field of MIECs point defects such as missing atoms (vacancies) or additional atoms (interstitials) play a decisive role for their performance.

1.4.1.1 Ionic conduction via vacancies in perovskite oxides

In perovskite oxides the oxygen conduction follows a vacancy mechanism. The ideal ABO_3 perovskite consists of a large fixed valent cation on the A site with a low oxidation state such as Ba^{2+} or Sr^{2+} and a smaller multivalent transition cations such as $Co^{2+/3+/4+}$ or $Fe^{2+/3+/4+}$ on the B site. It is known that for example BSCF is characterized by the ability to accommodate a large oxygen deficit with retention of the cubic perovskite structure. The overall higher positive charge on the cations is compensated by the formation of oxygen vacancies and electrons. This is normally presented in Kröger-Vink notation [74].



The created electrons are then responsible for the electronic conductivity (see chapter 1.4.2). The migration of the oxygen species through the lattice was shown to follow a vacancy mechanism through the faces of the BO_6 octahedra (Fig. 1.6a) [75].

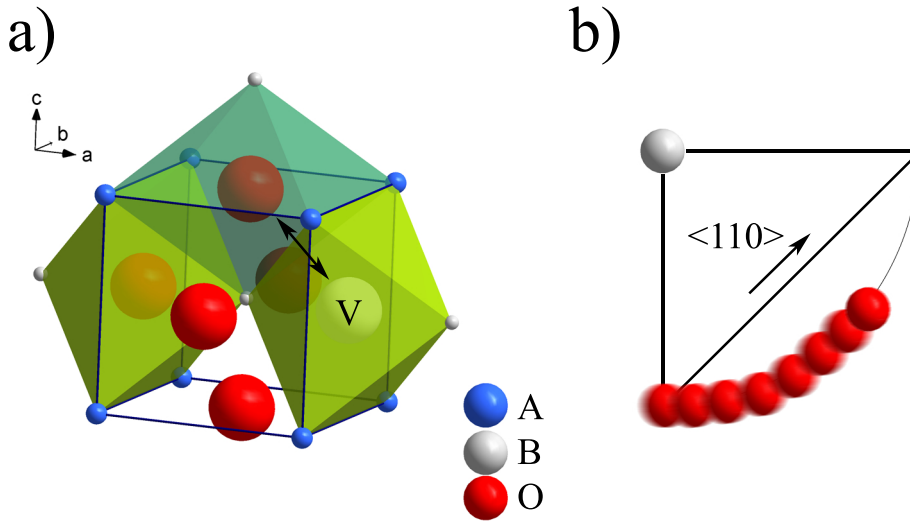


Figure 1.6: a) Unit cell of the ABO_3 perovskite with octahedral coordination of the oxygen ions. The white atoms indicate oxygen vacancies and the black arrow indicate oxygen diffusion along the $[10-1]$ direction into an unoccupied B_6O octahedron. b) Projection of the $\langle 110 \rangle$ edge of a B_6O octahedron and curved path for oxygen migration with constant B-O distance.

This triangle-shaped face is spanned by two A-site and one B-site cations. The migration can be expressed by a geometrical approach just taking the ionic radii of

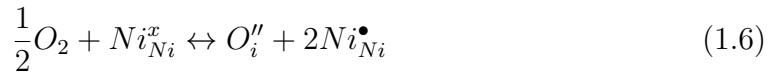
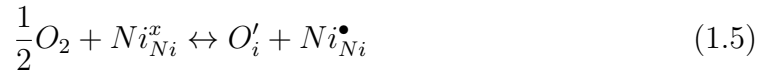
the involved cations into account as was shown by Cook & Sammells [76].

$$r_{critical} = \frac{r_A^2 + \frac{3}{4}(a_0^2) - \sqrt{2}(a_0)(r_B) + r_B}{2r_A + \sqrt{2}a_0 + 2(r_B)} \quad (1.4)$$

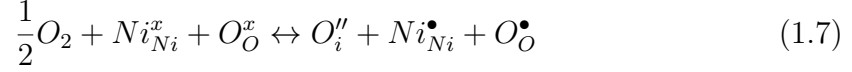
With r_a the radius of the A-site cation, r_b the radius of the B-site cation, and a_0 the cubic unit cell. The value $r_{critical}$ is defined as a circle just touching the radii of the three involved cations. However, recent experimental and computational studies reveal that the migration does not follow a straight line but rather a curved migration path, which keeps the B-O distance constant (Fig. 1.6b). The curved path is energetically more favorable than the direct path [77]. This was shown for a lot of perovskite compositions such as $\text{La}_{0.6}\text{Sr}_{0.4}\text{Co}_{0.8}\text{Fe}_{0.2}\text{O}_{3-\delta}$ [78], $\text{La}_{0.6}\text{Sr}_{0.4}\text{CoO}_{3-\delta}$ [80], $\text{La}_{0.8}\text{Sr}_{0.2}\text{Ga}_{0.8}\text{Mg}_{0.15}\text{Co}_{0.05}\text{O}_{2.8}$ [80], and $\text{La}_{0.64}\text{Sr}_{0.4}\text{Ti}_{0.92}\text{Nb}_{0.08}\text{O}_{2.99}$ [81]. This migration path should be common in mixed ionic electronic conductors with perovskite structure.

1.4.1.2 Ionic conduction via interstitials in perovskite-related Ruddlesden-Popper oxides

The layered $\text{A}_2\text{BO}_{4+\delta}$ Ruddlesden-Popper structure exhibits the ability to take up additional oxygen inside the rock-salt layers. This excess has to be compensated by one of the following mechanisms: cation antisite, oxygen vacancies, oxidized lattice oxygen ions or oxidized nickel ions. For $\text{La}_2\text{NiO}_{4+\delta}$ defect energy calculations show that the most likely mechanism involves oxidation of nickel ions or lattice oxygen ions [?]. The amount of excess oxygen is a critical value. For low amounts of excess oxygen, i.e. small delta values, the existence of isolated defects is most probable and the charge-compensating electron holes are introduced on the nickel sites by the following equations.



With increasing excess oxygen, defect clustering becomes significant and the electron holes are additionally compensated on lattice oxygen sites by the following equation.



The generated holes remain preferentially in the NiO planes. The excess oxygen is introduced in the interstitial position in the La_2O_2 planes (Fig. 1.4, Wyckoff position 8e). Experimental studies show conflicting results. Buttrey et al. describes O_2^{2-} as the main defects [82]. Several other groups believe that the main charge compensation mechanism involves the nickel site with a mixed valent $Ni^{2+/3+}$ state [83–85]. This discrepancy may be related to different delta values. The migration of mobile species in $La_2NiO_{4+\delta}$ takes place via an interstitial mechanism. Migration in the a-b plane along the rock-salt layers is reported to require lower activation energies than through the perovskite sheets along the c axis, so that the oxygen conduction is highly anisotropic [58]. The migrating oxygen ions move into the apical oxygen sites whereby charge transfer occurs after the following equation.



The migration through the perovskite layers happens also via an interstitial mechanism, but with far higher activation energies. The migrating oxygen is bonded to Ni^{3+} and this complex migrates preferentially through the NiO planes rather than the La_2O_2 planes. The calculated activation energies are lower than the experimental values on polycrystalline $La_2NiO_{4+\delta}$ powder [86], because in a randomly oriented sample both mechanisms contribute to the overall measured activation energy. If it is possible to obtain specially textured samples, the high anisotropy could be used as an advantage.

1.4.2 Electrical conductivity

The electrical conductivity is differentiated in n-type and p-type conductivity [87]. In the case of n-type conduction electrons are the main charge carriers, which are formed by introducing oxygen vacancies according to equation 1.3. In the case of p-type conduction the main charge carriers are electron holes, which are formed by the reduction of B-site cations according to:



The type of conduction of metal oxides is defined by the different defect reactions and equilibria and their dependence on temperature and the oxygen partial pressure.

The following equations show all important conditions.



By applying the law of mass action the resulting defect concentrations can be calculated and it is common to present the results graphical as Brouwer diagrams⁴. Most of the mixed ionic electronic materials such as acceptor doped ABO_3 perovskites and the $La_2BO_{4+\delta}$ Ruddlesden-Popper-phases exhibit a positive Seebeck coefficient, which means predominant p-type conduction at ambient oxygen pressure and low temperatures. In the case of a $LaBO_3$ perovskite, which is acceptor doped with divalent strontium ions the additional negative charge can be compensated by reduction of B-site cations (electronic compensation) or release of oxygen and formation of vacancies (ionic compensation) [89]. At lower temperatures the compensation is mainly electronic. The electron holes as localized charge carriers follow a thermally activated small polaron hopping mechanism along the O-B-O bonds. This behavior can be described with an Arrhenius approach [90].

$$\sigma_e = \frac{C}{T} \exp \frac{-E_a}{kT} \quad (1.14)$$

In this equation E_a is the activation energy of oxygen migration, k is the Boltzmann constant and C is the pre-exponential constant, which includes carrier concentration and other material-dependent parameters. With increasing temperature the conductivity reaches a maximum and then decreases slowly, which is associated with oxygen vacancy formation and the consumption of electron holes due to ionic compensation.

⁴In a Brouwer diagram also known as a Kröger-Vink diagram the concentration of defects is plotted in a log-log representation against the oxygen partial pressure [87, 88].

1.4.3 Oxygen transport through dense oxide membranes

The main driving force of oxygen transport is the difference in the oxygen chemical potential on the feed and sweep side of the membrane. Therefore, the migration oxygen anions are transported along the gradient of chemical potential ($\nabla\mu$). The process of oxygen transport is divided in three steps [91–93]. i) surface exchange with the gas phase on the feed side ii) bulk diffusion iii) and surface exchange on the sweep side of the membrane. Hereby the slowest process is the overall rate limiting step.

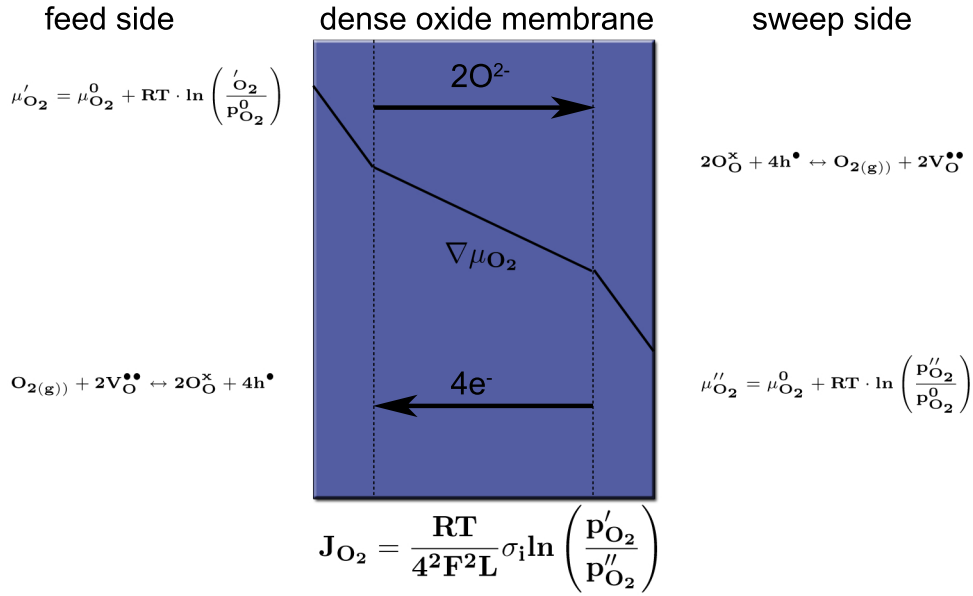


Figure 1.7: The oxygen permeation through a dense MIEC oxide membrane with indicated gradient of oxygen partial pressure. Surface exchange reactions on the feed and sweep side and Wagner equation for the bulk diffusion controlled regimant.

For relatively thick membranes the oxygen flux can be described by Wagner theory [94–96].

$$J_{O_2} = \frac{1}{16F^2L} \int_{\mu''_{O_2}}^{\mu'_{O_2}} \frac{\sigma_e \cdot \sigma_i}{\sigma_e + \sigma_i} d\mu_{O_2} \quad (1.15)$$

With F = Faraday constant, L = membrane thickness, μ = chemical potential, σ_e = electrical conductivity, σ_i = ionic conductivity.

By decreasing the thickness, bulk diffusion becomes insignificant and the exchange

processes on the gas interfaces are rate limiting. In this case the Wagner equation can not be used anymore. To distinguish between diffusion and kinetic controlled regiments the oxygen permeation flux of membranes with different thicknesses is measured. Another approach was introduced by Bouwmeester et al. [93], who introduced the critical thickness L_c . It is defined as the quotient of the ionic diffusion coefficient (D_i) or tracer diffusion coefficient (D^*) and the surface exchange coefficient (k). These values can be obtained from ^{18}O - ^{16}O isotope exchange secondary ion mass spectrometry (SIMS) measurements.

$$L_c = \frac{D_i}{k} = \frac{D^*}{k} \quad (1.16)$$

This equation can give a rough estimation about surface controlled ($L \ll L_c$) or bulk diffusion controlled ($L \gg L_c$) regiments of thin and thick membranes. In most cases both processes will affect the obtained oxygen permeation flux [93]. The bulk diffusion can be limited either by the oxygen migrating species, the electrons, or the electron holes. The electronic conductivity of the MIECs in focus is typically several magnitudes higher than the ionic conductivity [97]. The contribution of electrical conductivity can be disregarded and the Wagner equation simplifies to:

$$J_{O_2} = \frac{1}{16F^2L} \int_{\mu'_{O_2}}^{\mu'_{O_2}} \sigma_i d\mu_{O_2} \quad (1.17)$$

The ionic conductivity of the migrating species can be described by the Nernst-Einstein equation in dependence of concentration and diffusion coefficient [98]:

$$\sigma_i = \frac{4F^2}{RT} [c_{V_{O^{\bullet\bullet}}}] D_{V_{O^{\bullet\bullet}}} \quad (1.18)$$

This leads to:

$$J_{O_2} = \frac{1}{4LRT} \int_{\mu'_{O_2}}^{\mu'_{O_2}} [c_{V_{O^{\bullet\bullet}}}] D_{V_{O^{\bullet\bullet}}} d\mu_{O_2} \quad (1.19)$$

Assuming a constant diffusion coefficient and constant concentration of vacancies by using a small oxygen pressure gradient ($\Delta p = 0.01$ atm) the equation can be integrated to [100]:

$$J_{O_2} = \frac{[c_{V_{O_2}}]}{4L} D_{V_{O_2}} \ln \frac{p'_{O_2}}{p''_{O_2}} \quad (1.20)$$

However, since the diffusion coefficient and the concentration of vacancies depend heavily on the oxygen partial pressure this equation can not be used for larger pressure differences. More detailed discussion is available in literature [101–104].

1.5 Integration of OTMs into fossil-fuel power plants

A worthwhile approach to produce the required oxygen for the oxy-fuel combustion process is the use of OTMs. The membranes can be operated in a four-end or three-end process [105].

1.5.1 Four-end process: requirement for CO₂-tolerant membranes

In four-end operation the membrane is operated in sweep-gas mode using the formed flue gas CO₂ as sweep. This sweep-gas operation can remarkably save energy compared to other operations modes such as high-pressure operation or vacuum extraction [106, 107]. Furthermore, the four-end operation offers the great advantage of diluting the oxygen to optimize the flame temperature in the combustor and as well to use the generated process heat to hold the MIEC membrane unit at the high temperatures, which are needed for sufficient oxygen permeation performance [108–110]. Fig. 1.8 shows the concept of an oxy-fuel combustion power plant with integrated OTM module.

The known high-flux materials are on basis of alkaline-earth elements, mainly barium and strontium, and several studies show the severe degradation of CO₂ on the oxygen permeation flux [39, 40, 111]. A good approach to design CO₂-tolerant materials is to use thermodynamic values to estimate the stability of certain oxides against carbon dioxide. It was proven that the stability of a carbonate compound is directly connected to the polarizing power of the associated cation due to distortion and weakening of the intra-ionic bonds in the carbonate anion [112]. Since the polarizing power of a cation depends inversely on the cation size⁵, the alkaline cations Cs, Rb, K, Na form the most stable carbonate compounds. The stability

⁵This is only valid for a constant charge. The polarizing power of a cation can be estimated from the ratio of the charge to the ionic radius ($\frac{Z}{r}$) [50].

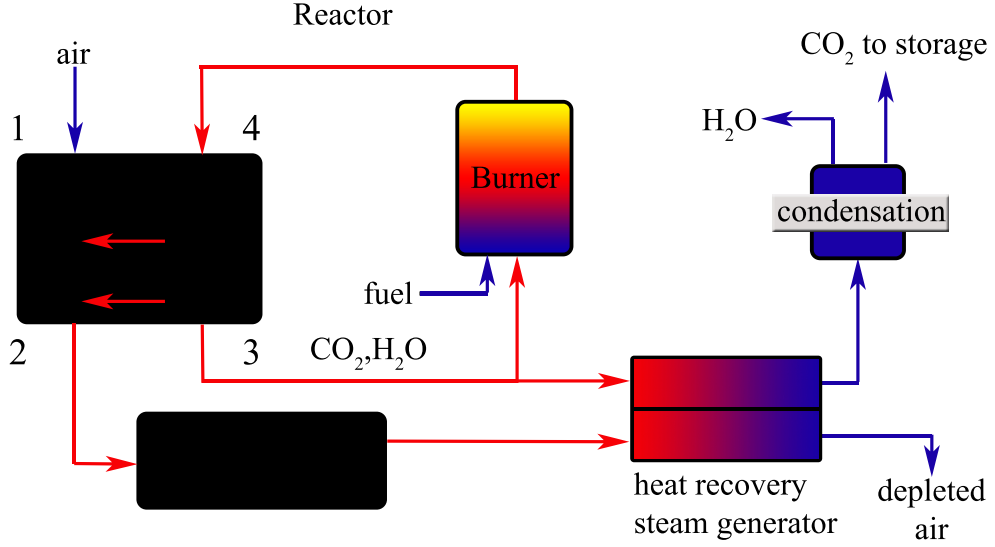


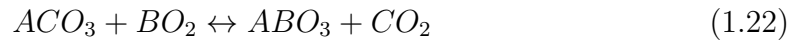
Figure 1.8: Principle of a oxy-fuel combustion power plant operated in four-end mode with integrated oxygen-transporting membrane module (after [105, 108]).

of the carbonates then decreases for the alkaline-earth elements from $Ba > Sr > Ca \geq$ the rare-earth cations (such as La, Ce, Gd). The rare-earth cations are similar in size to calcium, but exhibit normally a higher charge (3+ compared to 2+) [113]. This is also proven by explicit calculation of the decomposition reactions in an Ellingham diagram (Fig 1.9).

The approach of avoiding the alkaline-earth elements was followed in Chapter 2 by using the Ruddlesden-Popper $La_2NiO_{4+\delta}$ phases. Further thermodynamic considerations lead to the perovskite stabilization energies introduced by Yokokawa et al. [116].

$$\Delta_r H(ABO_3) = \Delta H_f^0(ABO_3) - \Delta H_f^0(AO_n) - \Delta H_f^0(BO_m) \quad (1.21)$$

Considering the following reaction equation 1.22 describes the perovskite formation from carbonate and metal oxide.



Then the following reaction energy can be formed:

$$\Delta_r H^0(eq.1.22) = \Delta_r H^0(ABO_3) - \Delta_r H^0(ACO_3) \quad (1.23)$$

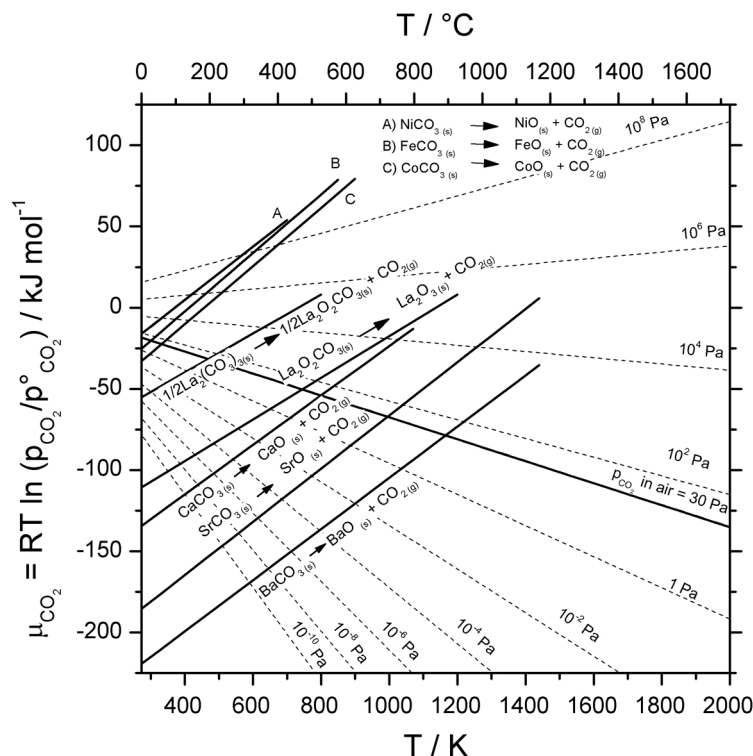


Figure 1.9: Ellingham diagram with decomposition temperatures of carbonates under different CO_2 partial pressures. Chemical potential of CO_2 above NiCO_3 , FeCO_3 , CoCO_3 , $\text{La}_2\text{O}_2\text{CO}_3$, SrCO_3 , and BaCO_3 were calculated from thermodynamic data [114]. The chemical potential of $\text{La}_2(\text{CO}_3)_3$ was determined experimentally [115]. The dashed lines represent the chemical potential of CO_2 in the surrounding atmosphere for different partial pressures. $p^\circ(\text{CO}_2)=101.3 \text{ kPa}$ refers to standard conditions.

A stabilization of the perovskite structure can be achieved by increasing the stability of the perovskite or decreasing the stability of the carbonate. By introducing elements with higher stability against the carbonate formation CO_2 -tolerant materials can be expected even with alkaline-earth elements inside the solid solution. In chapter 3 the A site of calcium- and strontium-containing perovskites was partially exchanged with rare-earth elements. The $\text{La}_{0.6}\text{Ca}_{0.4}\text{Co}_{0.8}\text{Fe}_{0.2}\text{O}_{3-\delta}$, $\text{La}_{0.6}\text{Ca}_{0.4}\text{FeO}_{3-\delta}$, $\text{La}_{0.6}\text{Sr}_{0.4}\text{Co}_{0.8}\text{Fe}_{0.2}\text{O}_{3-\delta}$, and $\text{Pr}_{0.6}\text{Sr}_{0.4}\text{FeO}_{3-\delta}$ materials show good tolerance in long-term oxygen permeation experiments in CO_2 -containing atmospheres.

1.5.2 Three-end process: requirement for high-flux and long-term stable membranes

In three-end operation the separated oxygen is extracted by vacuum pumps (Fig 1.10) [105]. The membrane is not in contact with CO_2 and known high-flux materials can be used. An influence of the membrane microstructure on oxygen permeation properties was reported for many perovskite systems [117–120].

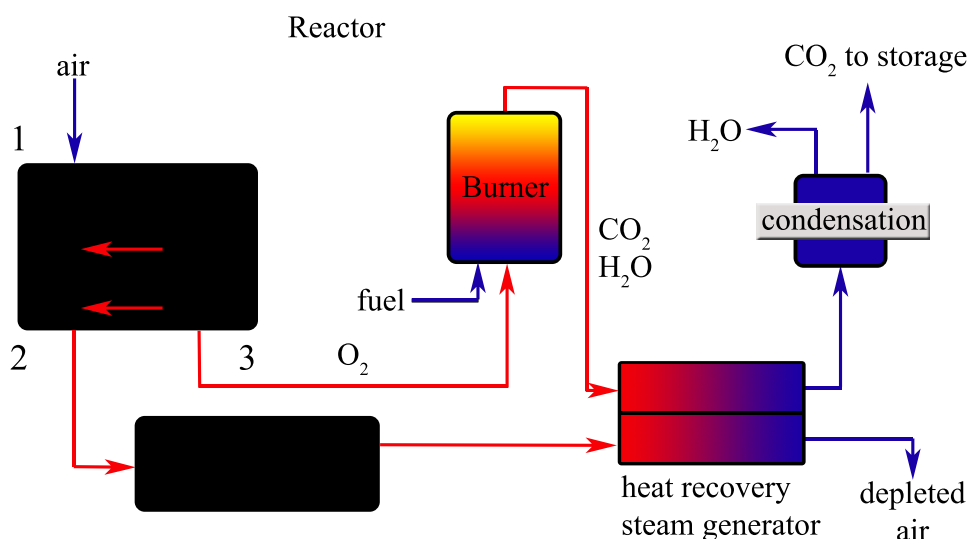


Figure 1.10: Principle of a oxy-fuel combustion power plant operated in three-end mode with integrated oxygen-transporting membrane module (after [105]).

In Chapter 4.1 the optimization of the microstructure of SCF and BSCF was investigated. Another problem is that the prominent BSCF material exhibits stability problems in the intermediate temperature range. The operation at high temperatures ($T > 850\text{ }^\circ\text{C}$) may be non-economical and need to be reduced to the intermediate range ($T < 850\text{ }^\circ\text{C}$). The BSCF material shows a slow phase decomposition from the cubic perovskite structure to a hexagonal polymorph, which is impermeable for oxygen. This was investigated in detail by transmission electron microscopy (TEM) [121]. Some strategies to overcome this problem were proposed in literature. Yakolev et al. reported that doping small amounts of zirconium ($< 10\text{ mol.}\%$) significantly improves the stability of BSCF in the intermediate temperature range [122]. This approach was pursued in chapter 4.2 where the stabilization of the BSCF structure by zirconium doping was investigated by long-term oxygen permeation experiments, in-situ XRD, scanning electron microscopy (SEM) and TEM.

1.6 Bibliography

- [1] International Energy Agency, World energy outlook 2011, OECD, Paris, 2011.
- [2] P. Moriarty, D. Honnery, What energy levels can the Earth sustain?, Energy Policy **37** (2009) 2469-2474.
- [3] J. Chow, R.J. Kopp, P.R. Porney, Energy resources and global development, Science **28** (2003) 1528-1531.
- [4] SRU: Sachverständigenrat für Umweltfragen, Wege zur 100% erneuerbaren Stromversorgung: Sondergutachten Jan. 2011, Erich Schmidt Verlag (ESV), Berlin, 2011.
- [5] T.A. Bodem, G. Marland, R.J. Andres, Global, regional and national fossil-fuel CO₂ emissions, Carbon Dioxide Information Analysis Center, Oak Ridge National Laboratory, U.S. Department of Energy, Oak Ridge, Tenn., U.S.A., (2011).
- [6] A. Schreiber, P. Zapp, W. Kuckshinrichs, Environmental assessment of german electricity generation from coal-fired power plants with amine-based carbon capture, Int. J. Life. Cycle Assess. **14** (2009) 547-559.
- [7] United Nations framework convention on climate change, Status of ratification of the Kyoto Protocol, http://unfccc.int/kyoto_protocol/status_of_ratification/items/2613.php (18.12.2012).
- [8] V.V. Kharton, A.A. Yaremchenko, E.N. Naumovich, Research on the electrochemistry of oxygen ion conductors in the former Soviet Union. II. Perovskite-related oxides, J. Solid State Electrochem. **3** (1999) 303-326.
- [9] J. Sunarso, S. Baumann, J.M. Serra, W.A. Meulenber, S. Liu, Y.S. Lin, J.C. Diniz da Costa, Mixed ionic-electronic conducting (MIEC) ceramic-based membranes for oxygen separation, J. Membr. Sci. **320** (2008) 13-41.

- [10] D.R. Lide, CRC Handbook of chemistry and physics, CRC Press, Boca Raton, 1997.
- [11] H.J.M. Bouwmeester, A.J. Burggraf, Dense ceramic membranes for oxygen separation, in: A.J. Burggraf, L. Cot (Eds.), Fundamentals of inorganic membrane science and technology, Elsevier, Amsterdam, 1996.
- [12] A.G. Dixon, Recent research in catalytic inorganic membrane reactors, Int. J. Chem. Reactor Eng. **1** (2003) R6 1-35.
- [13] F.M. Orr, CO₂ capture and storage: are we ready?, Energy Environ. Sci. **2** (2009) 449-458.
- [14] S. Pacala, R. Socolow, Stabilization wedges: solving the climate problem for the next 50 years with current technologies, Science **305** (2004) 968-972.
- [15] M.I. Hoffert, K. Caldeira, G. Benford, D.R. Criswell, C. Green, H. Herzog, A.K. Jain, H.S. Kheshgi, K.S. Lackner, J.S. Lewis, H.D. Lightfoot, W. Manheimer, J.C. Mankins, M.E. Mauel, L.J Perkins, M.E. Schlesinger, T. Volk, T.M.L. Wigley, Advanced technology paths to global climate stability: energy for a greenhouse planet, Science **298** (2002) 987-987.
- [16] N. Jones, Sucking it up, Nature **458** (2009) 1094-1097.
- [17] D.P. Schrag, Preparing to capture carbon, Science **315** (2007) 812-813.
- [18] H. Hack, Z. Fan, A. Seltzer, Advanced oxyfuel combustion leading to zero emission power generation, The 35th international technical conference on clean coal & fuel systems, Florida.
- [19] M. Czaperek, P. Zapp, H.J.M. Bouwmeester, M. Modigell, K. Ebert, I. Voigt, W.A. Meulenber, L. Singheiser, D. Stöver, Gas separation for zero-emission fossil power plants: MEM-BRAIN, J. Membr. Sci. **359** (2010) 149-159.
- [20] R. Bredesen, K. Jordal, O. Bolland, High-temperature membranes in power generation with CO₂ capture, Chem. Eng. Processes **43** (2004), 1129-1158.
- [21] F.M. Orr, Onshore geologic storage of CO₂, Science **325** (2009) 1656-1658.
- [22] C. Marchetti, On geoengineering and the CO₂ problem, Clim. Change **1** (1977) 59-68.

-
- [23] B.A. Seibel, P.J. Walsh, Potential impacts of CO₂ injection on deep-sea biota, *Science* **294** (2001) 319-320.
- [24] D.P. Schrag, Storage of carbon dioxide in offshore sediments, *Science* **325** (2009) 1656-1658.
- [25] F.T. Akin, Y.S. Lin, Selective oxidation of ethane to ethylene in a dense tubular membrane reactor, *J. Membr. Sci.* **209** (2002) 457-467.
- [26] C. Chen, S. Feng, S. Ran, D. Zhu, W. Liu, H.J.M. Bouwmeester, Conversion of methane to syngas by a membrane-based oxidation-reforming process, *Angew. Chem., Int. Ed.* **42** (2003) 5196-5198.
- [27] H. Jiang, H. Wang, F. Liang, S. Werth, T. Schiestel, J. Caro, Direct decomposition of nitrous oxide to nitrogen by in situ oxygen removal with a perovskite membrane, *Angew. Chem., Int. Ed.* **48** (2009) 2983-2986.
- [28] A.B. Stambouli, E. Traversa, Fuel cells, an alternative to standard sources of energy, *Renewable Sustainable Energy Rev.* **6** (2002) 297-306.
- [29] L. Carrette, K.A. Friedrich, U. Stimming. Fuel cells, fundamentals and applications, *Fuel Cells* **1** (2005) 5-39.
- [30] J. Richter, P. Holtappels, T. Graule, T. Nakamura, L.J. Gauckler, Materials design for perovskite SOFC cathodes, *Monatsh. Chem* **140** (2009) 985-999.
- [31] Y. Teraoka, H. Zhang, S. Furukawa, N. Yamazoe, Oxygen permeation through perovskite oxides, *Chem. Lett.* **11** (1985) 1743-1746.
- [32] Y. Teraoka, T. Nobunaga, N. Yamazoe, Effect of cation substitution on the oxygen semipermeability of perovskite-type oxides, *Chem. Lett.* **3** (1988) 503-506.
- [33] L. Qiu, T.H. Lee, L.-M. Liu, Y.L. Yang, A.J. Jacobson, Oxygen permeation studies of SrCo_{0.8}Fe_{0.2}O_{3-δ}, *Solid State Ionics* **76** (1995) 321-329.
- [34] S. Pei, M.S. Kleefisch, T.P. Kobylinski, J. Faber, C.A. Udovich, V. Zhang-McCoy, B. Dabrowski, U. Balachandran, R.L. Mieville, R.B. Poeppel, Failure mechanisms of ceramic membrane reactors in partial oxidation of methane to synthesis gas, *Catal. Lett.* **30** (1995) 201-212.

- [35] H. Kruidhof, H.J.M. Bouwmeester, R.H.E. van Doorn, A.J. Burggraaf, Influence of order-disorder transitions on oxygen permeability through selected non-stoichiometric perovskite-oxides, *Solid State Ionics* **63** (1993) 816-822.
- [36] Z.P. Shao, W.S. Yang, Y. Cong, H. Dong, J.H. Tong, G.X. Xiong, Investigation of the permeation behavior and stability of a $\text{Ba}_{0.5}\text{Sr}_{0.5}\text{Co}_{0.8}\text{Fe}_{0.2}\text{O}_{3-\delta}$ oxygen membrane, *J. Membr. Sci.* **172** (2000) 177-188.
- [37] Z.P. Shao, G.X. Xiong, J.H. Tong, H. Dong, W.S. Yang, Synthesis, oxygen permeation study and membrane performance of a $\text{Ba}_{0.5}\text{Sr}_{0.5}\text{Co}_{0.8}\text{Fe}_{0.2}\text{O}_{3-\delta}$ oxygen-permeable dense ceramic reactor for partial oxidation of methane to syngas, *Sep. Purif. Tech.* **25** (2001) 97-116.
- [38] P. Zeng, Z. Chen, W. Zhou, H. Gu, Z. Shao, S. Liu, Re-evaluation of $\text{Ba}_{0.5}\text{Sr}_{0.5}\text{Co}_{0.8}\text{Fe}_{0.2}\text{O}_{3-\delta}$ perovskite as oxygen semi-permeable membrane, *J. Membr. Sci.* **291** (2007) 148-156.
- [39] M. Arnold, H. Wang, A. Feldhoff, Influence of CO_2 on the oxygen permeation performance and the microstructure of perovskite-type $(\text{Ba}_{0.5}\text{Sr}_{0.5})(\text{Co}_{0.8}\text{Fe}_{0.2})\text{O}_{3-\delta}$ membranes, *J. Membr. Sci.* **293** (2007) 44-52.
- [40] K. Efimov, O. Czuprat, A. Feldhoff, In-situ X-ray diffraction study of carbonate formation and decomposition in perovskite-type $\text{BaCo}_x\text{Fe}_y\text{Zr}_z\text{O}_{3-\delta}$, *J. Solid State Chem.* **184** (2011) 1085-1089.
- [41] A.L. Shaula, E.N. Naumovich, A.P. Viskup, V.V. Pankov, A.V. Kovalevsky, V.V. Kharton, Oxygen transport in $\text{La}_2\text{NiO}_{4+\delta}$: Assessment of surface limitations and multilayer membrane architectures, *Solid State Ionics* **180** (2009) 812-816.
- [42] G. Amow, I.J. Davidson, S.J. Skinner, A comparative study of the Ruddlesden-Popper series, $\text{La}_{n+1}\text{Ni}_n\text{O}_{3n+1}$ ($n=1, 2$ and 3), for solid-oxide fuel-cell cathode applications, *Solid State Ionics* **117** (2006) 1205-1210.
- [43] H. Luo, K. Efimov, H. Jiang, A. Feldhoff, H. Wang, J. Caro, CO_2 -stable and cobalt-free dual phase membrane for oxygen separation, *Angew. Chem., Int. Ed.* **50** (2011) 759-763.

-
- [44] G. Rose, Reise nach dem Ural, dem Altei und dem Kaspischen Meere (Mineralogisch-geognostischer Theil und historischer Bericht der Reise), Verlag der Sanderschen Buchhandlung (G.E. Reimer), Berlin, 1842.
- [45] G. Rose, Beschreibung einiger neuen Minerale des Urals, Poggendorff's Annalen (Annalen der Physik und Chemie), Verlag Johann Ambrosius Barth, Leipzig, Band **48** (1839) 551-573.
- [46] R.H. Buttner, E.N. Maslen, Electron difference density and structural parameters in CaTiO_3 , Acta Cryst. B **48** (1992) 644-649.
- [47] Y.A. Abramov, V.G. Tsirelson, V.E. Zavodnik, S.A. Ivanov, I.D. Brown, The chemical bond and atomic displacements in SrTiO_3 from X-ray diffraction analysis, Acta Cryst. B **51** (1995) 942-951.
- [48] H.D. Megaw, Crystal structure of double oxides of the perovskite type, Proc. Phys. Soc. **58** (1946) 133-152.
- [49] T. Barth, Die Kristallstruktur von Perowskit und verwandten Verbindungen, Norsk geol. Tidsskr. **8** (1925) 201-216.
- [50] V.M. Goldschmidt, Die Gesetze der Kristallchemie, Naturwiss. **14** (1926) 477-485.
- [51] L. Pauling, Nature of the chemical bond, Cornell University Press, Ithaca NY, 1960.
- [52] A. Reller, J.G. Bednorz, K.A. Müller, Alternate structure for $\text{Ba}_2\text{YCu}_3\text{O}_7$, Z. Phys. B **67** (1987) 285-289.
- [53] K. Domen, A. Kudo, T. Onishi, Mechanism of photocatalytic decomposition of water into H_2 and O_2 over NiO-SrTiO_3 , J. Catal. **102** (1986) 92-98.
- [54] S. Miyake, R. Ueda, On polymorphic change of BaTiO_3 , J. Phys. Soc. Jpn. **1** (1946) 32-33.
- [55] J. Ryu, J. Choi, H. Kim, Effect of heating rate on the sintering behavior and the piezoelectric properties of lead zirconate titanate ceramics, J. Am. Ceram. Soc. **84** (2001) 902-904.

- [56] D. Pantel, S. Goetze, D. Hesse, M. Alexe, Reversible electrical switching of spin polarization in multiferroic tunnel junctions, *Nature Materials* **11** (2012) 289-293.
- [56] D. Balz, K. Plieth, Die Struktur des Kaliumnickelfluorids, K_2NiF_4 , *Z. Elektrochem.* **59** (1955) 545-551.
- [57] S.N. Ruddlesden, P. Popper, New compounds of the K_2NiF_4 type, *Acta Cryst.* **10** (1957) 538-539.
- [58] L. Minervini, R.W. Grimes, J.A. Kilner, K.E. Sickafus, Oxygen migration in $La_2NiO_{4+\delta}$, *J. Mater. Chem.* **10** (2000) 2349-2354.
- [59] S.J. Skinner, Characterisation of $La_2NiO_{4+\delta}$ using in-situ high temperature neutron powder diffraction, *Solid State Sci.* **5** (2003) 419-426.
- [60] B. Grande, H.K. Müller-Buschbaum, Zur Kenntnis von $Sr_2CuO_2Br_2$ mit einem Beitrag über La_2NiO_4 , *Z. anorg. allg. Chem.* **433** (1977) 152-156.
- [61] J.D. Jorgensen, B. Dabrowski, S. Pei, D.R. Richards, D.G. Hinks, Structure of the interstitial oxygen defect in $La_2NiO_{4+\delta}$, *Phys. Rev. B: Condens. Matter* **40** (1989) 2187-2199.
- [62] D.E. Rice, D.J. Buttrey, An X-ray diffraction study of the oxygen content phase diagram of $La_2NiO_{4+\delta}$, *J. Solid State Chem.* **105** (1993) 197-210.
- [63] P. Cousin, R.A. Ross, Preparation of mixed oxides: a review, *Mater. Sci. Eng. A* **130** (1990) 119-125.
- [64] Y.G. Metlin, Y.D. Tretyakov, Chemical routes for preparation of oxide high-temperature superconducting powders and precursors for superconductive ceramics, coatings and composites, *J. Mater. Chem.* **4** (1994) 1659-1665.
- [65] S. Liu, X. Tan, K. Li, R. Hughes, Synthesis of strontium cerates-based perovskite ceramics via water-soluble complex precursor routes, *Ceram. Int.* **28** (2002) 327-335.
- [66] J. Martynczuk, M. Arnold, J. Caro, H. Wang, A. Feldhoff, How $(Ba_{0.5}Sr_{0.5})(Fe_{0.8}Zn_{0.2})O_{3-\delta}$ and $(Ba_{0.5}Sr_{0.5})(Co_{0.8}Fe_{0.2})O_{3-\delta}$ perovskites form via an EDTA/citric acid complexing method, *Adv. Mater.* **19** (2007) 2134-2140.

-
- [67] K. Efimov, M. Arnold, J. Martynczuk, A. Feldhoff, Crystalline intermediate phases in the sol-gel-based synthesis of $\text{La}_2\text{NiO}_{4+\delta}$, *J. Am. Ceram. Soc.* **92** (2009) 876-880.
- [68] R.H.E. van Doorn, H. Kruidhof, A. Nijmeijer, L. Winnubst, A.J. Burggraaf, Preparation of $\text{La}_{0.3}\text{Sr}_{0.7}\text{CoO}_{3-\delta}$ perovskite by thermal decomposition of metal-EDTA complexes, *J. Mater. Chem.* **8** (1998) 2109-2112.
- [69] A. Feldhoff, J. Martynczuk, H. Wang, Advanced $\text{Ba}_{0.5}\text{Sr}_{0.5}\text{Zn}_{0.2}\text{Fe}_{0.8}\text{O}_{3-\delta}$ perovskite-type ceramics as oxygen selective membranes: Evaluation of the synthetic process, *Progress Solid State Chem.* **35** (2007) 339-353.
- [70] A. Feldhoff, M. Arnold, J. Martynczuk, T.M. Gesing, H. Wang, The sol-gel synthesis of perovskites by an EDTA/citrate complexing method involves nanoscale solid state reactions, *Solid State Sci.* **10** (2008) 689-701.
- [71] M.N. Rahaman, *Ceramic processing and sintering* 2nd edition, Taylor & Francis Group, Boca Raton, 2003.
- [72] W.D. Kingery, H.K. Bowen, D.R. Uhlmann, *Introduction to Ceramics*, John Wiley & Sons, Toronto, 1976.
- [73] A.R. West, *Solid State Chemistry and Its Applications*, John Wiley & Sons, Chichester, 1984.
- [74] F.A. Kröger, H.J. Vink, Relations between the concentrations and imperfections in crystalline solids, *Solid State Phys.* **3** (1956) 307-435.
- [75] J.A. Kilner, P. Barrow, R.J. Brook, Electrolytes for the high temperature fuel cell: experimental and theoretical studies of the perovskite LaAlO_3 , *J. Power Sources* **3** (1978) 67-80.
- [76] R.L. Cook, A.F. Sammells, On the systematic selection of perovskite solid electrolytes for intermediate temperature fuel cells, *Solid State Ionics* **45** (1991) 311-321.
- [77] M. S. Islam, Ionic transport in ABO_3 perovskite oxides: a computer modelling tour, *J. Mater. Chem.* **10** (2000) 1027-1038.

- [78] M. Yashima, T. Kamioka, Neutron diffraction study of the perovskite-type lanthanum cobaltite $\text{La}_{0.6}\text{Sr}_{0.4}\text{Co}_{0.8}\text{Fe}_{0.2}\text{O}_{3-\delta}$ at 1260 °C and 394 °C, *Solid State Ionics* **178** (2008) 1939-1943.
- [79] M. Yashima, T. Tsuji, Structural investigation of the cubic perovskite-type doped lanthanum cobaltite $\text{La}_{0.6}\text{Sr}_{0.4}\text{CoO}_{3-\delta}$ at 1531 K: possible diffusion path of oxygen ions in an electrode material, *J. Appl. Cryst.* **40** (2007) 1166-1168.
- [80] M. Yashima, K. Nomura, H. Kageyama, Y. Miyazaki, N. Chitose, K. Adachi, Conduction path and disorder in the fast oxide-ion conductor $\text{La}_{0.8}\text{Sr}_{0.2}\text{Ga}_{0.8}\text{Mg}_{0.15}\text{Co}_{0.05}\text{O}_{2.8}$, *Chem. Phys. Lett.* **380** (2003) 391-396.
- [81] R. Ali, M. Yashima, F. Izumi, Diffusion path of oxide ions in an oxide ion conductor $\text{La}_{0.64}\text{Sr}_{0.4}\text{Ti}_{0.92}\text{Nb}_{0.08}\text{O}_{2.99}$ with a double perovskite-type structure, *Chem. Mater.* **19** (2007) 3260-3264.
- [82] D.J. Buttrey, P. Ganguly, J.M. Honig, C.N.R. Rao, R.R. Schartman, G.N. Subbanna, Oxygen excess in layered lanthanide nickelates, *J. Solid State Chem.* **74** (1988) 233-238.
- [83] M.S.D. Read, M.S. Islam, F. King, F.E. Hancock, Defect chemistry of $\text{La}_2\text{Ni}_{1-x}\text{M}_x\text{O}_4$ (M = Mn, Fe, Co, Cu): Relevance to catalytic behavior, *J. Phys. Chem. B* **103** (1999) 1558-1562.
- [84] R.S. Puche, J.L. Rodriguez, F. Fernandez, Non-stoichiometric aspects and physical properties of La_2NiO_4 oxide, *Inorg. Chim. Acta* **140** (1987) 151-153.
- [85] J. DiCarlo, A. Mehta, D. Banschick, A. Navrotsky, The energetics of $\text{La}_{2-x}\text{A}_x\text{NiO}_{4-y}$ (A = Ba, Sr), *J. Solid State Chem.* **103** (1993) 186-182.
- [86] S.J. Skinner, J.A. Kilner, Oxygen diffusion and surface exchange in $\text{La}_{2-x}\text{Sr}_x\text{NiO}_{4+\delta}$, *Solid State Ionics* **135** (2000) 709-712.
- [87] J. Maier, *Festkörper - Fehler und Funktionen (Prinzipien der Physikalischen Festkörperchemie)*, B.G. Teubner, Stuttgart, 2000.
- [88] G.A. Brouwer, A general asymptotic solution of reaction equations common in solid state chemistry, *Philips Res. Rept.* **9** (1954) 366-376.

-
- [89] J.W. Stevenson, T.R. Armstrong, R.D. Carneim, L.R. Pederson, W.J. Weber, Electrochemical properties of mixed conducting perovskites $\text{La}_{1-x}\text{M}_x\text{Co}_{1-y}\text{Fe}_y\text{O}_{3-\delta}$ ($\text{M} = \text{Sr}, \text{Ba}, \text{Ca}$), *J. Electrochem. Soc.* **143** (1996) 2722–2729.
- [90] D.P. Karim, A.T. Aldred, Localized level hopping transport in $\text{La}(\text{Sr})\text{CrO}_3$, *Phys. Rev. B* **20** (1979) 2255–2263.
- [91] G. Z. Cao, Electrical conductivity and oxygen semipermeability of terbia and yttria stabilized zirconia, *J. Appl. Electrochem.* **24** (1994) 1222–1227.
- [92] Y.S. Lin, W. Wang, J. Han, Oxygen permeation through thin mixed-conducting solid oxide membranes, *AIChE J.* **40** (1994) 786–798.
- [93] H.J.M. Bouwmeester, H. Kruidhof, A.J. Burggraf, Importance of the surface exchange kinetics as rate limiting step in oxygen permeation through mixed-conducting oxides, *Solid State Ionics* **72** (1994) 185–194.
- [94] C. Wagner, Beitrag zur Theorie des Anlaufvorgangs, *Z. Phys. Chem. B* **21** (1933) 25–41.
- [95] C. Wagner, Beitrag zur Theorie des Anlaufvorgangs II, *Z. Phys. Chem. B* **32** (1936) 447–462.
- [96] C. Wagner, Equations for transport in solid oxides and sulfides of transition metals. *Prog. Solid State Chem.* **10** (1975) 3–16.
- [97] H.J.M Bouwmeester, Dense ceramic membranes for methane conversion, *Catal. Today* **82** (2003) 141–150.
- [98] J.B. Goodenough, Crystalline solid electrolytes, Part 2 Material design, in: *Solid state electrochemistry*, ed. by P.G. Bruce, Cambridge University Press, Cambridge, 1995.
- [100] L. Qiu, T. H. Lee, L.-M. Liu, Y. L. Yang, A. J. Jacobson, Oxygen permeation studies of $\text{SrCo}_{0.8}\text{Fe}_{0.2}\text{O}_{3-\delta}$, *Solid State Ionics* **76** (1995) 321–329.
- [101] B.A. van Hassel, T. Kawada, N. Sakai, H. Yokokawa, M. Dokiya, Oxygen permeation modelling of $\text{La}_{1-y}\text{Ca}_y\text{CrO}_{3-\delta}$, *Solid State Ionics* **66** (1993) 41–47.

- [102] B. A. van Hassel, T. Kawada, N. Sakai, H. Yokokawa, M. Dokiya, H. J. M. Bouwmeester, Oxygen permeation modelling of perovskites, *Solid State Ionics* **66** (1993) 295-305.
- [103] Z. Yang, Y.S. Lin, A semi-empirical equation for oxygen nonstoichiometry of perovskite-type ceramics, *Solid State Ionics* **150** (2002) 245-254.
- [104] S. Kim, Y. L. Yang, A. J. Jacobson, B. Abeles, Diffusion and surface exchange coefficients in mixed ionic electronic conducting oxides from the pressure dependence of oxygen permeation, *Solid State Ionics* **106** (1998) 189-195.
- [105] S. Engels, F. Beggel, M. Modigell, H. Stadler, Simulation of a membrane unit for oxyfuel power plants under consideration of realistic BSCF membrane properties, *J. Membr. Sci.* **359** (2010) 93-101.
- [106] H. Stadler, F. Beggel, M. Habermehl, B. Persigehl, R. Kneer, M. Modigell, P. Jeschke, Oxyfuel coal combustion by efficient integration of oxygen transport membranes, *Int. J. Greenhouse Gas Control* **5** (2011) 7-15.
- [107] X. Tan, K. Li, Oxygen production using dense ceramic hollow fiber membrane modules with different operating modes, *AIChE J.* **53** (2007) 838-845.
- [108] K. Eichhorn Colombo, O. Bolland, V.V. Kharton, C. Stiller, Simulation of an oxygen membrane-based combined cycle power plant: part-load operation with operational and material constraints, *Energy Environ. Sci.* **2** (2009) 1310-1324.
- [109] K. Eichhorn Colombo, V.V. Kharton, O. Bolland, Simulation of an oxygen membrane-based gas turbine power plant: dynamic regimes with operational and material constraints, *Energy fuels* **24** (2010) 590-608.
- [110] K. Eichhorn Colombo, V.V. Kharton, A.P. Viskup, A.V. Kovalevsky, A.L. Shaula, O. Bolland, Simulation of a mixed-conducting membrane-based gas turbine power plant for CO₂ capture: system level analysis of operation stability and individual process unit degradation, *J. Solid State Electrochem.* **15** (2011) 329-347.
- [111] J. Martynczuk, K. Efimov, L. Robben, A. Feldhoff, Performance of zinc-doped perovskite-type membranes at intermediate temperatures for long-term oxygen permeation and under a carbon dioxide atmosphere, *J. Membr. Sci.* **344** (2009) 62-70.

- [112] K.H. Stern, E.L. Weise, High temperature properties and decomposition of inorganic salts, Part 2: carbonates, NSRDS-NBS **30** (1969) 1-27.
- [113] R.D. Shannon, Revised effective ionic radii and systematic studies of interatomic distances in halides and chalcogenides, Acta Crystallogr., Sect. A: Found. Crystallogr. **32** (1976) 751-767.
- [114] I. Barin, F. Sauert, G. Patzki, Thermochemical data of pure substances, 3rd ed., vols. I and II, VCH, Weinheim, 1995.
- [115] K. Efimov, M. Arnold, J. Martynczuk, A. Feldhoff, Crystalline intermediate phases in the sol-gel-based synthesis of $\text{La}_2\text{NiO}_{4+\delta}$, J. Am. Ceram. Soc. **92** (2009) 876-880.
- [116] H. Yokokawa, N. Sakai, T. Kawada, M. Dokiya, Thermodynamic stabilities of perovskite oxides for electrodes and other electrochemical materials, Solid State Ionics **52** (1992) 43-56.
- [117] J. Martynczuk, M. Arnold, A. Feldhoff, Influence of grain size on the oxygen permeation performance of perovskite-type $(\text{Ba}_{0.5}\text{Sr}_{0.5})(\text{Co}_{0.8}\text{Fe}_{0.2})\text{O}_{3-\delta}$ membranes, J. Membr. Sci. **322** (2008) 375-382.
- [118] P. Zeng, R. Ran, Z. Chen, H. Gu, Z. Shao, J.C. Diniz da Costa, S. Liu, Significant effects of sintering temperature on the performance of $\text{La}_{0.6}\text{Sr}_{0.4}\text{Co}_{0.2}\text{Fe}_{0.8}\text{O}_{3-\delta}$ oxygen selective membranes, J. Membr. Sci. **302** (2007) 171-179.
- [119] M. Arnold, J. Martynczuk, K. Efimov, H. Wang, A. Feldhoff, Grain boundaries as barrier for oxygen transport in perovskite-type membranes, J. Membr. Sci. **316** (2008) 137-144.
- [120] S. Baumann, F. Schulze-Kueppers, S. Roitsch, M. Betz, M. Zwick, E.M. Pfaff, W.A. Meulenbergh, J. Mayer, D. Stoeber, Influence of sintering conditions on microstructure and oxygen permeation of $\text{Ba}_{0.5}\text{Sr}_{0.5}\text{Co}_{0.8}\text{Fe}_{0.2}\text{O}_{3-\delta}$ (BSCF) oxygen transport membranes, J. Membr. Sci. **359** (2010) 102-109.
- [121] K. Efimov, Q. Xu, A. Feldhoff, Transmission electron microscopy study of $\text{Ba}_{0.5}\text{Sr}_{0.5}\text{Co}_{0.8}\text{Fe}_{0.2}\text{O}_{3-\delta}$ perovskite decomposition at intermediate temperatures, Chem. Mater. **22** (2010) 5866-5875.

- [122] S. Yakovlev, C.Y. Yoo, S. Fang, H.J.M. Bouwmeester, Phase transformation and oxygen equilibration kinetics of pure and Zr-doped $\text{Ba}_{0.5}\text{Sr}_{0.5}\text{Co}_{0.8}\text{Fe}_{0.2}\text{O}_{3-\delta}$ perovskite oxide probed by electrical conductivity relaxation, *Appl. Phys.Lett.* **96** (2010) 254101-254103.

2 Chapter 2

CO₂-tolerant alkaline-earth free membrane materials

2.1 Summary

This chapter deals with the properties of alkaline-earth free CO₂-tolerant membrane materials. Section 2.2 describes basic investigations of the Ruddlesden-Popper phase La₂NiO_{4+δ}. The effect of substitution on the nickel position with cations of different ionic radius and valence (Co²⁺, Cu²⁺, Mg²⁺, Al³⁺, Fe³⁺, Zr⁴⁺) was investigated with regards to oxygen permeation performance and membrane microstructure. *In-situ* XRD and long-term oxygen permeation experiments confirmed a high tolerance of La₂NiO_{4+δ} towards CO₂. In the La₂Ni_{0.9}Fe_{0.1}O_{4+δ} system, a secondary phase was found by Mössbauer spectroscopy, which was identified by TEM as the higher order Ruddlesden-Popper phase La₄Ni_{2.1}Fe_{0.9}O_{10-δ}.

In section 2.2 the iron-doped La₂NiO_{4+δ} and La₄Ni₃O_{10-δ} phases were further characterized. The oxygen permeation flux of La₂Ni_{1-x}Fe_xO_{4+δ} (x = 0.02, 0.1) and the electrical conductivity of La₂Ni_{1-x}Fe_xO_{4+δ} (x = 0.02, 0.1) and La₄Ni_{3-x}Fe_xO_{10-δ} (x = 0.3, 0.9) were found to slightly decrease with increasing iron content. For the first time oxygen partial pressure and high temperature dependent Mössbauer studies were used to examine the materials. The TEM and SEM investigations revealed that the La₂Ni_{0.98}Fe_{0.02}O_{4+δ} system is single phase in contrast to La₂Ni_{0.9}Fe_{0.1}O_{4+δ}.

Section 2.3 describes a new alkaline-earth free 40 Mn_{1.5}Co_{1.5}O_{4-δ} - 60 Ce_{0.9}Pr_{0.1}O_{2-δ} dual-phase membrane synthesized by a rapid one-pot combustion synthesis. The microstructure analysis by backscattered SEM and energy dispersive X-ray spectroscopy (EDXS) revealed a micro-scale mixture of the electron and ion conducting phases, which form an interpenetrating, percolating network. *In-situ* XRD and long-term permeation measurements revealed an excellent tolerance towards CO₂.

2.2 Effect of doping, microstructure and CO₂ on La₂NiO_{4+δ}-based oxygen-transporting materials

Tobias Klande, Konstantin Efimov, Salvatore Cusenza, Klaus-Dieter Becker, and
Armin Feldhoff

Journal of Solid State Chemistry **184** (2011) 3310-3318



Effect of doping, microstructure, and CO₂ on La₂NiO_{4+δ}-based oxygen-transporting materials

Tobias Klande^{a,*}, Konstantin Efimov^a, Salvatore Cusenza^b, Klaus-Dieter Becker^b, Armin Feldhoff^a

^a Institute of Physical Chemistry and Electrochemistry, Leibniz Universität Hannover, Callinstr. 3-3a, D-30179 Hannover, Germany

^b Institute of Physical and Theoretical Chemistry, Technische Universität Braunschweig, Hans-Sommer-Str. 10, D-38106 Braunschweig, Germany

ARTICLE INFO

Article history:

Received 22 July 2011

Received in revised form

8 October 2011

Accepted 10 October 2011

Available online 17 October 2011

Keywords:

Mixed ionic-electronic conductor

K₂NiF₄ structure

Carbon dioxide

Long-term stability

Mössbauer

Transmission electron microscopy

ABSTRACT

Alkaline earth-free La₂NiO_{4+δ} based materials were synthesized by a sol-gel method and studied by X-ray diffraction (XRD), scanning electron microscopy (SEM) and transmission electron microscopy (TEM) techniques as well as oxygen permeation experiments. Effects of doping the nickel position with a variety of cations (Al, Co, Cu, Fe, Mg, Ta, and Zr) were investigated with regards to oxygen flux and microstructure. Doping was always found to diminish the oxygen flux as compared to the reference composition. However, larger grains, which were achieved by longer annealing times at 1723 K have a minor negative impact on oxygen permeation flux in case of La₂NiO_{4+δ} and La₂Ni_{0.9}Fe_{0.1}O_{4+δ} system. Mössbauer spectroscopy shows that the iron-doped system exhibits a secondary phase, which was identified by high-resolution transmission electron microscopy (HRTEM) as a higher Ruddlesden-Popper phase. *In-situ* XRD in an atmosphere containing 50 vol% CO₂ and long-term oxygen permeation experiments using pure CO₂ as the sweep gas revealed a high tolerance of the materials towards CO₂.

© 2011 Elsevier Inc. All rights reserved.

1. Introduction

Mixed ionic-electronic conductors (MIECs) have received considerable interest over the last few years because of their applicability as oxygen-transporting membranes (OTMs). They can be used in a wide range of applications such as the production of high-purity oxygen [1], in petrochemical processes such as the oxidative coupling of methane to ethylene or ethane (OCM) [2], the partial oxidation of methane to syngas (POM) [3], or as cathode materials in solid-oxide fuel cells (SOFCs) [4]. Also, possible application of OTMs in power plants with CO₂ capture were discussed [5]. Good MIECs contain alkaline-earth metals, e.g., (La_xSr_{1-x})(Co_yFe_{1-y})O_{3-δ} (LSCF) and (Ba_xSr_{1-x})(Co_yFe_{1-y})O_{3-δ} (BSCF), which exhibit high oxygen permeabilities because of their high concentrations of oxygen vacancies [6,7]. However, they suffer from instability against CO₂ by forming thermodynamically stable carbonates that act as a barrier for oxygen permeation [8,9]. From thermodynamical calculations via an Ellingham diagram, shown in Fig. 1, it can be expected that La₂NiO_{4+δ} is stable in CO₂ containing atmospheres at elevated temperatures. However, at temperatures below 1073 K and 1 atm CO₂ the expected decomposition into lanthanum carbonate and nickel oxide may be slow due to kinetic reasons. Recently, Eichhorn Colombo et al. showed long-term CO₂ stability of La₂NiO₄ using permeation experiments in CO₂ at different temperatures [14].

In the present article the CO₂ stability was further investigated by *in-situ* XRD and long-term permeation experiments under CO₂ containing atmospheres. Another hindrance is the relative high coefficient of linear thermal expansion (CTE) of 3D conducting perovskites, typically between 20×10^{-6} and $24 \times 10^{-6} \text{ K}^{-1}$ [15,16]. Compared to the CTEs of standard electrolytes such as yttrium-stabilized zirconia (YSZ) or gadolinium-doped ceria (CGO), which exhibit CTE values of approximately $10 \times 10^{-6} \text{ K}^{-1}$, this poor thermomechanical compatibility may lead to mechanical stress and cracking during operational processes. With relatively low CTE values between $11.9 \times 10^{-6} \text{ K}^{-1}$ and $13.8 \times 10^{-6} \text{ K}^{-1}$ La₂NiO_{4+δ} seems to be suitable for applications in integrated systems [17,18]. The Ruddlesden-Popper-phase perovskite-related La₂NiO_{4+δ} is a prominent candidate for ceramic membranes with long-term stability. The crystal structure, as shown in Fig. 2, is built from alternating perovskite-like and rock-salt-like layers arranged along the *c*-axis. The oxygen transport through La₂NiO_{4+δ} occurs at elevated temperatures mainly via a 2D interstitial migration mechanism in the rock-salt-like layers [19] but also to a small extent via oxygen-vacancy migration through the perovskite-like layers. Several groups observed ordering of bound interstitial excess oxygen in superstructures at 9 and 300 K by transmission electron microscopy (TEM) [20,21]. Furthermore, Skinner et al. reported phase transitions in this system that were detected with *in-situ* high-temperature neutron powder diffraction. The transitions occur between the orthorhombic and tetragonal modifications at low temperatures ($T < 423 \text{ K}$) [22]. The tetragonal structure is then maintained over a temperature range of 423–1073 K on heating and cooling, and loss of

* Corresponding author.

E-mail address: tobias.klande@pci.uni-hannover.de (T. Klande).

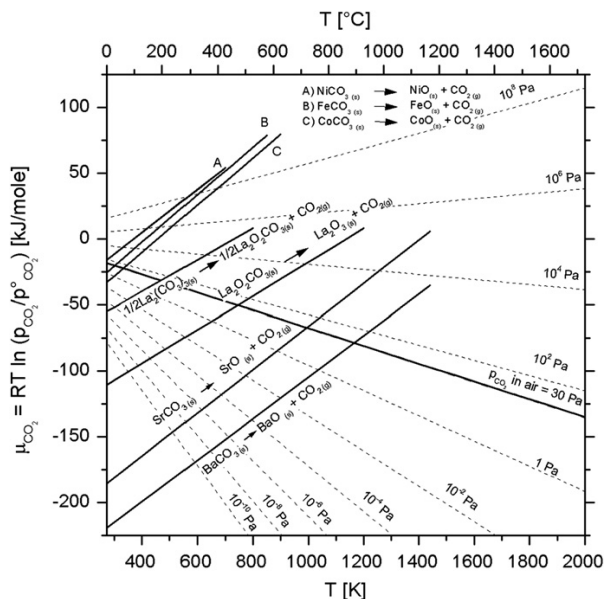


Fig. 1. Ellingham diagram with decomposition temperatures of carbonates under different CO₂ partial pressures. Chemical potential of CO₂ above NiCO₃, FeCO₃, CoCO₃, La₂O₂CO₃, SrCO₃, and BaCO₃ were calculated from thermodynamic data [10–12]. The chemical potential of La₂(CO₃)₂ was determined experimentally [13]. The dashed lines represent the chemical potential of CO₂ in the surrounding atmosphere for different partial pressures. p^o(CO₂)=101.3 kPa refers to standard conditions.

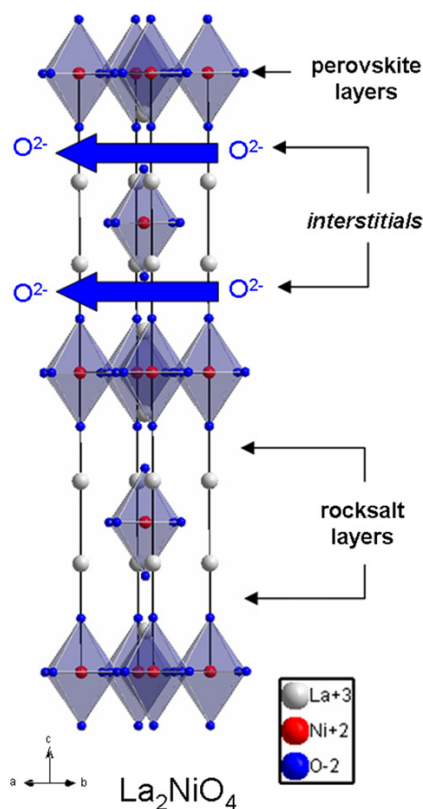


Fig. 2. La₂NiO_{4+δ} shown with arrangement of building blocks along the c-axis; the arrows indicate the diffusion of interstitial oxygen through the rock-salt layers (structure data ICSD no. 1179).

interstitial oxygen was detected up to a temperature of 723 K. These phase transitions do not influence oxygen-permeation properties in the intermediate temperature range ($T=773\text{--}1073\text{ K}$) and the behavior at these temperatures has yet to be investigated by *in-situ* TEM. La₂NiO_{4+δ} offers the above mentioned advantages, but the oxygen flux is poor compared to perovskite materials such as BSCF. The present work is focused on a systematical overview of the influence of different dopants on the oxygen-permeation fluxes in the La₂NiO_{4+δ} system. In the stoichiometric base compound, the A-site cation lanthanum is trivalent and the B-site cation nickel is divalent. Due to oxygen hyperstoichiometry a significant amount of nickel is oxidised to the trivalent state. By doping of the B-site with different cations of increasing valence the interstitial oxygen content can be influenced. By changing the concentration of interstitials, which are the main diffusing species [19], an effect can be assumed on oxygen permeation, which may result in oxygen transport membranes with enhanced properties. Furthermore, in this article the influence of grain size on oxygen flux was investigated for La₂NiO_{4+δ} and La₂Ni_{0.9}Fe_{0.1}O_{4+δ}. Previously, various groups reported an influence of grain size on the functional characteristics of several MIEC materials [23–26]. By optimizing the microstructure of the perovskite related La₂NiO_{4+δ} materials properties can be improved. The results of TEM studies and Mössbauer experiments on the iron-doped La₂NiO_{4+δ} are also reported.

2. Experimental

2.1. Sample preparation

The powders were synthesized by the sol-gel route using stoichiometric amounts of metal oxides, ethylenediaminetetraacetic acid (EDTA) and citrate, as described elsewhere [27–29]. After the reactants were fired in a heating mantle, the obtained products were pre-calcined at 1173 K with a heating and cooling rate of 3 K min⁻¹. The powders were uniaxially pressed into 16 mm green bodies at 50 kN for 15 min. Gas-tight membranes for oxygen-permeation measurements with a thickness of 1 mm were then sintered in air at 1723 K with an annealing time of 10, 40 or 140 h with a heating and cooling rate of 2 K min⁻¹. Samples for Mössbauer experiments, enriched with ⁵⁷Fe, were prepared under the same conditions with an annealing time of 10 h at 1723 K. An overview of all doped materials is shown in Table 1.

2.2. X-ray diffraction analysis

X-Ray diffraction (XRD) analysis was performed at room temperature using a Bruker-AXS D8 Advance diffractometer equipped with a

Table 1
Overview of the base material La₂NiO_{4+δ} and doped La₂Ni_{0.9}M_{0.1}O_{4+δ} solid solutions: unit cell parameters from XRD, estimated effective grain diameter from scanning electron microscope surface-views, activation energy of oxygen permeation in the temperature range from 1023 to 1123 K, and secondary phases obtained by XRD except for the iron-doped sample (marked by *) by high-resolution transmission electron microscopy and Mössbauer spectroscopy.

Composition	Unit cell parameters		Grain diameter (μm)	Activation energy (kJ mol ⁻¹)	Secondary phase
	a (nm)	c (nm)			
La ₂ NiO _{4+δ}	0.3862	1.2683	1.8	56.7	–
La ₂ Ni _{0.9} Zr _{0.1} O _{4+δ}	0.3863	1.2698	0.4	67.0	La ₂ Zr ₂ O ₇
La ₂ Ni _{0.9} Al _{0.1} O _{4+δ}	0.3862	1.2689	0.8	75.9	La ₃ Ni ₂ O ₇
La ₂ Ni _{0.9} Fe _{0.1} O _{4+δ}	0.3876	1.2671	1.2	75.3	La ₄ Ni _{2.1} Fe _{0.9} O ₁₀ *
La ₂ Ni _{0.9} Co _{0.1} O _{4+δ}	0.3867	1.2649	2.7	54.1	–
La ₂ Ni _{0.9} Mg _{0.1} O _{4+δ}	0.3864	1.2687	3.3	58.4	La ₂ O ₃
La ₂ Ni _{0.9} Cu _{0.1} O _{4+δ}	0.3858	1.2729	5.3	66.9	La ₃ Ni ₂ O ₇

Cu K α radiation source. Data sets were recorded in step-scan mode in the angular range of $20^\circ \leq 2\theta \leq 60^\circ$ at an interval of 0.02° . High-temperature measurements were conducted in an *in-situ* cell (HTK-1200 N, Anton Paar) between room temperature and 1273 K under an atmosphere of 50 vol% CO₂/50 vol% air. The heating rate was 12 K min⁻¹ with an equilibration time of 30 min before each measurement.

2.3. Mössbauer spectroscopy

Transmission Mössbauer spectroscopy (TMS) was performed on La₂Ni_{0.9}Fe_{0.1}O₄ powder, which was obtained by grinding dense ceramics. The powder was synthesized by using a metallic iron precursor, which was 96.63% enriched in ⁵⁷Fe (Chemotrade) and were used without any further treatment. A standard Halder Mössbauer system was employed in constant acceleration mode with a ⁵⁷Co/Rh γ -ray source. The spectra were fitted by employing the general Mössbauer spectral analysis software Recoil [30] using lineshape functions accounting for a distribution of quadrupolar interactions. The velocity calibration was performed using α -Fe foil, and the isomer shifts are stated relative to the center of this calibration.

2.4. Scanning electron microscopy

Field-emission scanning electron microscopy (FE-SEM) imaging was performed using a JEOL JSM-6700 F field-emission instrument at a low excitation voltage of 2 kV. For backscattered-electron channeling contrast imaging at higher excitation voltages, samples were polished to crystallinity by vibration polishing and then investigated using a JEOL JSM-6510 QSEM.

2.5. Transmission electron microscopy

TEM investigations were performed at an accelerating voltage of 200 kV on a JEOL JEM-2100 F-UHR field-emission instrument ($C_s=0.5$ mm, $C_c=1.2$ mm). The microscope was operated as a high-resolution TEM (HRTEM) as well as a scanning TEM (STEM) in high-angle angular dark field (HAADF) mode. The preparation method of the TEM specimen is described in detail elsewhere [8]. HRTEM multislice simulations were performed using JEMS software.

2.6. Oxygen permeation measurements

Oxygen permeation was measured in a custom-made high-temperature permeation cell, as described elsewhere [23,31]. The membranes were sealed on an alumina tube with a gold cermet (Heraeus). The feed side was fed with synthetic air (20 vol% O₂/80 vol% N₂) at a rate of 150 mL min⁻¹, whereas Ne (1.0 mL min⁻¹, 99.995%) and He (29.0 mL min⁻¹, 99.995%) or CO₂ (29.0 mL min⁻¹, 99.995%) were fed to the sweep side. An Agilent 7890 gas chromatograph with a Carboxen 1000 column was employed to analyze the gas mixture. The absolute flux rate was calculated using neon as an internal standard. The total O₂ leakage was calculated and subtracted from the total O₂ flux after the N₂ concentration was measured.

3. Results and discussion

3.1. X-ray diffraction

The XRD patterns of the different materials (Fig. 3) showed the formation of La₂NiO_{4+δ}-type phases, which can be indexed as the tetragonal K₂NiF₄ (S.G. *I4/mmm*) structure (ICSD no. 1179), which is typical for La₂NiO_{4+δ} at high temperatures and air atmosphere. This structure is metastable at room temperature and can accommodate

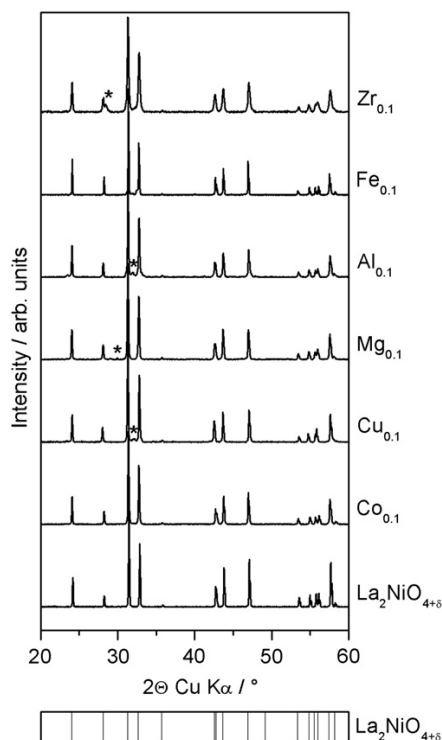


Fig. 3. Room-temperature XRD patterns of La₂NiO_{4+δ} membranes with different dopants on the Ni site. The theoretical Bragg positions for La₂NiO_{4+δ} (ICSD 1179) are labeled at the bottom of the figure.

various oxygen hyperstoichiometries. No other main crystalline phases were observed. However, some powders exhibited a low amount of additional reflections, which are marked by asterisks. In the Zr-doped system, the additional reflection at 28.3° can be attributed to the (2 2 2) reflection of La₂Zr₂O₇ (ICSD no.154752). The Al- and Cu-doped systems exhibit additional reflections at 31.9° , which can be assigned to the (1 0 5) reflection of Ruddlesden-Popper type by-phase La₃Ni₂O₇ (ICSD no. 155320). In the Mg-doped system, the reflection at 29.9° corresponds to the (0 1 1) reflection of La₂O₃ (ICSD no. 56166). No pure phase could be obtained by tantalum doping. With respect to the sensitivity of XRD, no other crystalline phases were found. By doping the B-site with cations of different valence oxygen hyperstoichiometry should be affected. The general trend for La₂NiO_{4+δ} observed by Rice and Buttrey [32] is for unit cell parameter *a* to decrease and *c* to increase with increasing δ . Furthermore, it can be expected that cell parameters change by doping according to the dopant's ionic radius. However, no trend can be derived from variation in lattice parameters for the Al-, Cu-, Mg- and Zr-doped systems (see table 1). The change is within the limits of experimental error. The unit cell parameters for the base system as well as for the cobalt- and iron-doped systems are in good agreement with the literature [33–35]. Because CO₂ stability is an important factor for membrane applicability, *in-situ* XRD measurements were performed on the undoped La₂NiO_{4+δ} system in the temperature range of 303–1273 K in an atmosphere containing 50 vol% CO₂ and 50 vol% air. Fig. 4 shows no additional reflections that would indicate the presence of other phases, e.g., carbonates or phase transitions during heating or cooling. Using the temperature-dependent shift of the cell volume during these measurements, the CTE was estimated to be $15.1 \times 10^{-6} \text{ K}^{-1}$ in an atmosphere containing 50 vol% CO₂ and 50 vol% air. This result agrees with the values reported in the literature of $11.9 \times 10^{-6} \text{ K}^{-1}$ and $13.8 \times 10^{-6} \text{ K}^{-1}$

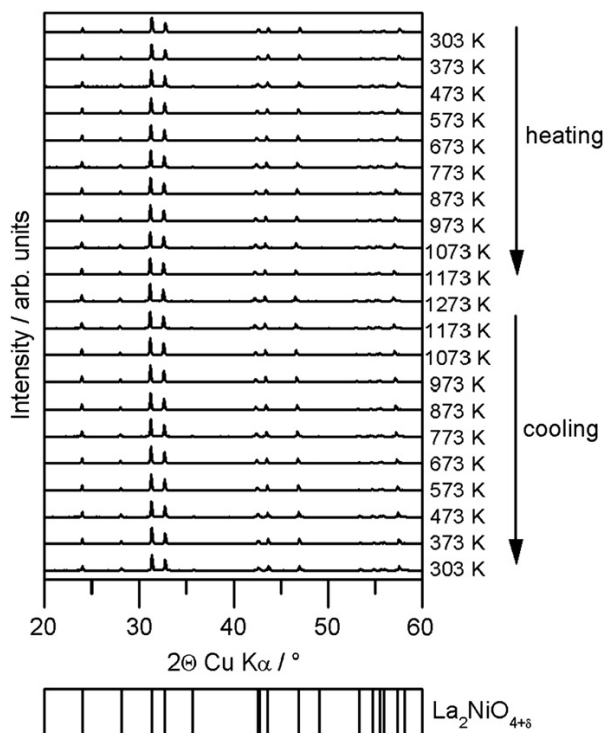


Fig. 4. In-situ XRD patterns of $\text{La}_2\text{NiO}_{4+\delta}$ under 50 vol% CO_2 and 50 vol% air; heating and cooling rate: 12 K min^{-1} , equilibration time at each temperature: 30 min.

measured in air [17,18]. Compared to 3D perovskites, which exhibit values between $20 \times 10^{-6} \text{ K}^{-1}$ and $24 \times 10^{-6} \text{ K}^{-1}$ [15,16,36,37], $\text{La}_2\text{NiO}_{4+\delta}$ possesses a better thermomechanical compatibility, which assures stability in integrated systems such as membrane reactors or SOFCs.

3.2. Membrane microstructure

The microstructures of all membranes were examined using FE-SEM. No cracks or pores were visible on the surfaces of the membranes. In the bulk material only a few non-connected pores were observed. The average grain size was analyzed using the Image J [38] particle analyzer by measuring the grain area in μm^2 and then the effective grain diameter was estimated by assuming circle-shaped grains. Table 1 shows the average grain size for the base material and $\text{La}_2\text{Ni}_{0.9}\text{M}_{0.1}\text{O}_{4+\delta}$ ($M = \text{Al}, \text{Co}, \text{Cu}, \text{Fe}, \text{Mg}, \text{Zr}$). Although the amount of doping is as low as 10 mol%, significant differences in the average grain-size area were observed which increased in the order $\text{Zr}^{4+} < \text{Al}^{3+} < \text{Fe}^{3+} < \text{Ni}^{+2} < \text{Co}^{+2} < \text{Mg}^{+2} < \text{Cu}^{+2}$. The copper-doped $\text{La}_2\text{NiO}_{4+\delta}$ solid solution exhibited the largest grains, with an average size of $5.3 \mu\text{m}$, whereas mixed crystals with the highly charged zirconium provided the smallest grains at $0.4 \mu\text{m}$. From our data, a general trend can be discerned. Cations with low oxidation states favor the formation of large grains, whereas more highly charged ions favor the formation of small grains. Grain size can therefore be directly controlled by doping with metal cations possessing different valences, which results in tailor-made solid solutions. This doping may affect the oxygen-permeation properties with respect to grain or grain-boundary diffusion and surface exchange reactions. However, it is difficult to differentiate between grain size and doping effects and to correlate this to functional properties such as chemical stability and, especially, oxygen flux.

3.3. Oxygen permeation

Oxygen-permeation measurements were conducted in the temperature range of 1023–1223 K. Fig. 5 shows the oxygen-permeation flux of the base material and $\text{La}_2\text{Ni}_{0.9}\text{M}_{0.1}\text{O}_{4+\delta}$ ($M = \text{Al}, \text{Co}, \text{Cu}, \text{Fe}, \text{Mg}, \text{Ni}, \text{Zr}$) from air (feed side) to helium (sweep side) at different temperatures. The doping of the Ni site affects the oxygen-permeation performance of the membranes. The highest flux rate of $0.47 \text{ mL min}^{-1} \text{ cm}^{-2}$ at 1223 K was achieved on a 1 mm thick undoped $\text{La}_2\text{NiO}_{4+\delta}$ membrane. The iron-doped membrane $\text{La}_2\text{Ni}_{0.9}\text{Fe}_{0.1}\text{O}_{4+\delta}$ exhibited a flux rate of $0.46 \text{ mL min}^{-1} \text{ cm}^{-2}$ at 1223 K, which is similar to that of the undoped system. However, doping was found to always diminish the oxygen-permeation rate at 1223 K, which decreases in the order $\text{Fe}^{3+} > \text{Co}^{2+} > \text{Zr}^{4+} \approx \text{Mg}^{+2} \approx \text{Al}^{3+} \approx \text{Cu}^{+2}$. No dependence of the permeation rate on the doped ion's regular valence was observed. The regular oxidation state of Ni cations in the $\text{La}_2\text{NiO}_{4+\delta}$ structure is divalent, and a partial amount of the Ni is oxidised to the trivalent state to compensate for the incorporation of excess oxygen. From this point of view, it would be favorable to insert higher-valence cations to increase the oxygen-carrier concentrations and, therefore, the oxygen-permeation performance. However, no significant improvement was observed in this respect. It can be expected that the interstitial oxygen content increases by doping with Al^{3+} , Fe^{3+} , and Zr^{4+} and decreases with Cu^{2+} , Mg^{2+} and Co^{2+} . However, recently, Kharton et al. reported the results of static lattice and molecular dynamics calculations [39] on the $\text{La}_2\text{NiO}_{4+\delta}$ system and the incorporation of iron, copper and cobalt. These computations showed that the incorporation of higher-valence ions increases the ionic charge-carrier concentration, but the mobility of the oxygen anions in both layers of the $\text{La}_2\text{NiO}_{4+\delta}$ structure is reduced. We observed, in general, that the doping of the Ni site leads to a reduction of the oxygen-permeation performance. However, as proposed by Kharton et al. [35] two contributions to the total ionic conductivity play a decisive role: ionic conduction in the perovskite layers due to oxygen vacancy migration and the interstitial oxygen mechanism. By doping on the B-site both mechanisms may be affected in a positive or negative way. This may explain our above described experimental results and is consistent with literature data on $\text{La}_2\text{Ni}_{0.9}\text{Co}_{0.1}\text{O}_{4+\delta}$ [34] and $\text{La}_2\text{Ni}_{0.9}\text{Fe}_{0.1}\text{O}_{4+\delta}$ [35] membrane materials, which exhibit a smaller flux than undoped $\text{La}_2\text{NiO}_{4+\delta}$ [40]. A correlation of the grain sizes, which were reported in Section 3.2, with the oxygen-permeation rates is difficult. Apparently, larger grains, as observed in the copper- and

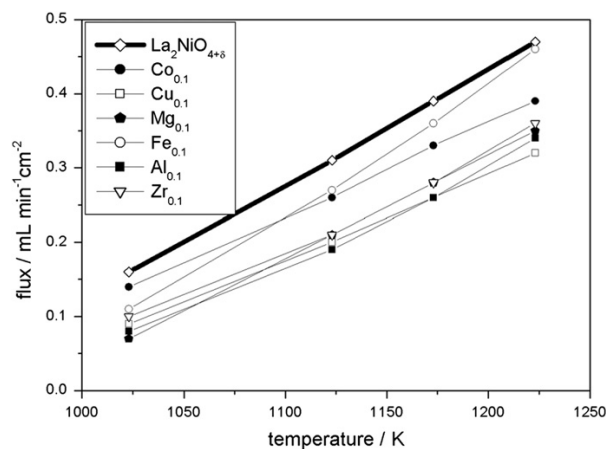


Fig. 5. Oxygen permeation rate of the base material, $\text{La}_2\text{NiO}_{4+\delta}$, and $\text{La}_2\text{Ni}_{0.9}\text{M}_{0.1}\text{O}_{4+\delta}$ ($M = \text{Al}, \text{Co}, \text{Cu}, \text{Fe}, \text{Mg}, \text{Zr}$); membrane thickness: 1 mm, feed side: 150 mL min^{-1} synthetic air, sweep side: 29 mL min^{-1} He and 1 mL min^{-1} Ne.

magnesium-doped La₂NiO_{4+δ}, exhibit low oxygen fluxes. In contrast to this observation, the zirconium- and aluminum-doped samples, which provide the smallest grains, also show low fluxes. This disagreement shows as well, that for improving the overall permeation flux all parameters have to be carefully considered. The activation energies of oxygen diffusion in the temperature range from 1023 to 1223 K were estimated from the Arrhenius representation; the results are summarized in Table 1. The base and cobalt-doped materials exhibit the lowest activation energies of 56.7 kJ mol⁻¹ and 54.1 kJ mol⁻¹, respectively. The activation energy of the iron-doped system, at 75.3 kJ mol⁻¹, is slightly higher. These results are in good agreement with data from the literature, where values of 52.1 kJ mol⁻¹ for La₂NiO_{4+δ} [41] and 69–80 kJ mol⁻¹ for La₂Ni_{0.9}Fe_{0.1}O_{4+δ} [42] were reported. To assess the CO₂ stability during the permeation experiments, a long-term measurement was conducted over 120 h using pure CO₂ as the sweep gas. As is evident in Fig. 6, a constant O₂ permeation flux was observed. Nevertheless, the oxygen-permeation rate is lower than that achieved with pure helium on the sweep side. The decrease of oxygen flux at the start of the measurement may be explained by the inhibiting effect of CO₂ on the surface exchange reaction, which hinders the release of oxygen from the solid surface due to reaction of absorbed CO₂ species with the oxygen vacancies on the membrane surface [43]. Furthermore, the fact that the oxygen surface exchange had various rates in different gas atmospheres is well known and was discussed in detail elsewhere [44–46]. Compared to alkaline-earth-containing materials, e.g., (La_{0.4}Sr_{0.6})(Co_{0.8}Fe_{0.2})O_{3-δ}, which was measured by our group, the oxygen-permeation flux of La₂NiO_{4+δ} is maintained for more than 100 h, whereas the Sr-containing material exhibits a slow decline in the flux and broke down completely after operating for 60 h. Although La₂NiO_{4+δ} shows a lower flux than (La_{0.4}Sr_{0.6})(Co_{0.8}Fe_{0.2})O_{3-δ}, it possesses excellent long-term stability in nearly 100 vol% CO₂ sweep gas at 1173 K.

3.4. Influence of membrane microstructure on oxygen permeation

It was reported that grain or grain boundary interactions play a key role in ionic conduction [23–26]. Many perovskite materials show an increase in oxygen conductivity by increasing the grain size. For perovskite related La₂NiO₄ based materials this was not yet investigated. To investigate the influence of the grain size and grain boundaries in detail, two samples were chosen. To change the grain size, annealing times of 10, 40 and 140 h at 1723 K were applied to

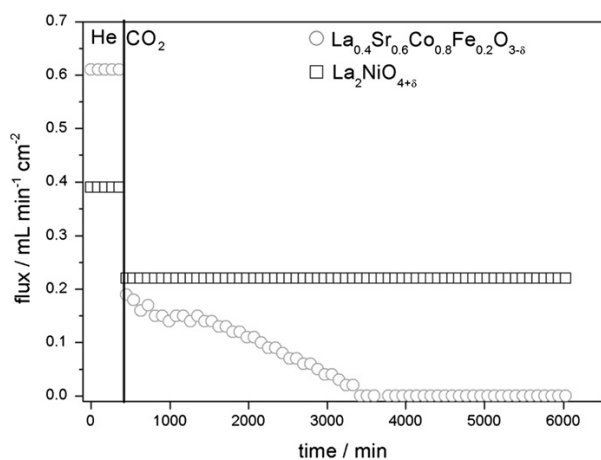


Fig. 6. Oxygen flux rate of La₂NiO_{4+δ} and (La_{0.4}Sr_{0.6})(Co_{0.8}Fe_{0.2})O_{3-δ} membranes at 1173 K with a thickness of 1 mm, feed side: 150 mL min⁻¹ synthetic air, sweep side: 29 mL min⁻¹ He or CO₂ and 1 mL min⁻¹ Ne.

Table 2

The dependence of the average grain size on annealing time and the estimated effective grain diameters for La₂NiO_{4+δ} and La₂Ni_{0.9}Fe_{0.1}O_{4+δ}.

Dwell time (h)	10	40	140
Effective grain diameter La ₂ NiO _{4+δ} (μm)	1.8	2.7	4.6
Effective grain diameter La ₂ Ni _{0.9} Fe _{0.1} O _{4+δ} (μm)	1.2	1.7	8.2

samples of La₂NiO_{4+δ} and La₂Ni_{0.9}Fe_{0.1}O_{4+δ}. Table 2 shows the average grain sizes that were obtained by this treatment, whereas Fig. 7 a–c shows the SEM images of the surfaces of the La₂Ni_{0.9}Fe_{0.1}O_{4+δ} membranes that were sintered for different annealing times. In addition, a surface view of a La₂NiO_{4+δ} membrane that was polished to crystallinity and then examined by the channeling contrast technique is shown in Fig. 7d. As is evident in the figures, grain growth was induced by longer sintering times. The base material exhibits grain sizes of 1.8, 2.7 and 4.6 μm² for the membranes sintered for 10, 40 and 140 h, respectively. The oxygen flux decreases from 0.47 to 0.41 to 0.31 mL min⁻¹ cm⁻² with increasing grain size and, therefore, with decreasing amount of grain boundaries. For the iron-doped sample, average grain sizes of 1.2, 1.7 and 8.2 μm² were obtained after annealing times of 10, 40 and 140 h. The oxygen flux was 0.46 mL min⁻¹ cm⁻², which increased slightly to 0.49 mL min⁻¹ cm⁻² and then decreased to 0.39 mL min⁻¹ cm⁻². Thus, the base material shows lower fluxes with increasing grain size (Fig. 8), whereas for the iron-doped samples, this effect is less pronounced. To conclude, our experimental findings show a negative effect of an increased grain size on oxygen permeation. This may be related to faster grain boundary diffusion, which may be more favorable in case of the predominantly 2D-conducting interstitial mechanism in La₂NiO_{4+δ}.

3.5. Mössbauer measurements on La₂Ni_{0.9}Fe_{0.1}O₄

Transmission Mössbauer measurements were performed at 298 K, Fig. 9. As is evident in the figure, the spectra are dominated by a doublet with a quadrupole splitting of about QS(I) = 1.4 mm/s. However, due to the slight asymmetry visible at its center, a second doublet with a smaller splitting, QS(II), of about 0.4 mm/s is required for a consistent and appropriate fit of the spectrum. The spectrum was fitted with Voigt model functions which allow for a distribution of quadrupolar interactions at the nuclei. According to Menil et al. [47], the observed isomer shift IS(I) of the doublet with the larger quadrupole splitting, Table 3, can be attributed to octahedrally coordinated Fe³⁺. The shift IS(II) of the second quadrupole doublet approaches the range expected for Fe⁴⁺. Thus, the second doublet may be attributed to an iron species with a mixed Fe³⁺/Fe⁴⁺ charge state where the difference in the experimental isomer shifts, IS(I)–IS(II), amounts to about 0.2 mm/s. For comparison, note that in the case of the system (La,Sr)(Fe,Mn)O₃ a value of 0.3 mm/s was obtained for the difference in shifts for Fe³⁺ and Fe⁴⁺ [48]. Because Fe³⁺ is known to occupy Ni²⁺ regular positions in La₂Ni_{0.9}Fe_{0.1}O_{4+δ} [49], the spectroscopically detected presence of a second iron species possessing a Fe³⁺/Fe⁴⁺ charge state suggests the presence of a secondary phase. In fact, according to the phase diagram for La–Fe–Ni–O reported by Kiselev et al. for 1370 K, the sample under investigation in the present study, La₂Ni_{0.9}Fe_{0.1}O_{4+δ}, should consist of three phases at high temperatures: La₂O₃, La₂Ni_{0.9}Fe_{0.1}O_{4+δ} and La₄Ni_{2.1}Fe_{0.9}O_{10-δ} [50]. Here, the latter phase may contain a mixed-valent iron component and, thus may be associated with the experimentally observed secondary phase. This phase composition is also consistent with our TEM observations, see below. In conclusion, our observation of two quadrupole-split subspectra due to iron ions of different valency is compatible

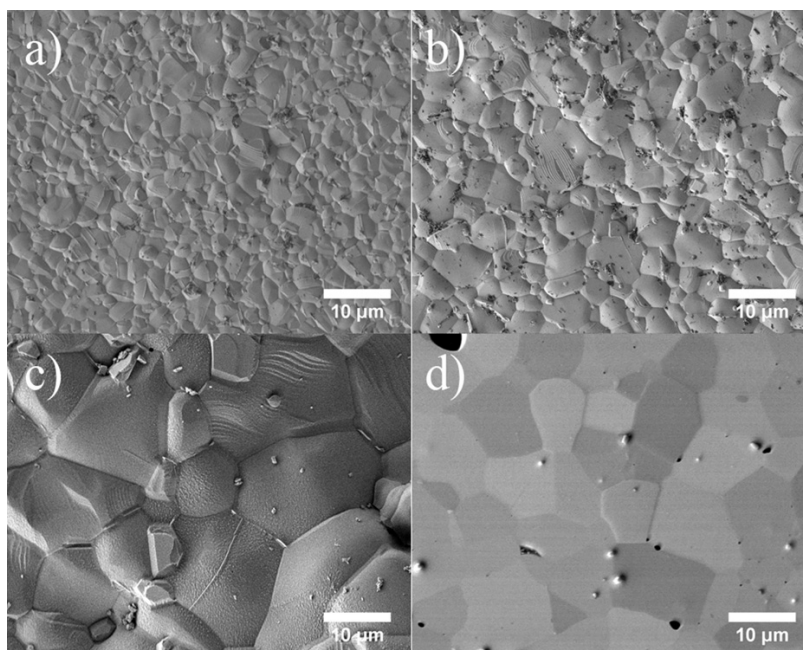


Fig. 7. SE surface view micrographs of the grain structure of $\text{La}_2\text{Ni}_{0.9}\text{Fe}_{0.1}\text{O}_{4+\delta}$ with different sintering times (a) 10 h, (b) 40 h and (c) 140 h and (d) $\text{La}_2\text{NiO}_{4+\delta}$ 140 h channeling contrast image.

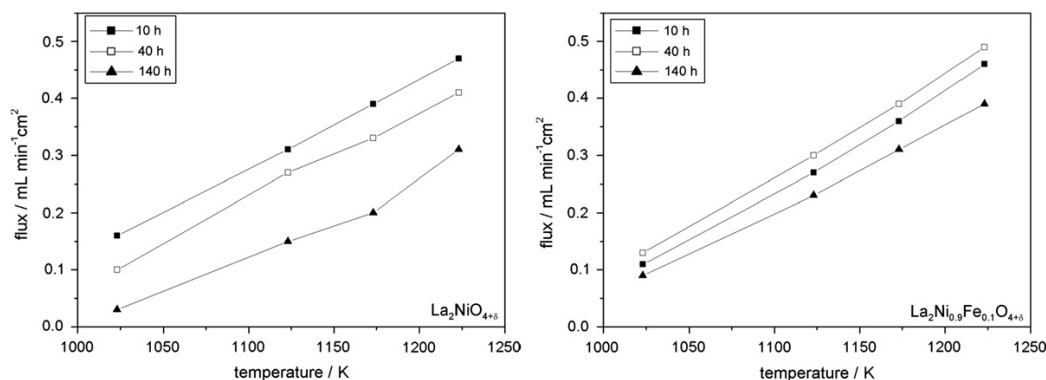


Fig. 8. Oxygen-permeation flux of the base material, $\text{La}_2\text{NiO}_{4+\delta}$, and $\text{La}_2\text{Ni}_{0.9}\text{Fe}_{0.1}\text{O}_{4+\delta}$ after different annealing times.

with the admittedly incomplete information available for the La–Fe–Ni–O phase diagram.

Previously, ^{57}Fe Mössbauer absorption spectra of $\text{La}_2\text{Ni}_{1-x}\text{Fe}_x\text{O}_{4+\delta}$ have been reported by Fontcuberta et al. ($x \approx 0.02$) [49] and by Tsipis et al. ($x=0.1$) [51]. However, whereas Tsipis et al. [51] reported a strictly symmetrical signal that could be fitted with a single quadrupole doublet, the spectrum obtained by Fontcuberta et al. [49] is strongly asymmetric and requires three quadrupole doublets for an acceptable fit. Good agreement is observed between the present study and spectral parameters reported in the literature for the dominating doublet possessing the largest splitting, see Table 3. In respect to the secondary contributions in their spectrum which amount up to 30% of total intensity, Fontcuberta et al. [49] speculate that these could be due to iron ions incorporated into intergrowth phases, $\text{La}_{2+n}\text{Ni}_{1+n}\text{O}_{4+3n}$. Indeed, the presence of such a phase, $\text{La}_4\text{Ni}_3\text{O}_{10}$ with $n=2$, is confirmed by the present results obtained by TEM as is reported below. A striking discrepancy, however, remains in respect to the isomer shift of the secondary contribution(s) to the Mössbauer spectra. Whereas the two secondary subspectra

observed by Fontcuberta et al. [49] most probably are due to Fe^{3+} ions, the isomer shift observed in the present work indicates a $\text{Fe}^{3+}/\text{Fe}^{4+}$ mixed-valent charge state of iron. According to Tsipis et al. [52], in bulk $\text{La}_4\text{Ni}_{2.7}\text{Fe}_{0.3}\text{O}_{10-\delta}$ iron is present as Fe^{3+} exclusively. A possible reason for this discrepancy with the present work may be due to the fact that the secondary intergrowth phase in our sample is present as lamellae possessing thicknesses of the order of 10 nm, see below, and that the electronic structure of these nanophases is not yet comparable with that of the bulk. Alternatively, the secondary signal observed in our sample could be due to iron ions in the bulk of $\text{La}_2\text{Ni}_{1-x}\text{Fe}_x\text{O}_{4+\delta}$ which compensate for the excess of interstitial oxygen. Further work, including an *in-situ* Mössbauer study at high temperatures, is under way to solve these open questions.

3.6. HRTEM and SAED

Samples of $\text{La}_2\text{NiO}_{4+\delta}$ and $\text{La}_2\text{Ni}_{0.9}\text{Fe}_{0.1}\text{O}_{4+\delta}$ were vibrational polished to preserve crystallinity to the very surface and then

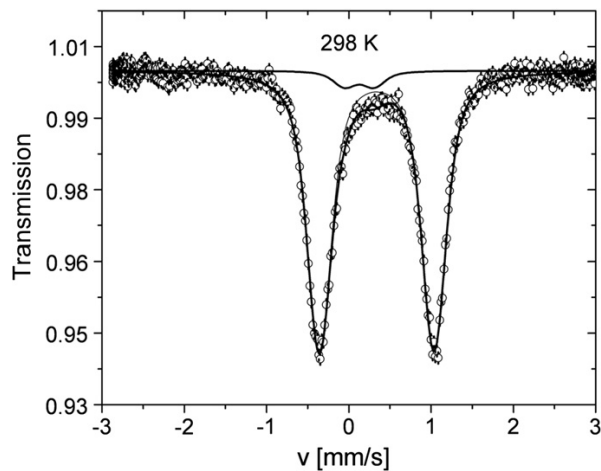


Fig. 9. Mössbauer spectrum of La₂Ni_{0.9}Fe_{0.1}O_{4+δ} at 298 K.

Table 3
Mössbauer fitting result for La₂Ni_{0.9}Fe_{0.1}O_{4+δ} at room temperature from present work and from literature: A – area fraction (error), <δ> – mean values of isomer shift (vs α-Fe) and <A> – mean values of quadrupolar splitting.

temperature (K)	State	A (%)	<δ> (mm/s)	<A> (mm/s)	Ref.
298	Fe ³⁺	95.2(14)	0.339(1)	1.409(3)	This work
	Fe ³⁺ /Fe ⁴⁺	4.8(14)	0.13(4)	0.36(6)	
295	Fe ³⁺	68(2)	0.322(1)	1.440(4)	[49]
	Fe ³⁺	19(4)	0.295	0.85(2)	
	Fe ³⁺	13(4)	0.267(6)	0.40(3)	
295	Fe ³⁺	100	0.33	1.35	[51] in air
	Fe ³⁺	100	0.34	1.31	

investigated using backscattered-electron channeling contrast imaging. In Fig. 10, La₂NiO_{4+δ} showed no formation of a foreign phase, whereas La₂Ni_{0.9}Fe_{0.1}O_{4+δ} showed numerous lamella-like structures inside the host grains. A different iron-containing phase was detected by our Mössbauer experiment. The grain boundaries were examined in detail to find possible by-phases. Furthermore, the nature of the grain boundaries might be a key factor for the oxygen permeation performance. Three grains are shown in Fig. 11a: the upper grain is oriented along zone axis [3 1 1], the lower is oriented along zone axis [1 1 0] and the grain on the left side of the micrograph is not oriented. No amorphous or other phases were observed at the interface between the two oriented grains, see Fig. 11b. Therefore, the different grains are in intimate contact without contaminations inside the grain boundaries. As stated previously, according to the phase diagram of Kiselev et al. [50], the sample should consist at high temperatures of the three different phases: La₂O₃, La₂Ni_{0.95}Fe_{0.05}O_{4+δ}, and La₄Ni_{2.1}Fe_{0.9}O_{10-δ}. As shown in Section 3.1, La₂Ni_{1-x}Fe_xO_{4+δ} is indeed the main phase, as confirmed by XRD. With respect to the sensitivity of XRD, the other phases in low concentrations may not be detectable. The perovskite-related Ruddlesden–Popper phase, which is characterized by a different stacking sequence of the successive c-axis, was observed as an intergrowth in several La₂Ni_{1-x}Fe_xO_{4+δ} host grains. As seen in the HAADF-STEM image (Fig. 12 a), the lamella goes through the whole host grain. HRTEM (Fig. 12 b,c) reveals the interface between the La₂Ni_{1-x}Fe_xO_{4+δ} and La_{2+n}Ni_{1+n}O_{4+3n-δ} phases. The lamella is approximately 15–30 nm thick. The SAED pattern in Fig. 12d shows La₂Ni_{1-x}Fe_xO_{4+δ} along the

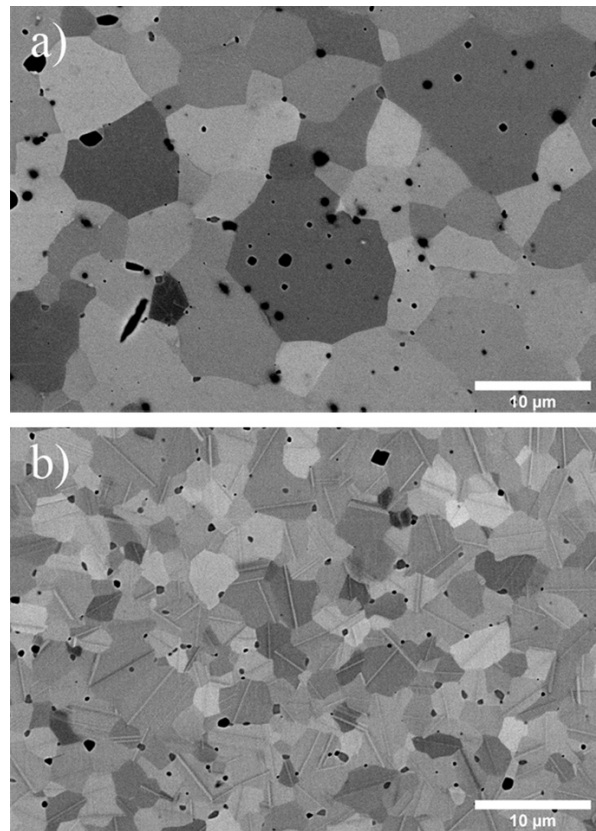


Fig. 10. (a) The polished-surface channeling contrast images of La₂NiO_{4+δ} sintered for 10 h and (b) La₂Ni_{0.9}Fe_{0.1}O_{4+δ} sintered for 10 h.

[1 1 0] zone axis. Fig. 12e shows the superposition of the SAED patterns from the host grain and the detected La_{2+n}Ni_{1+n}O_{4+3n-δ} intergrowth phase. Via EDXS, an enrichment of iron could be detected in the lamella. The simulated HRTEM contrast images for La₄Ni₃O₄ and La₂NiO₄ phases (Fig. 12c) via the JEMS software using the multislice method are in good agreement with our experimental data. Therefore, according to the SAED and the JEMS simulation, the intergrowth can be clearly indexed as an iron-containing La₄Ni₃O₄ phase which is in accordance with the present Mössbauer and TEM observations. Because La₂O₃ was also detected by EDXS, we conclude that La₂Ni_{0.95}Fe_{0.05}O_{4+δ} is the main phase and that La₄Ni_{2.1}Fe_{0.9}O_{10-δ} and La₂O₃ are by-phases. These intergrowths were not reported and discussed in a previous publication concerning the La₂Ni_{0.9}Fe_{0.1}O_{4+δ} system [51]. It may be difficult, but not impossible as shown by Kiselev et al. [50], to detect these phases by XRD. However, they can be seen directly in the electron microscope as seen in Figs. 10 and 12.

4. Conclusions

The La₂NiO_{4+δ} system exhibits good stability in CO₂-containing atmospheres and long-term operation compared to alkaline-earth-containing oxygen-transporting membranes. Doping the membranes with a variety of ions with different valences does not improve the oxygen flux, but the process can influence the surface microstructure and grain size. Furthermore, increasing grain size by annealing for longer times at high temperatures had a negative impact on the oxygen-permeation flux. Smaller grains

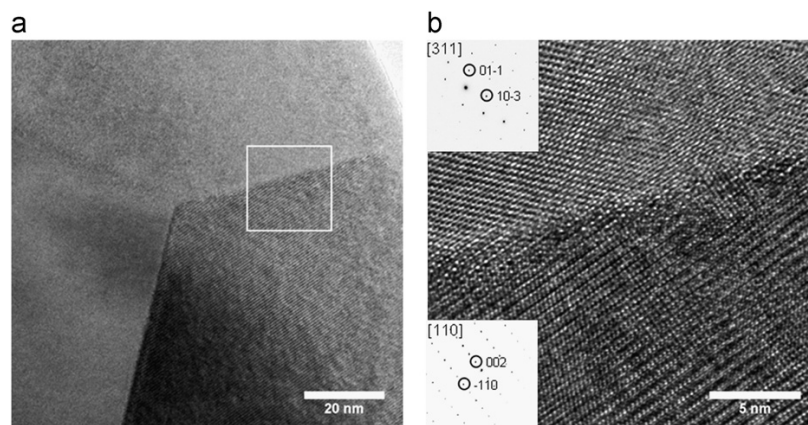


Fig. 11. (a) Bright-field TEM of three grains in close contact and (b) HRTEM of the two oriented grains with insets showing the SAED patterns of the grains.

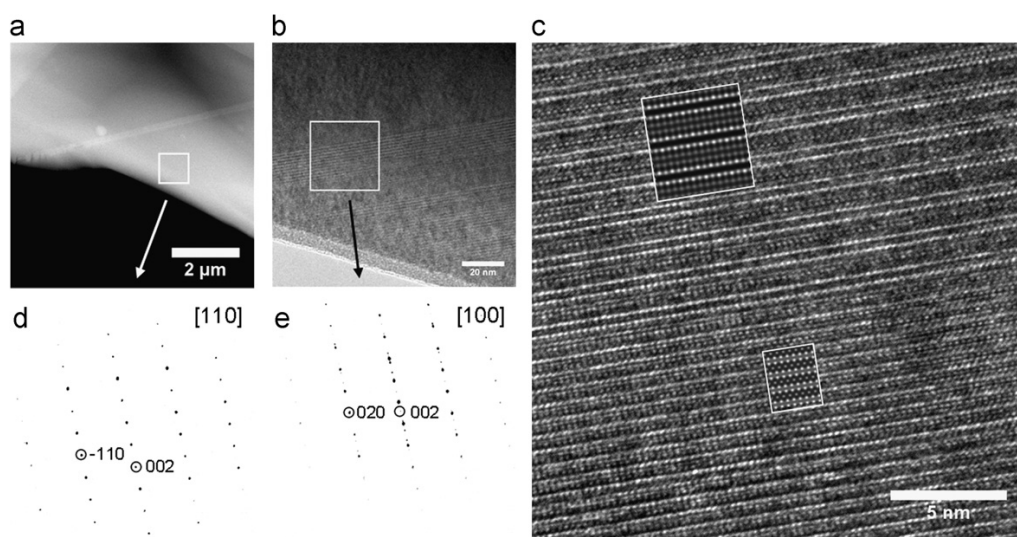


Fig. 12. (a) High-angular dark-field STEM of a $\text{La}_2\text{Ni}_{0.9}\text{Fe}_{0.1}\text{O}_{4+\delta}$ grain with lamella (b) HRTEM of a $\text{La}_2\text{Ni}_{0.9}\text{Fe}_{0.1}\text{O}_{4+\delta}$ grain with lamella (c) HRTEM of the interface between the $\text{La}_2\text{Ni}_{0.9}\text{Fe}_{0.1}\text{O}_{4+\delta}$ grain and lamella; the inset shows the image calculated with a 64 nm defocus and a sample thickness of 3.8 nm (d) SAED pattern of a $\text{La}_2\text{Ni}_{0.9}\text{Fe}_{0.1}\text{O}_{4+\delta}$ grain (e) SAED pattern of the lamella and the $\text{La}_2\text{Ni}_{0.9}\text{Fe}_{0.1}\text{O}_{4+\delta}$ host (\emptyset SAED aperture 125 nm).

are beneficial for oxygen-permeation performance in the case of $\text{La}_2\text{NiO}_{4+\delta}$ and $\text{La}_2\text{Ni}_{0.9}\text{Fe}_{0.1}\text{O}_{4+\delta}$. TEM and Mössbauer experiments reveal that $\text{La}_2\text{Ni}_{0.95}\text{Fe}_{0.05}\text{O}_{4+\delta}$ is accompanied by $\text{La}_4\text{Ni}_{2.1}\text{Fe}_{0.9}\text{O}_{10-\delta}$ and La_2O_3 by-phases.

Acknowledgments

Financial support from the State of Lower Saxony in the frame of NTH bottom-up project No. 21-71023-25-7/09 is gratefully acknowledged. The authors thank Dr. M. Rodewald and Dr. J. Heindl, JEOL (Germany) GmbH, for SEM measurements.

References

- [1] H. Wang, S. Werth, T. Schiestel, J. Caro, *Angew. Chem. Int. Ed.* 44 (2005) 6906.
- [2] F.T. Akin, Y.S. Lin, *J. Membr. Sci.* 209 (2002) 457.
- [3] C. Chen, S. Feng, S. Ran, D. Zhu, W. Liu, H.J.M. Bouwmeester, *Angew. Chem. Int. Ed.* 42 (2003) 5196.
- [4] Z. Shao, S.M. Haile, *Nature* 431 (2004) 170.
- [5] R. Bredesen, K. Jordal, O. Bolland, *Chem. Eng. Process.* 43 (2004) 1129.

- [6] Y. Teraoka, H. Zhang, S. Furukawa, N. Yamazoe, *Chem. Lett.* 11 (1985) 1743.
- [7] Z. Shao, W. Yang, Y. Cong, H. Dong, J. Tong, G.J. Xiong, *J. Membr. Sci.* 172 (2000) 177.
- [8] M. Arnold, H. Wang, A. Feldhoff, *J. Membr. Sci.* 293 (2007) 44.
- [9] J. Martynczuk, K. Efimov, L. Robben, A. Feldhoff, *J. Membr. Sci.* 344 (2009) 62.
- [10] I. Barin, F. Sauer, G. Patzki, *Thermochemical data of pure substances*, third ed., vols. I and II, VCH, Weinheim, 1995.
- [11] A.N. Shirsat, M. Ali, K.N.G. Kaimal, S.R. Bharadwaj, D. Das, *Thermochim. Acta* 399 (2003) 167.
- [12] Y. Watanabe, S. Miyazaki, T. Maruyama, Y. Saito, *J. Mater. Sci. Lett.* 5 (1996) 135.
- [13] K. Efimov, M. Arnold, J. Martynczuk, A. Feldhoff, *J. Am. Ceram. Soc.* 92 (2008) 876.
- [14] K. Eichhorn Colombo, V.V. Kharton, A.P. Viskup, A.V. Kovalevsky, A.L. Shaula, O. Bolland, *J. Solid State Electrochem.* 15 (2011) 329.
- [15] S. McIntosh, J.F. Vente, W.G. Haije, D.H.A. Blank, H.J.M. Bouwmeester, *Chem. Mater.* 18 (2006) 2187.
- [16] J.F. Vente, W.G. Haije, Z.S. Rak, *J. Membr. Sci.* 177 (2006) 2245.
- [17] M. Al Daroukh, V.V. Vashook, H. Ullmann, F. Tietz, I. Arual Raj, *Solid State Ionics* 158 (2003) 141.
- [18] G. Amow, S.J. Skinner, *J. Solid State Electrochem.* 10 (2006) 538.
- [19] L. Minervini, R.W. Grimes, J.A. Kilner, K.E. Sickafus, *J. Mater. Chem.* 10 (2000) 2349.
- [20] Z. Hiroi, T. Obata, M. Takano, Y. Bando, *Phys. Rev. B* 41 (1990) 11665.
- [21] A. Demourgues, F. Weill, B. Darriet, A. Wattiaux, J.C. Grenier, P. Gravereau, M. Pouchard, *J. Solid State Chem.* 106 (1993) 317.

- [22] S.J. Skinner, *Solid State Sci.* 5 (2003) 419.
- [23] J. Martynczuk, M. Arnold, A. Feldhoff, *J. Membr. Sci.* 322 (2008) 375.
- [24] L. Tan, X. Gu, L. Yang, W. Jin, L. Zhang, N. Xu, *J. Membr. Sci.* 212 (2003) 157.
- [25] A.L. Shaula, R.O. Fuentes, F.M. Figueiredo, V.V. Kharton, F.M.B. Marques, J.R. Frade, *J. Eur. Ceram. Soc.* 25 (2005) 2613.
- [26] K. Zhang, Y.L. Yang, D. Ponnusamy, A.J. Jacobson, K. Salama, *J. Mater. Sci.* 34 (1999) 1367.
- [27] J. Martynczuk, M. Arnold, J. Caro, H. Wang, A. Feldhoff, *Adv. Mater.* 19 (2007) 2134.
- [28] A. Feldhoff, M. Arnold, J. Martynczuk, T.M. Gesing, H. Wang, *Solid State Sci.* 10 (2008) 689.
- [29] A. Feldhoff, J. Martynczuk, H. Wang, *Prog. Solid State Chem.* 35 (2007) 339.
- [30] K. Lagarec, D.G. Rancourt, *Nucl. Instrum. Methods Phys. Res. Sect. B* 129 (1972) 266.
- [31] H. Wang, C. Tablet, A. Feldhoff, J. Caro, *J. Membr. Sci.* 262 (2005) 20.
- [32] D.E. Rice, D.J. Buttrey, *J. Solid State Chem.* 105 (1993) 197.
- [33] B. Grande, H. Müller-Buschbaum, *Z. Anorg. Allg. Chem.* 433 (1977) 152.
- [34] A.A. Yaremchenko, V.V. Kharton, M.V. Patrakeev, J.R. Frade, *J. Mater. Chem.* 13 (2003) 1136.
- [35] V.V. Kharton, A.P. Viskup, E.N. Naumovich, F.M.B. Marques, *J. Mater. Chem.* 9 (1999) 2623.
- [36] K. Efimov, T. Halfer, A. Kuhn, P. Heitjans, J. Caro, A. Feldhoff, *Chem. Mater.* 22 (2010) 1540.
- [37] A. Feldhoff, J. Martynczuk, M. Arnold, M. Myndyk, I. Bergmann, V. Šepelák, W. Gruner, U. Vogt, A. Hähnel, J. Woltersdorf, *J. Solid State Chem.* 182 (2009) 2961.
- [38] M.D. Abramoff, P.J. Magelhaes, S.J. Ram, *Biophotonics Int.* 11 (2004) 36.
- [39] E.N. Naumovich, V.V. Kharton, *J. Mol. Struct.* 946 (2010) 57.
- [40] V.V. Kharton, E.V. Tsipis, E.N. Naumovich, A. Thursfield, M.V. Patrakeev, V.A. Kolotygin, J.C. Waerenborg, I.S. Metcalfe, *J. Solid State Chem.* 181 (2008) 1425.
- [41] R. Sayers, R.A. De Souza, J.A. Kilner, S.J. Skinner, *Solid State Ionics* 181 (2010) 386.
- [42] E.V. Tsipis, E.N. Naumovich, A.L. Shaula, M.V. Patrakeev, J.C. Waerenborg, V.V. Kharton, *Solid State Ionics* 179 (2008) 57.
- [43] J.E. ten Elshof, H.J.M. Bouwmeester, H. Verweij, *Solid State Ionics* 89 (1996) 81.
- [44] J.A. Lane, J.A. Kilner, *Solid State Ionics* 136–137 (2000) 927.
- [45] K. Yashiro, S. Onuma, A. Kaimai, Y. Nigara, T. Kawada, J. Mizusaki, K. Kawamura, T. Horita, H. Yokokawa, *Solid State Ionics* 152–153 (2002) 469.
- [46] I.V. Khromushin, T.I. Aksenova, Zh.R. Zhotabaev, *Solid State Ionics* 162 (2003) 37.
- [47] F. Menil, *J. Phys. Chem. Solids* 46 (1985) 763.
- [48] K.L. da Silva, A. Börger, K.-D. Becker, F. Tietz, D. Stöver, *Solid State Ionics* 192 (2011) 552.
- [49] J. Fontcuberta, G. Longworth, J.B. Goodenough, *Phys. Rev. B* 30 (11) (1984) 6320.
- [50] E.A. Kiselev, N.V. Proskurnina, V.I. Voronin, V.A. Cherepanov, *Inorg. Mater.* 43 (5) (2007) 167.
- [51] E.V. Tsipis, E.N. Naumovich, M.V. Patrakeev, J.C. Waerenborg, Y.V. Pivak, B. Gacynski, V.V. Kharton, *J. Phys. Chem. Solids* 68 (2007) 1443.
- [52] E.V. Tsipis, M.V. Patrakeev, J.C. Waerenborg, Y.V. Pivak, A.A. Markov, P. Gacynski, E.N. Naumovich, V.V. Kharton, *J. Solid State Chem.* (2007) 1902.

2.3 In-situ Mössbauer studies of ⁵⁷Fe-doped Ruddlesden-Popper type lanthanum nickel oxides

Tobias Klande, Salvatore Cusenza, Piotr Gaczyński, Klaus-Dieter Becker, Lars Dör-
rer, Günther Borchardt, and Armin Feldhoff

Solid State Ionics **222-223** (2012) 8-15



In-situ Mössbauer studies of ^{57}Fe -doped Ruddlesden–Popper type lanthanum nickel oxides

Tobias Klande ^{a,*}, Salvatore Cusenza ^b, Piotr Gaczyński ^b, Klaus-Dieter Becker ^b, Lars Dörrer ^c, Günter Borchart ^c, Armin Feldhoff ^a

^a Institute of Physical Chemistry and Electrochemistry, Leibniz Universität Hannover, Callinstr. 3a, D-30179 Hannover, Germany

^b Institute of Physical and Theoretical Chemistry, Technische Universität Braunschweig, Hans-Sommer-Str. 10, D-38106 Braunschweig, Germany

^c Institute of Metallurgy, Technische Universität Clausthal, Robert-Koch-Str. 42, D-38678 Clausthal-Zellerfeld, Germany

ARTICLE INFO

Article history:

Received 1 February 2012
Received in revised form 4 June 2012
Accepted 19 June 2012
Available online xxxx

Keywords:

Ruddlesden–Popper phases
In-situ Mössbauer spectroscopy
Transmission electron microscopy
Electrical conductivity
Oxygen permeation

ABSTRACT

The Ruddlesden–Popper (RP) phases $\text{La}_2\text{Ni}_{1-x}\text{Fe}_x\text{O}_{4+\delta}$ ($x = 0.02, 0.1$) and $\text{La}_4\text{Ni}_{3-x}\text{Fe}_x\text{O}_{10-\delta}$ ($x = 0.3, 0.9$) were successfully synthesized via the sol–gel route. Even though X-ray diffraction did not show any secondary phases for $\text{La}_2\text{Ni}_{0.9}\text{Fe}_{0.1}\text{O}_{4+\delta}$, approximately 5–10% of the higher order RP phase $\text{La}_4\text{Ni}_{2.1}\text{Fe}_{0.9}\text{O}_{10-\delta}$ were detected in backscattered electron contrast imaging, whereas $\text{La}_2\text{Ni}_{0.98}\text{Fe}_{0.02}\text{O}_{4+\delta}$ exhibits no foreign phases. This was also confirmed by transmission electron microscopy (TEM). Furthermore, the oxygen permeation performance and electrical conductivity of $\text{La}_2\text{Ni}_{1-x}\text{Fe}_x\text{O}_{4+\delta}$ were found to decrease slightly with increasing iron content. The Mössbauer spectra of $\text{La}_2\text{Ni}_{1-x}\text{Fe}_x\text{O}_{4+\delta}$ ($x = 0.02, 0.1$) are dominated by a quadrupole-split doublet. With increasing temperature, however, a minority iron species is detected. The dominating doublet reveals an unusual high-temperature behavior of quadrupolar interactions, which was observed by *in-situ* Mössbauer measurements at high temperatures and different oxygen partial pressures. This is most likely related to ordering phenomena of oxygen.

© 2012 Elsevier B.V. All rights reserved.

1. Introduction

Mixed ionic electronic conductors (MIECs) with perovskite structure such as $\text{Ba}_{0.5}\text{Sr}_{0.5}\text{Co}_{0.8}\text{Fe}_{0.2}\text{O}_{3-\delta}$ (BSCF), perovskite-related Ruddlesden–Popper (RP) type phases $\text{La}_2\text{NiO}_{4+\delta}$ or the higher order $\text{La}_4\text{Ni}_3\text{O}_{10-\delta}$ phase have received considerable attention concerning their possible application as oxygen-transporting membranes (OTMs) for the production of high-purity oxygen, oxygen-enriched air, or as solid oxide fuel cell (SOFC) cathodes [1–3].

The RP series is formed by an arrangement of LaNiO_3 perovskite and LaO rock salt-type layers. The first member of the series $\text{La}_{n+1}\text{Ni}_n\text{O}_{3n+1}$ with $n = 1$ adopts the K_2NiF_4 structure, consisting of alternating perovskite and rock-salt layers, whereas the end member, LaNiO_3 with $n = \infty$ exhibits the perovskite structure [4].

In the orthorhombic $\text{La}_4\text{Ni}_3\text{O}_{10-\delta}$ structure ($n = 3$), three layers of NiO_6 octahedra and one rock-salt layer are stacked along the crystallographic c -axis. This leads to two different nickel sites. The nickel ions at Wyckoff position 4a in the middle of the perovskite layers are in close contact to other neighboring nickel octahedral sites (Fig. 1). On the other hand, the nickel ions at Wyckoff position 8i are sandwiched between a rock-salt and a perovskite layer [5]. The $\text{La}_4\text{Ni}_3\text{O}_{10-\delta}$ structure is orthorhombic at room temperature, but transformation to tetragonal symmetry at high temperatures was reported [2]. The oxygen content

of $\text{La}_4\text{Ni}_3\text{O}_{10-\delta}$ can be close to exact stoichiometry (in the literature values have been reported, e.g., of $\delta = -0.02$ [6] and -0.05 [7], corresponding to a slight oxygen excess), but can also exhibit a significant oxygen deficit, see e.g. Ref. [3] with $\delta = +0.22$.

The $\text{La}_2\text{NiO}_{4+\delta}$ structure, on the other hand, possesses only one distinct nickel site (Fig. 1), Wyckoff position 2a [8]. This compound, however, can accommodate a wide range of oxygen excess ($0 \leq \delta \leq 0.25$) at interstitial positions in the rocksalt layers, which results in different crystal lattice symmetries [9]. Studies using *in-situ* neutron diffraction show a transformation from orthorhombic to tetragonal symmetry between room temperature and 423 K under vacuum conditions [10]. The loss of excess oxygen can be detected up to 723 K.

The electrical conductivity of pure and doped $\text{La}_2\text{NiO}_{4+\delta}$ is characterized by a maximum which is observed between 600 and 750 K with conductivity values of about 60 S cm^{-1} [7,11,12]. Higher order RP phases exhibit a pronounced metallic behavior, mainly due to the increasing number of O–Ni–O bonds. Due to its high electrical conductivity of 180 S cm^{-1} at room temperature and of 120 S cm^{-1} at 650 K $\text{La}_4\text{Ni}_3\text{O}_{10-\delta}$ seems favorable for numerous applications [2].

The stability of the RP phases was investigated in detail by Zinkevich et al. [13] and Bannikov and Cherepanov [14]. They found that the higher RP phases decompose in air with $p_{\text{O}_2} = 0.2$ bar at 1230 K into $\text{La}_2\text{NiO}_{4+\delta}$, NiO, and O_2 . Thus, $\text{La}_2\text{NiO}_{4+\delta}$ seems to be a phase of high thermodynamic stability among the RP series. However, some groups reported about decomposition of this phase after long-term treatment. Gauquelin et al. annealed single crystals of

* Corresponding author. Tel.: +49 511 762 2943.

E-mail address: tobias.klande@pci.uni-hannover.de (T. Klande).

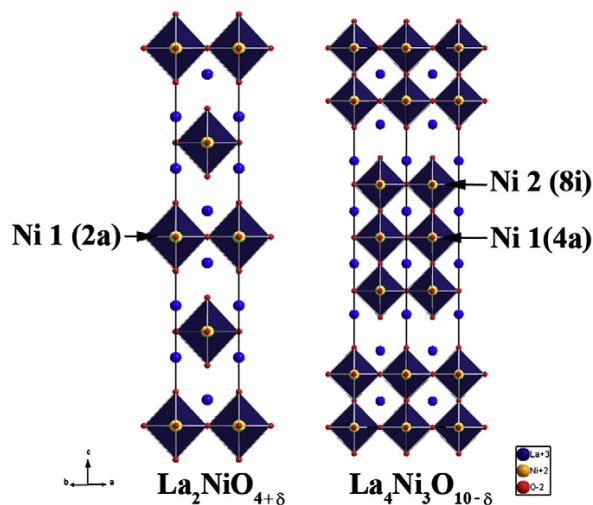


Fig. 1. Crystal structure of tetragonal $\text{La}_2\text{NiO}_{4+\delta}$ (s. g. $I4/mmm$, ICSD no. 1179) and orthorhombic $\text{La}_4\text{Ni}_3\text{O}_{10-\delta}$ (s. g. $Fmmm$, ICSD no. 80279) with indication of Wyckoff positions for nickel sites.

$\text{La}_2\text{NiO}_{4+\delta}$ for 13 days at 1273 K in air [15]. By detailed transmission electron microscopy (TEM) investigations they showed the formation of few Ni-enriched $\text{La}_4\text{Ni}_3\text{O}_{10-\delta}$ and $\text{La}_3\text{Ni}_2\text{O}_{7-\delta}$ lamellae on the surface of the crystals. Amow et al. found small amounts of $\text{La}_3\text{Ni}_2\text{O}_{7-\delta}$ and La_2O_3 after annealing $\text{La}_2\text{Ni}_{0.9}\text{Co}_{0.1}\text{O}_{4+\delta}$ for 14 days at 1223 K in air [16]. However, the decomposition of the materials was not analyzed quantitatively, as the foreign phases were only detected in small amounts at the surface and not in the bulk material. Stabilization of the $\text{La}_2\text{NiO}_{4+\delta}$ structure by iron doping was reported earlier [17]. Kiselev et al. investigated the phase relations in the La-Ni-Fe-O system in detail. They found that $\text{La}_2\text{NiO}_{4+\delta}$ can take up a maximum iron content of 5 mol% for samples quenched from 1370 K to room temperature [18]. However, some groups reported about single phase $\text{La}_2\text{Ni}_{0.9}\text{Fe}_{0.1}\text{O}_{4+\delta}$ and $\text{La}_2\text{Ni}_{0.8}\text{Fe}_{0.2}\text{O}_{4+\delta}$ solid solutions at room temperature [19,20]. Nevertheless, in a previous work we showed by vibration polishing and scanning electron microscopy (SEM) as well as by TEM that $\text{La}_2\text{Ni}_{0.9}\text{Fe}_{0.1}\text{O}_{4+\delta}$ is indeed composed of three different phases ($\text{La}_2\text{Ni}_{0.95}\text{Fe}_{0.05}\text{O}_{4+\delta}$, $\text{La}_4\text{Ni}_{2.1}\text{Fe}_{0.9}\text{O}_{10-\delta}$, La_2O_3) [21]. It is expected that iron promotes stabilization of perovskite layers leading to higher order RP phases due to its tendency to the higher formal valence of 3. This corroborates with thermodynamic data, as LaNiO_3 decomposes in air at 1123 K [14], whereas LaFeO_3 is stable up to its melting point at 2163 K [22].

Concerning earlier Mössbauer investigations of iron-doped $\text{La}_2\text{NiO}_{4+\delta}$ some discrepancies are observed. Tsipis et al. [11] obtained a symmetrical signal for $\text{La}_2\text{Ni}_{0.9}\text{Fe}_{0.1}\text{O}_{4+\delta}$ at room temperature, which could be fitted using a single quadrupole doublet, whereas Fontcuberta et al. [23] reported a strongly asymmetric spectrum for $\text{La}_2\text{Ni}_{0.98}\text{Fe}_{0.02}\text{O}_{4+\delta}$ which required three quadrupole doublets for an acceptable fit. Furthermore, Tsipis et al. measured spectra of $\text{La}_4\text{Ni}_{2.7}\text{Fe}_{0.3}\text{O}_{10-\delta}$ and observed two different iron environments, as expected from structural data (Fig. 1), with a relative area ratio close to 2:1, which indicates statistically distributed Fe^{3+} ions at Wyckoff positions 4a and 8i [24]. In contrast to these results, Carvalho et al. reported, that iron ions in $\text{La}_4\text{Ni}_{2.97}\text{Fe}_{0.03}\text{O}_{10-\delta}$ preferably occupy the nickel site 4a [25]. In a previous work we reported about $\text{La}_2\text{Ni}_{0.9}\text{Fe}_{0.1}\text{O}_{4+\delta}$ which showed a slight asymmetry in its room-temperature Mössbauer spectrum [21]. This motivated a detailed *in-situ* Mössbauer spectroscopy investigation of iron doped $\text{La}_2\text{NiO}_{4+\delta}$. Therefore, the present work is focused on the behavior of the iron environment, oxygen defect ordering and oxidation state at high temperatures and variable oxygen partial pressures to understand the behavior of this material at operation temperatures (1023–1223 K) in a membrane

reactor. Furthermore, supplementing results for XRD, electrical conductivity, oxygen permeation, scanning electron microscopy (SEM), and TEM are reported.

2. Materials and methods

2.1. Sample preparation

The materials were synthesized by the sol-gel route using stoichiometric amounts of metal oxides, ethylenediaminetetraacetic acid (EDTA) and citrate as described elsewhere [21,26,27]. All sintering processes were conducted in air atmosphere with heating and cooling rates of 2 K min^{-1} . Powders of $\text{La}_4\text{Ni}_{3-x}\text{Fe}_x\text{O}_{10-\delta}$ ($x=0.3, 0.9$) were sintered at 1373 K in air for 40 h. All powders were then uniaxially pressed to 16 mm green bodies under 50 kN for 15 min. For conductivity and oxygen permeation measurements gas-tight membranes of $\text{La}_2\text{Ni}_{1-x}\text{Fe}_x\text{O}_{4+\delta}$ ($x=0.02, 0.1$) with thicknesses of 1 mm were sintered at 1623 K for 10 h. The membranes of $\text{La}_4\text{Ni}_{3-x}\text{Fe}_x\text{O}_{10-\delta}$ ($x=0.3, 0.9$) were sintered for 10 h at 1373 K. The density of the $\text{La}_2\text{Ni}_{1-x}\text{Fe}_x\text{O}_{4+\delta}$ ($x=0.02, 0.1$) membranes was greater than 95% of the theoretical value. The density of the $\text{La}_4\text{Ni}_{3-x}\text{Fe}_x\text{O}_{10-\delta}$ ($x=0.3, 0.9$) ceramics was around 70%. The TEM specimen was prepared using a ceramic membrane. The samples used in the Mössbauer experiments were prepared in the same way but using metallic iron powder 96.63% enriched in the ^{57}Fe isotope (Chemotrade). The iron powder was dissolved in half concentrated nitric acid and then introduced in the sol-gel synthesis. The prepared ceramic membranes, which were sintered for 10 h at 1623 K, were crushed using an agate mortar to obtain powdered samples for the Mössbauer investigations.

2.2. X-ray diffraction analysis

X-ray diffraction (XRD) analysis was performed at room temperature using a Bruker AXS D8 Advance diffractometer with Cu K α radiation. Data sets were recorded in a step-scan mode in the angular range of $20^\circ \leq 2\theta \leq 60^\circ$ with intervals of 0.02° .

2.3. Conductivity measurements

The sintered ceramic samples were cut into rods of $1 \times 1.5 \text{ mm}^2$ with a length of 10 mm. A “4-stripe” geometry, made from 4 Pt wires each with 2 mm displacement between each other pressed on top of the samples, was used to measure the total DC conductivities. Markers of the Pt wires were clearly visible on top of the samples. After measurements and EDXS analysis it was shown that platinum is located at the contact region within a depth of up to 1 μm . So, any influence on the conductivity measurement can be ruled out. The samples were heated and cooled in air between 423 and 1223 K with a rate of 1 K min^{-1} . A direct current of 10 mA was fed to the sample and the voltage was recorded. The total DC conductivity, σ_{total} , was calculated according to the relation $\sigma_{\text{total}} = I/V \cdot d_{23}/A$, where the voltage V was measured between the inner contacts 2 and 3 with a distance, $d_{23} = 2 \text{ mm}$, and the current, I , between the outer contacts 1 and 4 with $d_{14} = 6 \text{ mm}$. A represents the cross-section area of the rods. Finite element method (FEM) analysis using COMSOL Multiphysics (Comsol) show that this calculation is correct for a homogeneous sample of the given geometry within an error of 1% or less.

2.4. Oxygen permeation measurements

Oxygen permeation was measured in a home-made high-temperature permeation cell as described elsewhere [28]. For sealing purpose, the membranes were sealed on the alumina tubes using a gold cermet (Heraeus). The feed side was fed with synthetic air (20 vol.% O_2 /80 vol.% N_2) at a rate of 150 mL min^{-1} , whilst Ne (1.0 mL min^{-1} , 99.995%) and He (29.0 mL min^{-1} , 99.995%) were applied to the sweep

side. An Agilent 7890 gas chromatograph with a Carboxen 1000 column was employed to analyze the gas mixture. Using neon as an internal standard, the absolute flux rate was calculated. By measuring the N_2 concentration, the total oxygen leakage was calculated and subtracted from the total oxygen flux.

2.5. Transmission electron microscopy

Transmission electron microscopy (TEM) investigations were made at 200 kV on a JEOL JEM-2100F-UHR field-emission instrument ($C_s = 0.5$ mm, $C_c = 1.2$ mm). The microscope was operated as a high-resolution TEM (HRTEM) and in the selected-area electron diffraction (SAED) mode. The preparation method of the TEM specimen is described in detail elsewhere [29].

2.6. Scanning electron microscopy

Field-emission scanning electron microscopy (FE-SEM) imaging was performed using a JEOL JSM-6700F field-emission instrument at a low excitation voltage of 2 kV. The samples were polished to crystallinity by vibrational-polishing and then investigated by a backscattered-electron channelling contrast technique with higher excitation voltage.

2.7. Mössbauer spectroscopy

A Mössbauer study was conducted of the RP phases $\text{La}_2\text{Ni}_{1-x}\text{Fe}_x\text{O}_{4+\delta}$ ($x = 0.02, 0.1$) and $\text{La}_4\text{Ni}_{3-x}\text{Fe}_x\text{O}_{10-\delta}$ ($x = 0.3, 0.9$). *In-situ* ^{57}Fe Mössbauer transmission spectra of the system $\text{La}_2\text{Ni}_{0.9}\text{Fe}_{0.1}\text{O}_{4+\delta}$ were taken in the temperature range from 298 to 1023 K in flowing atmospheres of He, O_2 , and synthetic air with total fluxes of 100 mL min^{-1} . Spectra were taken after equilibration times of 2–3 h at 673 K and higher temperatures. In view of the relatively low iron content and high electronic mass-absorption coefficient of the above mentioned iron-doped RP phases for the 14.4 keV Mössbauer γ -radiation, samples were prepared using metallic iron 96.63% enriched with the ^{57}Fe isotope. A standard Mössbauer system (Halder) was employed in constant acceleration mode using a $^{57}\text{Co/Rh}$ γ -source. The spectra were fitted by Voigt-type model functions accounting for a distribution of quadrupolar interactions at the iron nuclei using the Recoil code [30]. The velocity calibration was carried out using an α -Fe foil and the isomer shifts are stated relative to the center of this calibration. Oxygen partial pressures were measured using an oxygen gas sensor (Metrotec) at the outlet of the furnace.

3. Results and discussion

3.1. X-ray diffraction

The room-temperature XRD patterns, Fig. 2, of iron-doped $\text{La}_2\text{NiO}_{4+\delta}$ materials can be indexed as single phase tetragonal K_2NiF_4 structure (S.G. $I4/mmm$, ICSD no. 1179). This structure is characteristic for $\text{La}_2\text{NiO}_{4+\delta}$ at high temperatures in air [10]. Analysis of the Ruddlesden–Popper type $\text{La}_4\text{Ni}_{3-x}\text{Fe}_x\text{O}_{10-\delta}$ phases, see Fig. 3, showed the formation of a single $\text{La}_4\text{Ni}_3\text{O}_{10-\delta}$ phase of orthorhombic structure (s.g. $Fmmm$, ICSD no. 80279). The obtained unit cell parameters, presented in Table 1, are in good agreement with literature data on $\text{La}_2\text{Ni}_{0.98}\text{Fe}_{0.02}\text{O}_{4+\delta}$, $\text{La}_2\text{Ni}_{0.9}\text{Fe}_{0.1}\text{O}_{4+\delta}$, $\text{La}_4\text{Ni}_{2.7}\text{Fe}_{0.3}\text{O}_{10-\delta}$, and $\text{La}_4\text{Ni}_{2.1}\text{Fe}_{0.9}\text{O}_{10-\delta}$ [7,24,18]. The increase of the cell parameters with increasing iron content is compatible with the ionic radii of high-spin Fe^{3+} (78 pm) and Ni^{3+} (60 pm) [31].

3.2. Electrical conductivity

The conductivity measurements of $\text{La}_2\text{Ni}_{1-x}\text{Fe}_x\text{O}_{4+\delta}$ ($x = 0.02, 0.1$) and $\text{La}_4\text{Ni}_{2.1}\text{Fe}_{0.9}\text{O}_{10-\delta}$ reveal broad maxima. However, small differences in heating and cooling curves were observed. As an example,

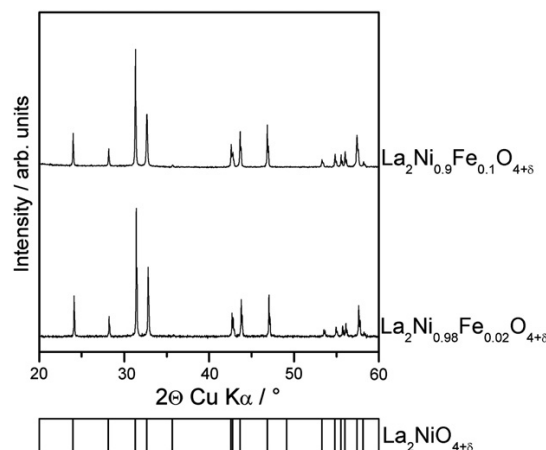


Fig. 2. Room-temperature XRD patterns of $\text{La}_2\text{Ni}_{0.98}\text{Fe}_{0.02}\text{O}_{4+\delta}$ and $\text{La}_2\text{Ni}_{0.9}\text{Fe}_{0.1}\text{O}_{4+\delta}$ with theoretical Bragg positions for $\text{La}_2\text{NiO}_{4+\delta}$ (ICSD no. 1179) labeled at the bottom of the figure.

the total conductivity of $\text{La}_2\text{Ni}_{0.98}\text{Fe}_{0.02}\text{O}_{4+\delta}$ and $\text{La}_4\text{Ni}_{2.1}\text{Fe}_{0.9}\text{O}_{10-\delta}$ on heating and cooling in air are shown in Fig. 4. In the case of $\text{La}_4\text{Ni}_{3-x}\text{Fe}_x\text{O}_{10-\delta}$ ($x = 0.3, 0.9$) compounds this difference between heating and cooling characteristics is located at temperatures between 500 and 623 K, and the conductivity in that range is lower on heating than on cooling. This behavior was also observed on heating for pure $\text{La}_4\text{Ni}_3\text{O}_{10-\delta}$ at 548 K by Amow et al. and was explained by a phase transformation from orthorhombic to tetragonal symmetry [2]. In contrast to that the $\text{La}_2\text{Ni}_{1-x}\text{Fe}_x\text{O}_{4+\delta}$ ($x = 0.02, 0.1$) compounds show a different behavior. At around 873 K, the conductivity maximum is higher on heating than on cooling because of the change in oxygen content, as is discussed below.

The electronic conductivity in MIEC materials is known to be several orders of magnitude higher than the ionic conductivity [32,33]. The contribution of the ionic conductivity to the measured values is therefore negligible. A p-type small polaron hopping mechanism accounts for the observed conductivity increase with increasing temperatures before the maximum value is reached. Due to the temperature driven oxygen loss and the subsequent generation of electrons the number of electron holes is decreased beyond the maximum and the conductivity decreases accordingly (pseudometallic), which was also observed for

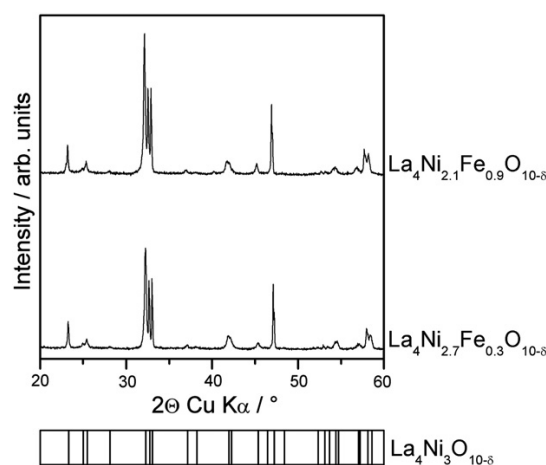


Fig. 3. Room-temperature XRD patterns of $\text{La}_4\text{Ni}_{2.7}\text{Fe}_{0.3}\text{O}_{10-\delta}$ and $\text{La}_4\text{Ni}_{2.1}\text{Fe}_{0.9}\text{O}_{10-\delta}$ with theoretical Bragg positions for $\text{La}_4\text{Ni}_3\text{O}_{10-\delta}$ (ICSD no. 80279) labeled at the bottom of the figure.

Table 1

Room-temperature unit cell parameters of La₂Ni_{1-x}Fe_xO₄ (s. g. *I4/mmm*, ICSD no. 1179) after sintering for 10 h at 1623 K in air and La₄Ni_{3-x}Fe_xO₁₀ (s. g. *Fmmm*, ICSD no. 80279) after sintering for 40 h at 1373 K in air.

Sample	Lattice parameters [Å]			Unit cell volume [Å ³]	Space group
	a	b	c		
La ₂ Ni _{0.98} Fe _{0.02} O ₄	3.8646(1)	–	12.6650(4)	189.15(2)	<i>I4/mmm</i>
La ₂ Ni _{0.9} Fe _{0.1} O ₄	3.8762(1)	–	12.6717(5)	190.38(2)	<i>I4/mmm</i>
La ₄ Ni _{2.7} Fe _{0.3} O ₁₀	5.4263(3)	5.4829(3)	28.018(2)	833.66(9)	<i>Fmmm</i>
La ₄ Ni _{2.1} Fe _{0.9} O ₁₀	5.4534(3)	5.5091(3)	28.137(2)	846.03(8)	<i>Fmmm</i>

other iron containing perovskite type materials like, e.g. Ba_{0.5}Sr_{0.5}Co_{0.8}Fe_{0.2}O_{3-δ} or Ba_{0.5}Sr_{0.5}Zn_{0.2}Fe_{0.8}O_{3-δ} [32,33]. The total DC conductivity on cooling for all investigated samples is shown in Fig. 5 in an Arrhenius representation. For La₂Ni_{1-x}Fe_xO_{4+δ} (x = 0, 0.02, 0.1) the observed maximum is in agreement with the literature [7]. However, in contrast to those investigations a decrease of electronic conductivity is observed with increasing iron content. The maximum conductivity value of La₂Ni_{0.98}Fe_{0.02}O_{4+δ} amounts to about 66 S cm⁻¹ and that of La₂Ni_{0.9}Fe_{0.1}O_{4+δ} to about 40 S cm⁻¹. The conductivity of undoped La₂NiO_{4+δ} behaves qualitatively similarly to the conductivity of the iron doped material (see Fig. 5 and Ref. [2]) with a maximum conductivity value of about 114 S cm⁻¹.

The conductivity of undoped La₄Ni₃O_{10-δ} is known to be metallic at temperatures of interest [2]. Our measurements show a decrease in conductivity with increasing iron content for the higher order Ruddlesden–Popper phases. Doping with 10% iron still preserves metallic conduction behavior with a maximum conductivity of 156 S cm⁻¹ at room temperature. For La₄Ni_{2.1}Fe_{0.9}O_{10-δ} the conductivity maximum was found at around 573 K. This may be explained by the increasing number of O–Fe–O bonds and by the knowledge that electronic conduction in LaFeO₃ occurs via an electron hopping mechanism [34]. Note that the density of the La₄Ni_{3-x}Fe_xO_{10-δ} (x = 0.3, 0.9) RP phases was only of about 70% of theoretical density because of the low sintering temperatures that had to be used to avoid phase decomposition.

3.3. Oxygen permeation

Permeation measurements were performed on La₂Ni_{0.98}Fe_{0.02}O_{4+δ}. Attempts to investigate the oxygen permeation of the higher order Ruddlesden–Popper phases La₄Ni_{2.7}Fe_{0.3}O_{10-δ} and La₄Ni_{2.1}Fe_{0.9}O_{10-δ}

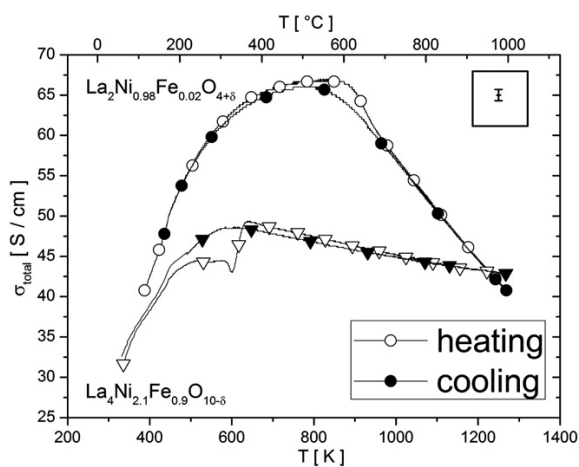


Fig. 4. Temperature-dependent total DC conductivity during heating and cooling of La₂Ni_{0.98}Fe_{0.02}O_{4+δ} and La₂Ni_{0.9}Fe_{0.1}O_{4+δ} in air. Error bar is indicated in the top right corner and of the same size as the symbols.

were not successful. Because of the relatively low sintering temperature (1373 K) no dense membranes could be obtained. Increasing the synthesis temperature induces phase decomposition into La₂Ni_{1-x}Fe_xO_{4+δ}, NiO, and release of oxygen as discussed by Zinkevich et al. [13]. However, there could be possible applications of such materials as, e.g., porous cathodes in solid oxide fuel cells [17].

Fig. 6 shows the oxygen permeation flux in the temperature range from 1023 to 1223 K for La₂Ni_{0.98}Fe_{0.02}O_{4+δ}. For comparison reasons, data for undoped La₂NiO_{4+δ} and La₂Ni_{0.9}Fe_{0.1}O_{4+δ} taken from [21] are displayed as well. Undoped La₂NiO_{4+δ} exhibits a better oxygen permeation performance than the iron-doped systems. It is known that the ionic conduction in lanthanum nickelates takes place via both oxygen interstitials and oxygen vacancies [3]. By adding Fe³⁺ ions, it is expected that the concentration of oxygen interstitials increases and the concentration of oxygen vacancies decreases [7]. Hereby, a predominant contribution of interstitial conduction may be anticipated for La₂Ni_{0.9}Fe_{0.1}O_{4+δ} rather than for La₂NiO_{4+δ}. The significant contribution of both conduction mechanisms results in an overall increased oxygen transport for undoped La₂NiO_{4+δ} [11]. By these assumptions, the oxygen permeation flux should decrease in the following order: La₂NiO_{4+δ} > La₂Ni_{0.98}Fe_{0.02}O_{4+δ} > La₂Ni_{0.9}Fe_{0.1}O_{4+δ}. This is in agreement with our experimental findings and literature data [7,11]. The difference between the permeation of La₂Ni_{0.98}Fe_{0.02}O_{4+δ} and La₂Ni_{0.9}Fe_{0.1}O_{4+δ} membranes is small and may be within the limits of experimental error. However, it is to be kept in mind that oxygen transport is often influenced strongly – or even determined – by ceramic microstructure and preparation conditions [21]. Oxygen diffusion coefficients in the grain boundaries and in the grain bulk may differ by orders of magnitude [35].

3.4. Transmission and scanning electron microscopy

The La₂Ni_{0.9}Fe_{0.1}O_{4+δ} sample, which is in the focus of the present study, shows noticeable formation of lamella-like intergrowth structures as was reported in detail in our previous work [21]. The investigation of La₂Ni_{0.98}Fe_{0.02}O_{4+δ} showed no formation of impurity phases, see for example Fig. 7, which is in accordance with literature data [7,18]. Furthermore, samples of La₂Ni_{0.98}Fe_{0.02}O_{4+δ} and La₂Ni_{0.9}Fe_{0.1}O_{4+δ} were vibrational-polished to preserve crystallinity to the very surface of the specimen. The SEM investigation in backscattered electron channeling contrast showed no formation of intergrowths in the La₂Ni_{0.98}Fe_{0.02}O_{4+δ} sample, whereas the La₂Ni_{0.9}Fe_{0.1}O_{4+δ} sample exhibits several about 20–30 nm wide lamellae-like structures inside the grains (Fig. 8). In a previous work we also investigated vibrational-polished La₂NiO_{4+δ} surfaces, which showed single-phase material [21]. By analyzing the micrographs obtained for La₂Ni_{0.9}Fe_{0.1}O_{4+δ}, it was found that the total area of impurity phase accumulated to around 5–10% for a slowly cooled sample at room temperature. On the basis of the decomposition reaction La₂Ni_{0.9}Fe_{0.1}O_{4+δ} → La₂Ni_{0.95}Fe_{0.05}O_{4+δ} + La₄Ni_{2.1}Fe_{0.9}O_{10-δ} + La₂O₃, the total amount of the La₄Ni_{2.1}Fe_{0.9}O_{10-δ} phase is calculated to be approximately 7%.

3.5. Mössbauer measurements of La₂Ni_{1-x}Fe_xO_{4+δ} and La₄Ni_{3-x}Fe_xO_{10-δ}

Fig. 9 shows ⁵⁷Fe Mössbauer spectra of La₂Ni_{1-x}Fe_xO_{4+δ} for x = 0.02 and 0.1 at room temperature. As seen, both spectra are fully symmetric and can be fitted with one quadrupole-split doublet. This indicates that the samples are single phase and that the ferric ions are located at a single crystallographic position. According to Menil [36] the observed isomer shift *IS* of the doublet can be identified as being due to octahedrally coordinated Fe³⁺ ions. These spectroscopic findings are in full agreement with the structural information for La₂NiO_{4+δ} at room temperature (space group *Fmmm*) yielding a distorted octahedral oxygen coordination for the Ni site. The observation of a fully symmetric spectrum of La₂Ni_{0.9}Fe_{0.1}O_{4+δ} at room

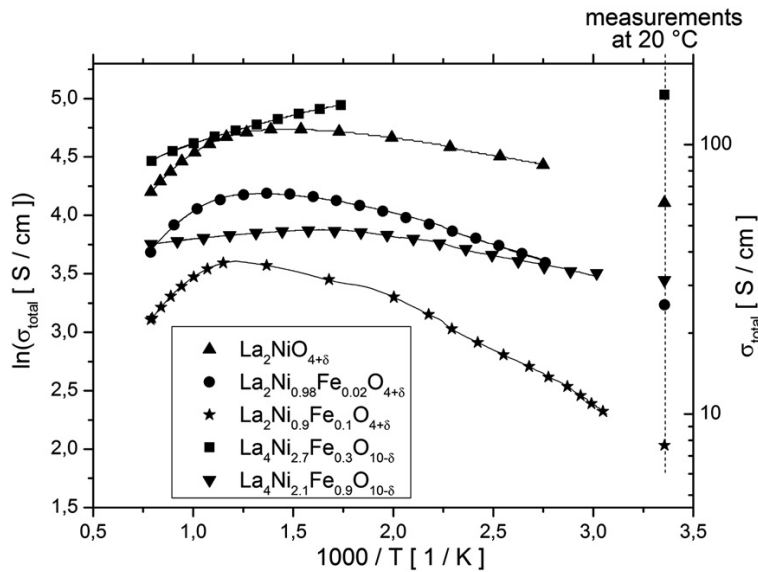


Fig. 5. Temperature-dependent total DC conductivity on cooling of $\text{La}_2\text{NiO}_{4+\delta}$, $\text{La}_2\text{Ni}_{0.98}\text{Fe}_{0.02}\text{O}_{4+\delta}$, $\text{La}_2\text{Ni}_{0.9}\text{Fe}_{0.1}\text{O}_{4+\delta}$, $\text{La}_4\text{Ni}_{2.7}\text{Fe}_{0.3}\text{O}_{10-\delta}$ and $\text{La}_4\text{Ni}_{2.1}\text{Fe}_{0.9}\text{O}_{10-\delta}$ in Arrhenius representation in air. The error in temperature is ± 2 K and the error in conductivity is $\pm 1\%$.

temperature is at slight variance with our previous work [21] where a second doublet of low intensity was needed to fit the slight asymmetry of the room-temperature spectrum. In the present work, however, such asymmetric spectra are observed at elevated temperatures see, e.g., the spectrum of $\text{La}_2\text{Ni}_{0.9}\text{Fe}_{0.1}\text{O}_{4+\delta}$ at 673 K, Fig. 10, and a small second doublet is required for producing an acceptable fit to the spectrum. This asymmetry increases with rising temperature and becomes clearly visible at the highest measuring temperature of 973 K (Fig. 10). The conflicting findings in the present and previous work [21] seem to indicate that equilibration of samples is difficult at room temperature.

Mössbauer spectra of $\text{La}_4\text{Ni}_{2.7}\text{Fe}_{0.3}\text{O}_{10-\delta}$ and $\text{La}_4\text{Ni}_{2.1}\text{Fe}_{0.9}\text{O}_{10-\delta}$ are also shown in Fig. 9 for reasons of comparison. $\text{La}_4\text{Ni}_3\text{O}_{10-\delta}$ is a Ruddlesden–Popper phase $\text{La}_{n+1}\text{Ni}_n\text{O}_{3n+1}$ with $n = 3$. In agreement with the two nonequivalent structural sites for nickel in this phase, the spectrum is given by a superposition of two doublets due to iron cations located at the Ni sites (Fig. 1). In agreement with the work on $\text{La}_4\text{Ni}_{2.97}\text{Fe}_{0.03}\text{O}_{10-\delta}$ reported by Carvalho et al. [25], it is found that iron cations in both $\text{La}_4\text{Ni}_{2.7}\text{Fe}_{0.3}\text{O}_{10-\delta}$ and $\text{La}_4\text{Ni}_{2.1}\text{Fe}_{0.9}\text{O}_{10-\delta}$ preferably occupy the higher symmetric 4a site, see Fig. 1, which possesses the

smaller quadrupolar splitting [24,25]. See Table 2 for isomer shifts, quadrupole splittings and area fractions of the room-temperature spectra.

Fig. 10 shows a series of Mössbauer spectra of $\text{La}_2\text{Ni}_{0.9}\text{Fe}_{0.1}\text{O}_{4+\delta}$, taken at selected elevated temperatures in flowing oxygen. As seen, the spectra are dominated by a doublet (I) with a quadrupole splitting of about $QS(I) = 1.3$ mm/s. However, as it becomes more apparent with increasing temperatures, a second doublet of low intensity with a smaller splitting of about $QS(II) = 0.4$ mm/s is required for consistent fits of the complete set of spectra. The temperature dependence of the isomer shifts of the two subspectra is dominated by the second order Doppler shift. Because Fe^{3+} and Ni^{2+} ions occupy regular positions in $\text{La}_2\text{Ni}_{0.9}\text{Fe}_{0.1}\text{O}_{4+\delta}$ [23], the spectroscopically detected existence of a second iron species alludes the presence of another phase [21]. In fact, according to the ternary phase diagram for La-Fe-Ni-O reported by Kiselev et al. for 1370 K, the sample under investigation in the present study, $\text{La}_2\text{Ni}_{0.9}\text{Fe}_{0.1}\text{O}_{4+\delta}$, at high temperatures should consist of three phases, namely of La_2O_3 , $\text{La}_2\text{Ni}_{0.95}\text{Fe}_{0.05}\text{O}_{4+\delta}$, and $\text{La}_4\text{Ni}_{2.1}\text{Fe}_{0.9}\text{O}_{10-\delta}$ [18]. Hence, the observation of two quadrupole-split subspectra due to different iron species in $\text{La}_2\text{Ni}_{0.9}\text{Fe}_{0.1}\text{O}_{4+\delta}$ appears compatible with the, admittedly incomplete, information available on the ternary La-Fe-Ni-O phase diagram. However, this conclusion must be questioned on the basis of the following additional information. i) The second doublet (II) bears no similarity to the Mössbauer spectra of $\text{La}_4\text{Ni}_{2.7}\text{Fe}_{0.3}\text{O}_{10-\delta}$ and $\text{La}_4\text{Ni}_{2.1}\text{Fe}_{0.9}\text{O}_{10-\delta}$ (Fig. 9 and Table 2), especially in respect to the isomer shift. ii) The quadrupole doublet (II) is found to reversibly appear and disappear with temperature. The formation and dissolution of a second phase – even if structurally related Ruddlesden–Popper phases were involved – would require diffusion of cations to take place. This is difficult to reconcile with the expected low cation diffusivities in $\text{La}_2\text{NiO}_{4+\delta}$ – especially at the low temperatures relevant to the present discussion. In conclusion, the nature of the minority iron species II observed in the $\text{La}_2\text{Ni}_{0.9}\text{Fe}_{0.1}\text{O}_{4+\delta}$ sample is not sufficiently understood at present and will require more detailed investigation.

Another open question refers to the apparently conflicting concentration estimates of the secondary iron-containing phase. The estimate of 7% derived for $\text{La}_4\text{Ni}_{2.1}\text{Fe}_{0.9}\text{O}_{10-\delta}$ from the high-temperature phase diagram is in reasonable agreement with the findings from backscattered-electron channeling contrast SEM analysis (see Section 3.4). It should be noted, however, that the HRTEM technique was only applied for identification

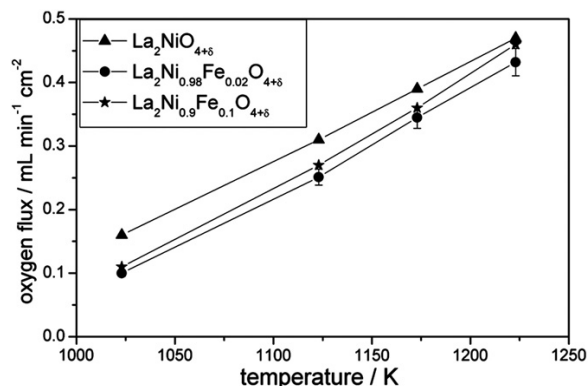


Fig. 6. Oxygen flux of iron-doped $\text{La}_2\text{NiO}_{4+\delta}$ materials. Data for $\text{La}_2\text{NiO}_{4+\delta}$ and $\text{La}_2\text{Ni}_{0.9}\text{Fe}_{0.1}\text{O}_{4+\delta}$ taken from [21]; membrane thickness: 1 mm, feed side: 150 mL min^{-1} synthetic air, sweep side: 29 mL min^{-1} He and 1 mL min^{-1} Ne. $\pm 5\%$ error bars are given as estimated measurement error.

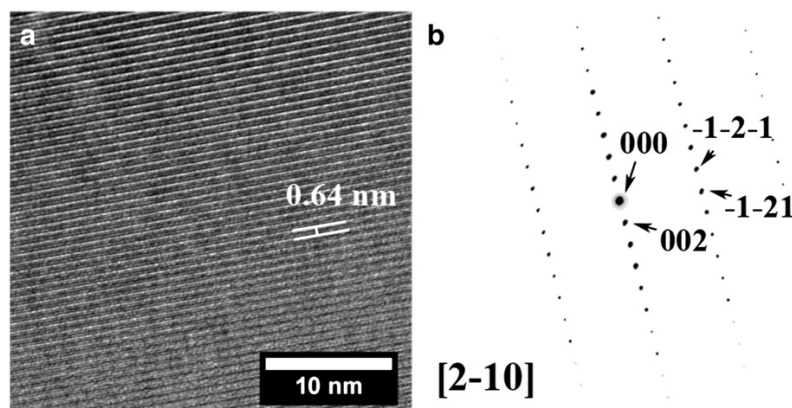


Fig. 7. (a) HRTEM image and (b) diffraction pattern for $\text{La}_2\text{Ni}_{0.98}\text{Fe}_{0.02}\text{O}_{4+\delta}$ membrane (diameter of SAED aperture 125 nm). The lattice plane distance was measured to be $d_{(002)} = 0.64$ nm.

of the different phases, and not for quantitative analysis of phase amount. In contrast, the room-temperature Mössbauer spectrum, Fig. 9, does not provide evidence for the mentioned minority phase, which is in agreement with the Mössbauer spectrum reported by Tsipis et al. [11]. Normally, one would expect detection of a macroscopic 7% minority phase by Mössbauer spectroscopy. However, the proposed secondary $\text{La}_4\text{Ni}_3\text{O}_{10}$ -type phase is strongly absorbing the γ -radiation due to its large amount of elements possessing high atomic numbers. This may be part of the reason for the reduced sensitivity of Mössbauer spectroscopy in the present case. Also the possibility is to be considered that the Mössbauer spectrum from the 20 nm wide lamellae-like secondary RP phase may not correspond to that of the corresponding macroscopic phase with well-defined quadrupolar interactions. Furthermore, the sample in question was identified by XRD to be single-phase K_2NiF_4 material.

At elevated temperatures, different crystallographic structures were reported for $\text{La}_2\text{NiO}_{4+\delta}$ (s.g. $I4/mmm$ [10] and $F4/mmm$ [37]) due to

oxygen ordering transformations. Nickel/iron atoms again were found to occupy the unique crystallographic position (4a) in the tetragonal structure and are surrounded by six oxygen atoms [10,37]. Transmission Mössbauer measurements of $\text{La}_2\text{Ni}_{0.9}\text{Fe}_{0.1}\text{O}_{4+\delta}$ in flowing atmospheres of oxygen, synthetic air, and helium were performed in the temperature range from 298 to 1023 K. The quadrupole splitting $QS(1)$ of the octahedrally coordinated Fe^{3+} ions reveals a most unusual temperature dependence. As shown in Fig. 11 for the measurements in pure oxygen, $QS(1)$ exhibits a discontinuity between 570 K and 670 K associated with a significant value change. Most probably, this observation can be attributed to the phase change from the orthorhombic low-temperature to the tetragonal high-temperature phase. Along with this discontinuity, also a switching occurs from a splitting which decreases with increasing temperature to one that increases with increasing temperature. The discontinuity in slopes is also

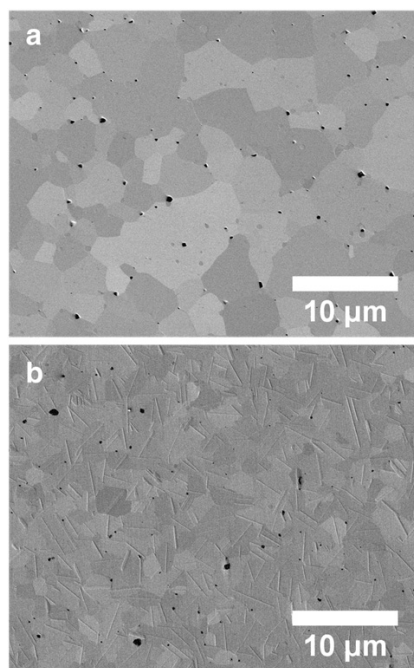


Fig. 8. Channeling contrast micrographs of vibrational-polished cross-sections of (a) $\text{La}_2\text{Ni}_{0.98}\text{Fe}_{0.02}\text{O}_{4+\delta}$ and (b) $\text{La}_2\text{Ni}_{0.9}\text{Fe}_{0.1}\text{O}_{4+\delta}$ sintered for 10 h at 1623 K.

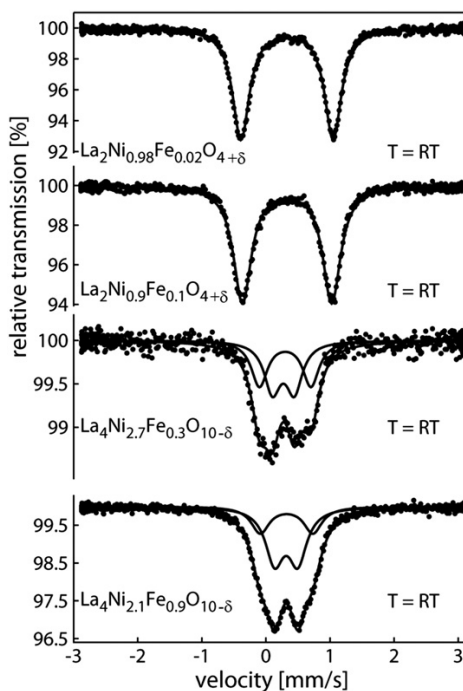


Fig. 9. Room-temperature Mössbauer spectra of $\text{La}_2\text{Ni}_{1-x}\text{Fe}_x\text{O}_{4+\delta}$, $x = 0.02$ and 0.1 , and $\text{La}_4\text{Ni}_{3-x}\text{Fe}_x\text{O}_{10-\delta}$, $x = 0.3$ and 0.9 .

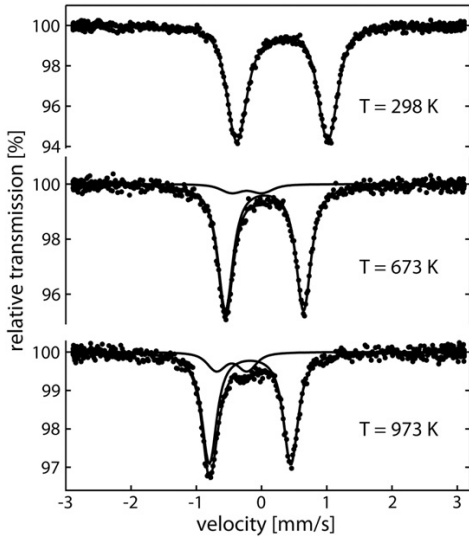


Fig. 10. In-situ Mössbauer spectra of $\text{La}_2\text{Ni}_{0.9}\text{Fe}_{0.1}\text{O}_{4+\delta}$ at 298, 673, and 973 K. Spectra were measured in flowing oxygen.

observed for measurements in synthetic air and in helium gas, Fig. 11. On the other hand, the quadrupole splitting $QS(\text{II})$ of the minority species is nearly independent of the ambient atmospheres used in our experiments (see Fig. 12 for spectra taken at 1023 K).

The temperature dependence of the quadrupolar interaction at low temperatures (<600 K) exhibits the behavior most commonly observed in temperature-dependent Mössbauer studies with $dQS(\text{I})/dT < 0$. The temperature coefficient of the splitting $(1/QS(\text{I}))(dQS(\text{I})/dT)$ takes a value of about -10^{-4} K^{-1} . This is of the right order of magnitude expected on basis of the approximate relation between the temperature coefficient of the splitting and the thermal volume expansion coefficient $(1/QS)(dQS/dT) \approx -(1/V)(dV/dT)$, where the latter was reported to take values of about $0.5 \cdot 10^{-4} \text{ K}^{-1}$ [37]. On the other hand, the high-temperature behavior with quadrupolar interaction increasing with rising temperature, Fig. 11, is to be considered a most unusual finding which demands an explanation most probably related to the disorder of oxygen in the material.

At 1023 K, in-situ Mössbauer spectra of $\text{La}_2\text{Ni}_{0.9}\text{Fe}_{0.1}\text{O}_{4+\delta}$ have been measured at different oxygen activities $a\text{O}_2$ in the range $-4 < \log(a\text{O}_2) < 0$, where $a\text{O}_2 = p\text{O}_2/p^0$ with $p^0 = 1$ bar. Results for the quadrupolar splittings are shown in Fig. 12. As seen, the splitting $QS(\text{I})$ of the octahedrally

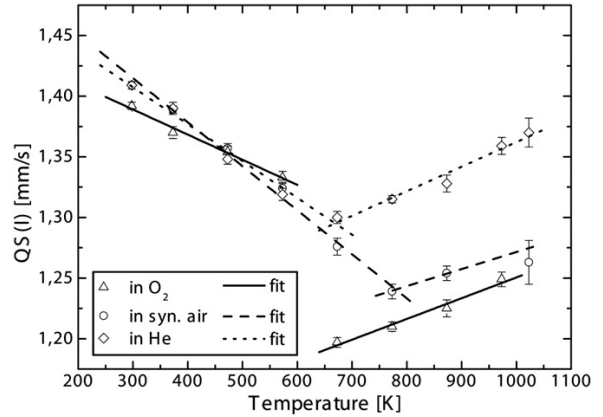


Fig. 11. Temperature dependence of quadrupolar splitting $QS(\text{I})$ in $\text{La}_2\text{Ni}_{0.9}\text{Fe}_{0.1}\text{O}_{4+\delta}$. In-situ high-temperature measurements in flowing atmospheres of oxygen, synthetic air, and helium.

coordinated Fe^{3+} ions increases linearly with decreasing $\log(a\text{O}_2)$, i.e. $dQS(\text{I})/d\log(a\text{O}_2) < 0$. Hence, the isothermal behavior observed for $QS(\text{I})$ indicates an increasing quadrupolar interaction for a decreasing stoichiometry parameter δ in $\text{La}_2\text{Ni}_{0.9}\text{Fe}_{0.1}\text{O}_{4+\delta}$. This is fully compatible with the observation made in the temperature-dependent measurements at constant oxygen activities above about 600 K. According to Refs. [38,39], in this temperature range the δ parameter at fixed oxygen partial pressure decreases with temperature which is reflected in the spectra by the increase of $QS(\text{I})$ with increasing temperature, Fig. 11. In conclusion, both types of measurements (i.e. the isothermal one and the one at variable temperature) reveal that the loss of excess oxygen results in an increase of the quadrupolar interaction at the iron nuclei, i.e. $dQS(\text{I})/d\delta < 0$.

This direct relation between quadrupolar interaction at the iron sites and crystal stoichiometry is the central result of the present Mössbauer investigation of the $\text{La}_2\text{Ni}_{1-x}\text{Fe}_x\text{O}_4$ system. In a first attempt to explain this relation one might speculate whether it is brought about by a changing ordering of the excess oxygen in the structure. On the other hand, a local defect arrangement involving iron may be considered responsible. According to Refs. [10,37], iron (Ni) atoms at elevated temperatures occupy a unique crystallographic position octahedrally coordinated by oxygen. Four of the anions (O1) with the same interatomic distances $d_{\text{Fe-O}}$ lie together with Fe in the ab -plane and represent the equatorial oxygen ions of the NiO_6 octahedra. The two apical oxygen atoms (O2 and O3), however, possess different interatomic distances $d_{\text{Fe-O}}$. Due to the presence of interstitial oxygen (O4), the O3 site splits up into four positions on

Table 2

Mössbauer fitting results for $\text{La}_2\text{Ni}_{1-x}\text{Fe}_x\text{O}_{4+\delta}$ ($x=0.02, 0.1$) and $\text{La}_4\text{Ni}_{3-x}\text{Fe}_x\text{O}_{10-\delta}$ ($x=0.1, 0.3$) at room-temperature from present work and literature: IS – mean values of isomer shift (vs $\alpha\text{-Fe}$), QS – mean values of quadrupolar splitting and A – area fraction.

	IS [mm/s]	QS [mm/s]	A [%]	Ref.
$\text{La}_2\text{Ni}_{0.98}\text{Fe}_{0.02}\text{O}_{4+\delta}$	0.33	1.44	100	This work
	0.322	1.44	68	[23]
	0.295	0.85	19	
	0.267	0.40	13	
$\text{La}_2\text{Ni}_{0.9}\text{Fe}_{0.1}\text{O}_{4+\delta}$	0.33	1.39	95	This work
	0.13	0.36	5	[11]
$\text{La}_4\text{Ni}_{2.97}\text{Fe}_{0.03}\text{O}_{9.95}$	0.33	1.35	100	
	0.26	0.43	58	[25]
$\text{La}_4\text{Ni}_{2.7}\text{Fe}_{0.3}\text{O}_{10-\delta}$	0.27	0.34	50	This work
	0.30	0.80	50	[24]
	0.28	0.26	32	
	0.30	0.72	68	
$\text{La}_4\text{Ni}_{2.1}\text{Fe}_{0.9}\text{O}_{10-\delta}$	0.32	0.36	67	This work
	0.32	0.82	33	

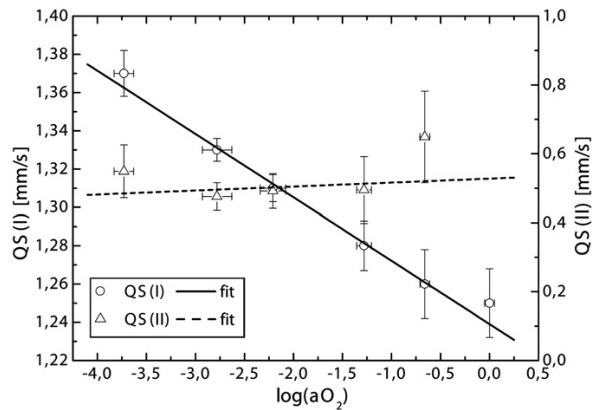


Fig. 12. Oxygen activity dependence of Mössbauer quadrupole splittings in $\text{La}_2\text{Ni}_{0.9}\text{Fe}_{0.1}\text{O}_{4+\delta}$ at 1023 K.

which oxygen can be locally disordered. Due to the small distances involved, temperature-dependent interatomic distances $d_{\text{Fe-O}}$ and/or changing occupation of these nearest neighbor sites will have a significant influence on the quadrupolar interactions at the iron nuclei. As a further possibility for explaining the origin of the observed unusual behavior of quadrupolar interactions in $\text{La}_2\text{Ni}_{1-x}\text{Fe}_x\text{O}_4$, local bonding properties may be considered, e.g., involving π -bonding between iron and oxygen as was proposed by Suzuki and Okubo [40] in the case of $\text{Fe}_{1.33}\text{Nb}_{2.67}\text{Se}_{10}$ in which a positive temperature dependence of quadrupolar interactions was observed, too. Clearly, for an improved understanding of these most unusual experimental observations, i.e. discontinuity in quadrupolar splittings and notably the discontinuity in slopes with $dQS/dT > 0$ at elevated temperatures, more detailed experimental as well as supporting theoretical studies will be required.

4. Conclusions

The Ruddlesden–Popper phases $\text{La}_2\text{Ni}_{1-x}\text{Fe}_x\text{O}_{4+\delta}$ ($x = 0.02, 0.1$) and $\text{La}_4\text{Ni}_{3-x}\text{Fe}_x\text{O}_{10-\delta}$ ($x = 0.3, 0.9$) were successfully synthesized via the sol–gel route. By doping with iron, the electrical conductivity and the oxygen permeation flux were slightly reduced. Transmission electron microscopy revealed phase decomposition of $\text{La}_2\text{Ni}_{0.9}\text{Fe}_{0.1}\text{O}_4$ yielding small amounts of the higher order Ruddlesden–Popper phase $\text{La}_4\text{Ni}_{2.1}\text{Fe}_{0.9}\text{O}_{10}$. This phase could not be detected by XRD on slowly cooled samples. The room-temperature Mössbauer measurements in present and previous work reflect slight influences of equilibrium conditions on the iron environment. *In-situ* Mössbauer measurements on $\text{La}_2\text{Ni}_{0.98}\text{Fe}_{0.02}\text{O}_4$ and $\text{La}_2\text{Ni}_{0.9}\text{Fe}_{0.1}\text{O}_4$ exhibited an unusual high-temperature behavior of quadrupolar interactions at the iron nuclei, which is most probably related to defects and/or ordering phenomena of the excess oxygen.

Acknowledgments

Financial support from the State of Lower Saxony in the frame of NTH bottom-up project No. 21-71023-25-7/09 is gratefully acknowledged. We like to thank Hannes Töpfer and Mladen Zec (TU Ilmenau) for the helpful discussions and for the FEM calculations of the four-point geometry of the conductivity measurements.

References

- [1] H. Wang, S. Werth, T. Schiestel, J. Caro, *Angew. Chem. Int. Ed.* 44 (2005) 6906.
- [2] G. Amow, I.J. Davidson, S.J. Skinner, *Solid State Ionics* 177 (2006) 1205.
- [3] G. Amow, S.J. Skinner, *J. Solid State Electrochem.* 10 (2006) 538.
- [4] L. Minervini, R.W. Grimes, J.A. Kilner, K.E. Sickafus, *J. Mater. Chem.* 10 (2000) 2349.

- [5] Z. Zhang, M. Greenblatt, *J. Solid State Chem.* 117 (1995) 236.
- [6] M.D. Carvalho, A. Wattiaux, J.M. Bassat, J.C. Grenier, M. Pouchard, M.I. da Silva Pereira, F.M.A. Costa, *J. Solid State Electrochem.* 7 (2003) 700.
- [7] V.V. Kharton, A.P. Viskup, E.N. Naumovich, F.M.B. Marques, *J. Mater. Chem.* 9 (1999) 2623.
- [8] B. Grande, H. Müller-Buschbaum, *Z. Anorg. Allg. Chem.* 433 (1977) 152.
- [9] D.E. Rice, D.J. Buttrey, *J. Solid State Chem.* 105 (1993) 197.
- [10] S.J. Skinner, *Solid State Sci.* 5 (2003) 419.
- [11] E.V. Tsipis, E.N. Naumovich, M.V. Patrakeev, J.C. Waerenborgh, Y.V. Pivak, P. Gaczyński, V.V. Kharton, *J. Phys. Chem. Solids* 68 (2007) 1443.
- [12] F. Gervais, P. Odier, Y. Nigara, *Solid State Commun.* 56 (1985) 371.
- [13] M. Zinkevich, N. Solak, H. Nitsche, M. Ahrens, F. Aldinger, *J. Alloys Compd.* 438 (2007) 92.
- [14] D.O. Bannikov, V.A. Cherepanov, *J. Solid State Chem.* 179 (2006) 2721.
- [15] N. Gauquelin, T.E. Weirich, M. Ceretti, W. Paulus, M. Schroeder, *Monatsh. Chem.* 140 (2009) 1095.
- [16] G. Amow, P.S. Whitfield, I.J. Davidson, R.P. Hammond, C.N. Munnings, S.J. Skinner, *J. Ceram. Int.* 30 (2004) 1635.
- [17] R. Chiba, F. Yoshimura, Y. Sakurai, *Solid State Ionics* 124 (1999) 281.
- [18] E.A. Kiselev, N.V. Proskurnina, V.I. Voronin, V.A. Cherepanov, *Inorg. Mater.* 43 (2007) 167.
- [19] E.V. Tsipis, E.N. Naumovich, A.L. Shaula, M.V. Patrakeev, J.C. Waerenborgh, V.V. Kharton, *Solid State Ionics* 179 (2008) 57.
- [20] C. Li, G. Yu, N. Yang, *Sep. Purif. Technol.* 32 (2003) 335.
- [21] T. Klände, K. Efimov, S. Cusenza, K.-D. Becker, A. Feldhoff, *J. Solid State Chem.* 184 (2011) 3310.
- [22] V.L. Moruzzi, M.W. Shafer, *J. Am. Ceram. Soc.* 43 (1960) 367.
- [23] J. Fontcuberta, G. Longworth, J.B. Goodenough, *Phys. Rev. B* 30 (11) (1984) 6320.
- [24] E.V. Tsipis, M.V. Patrakeev, J.C. Waerenborgh, Y.V. Pivak, A.A. Markov, P. Gaczyński, E.N. Naumovich, V.V. Kharton, *J. Solid State Chem.* (2007) 1902.
- [25] M.D. Carvalho, A. Wattiaux, L.P. Ferreira, J.M. Bassat, *J. Solid State Chem.* 182 (2009) 60.
- [26] J. Martynczuk, M. Arnold, J. Caro, H. Wang, A. Feldhoff, *Adv. Mater.* 19 (2007) 2134.
- [27] K. Efimov, M. Arnold, J. Martynczuk, A. Feldhoff, *J. Am. Ceram. Soc.* 92 (2009) 876.
- [28] A. Feldhoff, M. Arnold, J. Martynczuk, T.M. Gesing, H. Wang, *Solid State Sci.* 10 (2008) 689.
- [29] M. Arnold, H. Wang, A. Feldhoff, *J. Membr. Sci.* 293 (2007) 44.
- [30] K. Lagarec, D.G. Rancourt, *Nucl. Instrum. Methods Phys. Res. Sect. B* 129 (1972) 266.
- [31] R.D. Shannon, *Acta Crystallogr. Sect. A: Found. Crystallogr.* 32 (1976) 751.
- [32] H. Zhao, W. Shen, Z. Zhu, X. Li, Z. Wang, *J. Power Sources* 182 (2008) 503.
- [33] B. Wei, Z. Liu, X. Huang, M. Liu, N. Li, W. Su, *J. Power Sources* 176 (2008) 1.
- [34] V.V. Kharton, A.P. Viskup, E.N. Naumovich, V.N. Tikhonovich, *Mater. Res. Bull.* 8 (1999) 1311.
- [35] S.J. Benson, R.J. Chater, J.A. Kilner, In: in: T.A. Ramanarayanan (Ed.), *Ionic and Mixed Conducting Ceramics III*, Electrochemical Society, Pennington, New York, 1998, p. 596.
- [36] F. Menil, *J. Phys. Chem. Solids* 46 (1985) 763.
- [37] A. Aguadero, J.A. Alonso, M.J. Martínez-Lope, M.T. Fernández-Díaz, M.J. Escudero, L. Daza, *J. Mater. Chem.* 16 (2006) 3402.
- [38] M.V. Patrakeev, E.N. Naumovich, V.V. Kharton, A.A. Yaremchenkov, E.V. Tsipis, P. Nunez, J.R. Frade, *Solid State Ionics* 176 (2005) 179.
- [39] V.V. Kharton, E.V. Tsipis, E.N. Naumovich, A. Thursfeld, M.V. Patrakeev, V.A. Kolotygin, J.C. Waerenborgh, I.S. Metcalfe, *J. Solid State Chem.* 181 (2008) 1425.
- [40] T. Suzuki, N. Okubo, *Z. Naturforsch.* 57 a (2002) 627.

**2.4 Rapid glycine-nitrate combustion synthesis of the
CO₂-stable dual-phase membrane
40Mn_{1.5}Co_{1.5}O_{4-δ}-60Ce_{0.9}Pr_{0.1}O_{2-δ} for CO₂
capture via an oxy-fuel process**

Huixia Luo, Heqing Jiang, Tobias Klande, Fangyi Liang, Zhengwen Cao, Haihui Wang, and Jürgen Caro

Journal of Membrane Science **423-424** (2012) 450-458



Contents lists available at SciVerse ScienceDirect

Journal of Membrane Science

journal homepage: www.elsevier.com/locate/memsci

Rapid glycine-nitrate combustion synthesis of the CO₂-stable dual phase membrane 40Mn_{1.5}Co_{1.5}O_{4-δ}-60Ce_{0.9}Pr_{0.1}O_{2-δ} for CO₂ capture via an oxy-fuel process

Huixia Luo^a, Heqing Jiang^b, Tobias Klade^a, Fangyi Liang^a, Zhengwen Cao^a, Haihui Wang^{c,*}, Jürgen Caro^{a,**}

^a Institute of Physical Chemistry and Electrochemistry, Leibniz University of Hannover, Callinstr. 3a D-30167 Hannover, Germany

^b Max-Planck-Institut für Kohlenforschung, Kaiser-Wilhelm-Platz 1, D-45470 Mülheim an der Ruhr, Germany

^c School of Chemistry & Chemical Engineering, South China University of Technology, Wushan Road, Guangzhou 510640, China

ARTICLE INFO

Article history:

Received 21 May 2012

Received in revised form

21 August 2012

Accepted 24 August 2012

Available online 2 September 2012

Keywords:

Dual phase membrane

CO₂-stable membrane

Glycine-nitrate combustion synthesis

Oxygen permeation

ABSTRACT

A rapid one-pot combustion synthesis method based on glycine-nitrate, has been applied to prepare a novel oxygen transporting dual phase CO₂-stable membrane of the composition 40 wt% Mn_{1.5}Co_{1.5}O_{4-δ}-60 wt% Ce_{0.9}Pr_{0.1}O_{2-δ} (40MCO-60CPO). After sintering at 1300 °C in air for 10 h, the 40MCO-60CPO membranes were characterized by X-ray diffraction (XRD), scanning electron microscopy (SEM), back scattered SEM (BSEM), and energy dispersive X-ray spectroscopy (EDXS), showing that the 40MCO-60CPO composite represents a micro-scale mixture of mainly the two phases MCO and CPO, but small amounts of MnO₂ and (MnCo)(MnCo)₂O_{4-δ} were detected in the sintered membranes as well. The oxygen permeation fluxes through the 40MCO-60CPO dual phase membrane were measured at elevated temperatures (900–1000 °C) with one side of the membrane exposed to synthetic air and the other side to a CO₂/He sweep gas stream. A stable oxygen permeation flux of 0.48 mL cm⁻² min⁻¹ was obtained for a 0.3 mm thick membrane under an air/CO₂ oxygen partial pressure gradient at 1000 °C. It was also found that 40MCO-60CPO dual phase membranes are stable for more than 60 h even when pure CO₂ was used as the sweep gas, which recommends 40MCO-60CPO membranes as promising candidates for 4-end membrane operation in an oxy-fuel power plant.

© 2012 Elsevier B.V. All rights reserved.

1. Introduction

Recently, oxygen-permeable dense ceramic membranes with mixed ionic-electronic conductivity (MIEC) have attracted much attention as economical, efficient, and environment-friendly means to produce oxygen from air or other oxygen-containing gas mixtures [1]. In fact, an integration of oxygen transport membranes (OTMs) into oxy-fuel power plants can integrate CO₂ capture and sequestration strategies in order to reduce CO₂ emission. Further, OTMs allow process intensification [2,3] and enable thermal integration and energy saving [4–7]. A promising process route in the oxy-fuel power plant concept is the so-called 4-end membrane operation mode [8], in which a part of the flue gas is recycled as sweep gas on the permeate side of OTMs. The heat from natural gas or coal combustion offers the possibility of efficient membrane integration into the oxy-fuel process.

However, the development of the 4-end membrane operation mode technology is hampered since the state-of-the-art OTMs suffer from low chemical stability toward corrosive components of the flue gas such as CO₂ and SO₂, which lead to a poor oxygen permeation performance and even membrane destruction [9–14]. It is known that single phase perovskite-type OTM materials (ABO₃) with a high content of alkaline-earth metals on the A site, easily react with CO₂ and SO₂ forming carbonates and sulfates [15–18].

Another type of MIEC membranes is called “dual phase membranes”, which consist of a micro-scale mixture of well-separated grains of an oxygen ion conductor (OIC) and an electron conductor (EC). Dual phase membranes offer a promising approach for the 4-end membrane operation mode technology since their constituents can be tailored according to practical requirements. However, if noble metals are used as EC, their high price turns out as drawback. Further, often reactions between the OIC and EC at the high operational temperatures take place; new phases of lower ionic and electronic conductivity are formed and stability problems are reported. Recently, we have shown that novel dual-phase membranes without noble metals and

* Corresponding author. Tel./fax: +86 20 87110131.

** Corresponding author. Tel.: +49 511 762 3175; fax: +49 511 762 19121.

E-mail addresses: hhwang@scut.edu.cn (H. Wang), caro@pci.uni-hannover.de, juergen.caro@pci.uni-hannover.de (J. Caro).

alkaline-earth metals show a much higher CO₂-stability than the common alkaline-earth-containing membranes [19–21]. However, the traditional synthesis of dual phase oxides consists in a simple mixing of the two oxide powders [22–24], which often requires several sintering-milling steps to get uniform mixtures. This conventional preparation can be replaced by recent developments such as the one-pot EDTA-citric acid process [25] or the glycine-nitrate combustion process (GNP). Especially the GNP is reported to rapidly produce complex oxide ceramic powders of uniform composition on an atomic scale and fine enough in grain size for sintering to a ceramic with a high density [26,27]. Herein, we combine the rapid one-pot and GNP techniques to develop a new CO₂-stable oxygen-permeable membrane of the composition 40 wt% Mn_{1.5}Co_{1.5}O_{4-δ}-60 wt% Ce_{0.9}Pr_{0.1}O_{2-δ} (40MCO-60CPO), with MCO as the EC and CPO as the OIC.

It is generally accepted that oxygen permeation properties of dual phase membrane are dependent on their electronic and ionic conductivity, structural and phase stability, as well as thermal expansion compatibility between OIC and EC [28–31]. Thus, with these conclusions in mind, we designed our dual phase membrane as follows: (i) MCO spinel is reported to show excellent electronic conductivity and satisfactory thermal and structural stability as well as a thermal expansion which matches ferritic stainless steel. Therefore, MCO has been widely studied in solid oxide fuel cells (SOFCs) as a protective coating on stainless steel interconnections and as cathodes for intermediate temperature SOFCs [32–34]. (ii) Pr-doped ceria is well-known to exhibit high oxygen ionic conductivity and a good structural stability in a wide oxygen partial pressure range. These properties recommend CPO as a solid electrolyte in SOFCs [35] and an oxygen storage material [36]. On the other hand, the thermal expansion coefficient (TEC) of CPO is reported to be $10\text{--}11 \times 10^{-6} \text{ K}^{-1}$ [37], which is close to that of MCO ($11.7 \times 10^{-6} \text{ K}^{-1}$) [32] in the range of 500–900 °C. It can be expected, therefore, that the MCO and CPO show good thermal compatibility with each other. (iii) Because of the lack of alkaline-earth metals in MCO and CPO, high CO₂ stability can be expected. (iv) To guarantee a sufficient electron transport in the percolation network, the concentration of the highly electron conducting component MCO in the dual phase materials should not be < 40 wt%.

Therefore, the aim of this study is the fabrication of 40MCO-60CPO dual phase membrane via a one-pot GNP. Phase structure and stability as well as oxygen permeability for different sweep gases including CO₂ partial pressures on the permeate side of the membrane are investigated in detail.

2. Experimental

2.1. Preparation of powders and membranes

The glycine-nitrate combustion process (GNP), as a proven means to obtain fine and homogeneous powders [25], was used to prepare the 40 wt% Mn_{1.5}Co_{1.5}O_{4-δ}-60 wt% Ce_{0.9}Pr_{0.1}O_{2-δ} (40MCO-60CPO) dual phase composite powders directly. As shown in the process flow chart (Fig. 1), a precursor was prepared by combining glycine and the metal nitrates Mn(NO₃)₂, Co(NO₃)₂, Ce(NO₃)₃ and Pr(NO₃)₃ in their appropriate stoichiometric ratios in an aqueous solution. The molar ratio of glycine: total metal ions was 2: 1. The precursor was stirred and heated at 150 °C in air to evaporate excess water until a viscous liquid was obtained. Further heating of the viscous liquid up to 300 °C caused the precursor liquid to auto-ignite. Combustion was rapid and self-sustaining, and a precursor ash was obtained, which was calcined at 950 °C for 10 h. To get green membranes, the resulting powders were pressed to disk membranes under a pressure of 5 MPa and held for 15 min in a stainless steel mold with a diameter of 18 mm. These green disks were pressure-less sintered at 1300 °C in air for 10 h. The surfaces of the disks were carefully polished to 0.3 mm and 0.5 mm thickness, respectively, by using 1200 grit-sand paper (average particle diameter 15.3 μm), then the membranes were washed with ethanol.

2.2. Characterization of powders and membranes

X-ray diffraction (XRD, D8 Advance, Bruker-AXS, with Cu-K_α radiation) was used to determine the phase structure. Data sets were recorded in a step-scan mode in the 2θ range of 20–80° with intervals of 0.02° and using a counting time of 1 s per point. The morphology of precursor ash and dual phase oxide powder were

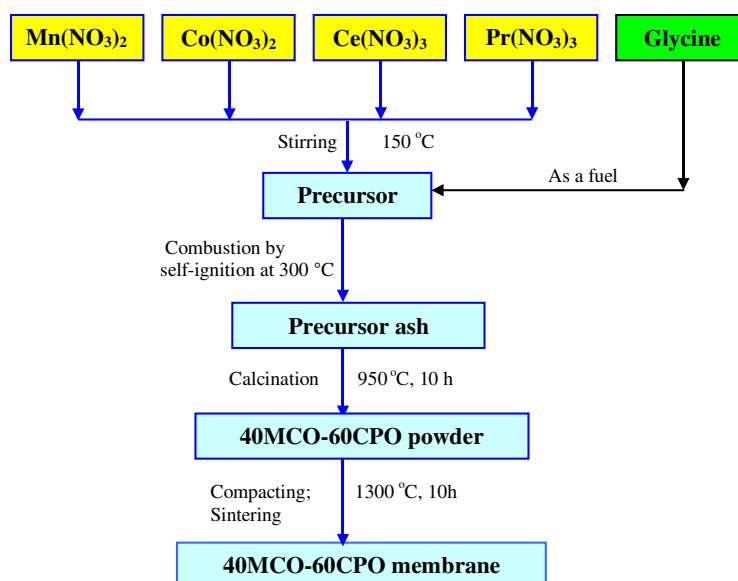


Fig. 1. Flow chart for the one-pot preparation of dual phase 40MCO-60CPO membranes by the glycine-nitrate combustion process (GNP).

characterized by scanning electron microscopy (SEM) and by energy dispersive X-ray spectroscopy (EDXS) at 15 keV. SEM and back scattered SEM (BSEM) were made using a Jeol-JSM-6700F operating at 15 keV. The element distribution in the grains of the dual phase membrane was studied on the same electron microscope by EDXS with Oxford Instruments INCA-300 EDX spectrometer at 15 keV.

2.3. Oxygen permeation performances of membranes

Oxygen permeation measurement was conducted in a home-made high-temperature oxygen permeation cell [38]. The disc-shaped membranes were sealed onto an alumina tube ($\varnothing=16$ mm) at 950 °C in air for 5 h with a gold paste (Heraeus, Germany). Another quartz tube ($\varnothing=24$ mm) served as the air side of the permeator. The temperature was maintained with a microprocessor temperature controller (HTM Reetz GmbH, Germany) coupled to a tubular furnace with a type K thermocouple setting inside the furnace. The effective areas of the membranes for oxygen permeation were 0.785 cm². The inlet gas flow rates were controlled by mass flow controllers (Bronkhorst, Germany) and the flow rates were regularly calibrated by using a bubble flow meter. During oxygen permeation measurement, synthetic air (20% O₂ and 80% N₂) at the rate of 200 mL min⁻¹ was used as feed gas. He/CO₂ was used as sweep gas to remove the permeated oxygen. 1 mL Ne min⁻¹ was used as an internal standard gas for calculating the total flow rate at the outlet on the sweep side. The effluents were analyzed by an on-

line gas chromatograph (GC, Agilent 7890A) equipped with a Carboxen 1000 column. The GC was frequently calibrated using standard gases in order to ensure the reliability of the experimental data. The calculation of oxygen permeation flux was demonstrated in detail in our previous papers [19,20].

3. Results and discussion

3.1. Characterization of the 40MCO–60CPO dual phase materials

Fig. 2a and b shows the XRD patterns of the membrane after sintering at 1300 °C in air for 10 h and of the powder after calcining the precursor ash at 950 °C in air for 10 h (Fig. 2a and b). For comparison, the XRD patterns of the pure phase CPO and MCO powders—also synthesized by the GNP and calcined at 950 °C in air for 10 h—are given (Fig. 2c and d). The XRD patterns of CPO (Fig. 3c) confirm its cubic structure (space group 225, Fm-3m) in agreement with literature [39]. From the Scherrer formalism, the mean crystallite size of pure CPO is determined to be about 85.4 nm. From the analysis of the XRD patterns of MCO (Fig. 3d) it follows that the MCO spinel phase consists of 57.9 wt% cubic MnCo₂O_{4- δ} (space group 227, Fd-3mZ) and 42.1 wt% tetragonal Mn₂CoO_{4- δ} (space group 141, 141/amdS), as known from literature [32–34]. According to the Scherrer equation, the mean crystallite size of MnCo₂O_{4- δ} and Mn₂CoO_{4- δ} are calculated to be 22 nm and 25.2 nm, respectively. Similar crystallite sizes can be derived from the XRD pattern of the mixture 40MCO–60CPO powder after

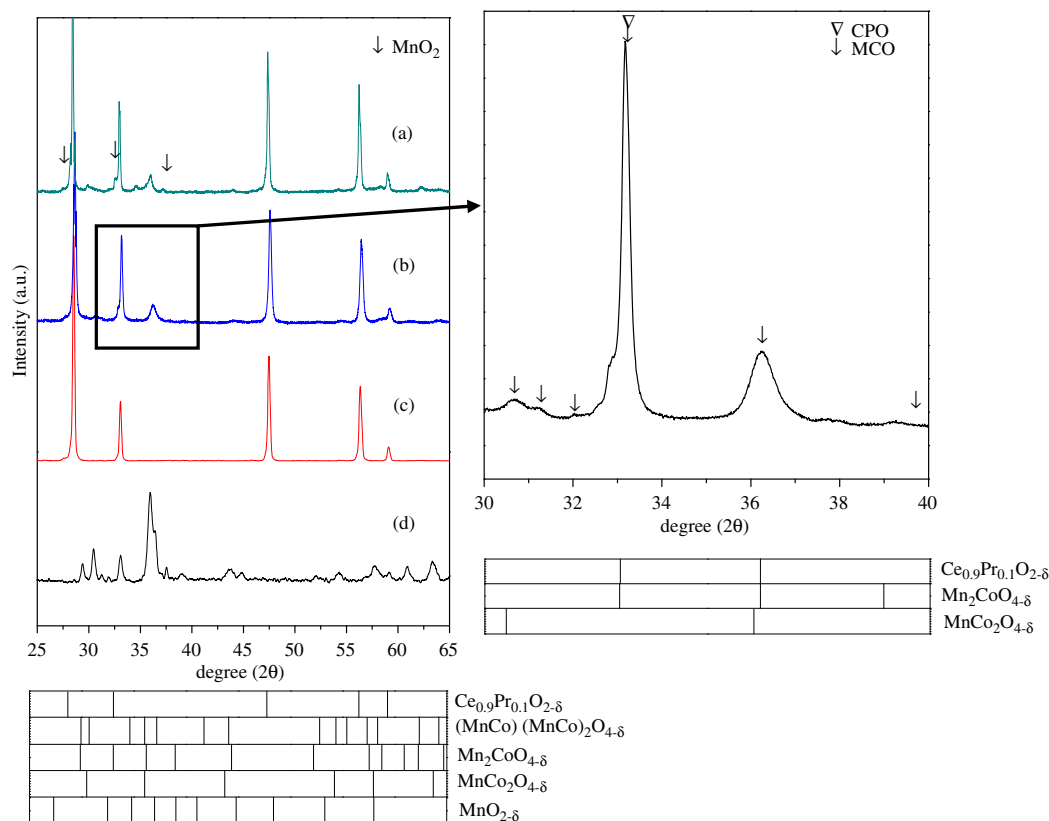


Fig. 2. XRD patterns of the 40MCO–60CPO membrane after sintered at 1300 °C in air for 10 h (a) and the as-prepared composite powder (b), pure phase powders CPO (c) and MCO (d), produced by the GNP method and calcined at 950 °C for 10 h in air (flow chart see Fig. 1, for the SEM see Fig. 3). Since MCO gives poor XRD patterns, the 30–40 2θ range of all samples has been measured for long time (10 h).

calcination at 950 °C (Fig. 2b); mean MCO and CPO crystallite sizes of 16.4 nm and 66.4 nm have been obtained. Comparing in Fig. 3 the XRD of the mixture 40MCO–60CPO powder with those of the pure MCO and CPO phases, no other crystalline phases except those of MCO and CPO were detected in the mixture powder after calcination at 950 °C. Since MCO gives much weaker XRD signals than CPO, the 2θ range between 30 and 40° was measured over 10 h, and the MCO line at 36° can be taken as a fingerprint for the

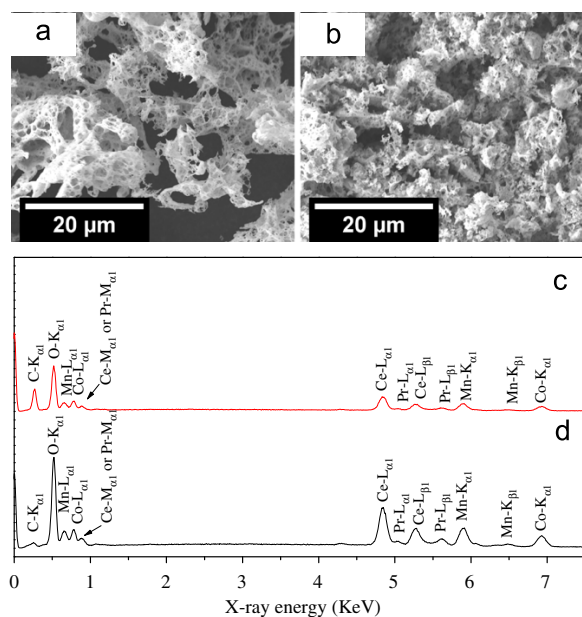


Fig. 3. SEM (a and b) pictures and EDXS (c and d) analysis of the precursor ash after burning the precursor (a and c) and the 40MCO–60CPO powder (b and d) after calcination of the precursor ash at 950 °C for 10 h in air (see Fig. 1).

existence of crystalline MCO. However, from the XRD patterns of the 40MCO–60CPO dual phase membrane sintered at 1300 °C in air for 10 h, small amounts of MnO₂ and the tetragonal (MnCo)₂O_{4-δ} can be found. This behavior may be related to the tetragonal-cubic structure transformations of Mn_{2-x}Co_xO_{4-δ} ($1.54 \geq x \geq 0.98$) at high temperature [40]. According to the phase diagram of the Mn–Co–O system reported by Aukrust et al., at 1300 °C exists in air for $X=1.5$ a stable mixture of cubic MnCo₂O_{4-δ}, tetragonal Mn₂CoO_{4-δ} and the mixed oxide (Mn,Co)O [41].

The precursor ash obtained by the combustion of the precursor in the GNP shows a foam-like open-pore structure because of the vigorous gas evolution (H₂O, N₂ and CO₂) during the GNP combustion synthesis (Fig. 3a). After sintering the precursor ash at 950 °C for 10 h, some densification can be stated (Fig. 3b). From the comparison of the EDXS of the precursor ash (Fig. 3c) and the powder after 950 °C calcination (Fig. 3d) it follows that the chemical composition of the ash and the powder is unchanged. Quantitative analysis based on the Cliff–Lorimer ratio technique, gave the element ratios Mn/Co=1:1 and Ce/Pr=9:1, which are in accurate agreement with the stoichiometry of the Mn_{1.5}Co_{1.5}O_{4-δ} spinel and of the Ce_{0.9}Pr_{0.1}O_{2-δ} cubic fluorite structure.

Fig. 4 shows the SEM and BSEM images of the 40MCO–60CPO dual phase membranes after sintering at 1300 °C for 10 h at two different magnifications. The grains of the two phases are well distributed with clear grain boundaries. The MCO and CPO grains can be easily distinguished by BSEM, the dark grains are MCO and the light ones represent CPO since the contribution of the back-scattered electrons to the SEM signal intensity is proportional to the atomic number. Furthermore, in the BSEM images of Fig. 4c and d, the mean grain size areas of MCO and CPO are found to be 0.265 μm² and 0.329 μm² through the analysis of 50 grains, respectively. The EDXS of the membrane (Fig. 5) shows the presence of Mn, Co, Ce and Pr (Fig. 5b). Fig. 5a shows the elemental mapping of the top view of the 40MCO–60CPO membrane obtained by EDXS. The green color (dark in BSEM) is an overlap of the Mn and Co signals, whereas the yellow color (light in BSEM) stems from an average of the Ce and Pr signals.

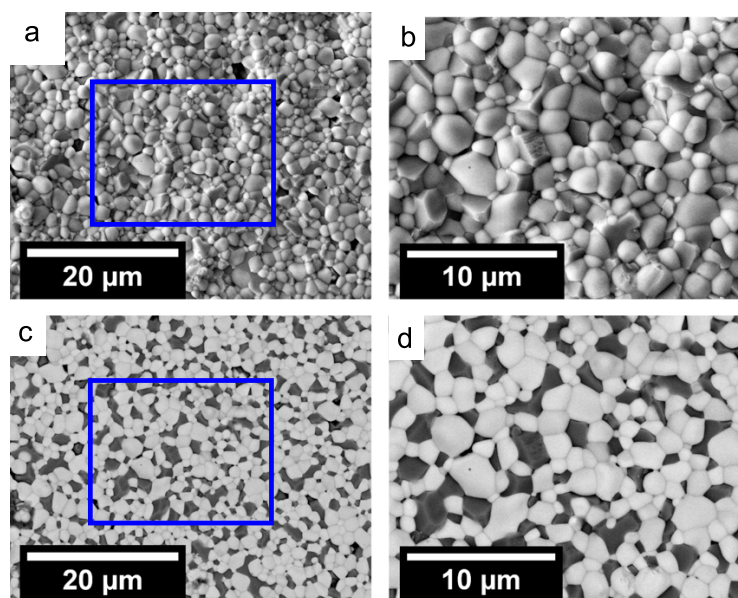


Fig. 4. SEM (a and b) and BSEM (c and d) of the surface of the 40MCO–60CPO dual phase membrane after sintered at 1300 °C in air for 10 h for different magnifications. In BSEM, the dark grains represent the MCO grains, the light ones represent the CPO grains, since the contribution of the backscattered electrons to the SEM signal intensity is proportional to the atomic number.

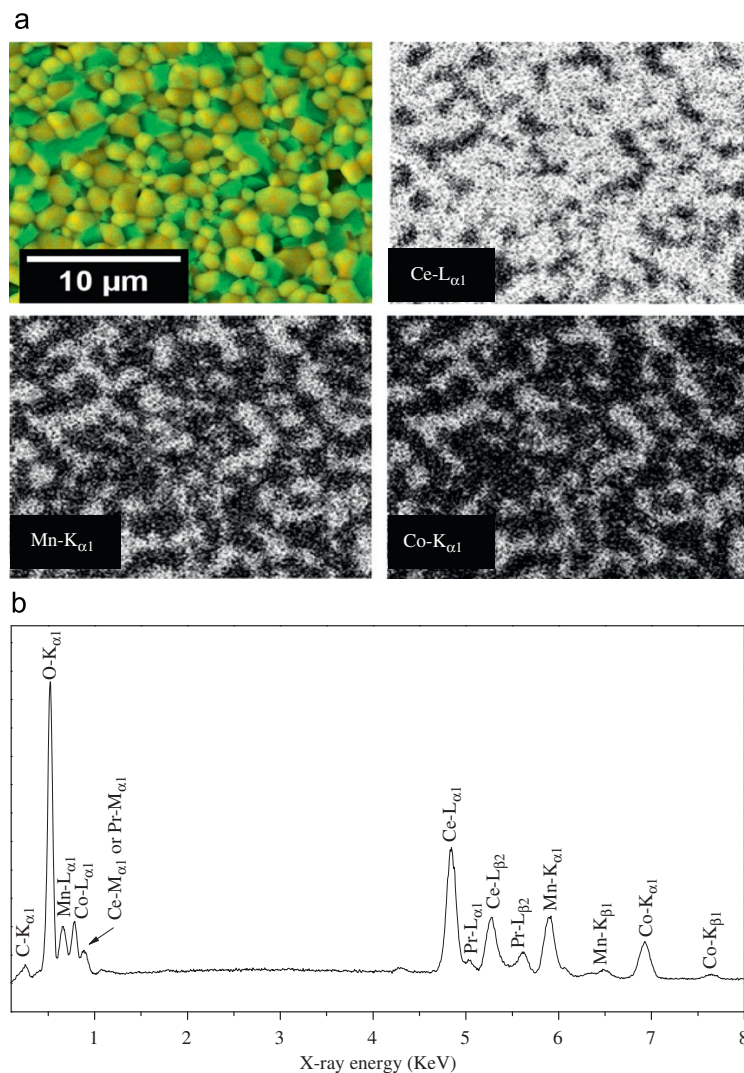


Fig. 5. EDXS analysis of 40MCO–60CPO composite membranes after sintered at 1300 °C for 10 h. In the EDXS map, the dark grains represent MCO grains (averaged and calibrated signals of Mn- $K_{\alpha 1}$, 2p→1s and Co- $K_{\alpha 1}$, 2p→1s), and the light grains represent CPO grains (averaged and calibrated signals of Ce- $L_{\alpha 1}$, 3d→2p and Pr- $L_{\alpha 1}$, 3d→2p).

3.2. Oxygen permeation properties and stability of the 40MCO–60CPO dual phase materials

The oxygen permeation flux through the 40MCO–60CPO dual phase membranes as a function of temperature with CO_2 as sweep gas is presented in Fig. 6. All the data were collected after oxygen permeation had reached steady state (after about 24 h). As shown in Fig. 6a, the oxygen permeation fluxes increase with increasing temperature. For example, when the temperature increases from 900 °C to 1000 °C, the oxygen permeation flux increases from $0.26 \text{ mL cm}^{-2} \text{ min}^{-1}$ to $0.48 \text{ mL cm}^{-2} \text{ min}^{-1}$. At 950 °C, a stable oxygen permeation flux of $0.37 \text{ mL cm}^{-2} \text{ min}^{-1}$ is obtained through a membrane with a thickness of 0.3 mm. Table 1 summarizes the oxygen permeation fluxes through several types of dual phase membranes [19–21,31,42,43]. As shown in Table 1, the oxygen permeation fluxes through our 40MCO–60CPO membrane are comparable with or even higher than those of other dual phase-type membranes reported in the open literature, e.g. the oxygen permeation fluxes through our

40MCO–60CPO membrane are comparable with those of the dual phase membranes $\text{NiFe}_2\text{O}_4\text{--Ce}_{0.9}\text{Gd}_{0.1}\text{O}_{2-\delta}$ [19,20] and $\text{Fe}_2\text{O}_3\text{--Ce}_{0.9}\text{Gd}_{0.1}\text{O}_{2-\delta}$ [21] at 950 °C under similar experimental conditions. Comparing with the dual phase membrane $\text{Ce}_{0.8}\text{Gd}_{0.2}\text{O}_{3-\delta}\text{--}15 \text{ vol}\% \text{ MnFe}_2\text{O}_{4-\delta}$ [31], our 40MCO–60CPO membrane shows slightly lower oxygen permeation flux under an air/He oxygen partial pressure gradient, unfortunately the oxygen permeation flux through the $\text{Ce}_{0.8}\text{Gd}_{0.2}\text{O}_{3-\delta}\text{--}15 \text{ vol}\% \text{ MnFe}_2\text{O}_{4-\delta}$ dual phase membrane was not studied under CO_2 atmosphere in [31]. Moreover, the $\text{Ce}_{0.8}\text{Sm}_{0.2}\text{O}_{2-\delta}\text{--La}_{0.8}\text{Sr}_{0.2}\text{CrO}_{3-\delta}$ dual phase membrane with a thickness of 0.3 mm exhibits an oxygen permeation flux of $1.4 \times 10^{-7} \text{ mol cm}^{-2} \text{ s}^{-1}$ ($0.19 \text{ mL cm}^{-2} \text{ min}^{-1}$) under an air/He oxygen partial pressure gradient at 950 °C [42], which is nearly two times lower than that on our 40MCO–60CPO membrane. Fig. 6b shows the gas permeation fluxes through the 40MCO–60CPO dual phase membrane with pure CO_2 as sweep gas as Arrhenius plot. The apparent activation energies were calculated to be 89 kJ mol^{-1} in the temperature range of 900–950 °C and 64 kJ mol^{-1} in the temperature range of 950–1000 °C.

It is known that the rate-limiting step of oxygen permeation through an MIEC membrane can be controlled either by oxygen surface exchange or by oxygen ions bulk diffusion. In order to identify the rate limiting step of oxygen transport through our 40MCO–60CPO membrane with CO₂ as sweep gas, we studied the oxygen permeation under different oxygen partial pressures on the sweep side at different temperatures while keeping the oxygen pressure on the air side constant at 0.20 bar. The different

oxygen partial pressures on the sweep side were adjusted by changing the CO₂ flow rate and measured by gas chromatography in this study. Fig. 7 displays the influence of different CO₂ flow rates on oxygen permeation on the 40MCO–60CPO membrane with 0.5 mm thickness at different temperatures. It was found that for all temperatures the oxygen permeation fluxes were increased with increasing the CO₂ flow rate. For example, when the CO₂ flow rate increased from 19 to 116 mL min⁻¹, the oxygen partial pressures on the permeate side decrease from 0.007 bar to 0.002 bar; whereas the oxygen permeation fluxes increased from 0.19 mL cm⁻² min⁻¹ to 0.23 mL cm⁻² min⁻¹ at 1000 °C. When using CO₂ as sweep gas, we can observe the usual behavior, namely that the oxygen permeation fluxes increase if the gradient of the oxygen partial pressure across the membrane is increased, which can be achieved by off-transporting the permeated oxygen as fast as possible by an increased sweep flow.

Following Kim et al. [44], J_{O_2} shows a linear relationship with $(P_h - P_o)^{0.5} - (P_l - P_o)^{0.5}$ according to

$$J_{O_2} = \frac{1}{2} \frac{C_{i1}C_{i2}}{C_{i1} + C_{i2}} k_{io} [(P_h/P_o)^n - (P_l/P_o)^n] \quad (1)$$

if the oxygen permeation process is limited by the surface exchange reaction. If the oxygen permeation process is controlled by oxygen ion bulk diffusion, J_{O_2} would be linearly proportional to $\ln(P_h/P_l)$ according to [44]

$$J_{O_2} = \frac{1}{4} \frac{\langle C_i D_a \rangle}{L} \ln \frac{P_h}{P_l} \quad (2)$$

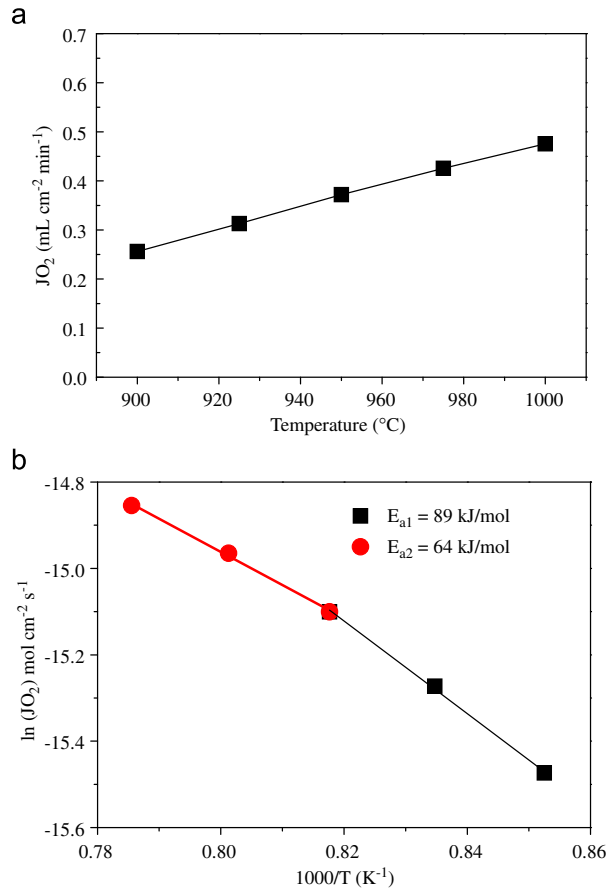


Fig. 6. Oxygen permeation fluxes (a) and its Arrhenius plot (b) through the 40MCO–60CPO dual phase gas permeation fluxes of membranes as a function of temperature with pure CO₂ as sweep gas. Conditions: 200 mL min⁻¹ air as feed gas, 29 mL/min CO₂ as sweep gas; 1 mL min⁻¹ Ne as internal standard gas; membrane thickness: 0.3 mm.

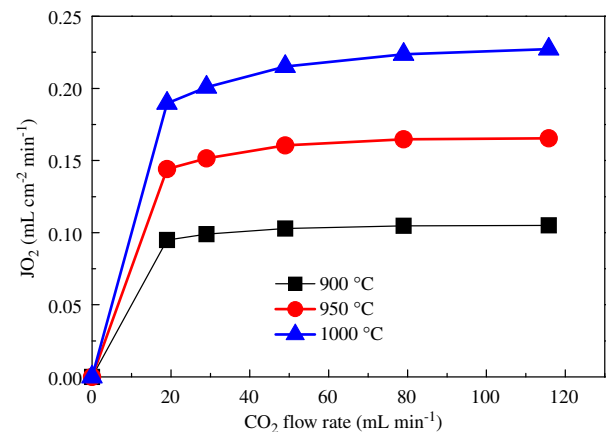


Fig. 7. Effect of different CO₂ sweep rates on oxygen permeation flux at different temperatures. Conditions: 200 mL min⁻¹ air as feed gas; 1 mL min⁻¹ Ne as internal standard gas; membrane thickness: 0.5 mm.

Table 1
Steady-state oxygen permeation flux (J_{O_2}) through different dual phase membranes in disk geometries.

Membrane materials	Thickness (mm)	Temperature (°C)	Oxygen flux (mL cm ⁻² min ⁻¹) air/He	Oxygen flux (mL cm ⁻² min ⁻¹) air/CO ₂	Refs.
40 wt% NiFe ₂ O _{4-δ} -60 wt% Ce _{0.9} Gd _{0.1} O _{2-δ} ^a	0.5	1000	0.30	0.27	[19,20]
40 wt% Fe ₂ O _{3-δ} -60 wt% Ce _{0.9} Gd _{0.1} O _{2-δ}	0.5	1000	0.18	0.16	21
Ce _{0.8} Gd _{0.2} O _{3-δ} -15 vol% MnFe ₂ O _{4-δ}	0.3	1000	0.40	-	31
60 vol% Ce _{0.8} Sm _{0.2} O _{2-δ} -40 vol% La _{0.8} Sr _{0.2} CrO _{3-δ}	0.3	950	0.19	-	42
50 wt% Ce _{0.8} Gd _{0.2} O _{2-δ} -50 wt% La _{0.8} Sr _{0.2} MnO _{3-δ}	1	750	0.02	-	43
40 wt% Mn _{1.5} Co _{1.5} O _{4-δ} -60 wt% Ce _{0.9} Pr _{0.1} O _{2-δ}	0.5	1000	0.22	0.2	This work
40 wt% Mn _{1.5} Co _{1.5} O _{4-δ} -60 wt% Ce _{0.9} Pr _{0.1} O _{2-δ}	0.3	950	-	0.37	This work

^a The air side of the 40 wt% NiFe₂O_{4-δ}-60 wt% Ce_{0.9}Gd_{0.1}O_{2-δ} dual phase membrane was coated with a La_{0.6}Sr_{0.4}CoO_{3-δ} porous layer.

where J_{O_2} is the oxygen permeation flux, C_i is the oxygen ion concentration, D_o is the diffusion coefficient of the oxygen ion-electron hole pairs, L is the thickness of the membrane, C_{i1} , C_{i2} are the oxygen concentrations at the interfaces of the membrane. n is the order of the chemical reaction at the gas-MIEC interface which is for the special case of a planar membrane $n=0.5$. k_{i0} is the surface-exchange coefficient, and P_h , P_l and P_o stand for high oxygen partial pressure on the feed side, low oxygen partial pressures on the sweep side and the normalized pressures of 1 bar, respectively.

Correlating and evaluating our oxygen permeation data according to the above theory of Kim et al. [44], we can state that the oxygen permeation fluxes J_{O_2} are a linear function of $(P_h/P_o)^{0.5} - (P_l/P_o)^{0.5}$ and not of $\ln(P_h/P_l)$ as shown in Fig. 8. From this finding, it follows that the oxygen permeation through the 40MCO–60CPO dual phase membrane of 0.5 mm thickness is controlled in the temperature region studied by the surface exchange reaction rather than by bulk diffusion.

Fig. 9 shows the oxygen permeation flux through 40MCO–60CPO dual phase composite membrane with a thickness 0.5 mm as a function of the CO_2 concentration in the sweep gas at 1000 °C. The

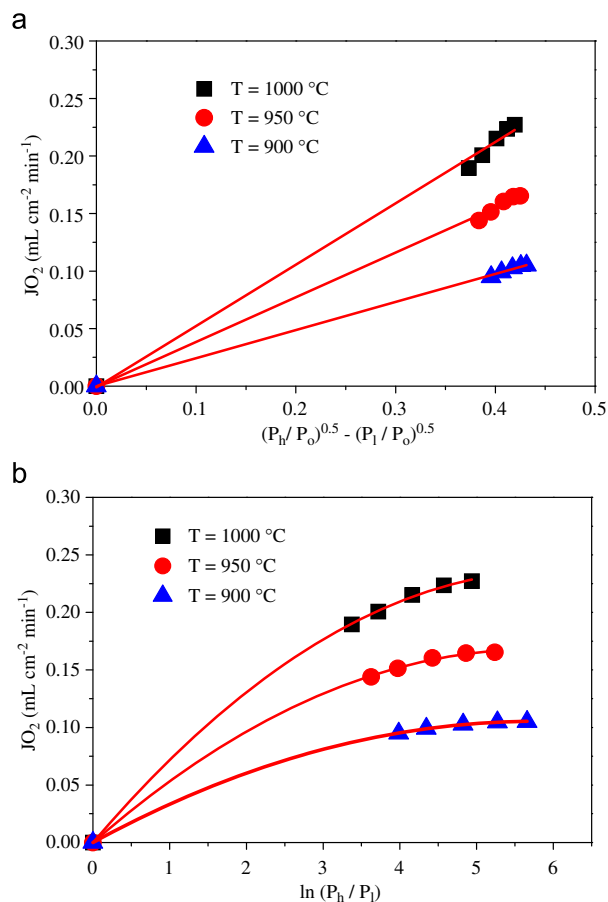


Fig. 8. Relationship between oxygen permeation fluxes through the 40MCO–60CPO membrane with 0.5 mm thickness at different temperatures and $\ln(P_h/P_l)$. P_h , P_l and P_o denote for high oxygen partial pressure on the feed side, low oxygen partial pressures on the sweep side and the normalized pressures of 1 bar, respectively. Conditions: 200 mL min⁻¹ air as feed gas, $F_{CO_2+He+Ne} = 30$ mL min⁻¹ as sweep gas; 1 mL/min Ne as internal standard gas. Membrane thickness: 0.5 mm.

different CO_2 concentrations have been obtained by mixing with He, the total flow rate of the sweep gas was kept constant at 30 mL/min with 1 mL Ne/min as calibration gas. With increasing CO_2 concentration of the sweep gas, only a slight decrease of the oxygen permeation flux can be seen. This behavior is different to those of alkaline-earth metals containing perovskites. Schulz et al. reported a strong decrease of the oxygen permeation flux through the perovskites $Ba_{0.5}Sr_{0.5}Co_{0.8}Fe_{0.2}O_{3-\delta}$ (BSCF) and $SrCo_{1-x}Nb_xO_{3-\delta}$ (SCN; $x=0.1, 0.2$) due to carbonate formation with increasing CO_2 concentrations in the sweep gas [45]. The slight decrease of the oxygen permeation flux can be explained by a stronger influence of CO_2 on the surface process compared with pure He which is in complete agreement with previous reports [19,21]. This finding is also in correspondence with our previous studies on $NiFe_2O_{4-\delta}-Ce_{0.9}Gd_{0.1}O_{2-\delta}$ composite materials and similar to the $La_{0.8}Sr_{0.2}MnO_{3-\delta}-Ce_{0.8}Sm_{0.2}O_{2-\delta}$ dual phase composite membrane of Chen et al., where also a slight reduction of the oxygen permeation flux was observed when pure CO_2 instead of a more inert sweep gas was used [46].

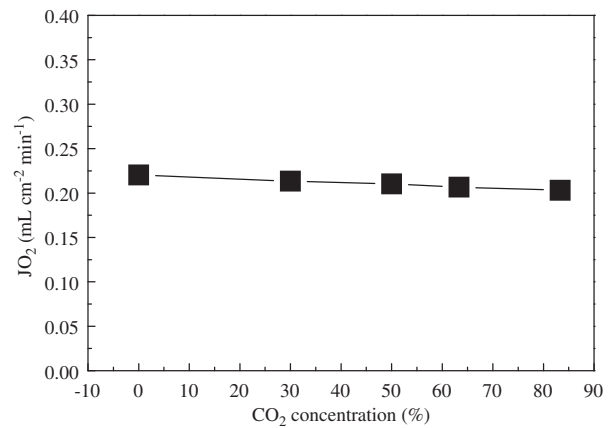


Fig. 9. Oxygen permeation flux through 40MCO–60CPO dual phase composite membrane as function of CO_2 concentration in the sweep gas at 1000 °C. Conditions: 200 mL min⁻¹ air as feed gas, $F_{CO_2+He+Ne} = 30$ mL min⁻¹ as sweep gas; 1 mL min⁻¹ Ne as internal standard gas. Membrane thickness: 0.5 mm.

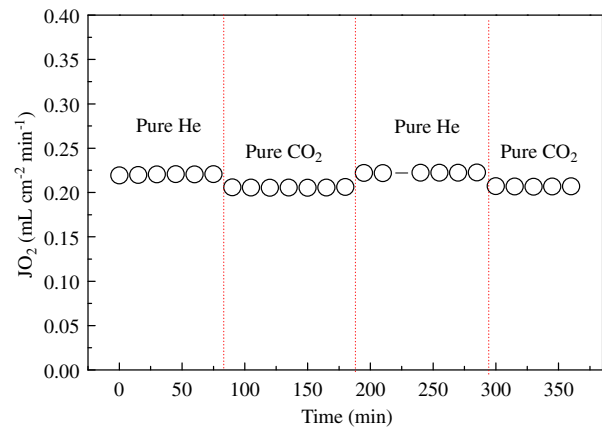


Fig. 10. Oxygen permeation fluxes as function of time while periodically changing the sweep gas. Conditions: 200 mL min⁻¹ air as feed gas, 29 mL min⁻¹ He and 1 mL min⁻¹ Ne or 29 mL min⁻¹ CO_2 and 1 mL min⁻¹ Ne as sweep gas; Membrane thickness: 0.5 mm. Temperature: 1000 °C.

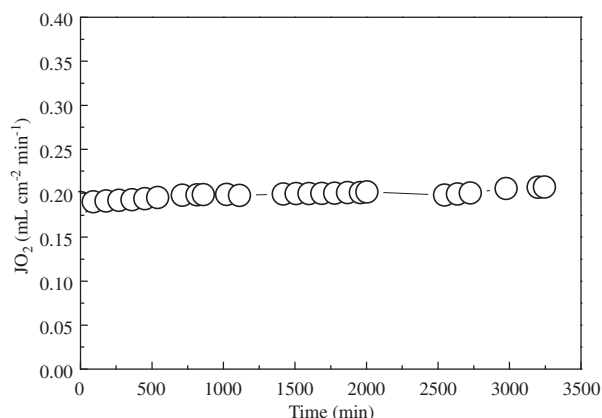


Fig. 11. Oxygen permeation flux through 40MCO–60CPO dual phase composite membrane as a function of time using pure CO₂ as sweep gas. Conditions: 200 mL min⁻¹ air as feed gas, 29 mL min⁻¹ CO₂ as sweep gas; 1 mL min⁻¹ Ne as internal standard gas. Membrane thickness: 0.5 mm. Temperature: 1000 °C.

Fig. 10 presents the reversibility of the oxygen permeation flux through the 40MCO–60CPO membrane while periodically changing the sweep gas between He and CO₂ at 1000 °C. When using He as sweep gas, a stable oxygen permeation flux of 0.22 mL cm⁻² min⁻¹ can be obtained, whereas the oxygen permeation flux decreases immediately to the slightly lower value of 0.20 mL cm⁻² min⁻¹ if CO₂ instead of He is used as sweep gas. This behavior is different to previous findings on the perovskite-type membranes. Arnold et al. reported an immediate stop of the oxygen permeation for BSCF membrane when pure CO₂ was used as sweep gas at 875 °C but the oxygen permeation flux recovered if the sweep gas CO₂ is switched back to pure helium [16]. A rapid breakdown of the oxygen permeability through a (Ba,Sr)(Zn,Fe)O_{3-δ} membrane at 750 °C in a CO₂ atmosphere due to the formation of a small amounts of carbonate on the surface of the membrane has been reported [47]. However, in our study, only a slight decrease of the oxygen permeation flux was observed. This behavior is ascribed to the slight inhibiting effect of CO₂ on the oxygen surface-exchange reaction but not to the formation of carbonates. Numerous papers have shown that the oxygen surface exchange reaction is influenced by the kind of sweep gas. Ten Elshof et al. have reported that the activation energy obtained from La_{1-x}Sr_xFeO_{3-δ} (x=0.1–0.3) under air/CO, CO₂ oxygen partial pressure gradients is much lower than that under air/He gradient due to the different oxygen exchange reaction rates in the presence of CO, CO₂ or He gas [48].

The oxygen permeation flux through the 40MCO–60CPO dual phase composite membrane with CO₂ as sweep gas is shown in Fig. 11 as a function of time. During the whole oxygen permeation test, an oxygen permeation flux of about 0.20 mL cm⁻² min⁻¹ was obtained at 1000 °C and no decrease was found. Kharton et al. have reported that obvious degradation of the oxygen permeation flux through Ce_{0.8}Gd_{0.2}O_{2-δ}–La_{0.7}Sr_{0.3}MnO_{3-δ} dual phase composite membrane with time was observed due to the formation of Sr(Ce, Ln)O_{3-δ} (Ln is Gd, La) in the grain boundaries, which can block the ionic transport [49]. From the stable oxygen permeation fluxes on our 40MCO–60CPO, we can exclude chemical reactions between the two MCO and CPO phases involved.

4. Conclusions

A novel oxygen transporting dual phase membrane of the composition 40 wt% Mn_{1.5}Co_{1.5}O_{4-δ}–60 wt% Ce_{0.9}Pr_{0.1}O_{2-δ} (40MCO–60CPO) was prepared with MCO as electron conductor

and CPO as oxygen ion conductor via a rapid one-pot glycine-nitrate combustion process. XRD confirmed that the 40MCO–60CPO membrane sintered at 1300 °C in air, represents a micro-scale mixture of mainly the two phases MCO and CPO, but also traces of MnO₂ and (MnCo)(MnCo)₂O_{4-δ} have been detected. An oxygen permeation flux of 0.48 mL cm⁻² min⁻¹ was obtained at 1000 °C under an air/CO₂ oxygen partial pressure gradient through a membrane with a thickness of 0.3 mm. The 40MCO–60CPO dual phase membrane can be operated for at least 60 h when pure CO₂ was used as sweep gas, suggesting that the 40MCO–60CPO dual phase membrane is CO₂ stable. The good stability under pure CO₂ recommends the 40MCO–60CPO material as a good candidate for the oxygen separation from air in the 4-end membrane operation mode in the oxy-fuel process.

Acknowledgments

H.X. Luo acknowledges the financial support by the China Scholarship Council (CSC). The authors acknowledge financial support from the EU through FP7 NASA-OTM project (Grant agreement no. 228701) and from the Sino-German Center for Science Promotion (GZ 676). T. Klande thanks the State of Lower Saxony for the NTH bottom up Grant no. 21-71023-25-7/09. The authors thank Dr. Feldhoff for stimulating discussions and F. Steinbach for technical support.

References

- [1] S. Baumann, J.M. Serra, M.P. Lobera, S. Escolástico, F. Schulze-Küppers, W.A. Meulenber, Ultrahigh oxygen permeation flux through supported Ba_{0.5}Sr_{0.5}Co_{0.8}Fe_{0.2}O_{3-δ} membranes, *J. Membr. Sci.* 377 (2011) 198–205.
- [2] J. Pérez-Ramírez, B. Vigeland, Perovskite membranes in ammonia oxidation: towards process intensification in nitric acid manufacture, *Angew. Chem. Int. Ed.* 44 (2005) 1112–1115.
- [3] E. Drioli, A. Brunetti, G. Di Profio, G. Barbieri, Process intensification strategies and membrane engineering, *Green Chem.* (2012), <http://dx.doi.org/10.1039/C2GC16668B>.
- [4] M.A. Habib, H.M. Badr, S.F. Ahmed, R. Ben-Mansour, K. Mezghani, S. Imashuku, G.J. la O', Y. Shao-Horn, N.D. Mancini, A. Mitsos, P. Kirchen, A.F. Ghoneim, A review of recent developments in carbon capture utilizing oxy-fuel combustion in conventional and ion transport membrane systems, *Int. J. Energy Res.* 35 (2011) 741–764.
- [5] S. Smart, C.X.C. Lin, L. Ding, K. Thambimuthu, J.C. Diniz da Costa, Ceramic membranes for gas processing in coal gasification, *Energy Environ. Sci.* 3 (2010) 268–278.
- [6] S.S. Hashim, A.R. Mohamed, S. Bhatia, Oxygen separation from air using ceramic-based membrane technology for sustainable fuel production and power generation, *Renew. Sust. Energy Rev.* 15 (2011) 1284–1293.
- [7] S. Engels, T. Markus, M. Modigell, L. Singheiser, Oxygen permeation and stability investigations on MIEC membrane materials under operating conditions for power plant processes, *J. Membr. Sci.* 370 (2011) 58–69.
- [8] S. Engels, F. Beggel, M. Modigell, H. Stadler, Simulation of a membrane unit for oxyfuel power plants under consideration of realistic BSCF membrane properties, *J. Membr. Sci.* 359 (2010) 93–101.
- [9] A. Waindich, A. Möbius, M. Müller, Corrosion of Ba_{1-x}Sr_xCo_{1-y}Fe_yO_{3-δ} and La_{0.3}Ba_{0.7}Co_{0.2}Fe_{0.8}O_{3-δ} materials for oxygen separating membranes under oxycoal conditions, *J. Membr. Sci.* 337 (2009) 182–187.
- [10] M. Schulz, R. Kriegel, A. Kämpfer, Assessment of CO₂ stability and oxygen flux of oxygen permeable membranes, *J. Membr. Sci.* 378 (2011) 10–17.
- [11] E. Tzimpilis, N. Moschoudis, M. Stoukides, P. Bekiaroglou, Ageing and SO₂ resistance of Pd containing perovskite-type oxides, *Appl. Catal. B Environ.* 87 (2009) 9–17.
- [12] N.P. Xu, S.G. Li, W.Q. Jin, J. Shi, Y.S. Lin, Experimental and modeling study on tubular dense membranes for oxygen permeation, *Am. Inst. Chem. Eng. J.* 45 (1999) 2519–2526.
- [13] J.X. Yi, M. Schroeder, T. Weirich, J. Mayer, Behavior of Ba(Co, Fe, Nb)O_{3-δ} perovskite in CO₂-containing atmospheres: degradation mechanism and materials design, *Chem. Mater.* 22 (2010) 6246–6253.
- [14] Q. Jiang, S. Faraji, K.J. Nordheden, S.M. Stagg-Williams, CO₂ reforming reaction assisted with oxygen permeable Ba_{0.5}Sr_{0.5}Co_{0.8}Fe_{0.2}O_x ceramic membranes, *J. Membr. Sci.* 368 (2011) 69–77.
- [15] J.X. Yi, S.J. Feng, Y.B. Zuo, W. Liu, C.S. Chen, Oxygen permeability and stability of Sr_{0.95}Co_{0.8}Fe_{0.2}O_{3-δ} in a CO₂- and H₂O-containing atmosphere, *Chem. Mater.* 17 (2005) 5856–5861.

- [16] M. Arnold, H.H. Wang, A. Feldhoff, Influence of CO₂ on the oxygen permeation performance and the microstructure of perovskite-type (Ba_{0.5}Sr_{0.5})(Co_{0.8}Fe_{0.2})O_{3-δ} membranes, *J. Membr. Sci.* 293 (2007) 44–52.
- [17] X. Tan, N. Liu, B. Meng, J. Sunarso, K. Zhang, S. Liu, Oxygen permeation behavior of La_{0.6}Sr_{0.4}Co_{0.8}Fe_{0.2}O₃ hollow fiber membranes with highly concentrated CO₂ exposure, *J. Membr. Sci.* 389 (2012) 216–222.
- [18] S. Li, W. Jin, P. Huang, N. Xu, J. Shi, Y.S. Lin, Tubular lanthanum cobaltite perovskite type membrane for oxygen permeation, *J. Membr. Sci.* 166 (2000) 51–61.
- [19] H.X. Luo, H.Q. Jiang, K. Efimov, H.H. Wang, J. Caro, Influence of the preparation methods on the microstructure and oxygen permeability of a CO₂-stable dual phase membrane, *Am. Inst. Chem. Eng. J.* 57 (2011) 2738–2745.
- [20] H.X. Luo, K. Efimov, H.Q. Jiang, A. Feldhoff, H.H. Wang, J. Caro, CO₂-stable and cobalt-free dual-phase membrane for oxygen separation, *Angew. Chem. Int. Ed.* 50 (2011) 759–763.
- [21] H.X. Luo, H.Q. Jiang, K. Efimov, F.Y. Liang, H.H. Wang, J. Caro, CO₂-tolerant oxygen-permeable Fe₂O₃-Ce_{0.9}Gd_{0.1}O_{2-δ} dual phase membranes, *Ind. Eng. Chem. Res.* 50 (2011) 13508–13517.
- [22] V.V. Kharton, A.V. Kovalevsky, A.P. Viskup, A.L. Shaula, F.M. Figueiredo, E.N. Naumovich, F.M.B. Marques, Oxygen transport in Ce_{0.8}Gd_{0.2}O_{2-δ}-based composite membranes, *Solid State Ionics* 160 (2003) 247–258.
- [23] E.J.E. Ten, N.Q. Nguyen, O.M.W. Den, H.J.M. Bouwmeester, Oxygen permeation properties of dense Bi_{1.5}Er_{0.5}O₃-Ag cermet membranes, *J. Electrochem. Soc.* 144 (1997) 4361–4366.
- [24] T. Chen, H.L. Zhao, N.S. Xu, Y. Li, X.G. Lu, W.Z. Ding, F.S. Li, Synthesis and oxygen permeation properties of a Ce_{0.8}Sm_{0.2}O_{2-δ}-LaBaCo₂O_{5+δ} dual-phase composite membrane, *J. Membr. Sci.* 370 (2011) 158–165.
- [25] X.F. Zhu, H.H. Wang, W.S. Yang, Relationship between homogeneity and oxygen permeability of composite membranes, *J. Membr. Sci.* 309 (2008) 120–127.
- [26] L.A. Chick, L.R. Pederson, G.D. Maupin, J.L. Bates, L.E. Thomas, G.J. Exarhos, Glycine-nitrate combustion synthesis of oxide ceramic powders, *Mater. Lett.* 10 (1990) 6–12.
- [27] Y.L. Zhang, H.C. Shin, J. Dong, M.L. Liu, Nanostructured LiMn₂O₄ prepared by a glycine-nitrate process for lithium-ion batteries, *Solid State Ionics* 171 (2004) 25–31.
- [28] H.H. Wang, W.S. Yang, Y. Cong, X.F. Zhu, Y.S. Lin, Structure and oxygen permeability of a dual-phase membrane, *J. Membr. Sci.* 224 (2003) 107–115.
- [29] X.F. Zhu, H.Y. Liu, Y. Cong, W.S. Yang, Novel dual-phase membranes for CO₂ capture via an oxyfuel route, *Chem. Commun.* 48 (2012) 251–253.
- [30] X.F. Zhu, W.S. Yang, Composite membrane based on ionic conductor and mixed conductor for oxygen permeation, *Am. Inst. Chem. Eng. J.* 54 (2008) 665–672.
- [31] H. Takamura, Y. Koshino, A. Kamegawa, M. Okada, Electrode and oxygen permeation properties of (Ce,Sm)O₂-MFe₂O₄ and composite thin films (M=Co and Mn), *Solid State Ionics* 179 (2006) 2185–2189.
- [32] Z.G. Yang, G.G. Xia, X.H. Li, J.W. Stevenson, Mn(Co)₃O₄ spinel coatings on ferritic stainless steels for SOFC interconnect applications, *Int. J. Hydrogen Energy* 32 (2007) 3648–3654.
- [33] M.C. Tucker, L. Cheng, L.C. DeJonghe, Glass-containing composite cathode contact materials for solid oxide fuel cells, *J. Power Sour.* 196 (2011) 8435–8443.
- [34] H.Y. Liu, X.F. Zhu, M.J. Cheng, Y. Cong, W.S. Yang, Novel Mn_{1.5}Co_{1.5}O₄ spinel cathodes for intermediate temperature solid oxide fuel cells, *Chem. Commun.* 47 (2011) 2378–2380.
- [35] D.L. Maricle, T.E. Swarr, S. Karavolis, Enhanced ceria—a low-temperature SOFC electrolyte, *Solid State Ionics* 52 (1992) 173–182.
- [36] P. Knauth, H.L. Tuller, Nonstoichiometry and relaxation kinetics of nanocrystalline mixed praseodymium-cerium oxide Pr_{0.7}Ce_{0.3}O_{2-x}, *J. Eur. Ceram. Soc.* 19 (1999) 831–836.
- [37] Ch. Ftikos, M. Nauer, B.C.H. Steele, Electrical conductivity and thermal expansion of ceria doped with Pr, Nb and Sn, *J. Eur. Ceram. Soc.* 12 (1993) 267–270.
- [38] H.X. Luo, B.B. Tian, Y.Y. Wei, H.H. Wang, H.Q. Jiang, J. Caro, Oxygen permeability and structural stability of a novel tantalum-doped perovskite BaCo_{0.7}Fe_{0.2}Ta_{0.1}O_{3-δ}, *Am. Inst. Chem. Eng. J.* 56 (2010) 604–610.
- [39] Z.Y. Pu, J.Q. Lu, M.F. Luo, Y.L. Xie, Study of oxygen vacancies in Ce_{0.9}Pr_{0.1}O_{2-δ} solid solution by in situ X-ray diffraction and in situ Raman spectroscopy, *J. Phys. Chem. C* 111 (2007) 18695–18702.
- [40] H. Bordeneuve, S. Guillemet-Fritsch, A. Rousset, S. Schuurman, V. Poulain, Structure and electrical properties of single-phase cobalt manganese oxide spinels Mn_{3-x}Co_xO₄ sintered classically and by spark plasma sintering (SPS), *J. Solid State Chem.* 182 (2009) 396–401.
- [41] E. Aukrust, A. Muan, Phase relations in the system cobalt oxide–manganese oxide in air, *J. Am. Ceram. Soc.—Discussions and Notes* 46 (1963) 511.
- [42] J.X. Yi, Y.B. Zuo, W. Liu, L. Winnubst, C.S. Chen, Oxygen permeation through a Ce_{0.8}Sm_{0.2}O_{2-δ}-La_{0.8}Sr_{0.2}CrO_{3-δ} dual-phase composite membrane, *J. Membr. Sci.* 280 (2006) 849–855.
- [43] V.V. Kharton, A.V. Kovalevsky, A.P. Viskup, F.M. Figueiredo, A.A. Yaremchenko, E.N. Naumovich, F.M.B. Marques, Oxygen permeability and Faradaic efficiency of Ce_{0.8}Gd_{0.2}O_{2-δ}-La_{0.7}Sr_{0.3}MnO_{3-δ} composites, *J. Eur. Ceram. Soc.* 21 (2001) 1763–1767.
- [44] S. Kim, Y.L. Yang, A.J. Jacobson, B. Abeles, Oxygen surface exchange in mixed ionic electronic conductor membranes, *Solid State Ionics* 121 (1999) 31–36.
- [45] M. Schulz, R. Kriegel, A. Kämpfer, Assessment of CO₂ stability and oxygen flux of oxygen permeable membranes, *J. Membr. Sci.* 378 (2011) 10–17.
- [46] W. Li, T.F. Tian, F.Y. Shi, Y.S. Wang, C.S. Chen, Ce_{0.8}Sm_{0.2}O_{2-δ}-La_{0.8}Sr_{0.2}MnO_{3-δ} dual-phase composite hollow fiber membrane for oxygen separation, *Ind. Eng. Chem. Res.* 48 (2009) 5789–5793.
- [47] J. Martynczuk, K. Efimov, L. Robben, A. Feldhoff, Performance of zinc-doped perovskite-type membranes at intermediate temperatures for long-term oxygen permeation and under a carbon dioxide atmosphere, *J. Membr. Sci.* 344 (2009) 62–70.
- [48] J.E. Ten Elshof, H.J.M. Bouwmeester, H. Verweij, Oxygen transport through La_{1-x}Sr_xFeO_{3-δ} membranes II. Permeation in air/CO, CO₂ gradients, *Solid State Ionics* 89 (1996) 81–92.
- [49] V.V. Kharton, A.V. Kovalevsky, A.P. Viskup, F.M. Figueiredo, E.N. Naumovich, F.M.B. Marques, Oxygen permeability of Ce_{0.8}Gd_{0.2}O_{2-δ}-La_{0.7}Sr_{0.3}MnO_{3-δ} composite membranes, *J. Electrochem. Soc.* 147 (2000) 2814–2821.

3 Chapter 3

CO₂-tolerant alkaline-earth containing membrane materials

3.1 Summary

Most of the membrane materials with 100% alkaline-earth elements on the A site, exhibit a poor tolerance towards CO₂. This chapter describes the partial substitution of alkaline-earth elements on the A site with rare-earth elements that exhibit a higher tolerance against CO₂. The basic idea is based on thermodynamic considerations via an Ellingham diagram and perovskite stabilization energies (see chapter 1.5.1).

In section 3.1 the series of La_{1-x}Sr_xCo_{0.8}Fe_{0.2}O_{3-δ} (x = 1, 0.8, 0.6, 0.4) was investigated regarding oxygen permeation flux and the stability towards CO₂. All materials exhibited the cubic perovskite structure except the rhombohedral La_{0.6}Sr_{0.4}Co_{0.8}Fe_{0.2}O_{3-δ}. In-situ XRD revealed a phase transition to cubic perovskite structure at higher temperatures. With increasing lanthanum content the oxygen permeation flux in an air/helium gradient decreased considerably. It was found by in-situ XRD and long-term permeation experiments that La_{0.6}Sr_{0.4}Co_{0.8}Fe_{0.2}O_{3-δ} exhibits a good stability towards CO₂. The microstructure of different membranes was investigated by SEM and TEM after operation in CO₂.

Section 3.2 presents investigations of the orthorhombic La_{0.6}Ca_{0.4}FeO_{3-δ} and the rhombohedral La_{0.6}Ca_{0.4}Co_{0.8}Fe_{0.2}O_{3-δ}. In-situ XRD investigations reveal a phase transition to cubic structure at high temperatures and a high tolerance towards CO₂. The CO₂ stability was further confirmed by long-term oxygen permeation measurements in pure carbon dioxide atmosphere. An increase of 50% in oxygen permeation flux was achieved by using an asymmetric membrane design, in which a porous support was coated with a thin dense layer of the same chemical perovskite composition.

3.2 Effect of A-site lanthanum doping on the CO₂ tolerance of SrCo_{0.8}Fe_{0.2}O_{3-δ} oxygen-transporting membranes

Tobias Klande, Olga Ravkina, and Armin Feldhoff

Journal of Membrane Science **437** (2013) 122-130



Effect of A-site lanthanum doping on the CO₂ tolerance of SrCo_{0.8}Fe_{0.2}O_{3-δ} oxygen-transporting membranes

Tobias Klande*, Olga Ravkina, Armin Feldhoff

Institute of Physical Chemistry and Electrochemistry, Leibniz Universität Hannover, Callinstraße 3a, D-30179 Hannover, Germany

ARTICLE INFO

Article history:

Received 19 November 2012
Received in revised form
12 February 2013
Accepted 24 February 2013
Available online 5 March 2013

Keywords:

Oxygen-transporting membrane
Carbon dioxide
In-situ X-ray diffraction
Long-term oxygen permeation
Transmission electron microscopy

ABSTRACT

The SrCo_{0.8}Fe_{0.2}O_{3-δ} (SCF) perovskite was systematically doped with increasing lanthanum content up to 60 wt% on the A-site to investigate the effect on CO₂ tolerance. Different powders were prepared by a sol-gel method and the materials were characterized by *in-situ* X-ray diffraction (XRD) and long-term oxygen permeation measurements in CO₂-containing atmospheres. The microstructure was investigated using scanning electron microscopy (SEM) and transmission electron microscopy (TEM). All powders exhibit cubic perovskite structure except the rhombohedral La_{0.6}Sr_{0.4}Co_{0.8}Fe_{0.2}O_{3-δ} (LSCF 6482), which however, shows a phase transition into cubic perovskite structure at higher temperature. By doping 20 wt% lanthanum, the tolerance against CO₂ is considerably increased and doping with 60 wt% lanthanum resulted in a stable oxygen permeation performance in CO₂ atmosphere for at least 200 h. Oxygen permeation experiments in an air/helium gradient showed that with increasing lanthanum content the oxygen permeation flux decreases. Microstructure analysis of the membranes after CO₂ operation showed that the carbonate preferentially forms a dense layer at the carbon dioxide exposed sweep side of the membranes.

© 2013 Elsevier B.V. All rights reserved.

1. Introduction

The increasing demand of electricity, which is mainly produced by combustion of fossil fuels, leads to global warming by emission of green-house gases [1]. To reduce the climate-damaging carbon dioxide, new processes such as oxy-fuel combustion [2], in which pure oxygen is directly combusted with fossil fuels, are needed. The formed products are mainly carbon dioxide and water vapor, which can be easily separated by condensation. However, the production of oxygen by means of cryogenic processes or pressure swing adsorption (PSA) are expensive and energy intensive [3]. Using ceramic oxygen-transporting membranes, which supply an unrivalled selectivity for O₂, these costs can be lowered, resulting in better overall efficiency and lower electricity costs. Because the flame temperature would be too high, the oxygen has to be diluted before combustion. This can be done by the formed carbon dioxide flue gas in order to achieve an economically reasonable process. Another advantage would be that the generated process heat can be used to hold the membrane at operation temperature. By operating the membrane in sweep-gas mode at ambient pressure

even more energy can be saved compared to highly pressurized operation or operation under vacuum conditions [4,5].

The prominent mixed-ionic electronic conducting (MIEC) materials contain alkaline-earth cations, mainly barium and strontium, on the A-site of the ABO₃ perovskite structure, which on the one hand supply high oxygen fluxes, but on the other hand lead to membrane degradation in the presence of CO₂, which was shown for Ba_{0.5}Sr_{0.5}Co_{0.8}Fe_{0.2}O_{3-δ} for example [6]. A way to handle this problem is to avoid alkaline-earth elements leading to CO₂ tolerant materials such as La₂NiO_{4+δ} [7] or dual-phase materials such as 40 wt% NiFe₂O₄–60 wt% Ce_{0.9}Gd_{0.1}O_{2-δ} [8]. A further approach is to stabilize the structure of known, but CO₂-intolerant materials by doping less reactive elements on the A- and/or B-site. For example Chen et al. and Zeng et al. doped SCF with 10% tantalum [9] or 10% titanium [10], which greatly improves tolerance towards CO₂. The A site is predestinated to be substituted by rare-earth cations or smaller alkaline-earth cations such as calcium. By a thermodynamic approach using an Ellingham diagram, which was provided by Efimov et al. [11], it can be seen that the smaller La³⁺ ion (*r* = 136 pm) shows improved tolerance against CO₂ as compared to the bigger Sr²⁺ ion (*r* = 144 pm). However, the substitution of elements may lead to structural changes, reduced lattice parameters and therefore to significantly lower oxygen fluxes. Although, Tan et al. investigated the stability of La_{0.6}Sr_{0.4}Co_{0.8}Fe_{0.2}O_{3-δ} hollow-fiber membranes in CO₂ atmospheres [12] a systematic study of the influence of the lanthanum concentration on the A-side of SCF is apparently missing.

* Corresponding author. Tel.: +49 511 762 2943; fax: +49 511 762 19121.
E-mail address: tobias.klande@pci.uni-hannover.de (T. Klande).

In the present work the effect of the lanthanum concentration in $\text{La}_{1-x}\text{Sr}_x\text{Co}_{0.8}\text{Fe}_{0.2}\text{O}_{3-\delta}$ ($x=1, 0.8, 0.6, 0.4$) on CO₂ tolerance was systematically examined by XRD, *in-situ* XRD in CO₂ atmospheres and long-term oxygen permeation experiments in an air/helium or air/CO₂ gradient. Furthermore the membranes were investigated by SEM before and after the CO₂ exposure. The results of TEM investigations are also reported.

2. Experimental

2.1. Sample preparation

The powders were synthesized by sol-gel-route using stoichiometric amounts of $\text{La}(\text{NO}_3)_3$, $\text{Sr}(\text{NO}_3)_2$, $\text{Co}(\text{NO}_3)_2$, $\text{Fe}(\text{NO}_3)_3$, ethylenediaminetetraacetic acid (EDTA) and citric acid. The resulting gel was heated and stirred over night and then precalcined in ambient air at 773 K. After thoroughly grinding, the product was calcined for 10 h at 1273 K in ambient air. Green bodies of membranes were obtained by uniaxially pressing the powders at 150 MPa for 30 min, followed by sintering at 1473 K for SCF ($\text{SrCo}_{0.8}\text{Fe}_{0.2}\text{O}_{3-\delta}$), 1523 K for LSCF 2882 ($\text{La}_{0.2}\text{Sr}_{0.8}\text{Co}_{0.8}\text{Fe}_{0.2}\text{O}_{3-\delta}$), and 1573 K for LSCF 4682 ($\text{La}_{0.4}\text{Sr}_{0.6}\text{Co}_{0.8}\text{Fe}_{0.2}\text{O}_{3-\delta}$) and LSCF 6482 ($\text{La}_{0.6}\text{Sr}_{0.4}\text{Co}_{0.8}\text{Fe}_{0.2}\text{O}_{3-\delta}$) in ambient air for 10 h. At all times heating and cooling rates of 3 K min⁻¹ were used.

2.2. X-ray diffraction

X-ray diffraction (XRD) analysis was performed at room temperature using a Bruker-AXS D8 Advance diffractometer with Cu K_α radiation. Data sets were recorded in a step-scan mode in the 2 Θ range of 20–100° with intervals of 0.02°. High-temperature measurements were conducted in an *in-situ* cell HTK-1200 N (Anton-Paar) between room temperature and 1273 K in an atmosphere consisting of 50 vol% CO₂/50 vol% N₂. The heating rate was 12 K min⁻¹ with an equilibrium time of

30 min before each measurement. The XRD data were analyzed using TOPAS 4.0 software (Bruker AXS). The displacement of oxygen at different temperatures was determined by the Rietveld method.

2.3. Oxygen permeation

Oxygen permeation was measured in a house-made high-temperature permeation cell as described elsewhere [13,14]. Before the measurements both sides of the membranes were carefully polished

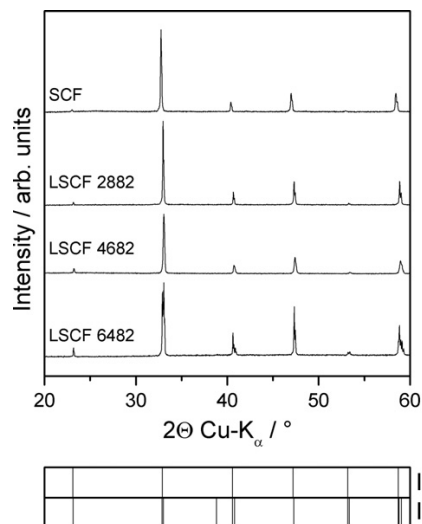


Fig. 1. Room-temperature XRD pattern of $(\text{La}_{1-x}\text{Sr}_x)(\text{Co}_{0.8}\text{Fe}_{0.2})\text{O}_3$ ($x=1, 0.8, 0.6, 0.4$) powders. The calculated Bragg positions for (I) cubic perovskite (s.g. $Pm\bar{3}m$, $a=3.875$ Å) and (II) rhombohedral perovskite (s.g. $R\bar{3}c$, $a=5.444$ Å, $c=13.241$ Å) are indicated at the bottom of the figure.

Table 1
Room-temperature unit cell parameters of $(\text{La}_{1-x}\text{Sr}_x)(\text{Co}_{0.8}\text{Fe}_{0.2})\text{O}_3$ ($x=1, 0.8, 0.6, 0.4$) after sintering for 10 h at the given temperature in air.

Sample	Lattice parameters [Å]			Unit cell volume [Å ³]	Space group
	<i>a</i>	<i>b</i>	<i>c</i>		
SCF (<i>T</i> =1473 K)	3.8651	–	–	57.74	$Pm\bar{3}m$
LSCF 2882 (<i>T</i> =1523 K)	3.8404	–	–	56.64	$Pm\bar{3}m$
LSCF 4682 (<i>T</i> =1573 K)	3.8380	–	–	56.54	$Pm\bar{3}m$
LSCF 6482 (<i>T</i> =1573 K)	5.4429	–	13.2406	339.70	$R\bar{3}c$

Table 2
Temperature-dependent lattice parameters of LSCF 6482. The rhombohedral distortion was calculated using the relationship: $\tan\omega = 2\sqrt{3}(0.5-x)$ [20]. *Z*=number of formula units per unit cell, *R*_{exp}=expected R-factor, *R*_{wp}=weighted profile R-factor.

	<i>T</i> /K	<i>a</i> /Å	<i>c</i> /Å	<i>V</i> /Å ³	<i>VZ</i> ⁻¹ /Å ³	<i>x</i> (O)	ω /°	<i>R</i> _{exp} /%	<i>R</i> _{wp} /%
Rhombohedral phase R3c <i>Z</i> =6	303	5.443	13.241	339.70	56.62	0.533	–6.6	3.34	4.13
	373	5.448	13.264	340.90	56.82	0.531	–6.1	3.29	4.03
	473	5.455	13.300	342.73	57.12	0.527	–5.3	3.24	4.02
	573	5.462	13.337	344.59	57.43	0.525	–4.9	3.22	3.91
	673	5.470	13.378	346.70	57.78	0.515	–2.9	3.19	4
Cubic phase $Pm\bar{3}m$ <i>Z</i> =1	773	3.875	–	58.17	–	0.5	–	3.17	4.07
	873	3.886	–	58.68	–	0.5	–	3.15	3.99
	973	3.899	–	59.26	–	0.5	–	3.13	3.88
	1073	3.912	–	59.88	–	0.5	–	3.12	3.83
	1173	3.926	–	60.53	–	0.5	–	3.1	3.78
	1273	3.941	–	61.21	–	0.5	–	3.09	3.68

with 800 mesh emery paper to obtain a uniform surface area. The membranes were sealed on an alumina tube using a gold cermet (Heraeus). The feed side was fed with synthetic air (20 vol% O₂/80 vol% N₂) at a rate of 150 mL min⁻¹, whilst Ne (1.0 mL min⁻¹, 99.995%) and He (29.0 mL min⁻¹, 99.995%) or CO₂ (29.0 mL min⁻¹, 99.995%) were applied to the sweep side. An online-coupled Agilent 7890 gas chromatograph with a Carboxen 1000 column was employed to analyze the gas mixture. Using neon as an internal standard, the absolute flux rate was calculated. By measuring the N₂ concentration, the total O₂ leakage was calculated and subtracted from the total O₂ flux.

2.4. Scanning electron microscopy

Field-emission scanning electron microscopy (FE-SEM) imaging was performed on a JEOL JSM-6700F field-emission instrument at low excitation voltage of 2 kV. For backscattered-electron channeling contrast imaging at higher excitation voltages, the samples were vibrational-polished to preserve crystallinity up to the very surface. An energy-dispersive X-ray spectrometer (EDXS), Oxford Instruments INCA-300, with an ultra-thin window was used for the elemental analysis at excitation voltage of 20 kV.

2.5. Transmission electron microscopy

Transmission electron microscopy (TEM) investigations were made at 200 kV on a JEOL JEM-2100F-UHR field-emission instrument ($C_s=0.5$ mm, $C_c=1.2$ mm). The microscope was operated in bright-field mode and as well as a scanning TEM (STEM) in high-angle annular dark-field (HAADF) mode including electron energy-loss spectroscopy (EELS) and electron-loss near-edge structures (ELNES) and in selected area electron diffraction (SAED) mode. An energy-dispersive X-ray spectrometer (EDXS), Oxford Instruments INCA-200, was used for the elemental analysis at excitation voltage of 200 kV. The preparation method of the TEM specimen is described in detail elsewhere [6].

3. Results and discussion

3.1. Characterization of powders

As seen in Fig. 1 all samples are single-phase materials. The La_{1-x}Sr_xCo_{0.8}Fe_{0.2}O₃ ($x=1, 0.8, 0.6$) powders exhibit the cubic perovskite structure (s.g. $Pm\bar{3}m$ 221), whereas LSCF 6482 exhibits rhombohedral structure at room temperature (s.g. $R\bar{3}c$ 167). The obtained unit cell parameters, presented in Table 1, are in good accordance with literature data on SCF [15], LSCF 4682 [16], and LSCF 6482 [17]. The decrease of the cell parameters with increasing lanthanum content is consistent with the decrease of the average A-site cation radius (Sr²⁺ (144 pm) is partly replaced by La³⁺ (136 pm)) [18]. The Goldschmidt tolerance factor of SCF is close to unity, which proposes cubic perovskite structure [19]. With increasing lanthanum content, the Goldschmidt tolerance factor decreases which may explain the shift to rhombohedral structure for the end member of our study LSCF 6482. The rhombohedral distortion was estimated to be $\omega=-6.6^\circ$ at room temperature (Table 2). It was calculated from the x coordinate of the displaced oxygen atom as obtained by XRD data calculated by the Rietveld method using the following relationship: $\tan\omega=2\sqrt{3}(0.5-x)$ [20]. The tilt around the c -axis could be positive (clockwise) or negative (anti-clockwise) whether the displacement of the oxygen is below 0.5 or above. The oxygen in the ideal cubic non-distorted perovskite structure is located at the highly symmetric crystallographic Wyckoff position 3d (0.5, 0, 0).

3.2. Membrane microstructure

The optimum sintering temperature for each membrane composition was found by several experiments at different temperatures. The effect of even small deviations from the optimum sintering temperature can have a huge impact on the microstructure. As an example, the surface of the LSCF 2882 membrane sintered at 1373 K for 10 h is shown in Fig. 2a. Because the sintering temperature was too low, no densification was observed, which leads to a large amount of porosity. However, sintering the membrane at 1573 K, which is only 50 K over the found optimum sintering temperature, leads to precipitation of cobalt-enriched perovskite in the grain boundaries as was proven by EDXS analysis (Fig. 2b). The relative elemental distribution of all cations is given in Table 3. The bulk composition of the material changes, which may have a significant influence on the materials properties. The optimum sintering temperatures were

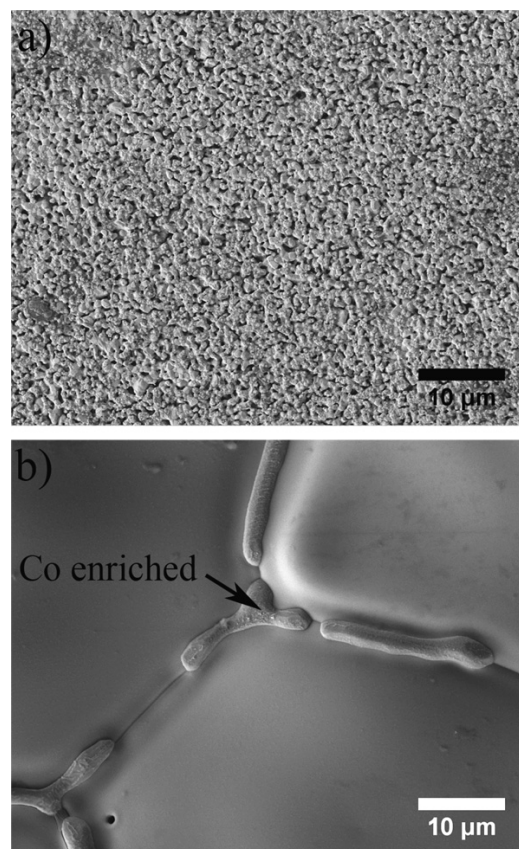


Fig. 2. LSCF 2882 sintered at (a) 1373 K and (b) 1573 K for 10 h in air.

Table 3
Summary of the elemental distribution of La, Sr, Co, and Fe (Σ metal cations=100 at%) obtained by EDXS of the LSCF 2882 membrane at the bulk and the segregated phase at the grain boundary (associated to Fig. 2b).

	Bulk membrane	Grain boundary
La/at%	10	7
Sr/at%	44	29
Co/at%	36	57
Fe/at%	10	7

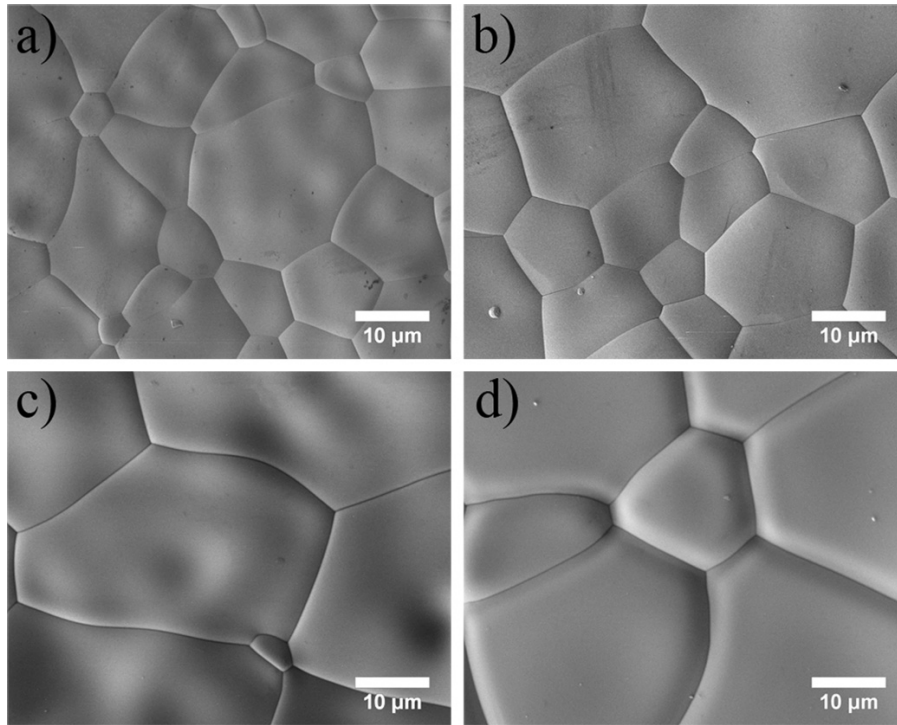


Fig. 3. SE surface view micrographs of the grain structure of (a) SCF (b) LSCF 2882 (c) LSCF 4682 and (d) LSCF 6482. For sintering times refer to Table 1.

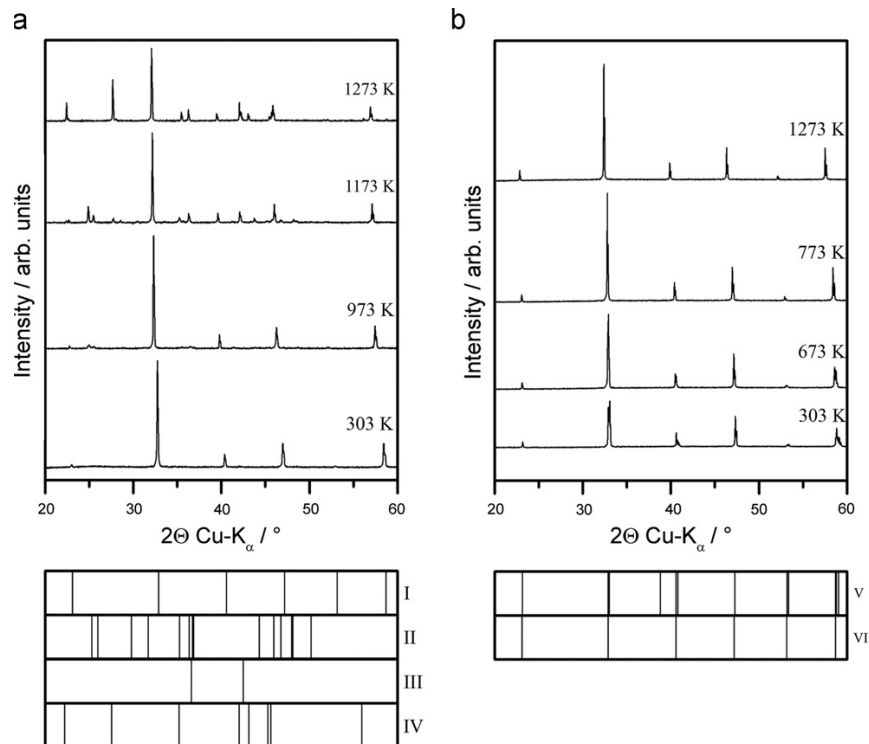


Fig.4. *In-situ* XRD at given temperatures in an atmosphere of 50 vol% CO₂/50 vol% N₂ of (a) SCF and (b) LSCF 6482. The calculated Bragg positions for (I) cubic SCF (ICSD 79022), (II) orthorhombic SrCO₃ (ICSD 15195), (III) cubic CoO (ICSD 28505), (IV) rhombohedral SrCO₃ (ICSD 27446), (V) rhombohedral LSCF 6482 (s. g. $R\bar{3}c$, $a=5.444$ Å, $c=13.241$ Å) and (VI) cubic LSCF 6482 (s.g. $Pm\bar{3}m$, $a=3.875$ Å) are given at the bottom of the figures. The total period including equilibration and measurement times was 60 min at a given temperature interval.

found to be 1473 K for SCF, 1523 K for LSCF 2882, and 1573 K for LSCF 4682 and LSCF 6482. The obtained surface micrographs show neither porosity nor any segregation of secondary phases inside the grain boundaries (Fig. 3). The average grain size was determined using the Image J [21] particle analyzer by measuring the grain area in μm^2 for a series of micrographs for each membrane, and then the grain diameter was estimated by assuming circle-shaped grains. The SCF membrane exhibits the smallest grains with an average grain size of 6.5 μm . With increasing lanthanum content and higher sintering temperature the grain size increases to 11.2 μm for LSCF 2882, 14.9 μm for LSCF 4682 and 22.5 μm for LSCF 6482. With higher sintering temperatures an increase of the average grain size was expected. Comparing the LSCF 4682 and LSCF 6482 membranes which were sintered at the same temperature a significant dependence of the lanthanum concentration on grain growth was found.

3.3. In-situ X-ray diffraction

To get an overview of the stability of the SCF and LSCF systems a series of high-temperature *in-situ* XRD measurements were conducted for each composition in an atmosphere consisting of 50 vol% CO₂ and 50 vol% N₂. Due to thermodynamic considerations presented in an Ellingham diagram it was shown that the SrCO₃ phase is stable until 1357 K at a CO₂ pressure of 5×10^4 Pa before it decomposes into SrO and CO₂ [11]. By doping with lanthanum, which exhibits a much higher resistance towards CO₂ and carbonate formation, it is therefore expected to improve the stability of the solid solutions against CO₂. The challenge is to find the optimum amount of strontium that has to be replaced to greatly enhance tolerance against CO₂ and simultaneously keep the oxygen permeation flux as high as possible.

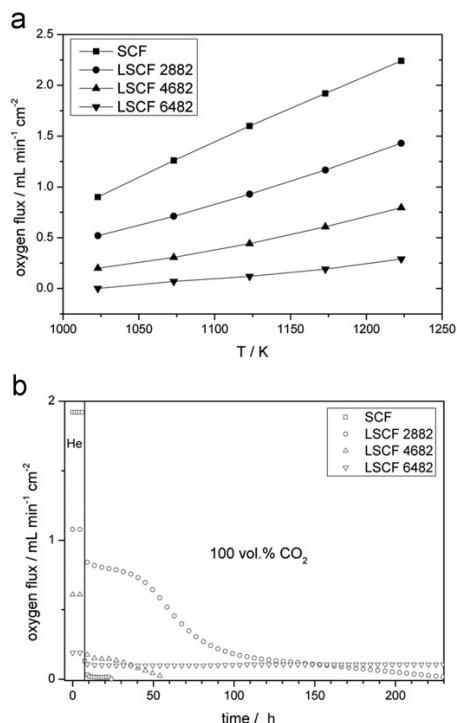


Fig. 5. (a) Oxygen permeation flux of 1 mm thick membranes. Conditions: feed flow rate: 150 mL min⁻¹ synthetic air (80 vol% N₂, 20 vol% O₂). Sweep flow rates He=29 mL min⁻¹, Ne=1 mL min⁻¹ (b) Long-term measurement at 1173 K. Sweep flow rates: CO₂=29 mL min⁻¹, Ne=1 mL min⁻¹.

In Fig. 4a a selection of high temperature *in-situ* XRD of SCF in an atmosphere of 50 vol% CO₂/50 vol% N₂ are shown. The cubic SrCo_{0.8}Fe_{0.2}O_{3-δ} system is stable from room temperature up to 873 K. At 973 K slow decomposition is initialized resulting in a phase mixture of cubic SCF perovskite and orthorhombic strontium carbonate phase. The dwelling time of 60 min was sufficient to facilitate the reaction. At 1073 K cubic cobalt oxide could be detected by XRD data. At 1173 K the orthorhombic SrCO₃ transforms into a rhombohedral modification. This behaviour has been already observed for barium and strontium carbonates. According to Strømme et al. this modification is stable at 1193 K [22], which is in good agreement with our high-temperature data. After quenching in CO₂ atmosphere, the formerly single-phase perovskite was decomposed into cubic SCF perovskite, orthorhombic strontium carbonate and cubic cobalt oxide.

The LSCF 2882 and LSCF 4682 solid solutions showed similar behavior as reported for SCF above. The formation of orthorhombic strontium carbonate begun at 973 K. The latter change into the rhombohedral carbonate modification was also observed. After cooling in 50 vol% CO₂/50 vol% N₂ containing atmosphere the perovskites were decomposed into cubic LSCF perovskite, orthorhombic strontium carbonate and cubic cobalt oxide, which was observed for the related BaCo_{0.4}Fe_{0.4}Zr_{0.2}O_{3-δ} by Efimov et al. [23].

The LSCF 6482 system showed tolerance against CO₂ (Fig. 4b). The perovskite structure is stable at all times on the time scale of the experiment (60 min at each temperature interval of 100 K). At room temperature the perovskite is in a rhombohedral modification. A phase transition from rhombohedral to cubic symmetry could be observed at 673–773 K, which is in agreement with previously reported transition temperatures by Wang et al. [24]. This behaviour was reported for the comparable perovskite system La_{0.6}Ca_{0.4}Co_{0.8}Fe_{0.2}O_{3-δ} (LCCF 6482) as well, but at

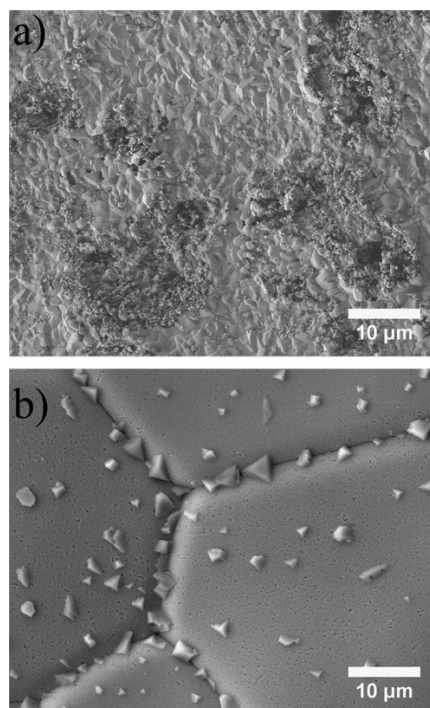


Fig. 6. (a) SCF membrane surface of the sweep side after operation for 24 h in 100 vol% CO₂ and (b) LSCF 6482 membrane surface after operation for over 100 h in 100 vol% CO₂.

slightly higher temperatures by Efimov et al. [11]. At room temperature, the rhombohedral tilt ω was determined to be around -6.6° . With increasing temperature this tilt decreases and turns over into cubic perovskite structure at around 773 K. The transformation took place without a significant change in the cell volume per each formula unit (Table 2). After quenching in 50 vol% CO₂ and 50 vol% N₂ the perovskite conserves the cubic symmetry. This is most probably related to the absence of oxygen during quenching from high temperatures.

3.4. Permeation

Oxygen permeation of all membranes was measured under the same conditions. Fig. 5a shows the oxygen permeation flux in an air helium gradient in the temperature range between 1023 and 1223 K. Before the measurements both sides of each membrane were carefully polished with 800 mesh emery paper to obtain a uniform surface area. It is obvious that the SCF solid solution exhibits the highest oxygen permeation flux with a value of $2.2 \text{ mL min}^{-1} \text{ cm}^{-2}$ at 1223 K. By increasing the lanthanum content to 0.2, 0.4 and 0.6 mol% the oxygen permeation flux decreases significantly to $1.4 \text{ mL min}^{-1} \text{ cm}^{-2}$ for LSCF 2882, $0.8 \text{ mL min}^{-1} \text{ cm}^{-2}$ for LSCF 4682 and $0.3 \text{ mL min}^{-1} \text{ cm}^{-2}$ for LSCF 6482. This observation is explained by point defect behavior. By introduction of trivalent lanthanum atoms in the SCF perovskite structure, the amount of oxygen vacancies is reduced to compensate the higher positive charge. Consequentially, this leads to lower oxygen transport. To analyze the materials as possible CO₂-tolerant materials, the membrane reactor was then switched to 100 vol% CO₂ as sweep gas at constant temperature of 1173 K. As is evident from Fig. 4b the oxygen flux of undoped SCF was strongly decreased and almost stopped after 3 h of operation. This is explained by formation of a dense layer of SrCO₃ and CoO

at the sweep side of the membrane and was proven by *in-situ* XRD and SEM (see Fig. 7 and Section 3.5). The oxygen flux of LSCF 2882 and LSCF 4682 shows a slow decrease with regions of different slopes. After switching to pure CO₂ the oxygen flux decreases slowly and after 40 h of operation for LSCF 2882 and 26 h of operation for LSCF 4682 the flux decreases faster. This is in contrast to SCF membrane. It was expected that the membranes with higher strontium content will lead to a quicker membrane degradation and failure. However, at the first glance contradicting results were obtained because the LSCF 2882 membrane exhibited a longer operation time in CO₂ than the LSCF 4682 membrane. With the addition of small amounts of lanthanum (starting at 0.2 mol%) the oxygen flux is not stopped immediately after switching to CO₂ gas (as observed for SCF) but decreases slowly with time. Since LSCF 2882 exhibited a higher initial oxygen flux (Fig. 5a) due to a higher amount of oxygen vacancies it took a longer time until oxygen permeation broke down completely. Yokokawa et al. described the thermodynamic aspect of the perovskite formation [25]. With increasing lanthanum content the perovskite stabilization energies are increased, which led to relative stabilization of LSCF 2882 and LSCF 4682 compared to the SCF membrane. For the LSCF 6482 composition the perovskite phase may be thermodynamically favored over the carbonate formation, which may explain the good CO₂ tolerance of the material. Furthermore, the process of oxygen transport through a dense membrane is controlled (i) by surface exchange with the gas phase on the sweep side, (ii) by bulk diffusion, and (iii) by surface exchange with the gas phase on the feed side of the membrane [26]. The CO₂ interacts with the membrane by forming carbonates and by adsorption on the surface, which hinders the release of O₂ molecules [27]. Tan et al. observed a correlation between the decreasing overall oxygen permeation flux and the increasing content of CO₂ (0, 20, 50, 70 and 100 vol% CO₂) in the

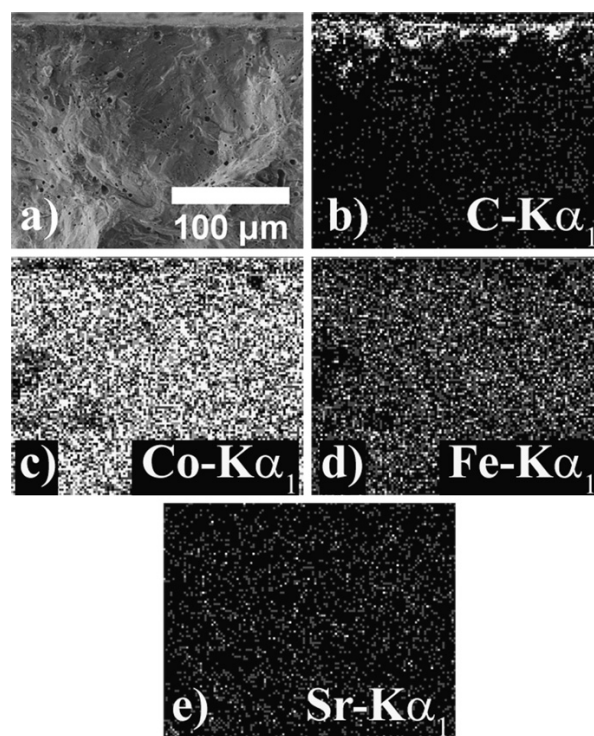


Fig. 7. (a) Fracture surface close to the sweep side of the SCF membrane after operation for 24 h in 100 vol%. CO₂ sweep gas. (b–f) Elemental distribution by EDXS of the area shown in (a).

sweep gas for LSCF 6482 hollow-fiber membranes [12]. They proposed that CO₂ molecules are chemically adsorbed at the membrane surface, thus reducing oxygen partial pressure gradient and surface exchange rates. This was discussed by several groups elsewhere [28–30]. By increasing the lanthanum content the stabilization energy of the perovskite is raised, as expected from the thermodynamic data from the Ellingham diagram [11], which accounts for a higher CO₂ tolerance of the materials. The 1 mm thick LSCF 6482 membrane achieved an oxygen permeation flux of 0.1 mL min⁻¹cm⁻² and was stable in 100 vol% CO₂ atmosphere for the investigated period of over 200 h continuous operation.

3.5. Membranes after operation in CO₂

Fig. 6 shows the SCF and LSCF 6482 membranes after operation in CO₂-containing atmospheres. For these experiments the membranes were not polished to provide a better comparability before and after exposure to CO₂. However, same conditions as in the oxygen permeation measurements were used. It is obvious that the surface of the SCF membrane (Fig. 6a) was changed as compared to the well defined grain structure as obtained before the CO₂ experiment (Fig. 3a). The segregated blooming phase on the surface was found to be cobalt and iron enriched, thus we expect that it is cobalt oxide as proven by XRD analysis in Section 3.3 and small amounts of iron oxide. The dense surface layer was depleted of iron and cobalt. From the presence carbon it could be concluded that it is strontium carbonate, as expected by *in-situ* XRD (Section 3.3). The operation in CO₂ atmosphere led to a severe etching of the membrane surface. The LSCF 6482 membrane, which was operated for over 200 h in CO₂ atmosphere showed no formation of carbonates or etchings on the surface (Fig. 6b). Segregation of small particles at the surface was observed. The EDXS analysis showed no change of composition compared to the bulk membrane material.

The fracture surface close to the sweep side of the SCF membrane after operation for 24 h in pure CO₂ showed an enrichment of carbon in an around 25 μm thick top layer (Fig. 7a and b). Cobalt, iron and strontium were homogeneously distributed. This is in contrast to observation for BSCF from Arnold et al. who found a 40–50 μm thick mixed carbonate and perovskite layer [6]. The thicker layer may be related to higher carbonate decomposition enthalpies (ΔH) for the bigger barium ions [31].

The fracture surface of LSCF 2882 and LSCF 6482 were vibrational polished to preserve crystallinity to the very surface and then investigated using backscattered-electron channeling contrast imaging. The LSCF 6482 showed no phase segregation up to the surface of the membrane (Fig. 8b), which shows the good CO₂ tolerance of the material. In Fig. 8a the sweep side region of LSCF 2882 showed phase segregation as expected by *in-situ* XRD. The elemental content could not be identified by EDXS in the SEM. See below for TEM analysis.

TEM Fig. 9a shows two grains in close contact with an inclusion inside the grain boundary. The obtained SAED patterns for the upper and lower grain exhibited the cubic perovskite structure (Fig. 9b and c). The upper grain is orientated along zone axis [0 0 1] and the lower grain is oriented along zone axis [2 0 1].

Furthermore, the region close to the surface was analyzed by different TEM techniques. The STEM annular dark-field micrograph shows regions with different phase composition, which show up with different contrasts (Fig. 10a). The inset shows a SAED pattern of the considered orthorhombic carbonate phase oriented along zone axis [2 1 1]. Following the *in-situ* XRD analysis it was expected to find different phases of cubic strontium-depleted perovskite, orthorhombic strontium carbonate and cubic cobalt oxide. The analysis of the phase composition was performed in STEM mode by EELS. The

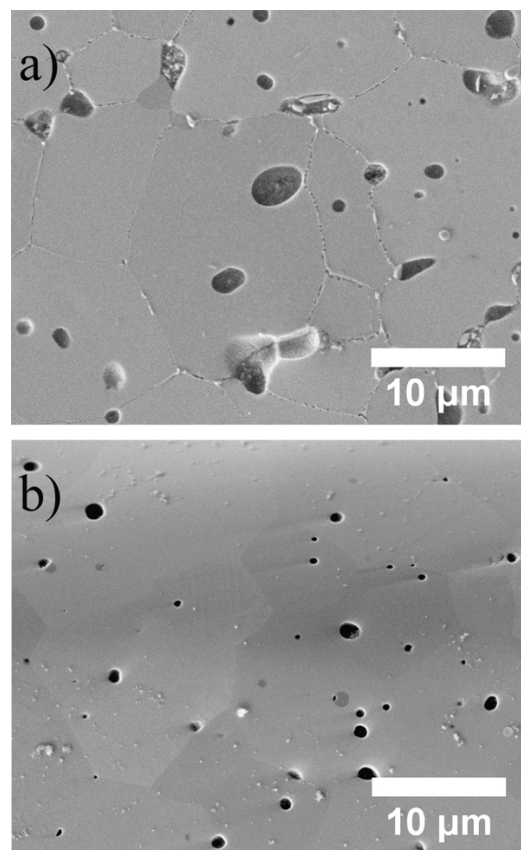


Fig. 8. Channeling contrast images of the membrane cross-section close to sweep side of (a) LSCF 2882 and (b) LSCF 6482 membranes (white residues are Al₂O₃ particles from polishing process, black pinholes are due to closed porosity).

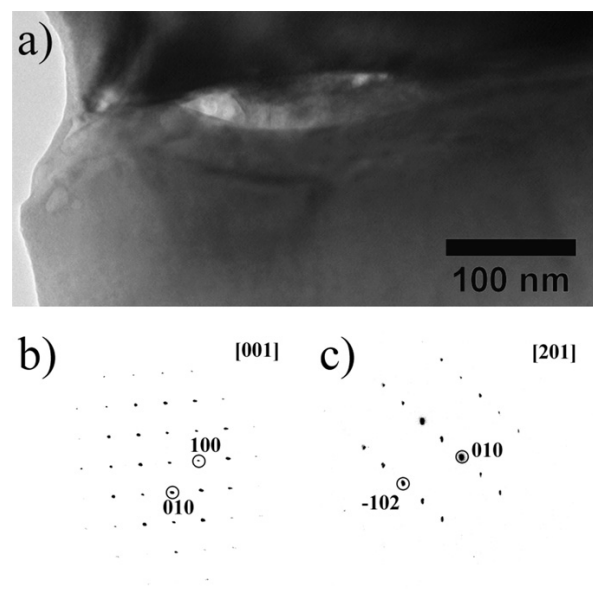


Fig. 9. CO₂-exposed sweep side of LSCF 2882 membrane after 200 h of operation. (a) Bright-field TEM of two grains in close contact. (b) SAED pattern of the upper grain. (c) SAED pattern of the lower grain.

EEL spectrum in Fig. 10b in the energy-loss range of 260–340 eV was obtained from carbonate areas in Fig. 10a. The energies of 272 and 282 eV correspond to the Sr–M_{2,3} edges and the energies of 290 and 300 eV correspond to C–K edges, which are typical for carbonates [32,33], indicating the transition of carbon 1s electrons into higher unoccupied levels, which correspond to the carbonate C=O double and C–O single bonds [34,35]. In the energy-loss range of 500–900 eV the EEL spectrum of the perovskite exhibits peaks of Fe–L_{2,3} (710 and 723 eV [36]), Co–L_{2,3} (782 and 796 eV) and La–M_{4,5} (837 and 854 eV). These elements were absent in the spectra of the carbonate phase (Fig. 10c). The O–K ELNES shown in Fig. 10d is very sensitive to the local environment of the oxygen atoms. The carbonate spectrum exhibits a narrow peak at 533 eV followed by the most intense peak at 539 and a smaller peak at 544 eV. This is in accordance with literature about SrCO₃ [34]. The O–K ELNES for the perovskite is slightly different. The leading peak at 530 eV corresponds to hybridization of the cobalt and iron d_{xy}, d_{xz} and d_{yz} orbitals with unoccupied oxygen 2p states via 2p–3d interactions, as observed for complex oxides [37]. The following peaks at 532 and 538 eV may be attributed to additional interactions with the ns and np states of lanthanum and strontium. The small peak at 541 eV is related to excitations of O 2p electrons into unoccupied Co, Fe d_{z²} and d_{x²-y²} orbitals [6]. Furthermore, cobalt oxide was detected in the near-surface region (spectra not shown). The carbonate areas are very sensitive to the high-energetic electron beam and holes were drilled easily into them. Beam irradiation causes the decomposition of SrCO₃ into SrO and CO₂, which lead to a change of the O–K edges [34]. The perovskite grains were not damaged by the electron beam in the typical time scale of an EELS experiment (several minutes).

4. Conclusions

The series of La_{1-x}Sr_xCo_{0.8}Fe_{0.2}O_{3-δ} (x=1, 0.8, 0.6, 0.4) was successfully synthesised by a sol-gel method. All powders and membranes exhibit cubic perovskite structure, except the rhombohedral LSCF 6482, which adopts cubic perovskite structure at temperatures above 673 K. *In-situ* XRD measurements and long-term oxygen permeation measurements in CO₂-containing atmosphere reveal the high tolerance of LSCF 6482 towards CO₂. Oxygen permeation experiments in an air/helium gradient showed that with increasing lanthanum content the oxygen permeation flux decreases. Microstructure analysis of the membranes after CO₂ operation showed that the carbonate preferentially forms a dense layer at the carbon dioxide exposed sweep side of the membranes.

Acknowledgements

The authors greatly acknowledge financial support from the Chinese-German Centre for Science (GZ676) and the Deutsche Forschungsgemeinschaft (FE 928/4-1) and fruitful discussions with Prof. Jürgen Caro.

References

- [1] International Energy Agency, World energy outlook 2011, OECD, Paris, 2011.
- [2] R. Bredesen, K. Jordal, O. Bolland, High-temperature membranes in power generation with CO₂ capture, Chem. Eng. Process 43 (2004) 1129–1158.

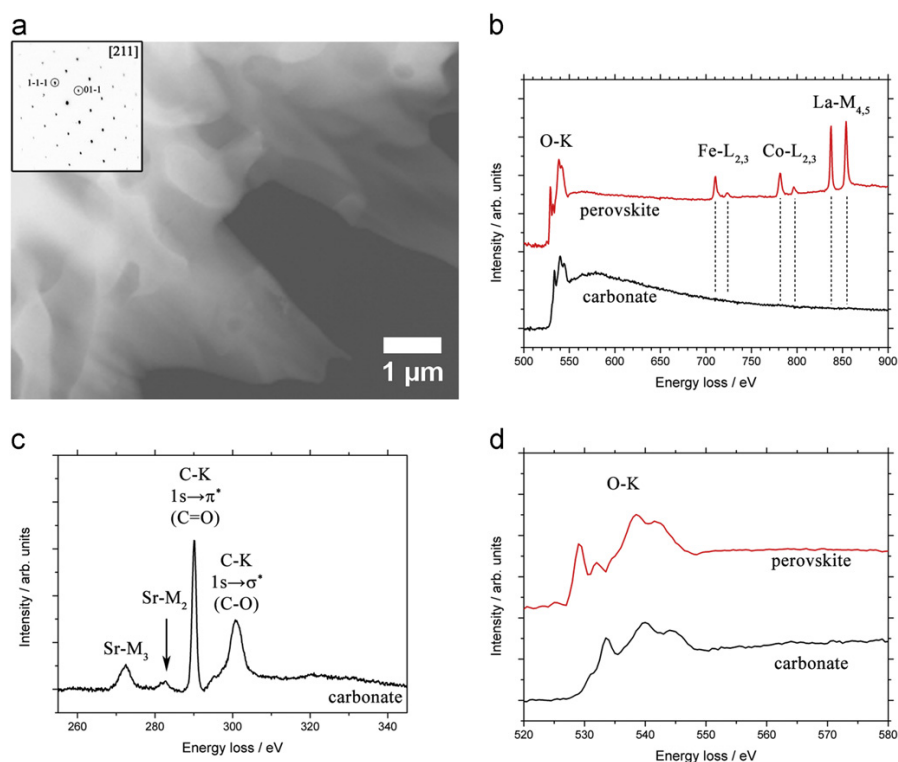


Fig. 10. (a) STEM-HAADF micrograph of the sweep-side surface of a LSCF 2882 membrane after 200 h of operation in 100 vol% CO₂. Inset shows the SAED pattern of the carbonate phase (b) EEL spectrum in the energy-loss range from 500 to 900 eV of the perovskite and carbonate phase with O–K, Fe–L, Co–L and La–M ionization edges. (c) EEL spectrum in the energy-loss range from 260 to 340 eV of the carbonate phase with Sr–M and C–K ionization edges. (d) Characteristic O–K ELNES of the perovskite and carbonate phase.

- [3] A.R. Smith, J. Klosek, A review of air separation technologies and their integration with energy conversion processes, *Fuel Process Technol.* 70 (2001) 115–134.
- [4] H. Stadler, F. Beggel, M. Habermehl, B. Persigehl, R. Kneer, M. Modigell, P. Jeschke, Oxyfuel coal combustion by efficient integration of oxygen transport membranes, *Int. J. Greenhouse Gas Control* 5 (2011) 7–15.
- [5] X. Tan, K. Li, Oxygen production using dense ceramic hollow fiber membrane modules with different operating modes, *AIChE J.* 53 (2007) 838–845.
- [6] M. Arnold, H. Wang, A. Feldhoff, Influence of CO₂ on the oxygen permeation performance and the microstructure of perovskite-type (Ba_{0.5}Sr_{0.5})(Co_{0.8}Fe_{0.2})O_{3-δ} membranes, *J. Membr. Sci.* 293 (2007) 44–52.
- [7] T. Klände, K. Efimov, S. Cusenza, K.D. Becker, A. Feldhoff, Effect of doping, microstructure, and CO₂ on La₂NiO_{4+δ}-based oxygen-transporting materials, *J. Solid State Chem.* 184 (2011) 3310–3318.
- [8] H. Luo, K. Efimov, H. Jiang, A. Feldhoff, H. Wang, J. Caro, CO₂-stable and cobalt-free dual phase membrane for oxygen separation, *Angew. Chem. Int. Ed.* 50 (2011) 759–763.
- [9] W. Chen, C. Chen, L. Winnubst, Ta-doped SrCo_{0.8}Fe_{0.2}O_{3-δ} membranes: phase stability and oxygen permeation in CO₂ atmosphere, *Solid State Ionics* 196 (2011) 30–33.
- [10] Q. Zeng, Y. Zuo, C. Fan, C. Chen, CO₂-tolerant oxygen separation membranes targeting CO₂ capture application, *J. Membr. Sci.* 335 (2009) 140–144.
- [11] K. Efimov, T. Klände, N. Juditzki, A. Feldhoff, Ca-containing CO₂-tolerant perovskite materials for oxygen separation, *J. Membr. Sci.* 389 (2012) 205–215.
- [12] X. Tan, N. Liu, B. Meng, J. Sunarso, K. Zhang, S. Liu, Oxygen permeation of La_{0.6}Sr_{0.4}Co_{0.8}Fe_{0.2}O₃ hollow fiber membranes with highly concentrated CO₂ exposure, *J. Membr. Sci.* 389 (2012) 216–222.
- [13] J. Martynczuk, M. Arnold, A. Feldhoff, Influence of grain size on the oxygen permeation performance of perovskite-type (Ba_{0.5}Sr_{0.5})(Co_{0.8}Zn_{0.2})O_{3-δ} membranes, *J. Membr. Sci.* 322 (2008) 375–382.
- [14] H. Wang, C. Tablet, A. Feldhoff, J. Caro, Investigation of phase structure, sintering, and permeability of perovskite-type Ba_{0.5}Sr_{0.5}Co_{0.8}Fe_{0.2}O_{3-δ} membranes, *J. Membr. Sci.* 262 (2005) 20–26.
- [15] W.T.A. Harrison, T.H. Lee, Y.L. Yang, D.P. Scarfe, L.M. Liu, A.J. Jacobson, A neutron diffraction study of two strontium cobalt iron oxides, *Mater. Res. Bull.* 30 (1995) 621–630.
- [16] T.V. AksenoVA, M.V. Anan'ev, L.Y. Gavrilova, V.A. Cherepanov, Phase equilibria and crystal structures of solid solutions in the system LaCoO₃–SrCoO_{2.5}–SrFeO₃–LaFeO₃, *Inorg. Mater.* 43 (2007) 296–300.
- [17] J.E. ten Elshof, J. Boeijisma, Powder diffraction of La_{1-x}Co_{0.8}Fe_{0.2}O₃ (A = Sr, Ba), *Powder Diff.* 11 (1996) 28–30.
- [18] R.D. Shannon, Revised effective ionic radii and systematic studies of interatomic distances in halides and chalcogenides, *Acta Crystallogr., Sect. A: Found. Crystallogr.* 32 (1976) 751–767.
- [19] V.M. Goldschmidt, Die Gesetze der Kristallchemie, *Naturwiss* 14 (1926) 477–485.
- [20] R.H. Mitchell, *Perovskites: Modern and Ancient*, Almaz Press Inc, Ontario, Canada, 2002.
- [21] M.D. Abramoff, P.J. Magelhaes, S.J. Ram, Image processing with image J, *Biophotonics Int.* 11 (2004) 36–42.
- [22] K.O. Strømme, On the crystal structures of the high-temperature forms of strontium and barium carbonate and structurally related compounds, *Acta Chem. Scand. A* 29 (1975) 105–110.
- [23] K. Efimov, O. Czuprat, A. Feldhoff, *In-situ* X-ray diffraction study of carbonate formation and decomposition in perovskite-type BCFZ, *J. Solid State Chem.* 184 (2011) 1085–1089.
- [24] S. Wang, M. Katsuki, M. Dokiya, T. Hashimoto, High temperature properties of La_{0.6}Sr_{0.4}Co_{0.8}Fe_{0.2}O_{3-δ} phase structure and electrical conductivity, *Solid State Ionics* 159 (2003) 71–78.
- [25] H. Yokokawa, N. Sakai, T. Kawada, M. Dokiya, Thermodynamic stabilities of perovskite oxides for electrodes and other electrochemical materials, *Solid State Ionics* 52 (1992) 43–56.
- [26] H.J.M. Bouwmeester, H. Kruidhof, A.J. Burggraf, Importance of the surface exchange kinetics as rate limiting step in oxygen permeation through mixed-conducting oxides, *Solid State Ionics* 72 (1994) 185–194.
- [27] J.E. ten Elshof, H.J.M. Bouwmeester, H. Verweij, Oxygen transport through La_{1-x}Sr_xFeO_{3-δ} membranes. II. Permeation in air/CO₂ gradients, *Solid State Ionics* 89 (1996) 81–92.
- [28] J.A. Lane, J.A. Kilner, Oxygen surface exchange on gadolinia doped ceria, *Solid State Ionics* 136–137 (2000) 927–932.
- [29] K. Yashiro, S. Onuma, A. Kaimai, Y. Nigara, T. Kawada, J. Mizusaki, K. Kawamura, T. Horita, H. Yokokawa, Mass transport properties of Ce_{0.9}Gd_{0.1}O_{2-δ} at the surface and in the bulk, *Solid State Ionics* 152–153 (2002) 469–476.
- [30] I.V. Khromushin, T.I. AksenoVA, Z.R. Zhotabaev, Mechanism of gas–solid exchange processes for some perovskites, *Solid State Ionics* 162–163 (2003) 37–40.
- [31] K.H. Stern, E.L. Weise, High temperature properties and decomposition of inorganic salts, Part 2: Carbonates, *NSRDS-NBS* 30 (1969) 1–27.
- [32] F. Hofer, P. Golob, New examples for near-edge fine structures in electron energy loss spectroscopy, *Ultramicroscopy* 21 (1987) 379–384.
- [33] M. Cai, S. Liu, K. Efimov, J. Caro, A. Feldhoff, H. Wang, Preparation and hydrogen permeation of BaCe_{0.95}Nd_{0.05}O_{3-δ} membranes, *J. Membr. Sci.* 343 (2009) 90–96.
- [34] J.L. Mansot, V. Golabkan, L. Romana, T. Césaire, Chemical and physical characterization by EELS of strontium hexanoate reverse micelles and strontium carbonate nanophase produced during tribological experiments, *J. Microsc.* 210 (2003) 110–118.
- [35] J. Martynczuk, M. Arnold, H. Wang, J. Caro, A. Feldhoff, How (Ba_{0.5}Sr_{0.5})(Fe_{0.8}Zn_{0.2})O_{3-δ} and (Ba_{0.5}Sr_{0.5})(Co_{0.8}Fe_{0.2})O_{3-δ} perovskites form via an EDTA/citric acid complexing method, *Adv. Mater.* 19 (2007) 2134–2140.
- [36] A. Feldhoff, J. Martynczuk, M. Arnold, M. Myndyk, I. Bergmann, V. Šepelák, W. Gruner, U. Vogt, A. Hähnel, J. Woltersdorf, Spin-state transition of iron in (Ba_{0.5}Sr_{0.5})(Fe_{0.8}Zn_{0.2})O_{3-δ} perovskite, *J. Solid State Chem.* 182 (2009) 2961–2971.
- [37] A.S. Sefat, G. Amow, M. Wu, G.A. Botton, J.E. Greedan, High-resolution EELS study of the vacancy-doped metal/insulator system, Nd_{1-x}TiO₃, x = 0 to 0.33, *J. Solid State Chem.* 178 (2005) 1008–1016.

3.3 Ca-containing CO₂-tolerant perovskite materials for oxygen separation

Konstantin Efimov, Tobias Klande, Nadine Juditzki, and Armin Feldhoff

Journal of Membrane Science **389** (2011) 205-215



Contents lists available at SciVerse ScienceDirect

Journal of Membrane Science

journal homepage: www.elsevier.com/locate/memsciCa-containing CO₂-tolerant perovskite materials for oxygen separation

Konstantin Efimov*, Tobias Klande, Nadine Juditzki, Armin Feldhoff

Institute of Physical Chemistry and Electrochemistry, Leibniz Universität, Hannover, Callinstr. 3-3A, D-30167 Hannover, Germany

ARTICLE INFO

Article history:

Received 3 June 2011

Received in revised form 3 September 2011

Accepted 22 October 2011

Available online 29 October 2011

Keywords:

Mixed ionic-electronic conductor

Perovskite, CO₂-stability

Asymmetric membrane

In-situ X-ray diffraction

Transmission electron microscopy

ABSTRACT

Perovskites (La_{1-x}Ca_x)FeO_{3-δ} and (La_{1-x}Ca_x)(Co_{0.8}Fe_{0.2})O_{3-δ} with varying La and Ca contents ($x = 0.4-0.6$) were designed by sol-gel route as model membrane materials to be an alternative to Ba- and Sr-based systems for operation in the presence of CO₂. It was found that only the first members of the systems with $x = 0.4$ consisted of almost pure perovskite phases. The materials containing more Ca ($x = 0.5-0.6$) exhibited a considerable amount of bi-phase material, such as brownmillerite and/or spinel, after calcination at 1223 K. The orthorhombically distorted (La_{0.6}Ca_{0.4})FeO_{3-δ} and rhombohedrally distorted (La_{0.6}Ca_{0.4})(Co_{0.8}Fe_{0.2})O_{3-δ} perovskites showed relatively high oxygen permeation fluxes at 1223 K of 0.26 cm³ min⁻¹ cm⁻² and 0.43 cm³ min⁻¹ cm⁻², respectively. The oxygen-ionic conductivity of the materials was improved by about 50% via an asymmetric configuration using a porous support and an approximately 10-μm thick dense layer with the same chemical composition. *In situ* XRD in an atmosphere containing 50 vol.% CO₂ and long-term oxygen permeation experiments using pure CO₂ as the sweep gas revealed a high tolerance of Ca-based materials toward CO₂. Thus, we suggest that Ca-containing perovskite can be considered promising membrane materials if operation in the presence of CO₂ is required.

© 2011 Elsevier B.V. All rights reserved.

1. Introduction

Over the last two decades, mixed oxygen ionic and electronic conductors (MIECs) have attracted a lot of attention. Because of their very high oxygen-ionic transport rates over a wide temperature range, the Ba- and Sr-containing perovskites [e.g., (Ba_{1-x}Sr_x)(Co_{0.8}Fe_{0.2})O_{3-δ} and (La_{1-x}Sr_x)(Co_{1-y}Fe_y)O_{3-δ}] rank among the state-of-the-art MIEC materials [1–3]. However, the wide practical employment of these materials is hindered by significant problems, like poor chemical and thermomechanical stability [4–10]. In particular, the degradation of these materials in the presence of CO₂, with the formation of carbonates, [11–16] handicaps their application in important processes, such as cathode materials in solid-oxide fuel cells (SOFCs) operated at intermediate temperatures, in oxyfuel processes or in hydrocarbon partial oxidations, where some CO₂ is formed as a bi-product of an undesired deeper oxidation [17–19].

Tolerance against CO₂ can be achieved by the complete replacement of Ba and Sr in the A lattice site of the perovskite structure by rare-earth elements, like La. Unfortunately, this leads to a dramatic loss in the oxygen-ionic conductivity of the materials, as caused by a reduced lattice parameter, which induces lower oxygen mobility, and by a lower amount of mobile oxygen vacancies, which

results from a higher oxidation state of the rare-earth cation [20]. To increase the oxygen deficiency in the perovskite lattice, a Ca cation with the stable valence state of 2+ can be regarded as a potential dopant.

The stability of alkaline earth-containing materials in the presence of CO₂ can be evaluated using the Ellingham diagram shown in Fig. 1. This figure demonstrates the thermodynamic stability of carbonates at a given CO₂ partial pressure and temperature. The compact lines with positive slope in the diagram represent chemical potentials of CO₂ during the decomposition of corresponding carbonate, which is equal to negative value of free enthalpy of decomposition reaction, as calculated with thermodynamic data using free enthalpy of formation of corresponding educts and products or determined experimentally [21–24]. The dashed lines give the chemical potential of CO₂ at different partial pressures. In general, if the CO₂ chemical potential of the carbonate decomposition reaction at the present temperature is higher than at the corresponding partial pressure, the carbonates are thermodynamically unstable. As can be seen in the Ellingham diagram, CaCO₃ is significantly less stable than BaCO₃ and SrCO₃. The relatively small ionic radius of 135 pm of the Ca²⁺ cation, as compared with Ba²⁺ ($r = 160$ pm) Sr²⁺ and ($r = 144$ pm) cations, leads to a decline of the crystal lattice energy of carbonate and can be considered a reason for the lower stability of CaCO₃ [25,26]. Note, the Ellingham diagram gives only a rough guide to estimate the possible tolerance of Ca-containing perovskite materials against CO₂ because the stabilization energy of perovskite may also play an important role

* Corresponding author. Tel.: +49 511 762 2943.

E-mail address: konstantin.efimov@pci.uni-hannover.de (K. Efimov).

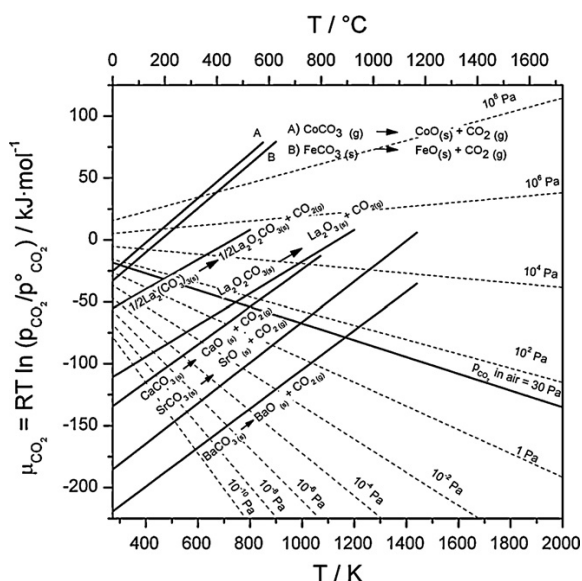


Fig. 1. Ellingham diagram for the decomposition of carbonates under different partial pressures. Chemical potential of CO₂ above FeCO₃, CoCO₃, CaCO₃, La₂O₂CO₃, SrCO₃, and BaCO₃ have been calculated from thermodynamic data [21–23]. The chemical potential of La₂(CO₃)₃ has been determined experimentally [24]. The dashed lines represent the chemical potential of CO₂ in the surrounding atmosphere for different partial pressures. $p^{\circ}(\text{CO}_2) = 101.3 \text{ kPa}$ refers to standard conditions.

[27,28]. Nevertheless, the desirable stability of Ca-containing materials in the presence of CO₂ can be expected from thermodynamic considerations and was reported for Ca(Ti_{1-x}Fe_x)O_{3-δ} [29].

Teraoka et al. have already reported a high oxygen permeation flux through the perovskite membrane with the composition (La_{0.6}Ca_{0.4})(Co_{0.8}Fe_{0.2})O_{3-δ} in 1988 [30]. Using a higher Ca content, Stevenson et al. have obtained a very high electrical conductivity using (La_{0.4}Ca_{0.6})(Co_{0.8}Fe_{0.2})O_{3-δ} perovskite in 1996 [31]. Since then, however, Ca-containing materials have gained little notice as promising MIEC materials [32–34]. One reason for this lack of attention may be the formation of secondary phases, like brownmillerite and/or the Grenier phase, during the preparation and operation of the perovskites. It has also been reported that this problem appears more pronounced with rising Ca content in the materials [31,35].

Recently, the group around Teraoka has developed asymmetrically structured membranes consisting of a porous support and thin dense layer and having the chemical composition (La_{0.6}Ca_{0.4})CoO_{3-δ} [36]. The main advantage of self-supported membranes is a result of the good chemical compatibility and thermomechanical stability of the materials. The oxygen permeation flux of the (La_{0.6}Ca_{0.4})CoO_{3-δ} was enhanced by the asymmetric configuration up to 300%, which has yielded a value of 1.66 cm³ min⁻¹ cm⁻² [37]. This feature draws a spotlight on the Ca-containing perovskites as promising candidate MIEC materials.

In the present work, model perovskite systems (La_{1-x}Ca_x)FeO_{3-δ} and (La_{1-x}Ca_x)(Co_{0.8}Fe_{0.2})O_{3-δ} ($x = 0.4–0.6$) were examined regarding phase purity and stability in the presence of CO₂. Furthermore, bulk and asymmetrically structured membranes were prepared and investigated for their oxygen-ionic conducting properties.

2. Experimental

2.1. Powder preparation

A sol-gel route using metal nitrates, citric acid, and ethylenediaminetetraacetic acid (EDTA) was applied to prepare the

La_{1-x}Ca_xFeO_{3-δ} and La_{1-x}Ca_xCo_{0.8}Fe_{0.2}O_{3-δ} ($x = 0.4–0.6$) materials as described elsewhere [38,39]. Given amounts of La(NO₃)₃ and Ni(NO₃)₂ were dissolved in water followed by the addition of EDTA as an organic ligand and citric acid as a network former. The molar ratio of metal nitrates:EDTA: citric acid was equal to 2:1:1.5. The pH value of the solution was adjusted to the range of 7–9 with NH₃·H₂O. The transparent reaction solution was then heated at 423 K under constant stirring for several hours to obtain a gel. The gel was pre-calcined in the temperature range of 573–673 K in order to remove organic compounds, followed by calcination for 10 h at 1223 K in air.

2.2. Preparation of bulk and asymmetric membranes

To obtain the bulk membranes, the powders were uniaxially pressed under 140–150 kN for 20 min into green bodies. The pellets were then calcined for 10 h at 1423–1523 K with a heating and cooling rate of 3 K/min.

The asymmetric membranes were manufactured as follows: the as synthesized powders were ground in a mortar with 20 wt.% of a pore former block co-polymer Pluronic F 127 (BASF). The mixture was then press-formed into pellets and fired at 1423 K for 2 h. The dense layers were obtained by spin coating of porous supports with 3 cm³ slurry (15 wt.% powder in ethanol), drying at room temperature for 5 h following by calcination at 1423–1523 K for 2–5 h.

2.3. Characterizations of materials

The phase structure of the powders and membranes were studied by X-ray diffraction (XRD, D8 Advance, Bruker-AXS, with Cu Kα_{1,2} radiation). Data sets were recorded in a step-scan mode in the 2θ range of 20–60° with intervals of 0.02°. *In situ* XRD tests were conducted in a high-temperature cell HTK 1200N (Anton-Paar) between room temperature and 1273 K. Tests in the atmosphere containing 50 vol.% CO₂/50 vol.% air and 50 vol.% CO₂/50 vol.% N₂ were carried out with heating and cooling rate of 12 °C/min. At each temperature step, the temperature was held for 30 min before diffraction data collection.

Scanning electron microscopy (SEM) imaging was performed on a JEOL JSM-6700F field-emission instrument at a low excitation voltage of 2 kV. An energy-dispersive X-ray spectrometer (EDXS), Oxford Instruments INCA-300, with an ultrathin window was used for the elemental analysis at an excitation voltage of 15 kV.

Transmission electron microscopy (TEM) investigations were made at 200 kV on a JEOL JEM-2100F-UHR field-emission instrument (C_s = 0.5 mm, C_c = 1.2 mm) equipped with a light-element EDXS detector (INCA 200 TEM, Oxford Instruments). The microscope was operated as scanning TEM (STEM) in high-angle annular dark-field (HAADF) mode. An energy filter of the type Gatan GIF 2001 was employed to acquire electron energy-loss spectra (EELS).

Specimens for electron microscopy were prepared as follow. First, the permeate side was glued with a polycrystalline corundum block using epoxy followed by cutting of membrane into 1 mm × 1 mm × 2 mm pieces. The protected membrane pieces were polished on polymer-embedded diamond lapping films to approximately 0.01 mm × 1 mm × 2 mm (Allied High Tech, Multiprep). Electron transparency for TEM was achieved by Ar⁺ ion sputtering at 3 kV (Gatan, model 691 PIPS, precision ion polishing system) under shallow incident angles of 10°, 6°, and 4°.

Oxygen permeation was measured in a high-temperature permeation cell according to the method described elsewhere [40,41]. Before measurements, the bulk membranes were polished with 30 μm polymer-embedded diamond lapping films. Air was fed at a

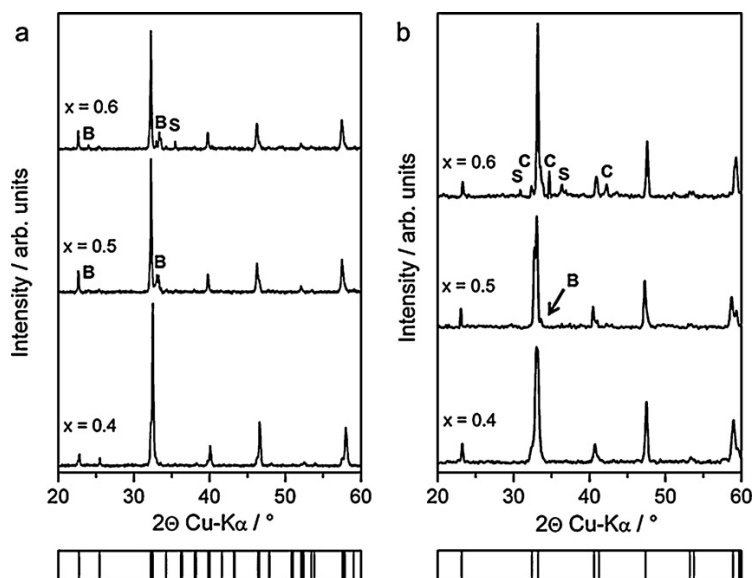


Fig. 2. (a) XRD pattern of $\text{La}_{1-x}\text{Ca}_x\text{FeO}_{3-\delta}$ ($x=0.4-0.6$) powders. The calculated Bragg positions for orthorhombic perovskite (space group $Pnma$; $a=5.496\text{ \AA}$, $b=7.772\text{ \AA}$ and $c=5.566\text{ \AA}$) are marked with ticks at the bottom of the figure. The intensities of non-perovskite phases are marked in the figure with B for $\text{Ca}_2\text{Fe}_2\text{O}_5$ brownmillerite and S for Ca_2FeO_4 spinel. (b) XRD pattern of $\text{La}_{1-x}\text{Ca}_x\text{Co}_{0.8}\text{Fe}_{0.2}\text{O}_{3-\delta}$ ($x=0.4-0.6$) powders. The calculated Bragg positions for rhombohedral perovskite (space group $R\bar{3}c$, $a=5.391\text{ \AA}$, $b=13.263\text{ \AA}$) are marked with ticks at the bottom. The intensity of impurity phases are marked in the figure with B for $\text{Ca}_2\text{Co}_{2-y}\text{Fe}_y\text{O}_5$, S for Co_3O_4 spinel and C for $\text{Ca}_3\text{Co}_{2-z}\text{Fe}_z\text{O}_6$.

rate of $150\text{ cm}^3\text{ min}^{-1}$ to the feed side; He or CO_2 ($29.0\text{ cm}^3\text{ min}^{-1}$) and Ne ($1.0\text{ cm}^3\text{ min}^{-1}$) gases were fed to the sweep side. The effluents were analyzed by gas chromatography on an Agilent 6890 instrument equipped with a Carboxen 1000 column. The gas concentrations in the effluent stream were calculated from a gas chromatograph calibration. The absolute flux rate of the effluents was determined by using neon as an internal standard. The relative leakage of O_2 , which was evaluated by measuring the amount of N_2 in the effluent stream, was subtracted in the calculation of the oxygen permeation flux.

3. Results and discussion

3.1. Characterization of powders

The Goldschmidt tolerance factors for perovskite systems ($\text{La}_{1-x}\text{Ca}_x\text{FeO}_{3-\delta}$ and $(\text{La}_{1-x}\text{Ca}_x)(\text{Co}_{0.8}\text{Fe}_{0.2})\text{O}_{3-\delta}$ ($x=0.4-0.6$) lie close to unity ($t \leq 1$), even for various ratios of $\text{Fe}^{4+}/\text{Fe}^{3+}$ and $\text{Co}^{4+}/\text{Co}^{3+}/\text{Co}^{2+}$ cations [25,42]. Accordingly, it may be expected that both systems crystallize in the perovskite structure. However, as can be seen in Fig. 2a and b, only the first members of

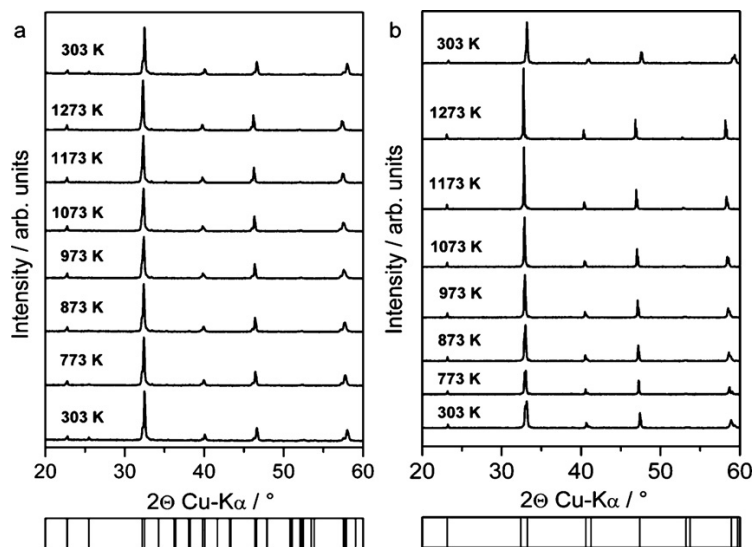


Fig. 3. *In situ* XRD pattern of (a) $\text{La}_{0.6}\text{Ca}_{0.4}\text{FeO}_{3-\delta}$ and (b) $\text{La}_{0.6}\text{Ca}_{0.4}\text{Co}_{0.8}\text{Fe}_{0.2}\text{O}_{3-\delta}$. The data were collected during heating and cooling in an atmosphere containing 50 vol.% $\text{CO}_2/50\text{ vol.}\% \text{ air}$. $F_{\text{total}} = 100\text{ cm}^3\text{ min}^{-1}$.

Table 1Lattice parameters of the LCF perovskite system. The orthorhombicity σ was calculated by: $\sigma = 2(a - c)/(a + c)$ [48].

T/K	Orthorhombic phase (<i>Pnma</i> , <i>Z</i> = 4)						Cubic phase (<i>Pm</i> $\bar{3}$ <i>m</i> , <i>Z</i> = 1)	
	<i>a</i> /Å	<i>b</i> /Å	<i>c</i> /Å	<i>V</i> /Å ³	<i>VZ</i> ⁻¹ /Å ³	σ	<i>a</i>	<i>V</i>
303	5.522	7.774	5.487	235.525	58.881	0.0065		
773	5.533	7.813	5.521	238.67	59.667	0.0021		
873	5.542	7.836	5.536	240.48	60.12	0.001		
973							3.923	60.372
1073							3.929	60.68
1173							3.936	61.016
1273							3.944	61.359

the systems (La_{1-x}Ca_x)FeO_{3- δ} and (La_{1-x}Ca_x)(Co_{0.8}Fe_{0.2})O_{3- δ} with $x = 0.4$ consisted of almost pure perovskites with the amount of the main phases at 97% and 98%, respectively. The compounds with higher calcium contents include significant fractions of bi-phases. For the iron-based system, these higher calcium contents were attributed to brownmillerite (Ca₂Fe₂O₅) and CaFe₂O₄ spinel. For cobalt-based materials, these were indexed as brownmillerite-like phase Ca₂Co_{2-y}Fe_yO₅, Co₃O₄ spinel and the layered complex oxide Ca₃Co_{2-z}Fe_zO₆. Brownmillerite exhibits ordered oxygen vacancies along the *c*-axis [43]. The Ca₃Co_{2-z}Fe_zO₆ structure contains chains of face-shared CoO₆ octahedra arranged along the *c*-axis [44]. These structures are unfavorable for oxygen-ionic transport. For this reason, the bi-phase-containing compounds with high calcium ratios have not been considered for further investigations.

The crystal symmetry and lattice parameters of the materials were determined by the Pawley method [45]. It was found that both systems showed the distorted perovskite structure. The (La_{0.6}Ca_{0.4})FeO_{3- δ} (LCF) exhibited an orthorhombic symmetry (space group *Pnma*, number of formula units per unit cell *Z* = 4), corresponding to the LaFeO₃ oxide with lattice parameters of $a = 5.496$ Å, $b = 7.772$ Å and $c = 5.566$ Å [46]. The structure of (La_{0.6}Ca_{0.4})(Co_{0.8}Fe_{0.2})O_{3- δ} (denoted as LCCF) was rhombohedrally

distorted (space group *R* $\bar{3}$ *c*, *Z* = 6) likewise in the LaCoO₃ perovskite with the lattice parameters of $a = 5.391$ Å and $b = 13.263$ Å [47].

The stability of the LCF and LCCF perovskites in different gas atmospheres and temperatures was investigated using an *in situ* XRD technique. Fig. 3a shows the diffraction pattern of LCF collected in an atmosphere containing 50 vol.% air and 50 vol.% CO₂. During heating and cooling in the temperature range of 303–1273 K, the oxide retained its perovskite structure. The formation of carbonates or additional phases was not observed in the measurements. However, an increase in the temperature above 973 K resulted in the

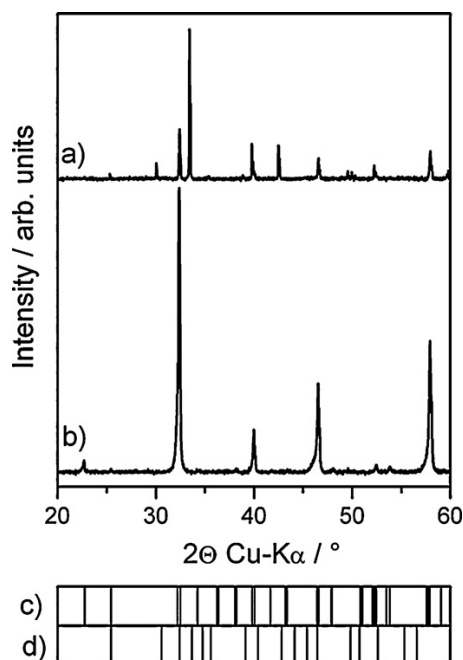


Fig. 4. XRD pattern of the (a) LCF membrane after sintering at 1523 K for 10 h and (b) polished LCF membrane. Bragg-positions of (c) orthorhombic LCF perovskite and (d) CaFe₂O₄.

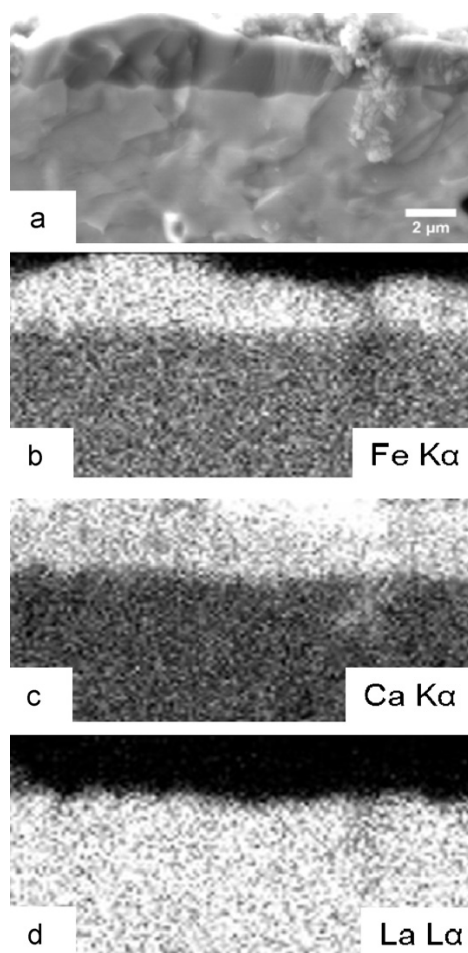


Fig. 5. (a) SEM micrograph from the cross-section of the unpolished LCF membrane sintered at 1523 K for 10 h showing formation of a tarnishing layer on the membrane surface (15 kV excitation voltage). (b–d) Elemental distribution by EDXS of corresponding area: (b) Fe, (c) Ca, (d) La.

Table 2
Lattice parameters of the LCCF perovskite system. The degree of rhombohedral strain ω was determined using the relationship: $c_H/a_H = \sqrt{6}/\cos \omega$ [49].

T/K	Rhomboedric phase ($R\bar{3}c$, $Z=6$)					Cubic phase ($Pm\bar{3}m$, $Z=1$)	
	$a/\text{\AA}$	$c/\text{\AA}$	$V/\text{\AA}^3$	$VZ^{-1}/\text{\AA}$	ω	a	V
303	5.391	13.263	333.837	55.639	5.5		
773	5.436	13.383	342.516	57.086	5.7		
873	5.449	13.411	344.819	57.47	5.6		
973	5.464	13.431	347.266	57.877	4.7		
1073	5.475	13.438	348.909	58.151	3.6		
1173						3.888	58.773
1273						3.898	59.227

reversible adoption of cubic perovskite symmetry. Table 1 summarizes the calculated lattice parameters and unit cell volumes at corresponding temperatures. The orthorhombicity σ decreased continuously with increasing temperature [48]. The crystal unit cell of orthorhombic perovskite growth with the temperature was almost independent from the direction. Furthermore, the transition from orthorhombic to cubic symmetry occurred without a jump in

unit cell volume. Hence, the thermal expansion coefficient (CTE) of the LCF oxide could be estimated from XRD data to be $15 \times 10^{-6} \text{ K}^{-1}$.

Similar behavior was observed for the LCCF powder (Fig. 3b). The perovskite material was stable over the whole temperature range. The reversible transformation of the rhombohedral to the cubic modification took place above 1173 K without a significant change of the cell volume per each formula unit (Table 2). The

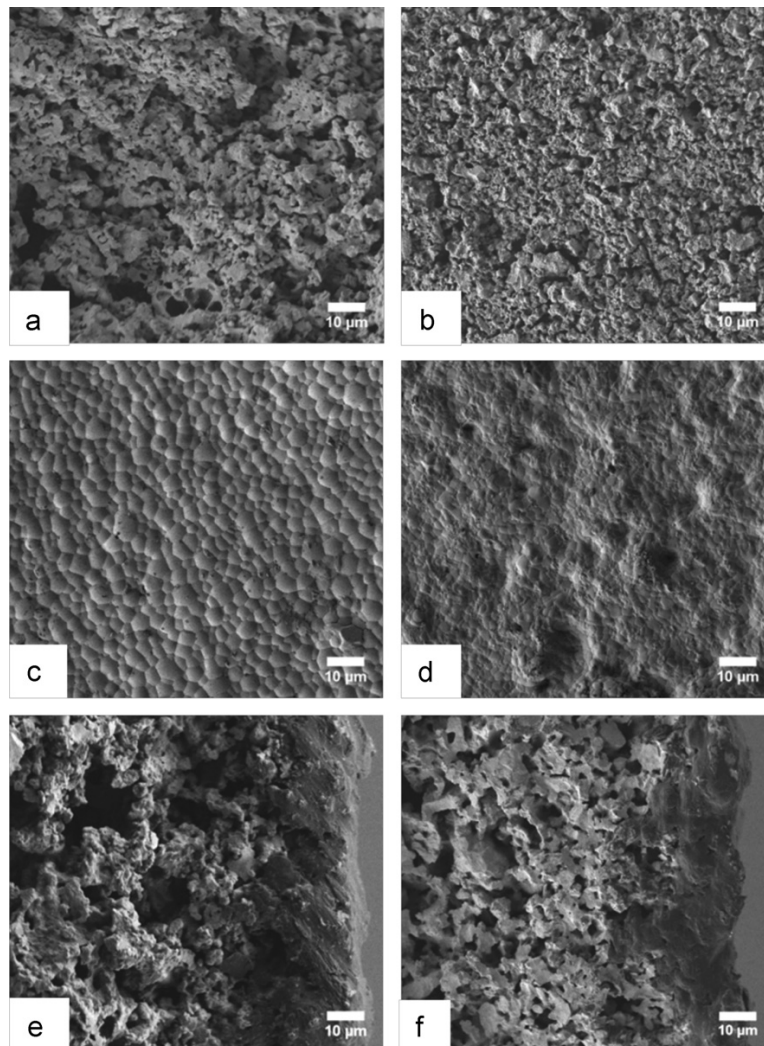


Fig. 6. (a and b) SEM micrographs of porous supports fired at 1423 K for 2 h: (a) LCCF and (b) LCF. (c and d) Surface of asymmetric membranes showing a dense layer obtained by spin coating and sintering: (c) LCCF sintered at 1443 K for 5 h and (d) LCF sintered at 1473 K for 5 h. (e and f) Fractured surface of asymmetric membranes: (e) LCCF sintered at 1443 K for 5 h and (f) LCF sintered at 1473 K for 5 h. Excitation voltage 2 kV.

parameter of rhombohedral strain ω remained almost constant until 873 K and decreased with further increasing temperature [49]. The lattice parameters of the LCCF perovskite unit cell expanded isotropically with increasing temperature. Thus, the CTE of the LCCF was evaluated from the XRD data to be $20 \times 10^{-6} \text{ K}^{-1}$.

Additionally, *in situ* experiments in an atmosphere containing 50 vol.% N₂ and 50 vol.% CO₂ were carried out for both perovskite systems. The LCF and LCCF oxides remained stable at these conditions. This result is evidence of the high tolerance of the Ca-containing perovskite materials against CO₂, as well as the desirable stability of LCF and LCCF at low oxygen partial pressures and temperatures between 303 and 1273 K.

3.2. Membrane preparation and characterization

The bulk membranes, having a thickness of 1 mm, were prepared by uniaxial pressing and subsequent sintering. Gas-tight membranes with densities above 90% and low porosities were obtained only after sintering at 1523 K for 10 h. However, in the unpolished LCF membrane, pronounced growth of CaFe₂O₄ and La₂O₃ bi-phases was observed by XRD, as shown in Fig. 4a. After polishing of the LCF membrane, the ratio of the bi-phases declined to a value of 3 wt.%, as determined by XRD (Fig. 4b), which equals their amount in the as-synthesized powder. To elucidate these findings, the unpolished LCF membrane surface was investigated by SEM. Fig. 5a shows an SEM micrograph from the cross-section of the LCF membrane acquired with 15 kV acceleration voltages. It is obvious that a tarnish film with average thickness of 2 μm was accrued on the membrane surface. Elemental distribution by EDXS (Fig. 5b–e) revealed the strong accumulation of iron and calcium combined with the absence of lanthanum in the tarnish layer. Using Cliff-Lorimer quantification, 66 at.% iron and 33 at.% calcium of the total value of cations were detected in the surface film. According to EDXS and XRD results, the tarnish layer on the unpolished LCF membrane can be understood as a CaFe₂O₄ phase. Thus, it can be concluded that the CaFe₂O₄ spinel formed in the LCF membrane at 1523 K preferentially on areas near the surface. A loss in oxygen from the perovskite structure, as induced by high temperatures, may be designated as the possible driving force for this process [35]. A decline in oxygen content led to the reduction of iron cations and formation of stoichiometric CaFe₂O₄ spinel. The preferential formation of CaFe₂O₄ instead of other stoichiometric compounds with higher oxygen content like LaFeO₃ is also consistent with this hypothesis. A stoichiometric oxide arose at the membrane surface because oxygen loss on the membrane surface occurred faster than in bulk. Due to poor oxygen-ionic conductivity caused by low amount of mobile oxygen vacancies as well as non-cubic crystal symmetry, the CaFe₂O₄ film can be considered a protective layer, which prevents further oxygen release and further perovskite decomposition. In addition, this hinders the recovery of the perovskite structure during cooling. Decomposition of the LCF ceramic at high temperatures due to irreversible oxygen release can be a handicap for operation of the material under long-term conditions with a steep oxygen gradient. These conclusions are supported by the fact that the unpolished LCF membranes sintered at 1523 K do not show any oxygen permeation flux.

For the LCCF membrane, the formation of a tarnish layer was not observed by XRD or SEM. Traces of a Ca₂Co_{2-y}Fe_yO₅ phase could be detected only with the help of XRD. These findings point out to the advantageous stability of LCCF perovskite at extremely high temperatures, as compared with LCF.

To prepare the LCCF and LCF asymmetric membranes, the powders obtained from the sol-gel synthesis were intermixed with 20 wt.% of block co-polymer Pluronic F 127 as a pore former. This material was utilized because the use of an organic pore former is widely applied for the fabrication of a porous support [50–53].

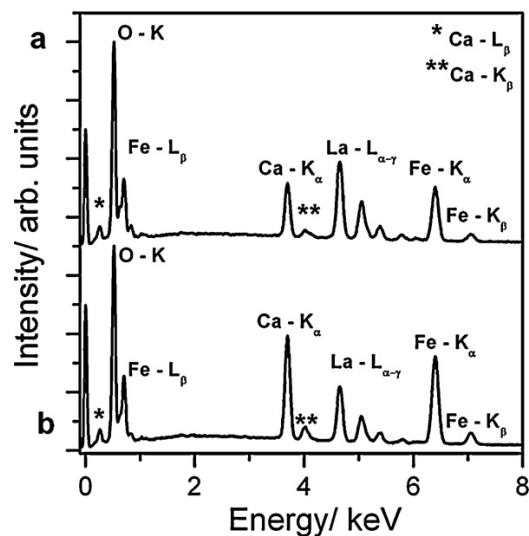


Fig. 7. EDX spectra from the surface of a cross-sectioned LCF membrane: (a) LCF porous support and (b) LCF dense layer showing the slight accumulation of Ca and Fe in the dense layer.

Then, porous membrane supports were constructed by press forming and calcination at 1423 K for 2 h. Fig. 6a and b shows SEM micrographs from the surface of LCCF and LCF porous supports, respectively. Obviously, both supports had very high porosities. The pore size distribution of the LCCF support differed from that of LCF materials. The LCCF support exhibited some open pores, with sizes of about 10 μm , alongside 0.5–3 μm large pores. In contrast, the pore size distribution of the LCF support was in the mostly homogeneously range of 0.5–2 μm . The high amount of open pores leads to good air permeability through both supports, which was in the range of approximately 20–25 $\text{cm}^3 \text{ min}^{-1} \text{ cm}^{-2}$ between 1123 and 1223 K.

The spin-coating method was applied to obtain dense membranes on the porous supports. Subsequently, the LCCF membrane was sintered at 1448 K for 5 h. Very low porosities and no cracks were observed in the membrane surface using SEM (Fig. 6c). Despite these occurrences, slightly elevated nitrogen leakage was detected during oxygen permeation measurements. This finding suggests that the dense layer was not completely homogeneously developed on the porous support. The size of the grains in the surface layer was found to be in the range of 2–6 μm . The LCF dense layer, shown in Fig. 6d, was also formed after sintering at 1473 K for 5 h. The LCF grains in the surface layer were smaller than that of LCCF and amounted to 1–3 μm . The average thickness of the dense layer of both materials was about 10 μm , as found in SEM micrographs from the cross-sections shown in Fig. 6e and f. Both supports maintained their open pore structure after sintering. The distribution of the pore size in the bulk of LCCF and LCF materials after generation of dense layers was similar to that on the surface before sintering. EDXS of the cross-sections revealed that the LCCF dense layer retained its initial composition. A slight accumulation of calcium in the LCF dense layer was detected by EDXS (Fig. 7), which is related to the formation of Ca₂FeO₄ at the membrane surface. The presence of the bi-phase in the dense layer should be critically viewed because the impurities cannot be removed by polishing. Because the formation of a stoichiometric bi-phase on the surface of the LCF membrane is due to oxygen loss, sintering of the ceramic material in an atmosphere with high oxygen content may be considered a possible method to prevent the perovskite decomposition and should be proven in a further investigation.

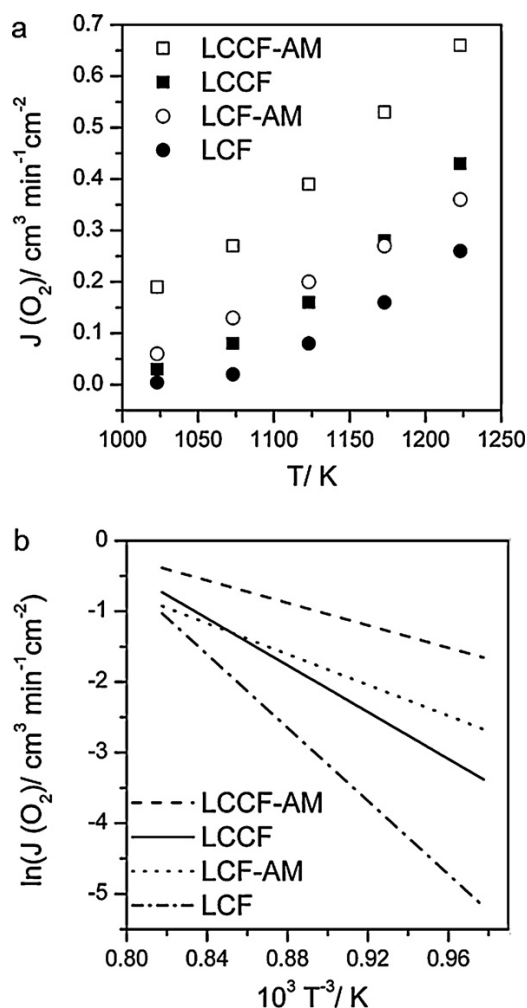


Fig. 8. (a) Oxygen permeation flux of 1 mm thick bulk membranes and asymmetrically structured membranes. Conditions: sweep flow rates: He = $29 \text{ cm}^3 \text{ min}^{-1}$, Ne = $1 \text{ cm}^3 \text{ min}^{-1}$; feed flow rates: $150 \text{ cm}^3 \text{ min}^{-1}$ synthetic air (80 vol.% N_2 , 20 vol.% O_2). (b) Arrhenius presentation of oxygen permeation.

3.3. Measurements of oxygen permeation through LCCF and LCF membranes

Measurements of oxygen permeation flux through bulk and asymmetric membranes were carried out in air/He gradients at temperatures between 1223 K and 1023 K with 50 K steps. Prior to the experiments, the bulk membranes were polished with polymer-embedded 30- μm diamond lapping film to achieve a uniform surface appearance. The tarnish CaFe_2O_4 layer, which formed on the LCF bulk membrane after sintering, was thereby removed. Fig. 8a shows the oxygen permeation fluxes of bulk and asymmetric membranes. For LCCF bulk membrane, a maximum flux of $0.43 \text{ cm}^3 \text{ min}^{-1} \text{ cm}^{-2}$ was observed at 1223 K. This value is comparable to that of $\text{La}_{0.6}\text{Ca}_{0.4}\text{CoO}_{3-\delta}$, as reported by Watanabe et al. [37]. The oxygen permeation flux through the asymmetric LCCF membrane at 1223 K was improved by 50% to a value of $0.66 \text{ cm}^3 \text{ min}^{-1} \text{ cm}^{-2}$. However, this value was approximately two orders of magnitude lower than expected from the Wagner equation, which states that the oxygen ionic conductivity is limited by bulk diffusion [54]. From our findings, we can assume that oxygen permeation through the asymmetric LCCF membrane is also

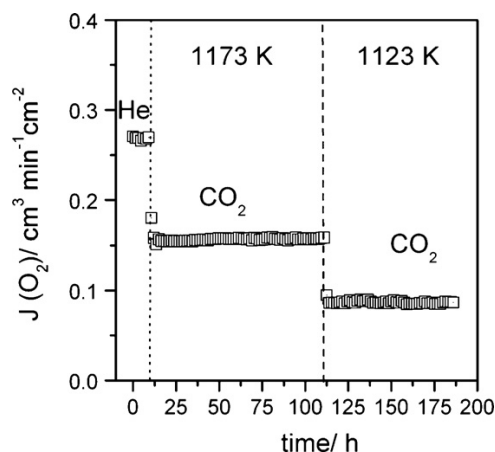


Fig. 9. Oxygen permeation flux of the LCCF bulk membrane with a thickness of 1 mm at 1173 K and 1123 K. Conditions: sweep flow rate He or $\text{CO}_2 = 29 \text{ cm}^3 \text{ min}^{-1}$, Ne = $1 \text{ cm}^3 \text{ min}^{-1}$; feed flow rate $150 \text{ cm}^3 \text{ min}^{-1}$ synthetic air (80 vol.% N_2 , 20 vol.% O_2).

strongly controlled by surface exchange reactions. Furthermore, the value of the oxygen permeation flux through the present asymmetric LCCF membrane was 2.5 times smaller than that reported by Watanabe et al. [37]. This result can be explained by the presence of low amount of bi-phases, like $\text{Ca}_2\text{Co}_{2-y}\text{Fe}_y\text{O}_5$ and Co_3O_4 , in the surface layer (see discussion related to Figs. 9 and 10), which diminish the active area for oxygen exchange on the surface, as well as oxygen permeation through the membrane. Furthermore, the inhomogeneous distribution of the pore size in the porous support is unfavorable and is caused by a reduction of the effective area for oxygen permeation [37].

The activation energy of the oxygen ionic conductivity for bulk and asymmetric LCCF membranes was determined from the temperature dependency of oxygen fluxes by an Arrhenius plot, as given in Fig. 8b. Although the asymmetric membrane structure has an effect on the oxygen permeability, which is considerably weaker than expected, the activation energy of the oxygen ionic conductivity was found to be half that of the bulk membrane. For the asymmetric LCCF membrane, the activation energy was determined to be 65 kJ mol^{-1} , compared with the activation energy of the bulk membrane, which had a value of 137 kJ mol^{-1} . This fact indicates the different rate limiting steps for oxygen permeation through asymmetric and bulk membranes. The activation energy for bulk LCCF membrane corresponds to the value that was calculated by Carter et al. from self-diffusion coefficients as a function of temperature [50]. Moreover, if activation energy is determined from the temperature dependency of surface exchange coefficients, it is around 70 kJ mol^{-1} [55]. Accordingly, we can assume that the oxygen surface exchange reaction is the rate limiting step for the asymmetric membrane. In contrast, oxygen permeability through a bulk membrane is limited by bulk diffusion.

The LCF material exhibited an oxygen permeation of $0.26 \text{ cm}^3 \text{ min}^{-1} \text{ cm}^{-2}$ at 1223 K for the bulk membrane and $0.36 \text{ cm}^3 \text{ min}^{-1} \text{ cm}^{-2}$ for the asymmetric membrane at 1223 K (Fig. 8a). The activation energies for bulk and asymmetric membranes were calculated to be 215 kJ mol^{-1} and 91 kJ mol^{-1} , respectively. It can be concluded that oxygen permeation through the bulk membrane is controlled by diffusion and by surface exchange reaction for the asymmetric membrane. Relatively low flux through the asymmetric LCF membrane can be explained by the accumulation of an CaFe_2O_4 phase in the surface layer during preparation.

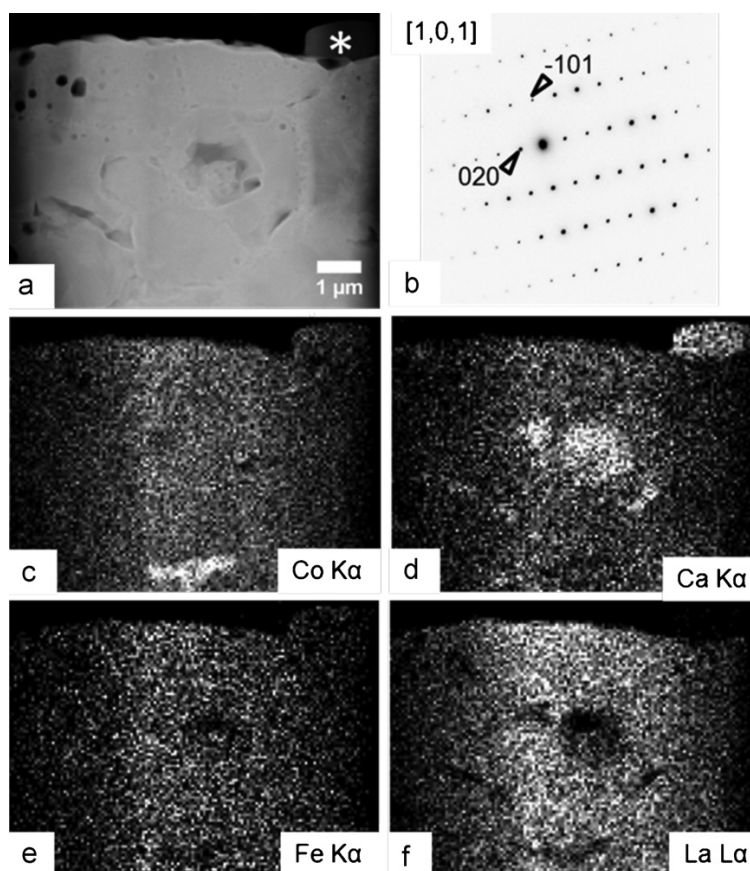


Fig. 10. (a) STEM-HAADF micrograph of the permeate side of an LCCF membrane quenched in the presence of CO₂. (b) SAED pattern from the area marked with an asterisk in (a). (c–f) Elemental distribution by EDXS of the area shown in (a): (c) Co, (d) Ca, (e) Fe and (f) La.

3.4. Stability of LCCF material against CO₂

To examine the stability of Ca-containing materials during operation in the presence of CO₂, a time-dependent oxygen permeation experiment on 1 mm thick LCCF bulk membrane was carried out using pure CO₂ as a sweep gas. As can be seen in Fig. 9, a steady state of oxygen flux was reached within 3 h after switching the sweep gas from He to CO₂ at 1173 K. Subsequently, the oxygen permeation declined from 0.27 cm³ min⁻¹ cm⁻² to 0.16 cm³ min⁻¹ cm⁻² and maintained this value for 100 h. The decrease of oxygen flux at the start of the measurement may be explained by the inhibiting effect of CO₂ on the surface exchange reaction, which hinders the release of oxygen from the solid surface due to reaction of absorbed CO₂ species with the oxygen vacancies on the membrane surface [15]. Furthermore, the fact that the oxygen surface exchange had various rates in different gas atmospheres is well known and has been discussed in detail elsewhere [56–58]. The constant oxygen permeation flux through the LCCF membrane after steady state conditions were achieved suggests a high tolerance of the LCCF material toward CO₂. In contrast, the functional performance of Ba- and Sr-containing perovskites completely collapses, even at lower CO₂ partial pressures, after a very short time.

The LCCF perovskite also exhibited constant oxygen permeation performance at 1123 K (Fig. 9). This result points to the desirable inherent stability of LCCF alongside its high CO₂ tolerance at temperatures below 1173 K. The temperature of 1173 K can be considered critical for many Co-containing perovskites because they tend to form hexagonal distorted perovskite phases below this

temperature [7,9,10]. The reason for this issue is a reduction of cobalt cations combined with the spin-state transition leading to a significant decrease in ionic radius from Co²⁺ (high spin) = 74.5 pm to Co³⁺ (high spin) = 61 pm, Co³⁺ (low spin) = 54.5 pm, and Co⁴⁺ (high spin) = 53 pm [25]. The small Co³⁺ (low spin) and Co⁴⁺ cations, especially together with large A-site cations like Ba²⁺ and/or Sr²⁺, resulted in a Goldschmidt tolerance factor higher than 1 for corresponding perovskites, which is unfavorable for cubic and orthorhombic symmetries [7–9]. As mentioned in section 3.1, the tolerance factor for LCCF perovskite did not exceed the value of 1 by any ratio of Co⁴⁺/Co³⁺/Co²⁺, because of the relatively small ionic radii of La³⁺ and Ca²⁺ cations. Furthermore, the high amount of La³⁺ cations in the LCCF may stabilize the valence and spin state of cobalt in a similar way as doping of Zr⁴⁺ or Ti⁴⁺, which is beneficial for the delayed phase transition kinetics of Ba- and Sr-containing cobaltites [10,59].

After the long-term oxygen permeation experiment, the LCCF membrane was quenched in a CO₂ atmosphere down to room temperature and investigated by XRD, SEM and TEM methods. XRD of the permeate site of the membrane revealed no CaCO₃ formation. Except for traces of Ca₂Co_{2-y}Fe_yO₅ and Co₃O₄, the LCCF material was found to consist of rhombohedrally distorted perovskite. SEM examination of the fractured surface of the permeate side proved that neither a tarnish layer nor cracks were formed on the membrane. However, the inclusion of phases, which have different chemical compositions than LCCF perovskite, in the regions near the surface and in the bulk were observed by the STEM HAADF technique (Fig. 10a) by areas with dark Z contrast. Selected area

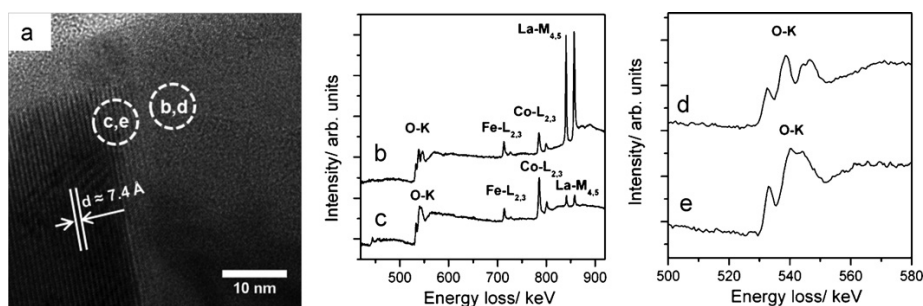


Fig. 11. (a) HRTEM micrograph showing two different phases on the cross-sectioned permeate side of LCCF membrane quenched in the presence of CO_2 . (b and c) EEL spectra from the areas marked in (a). (d and e) O-K ELNES from the areas marked in (a).

electron diffraction was applied to the area marked with an asterisk in Fig. 10a and showed no perovskite structures. The intensity distribution of the diffraction data in Fig. 10b from the corresponding area can be attributed to a brownmillerite phase with an orthorhombic symmetry (space group $Pnma$) oriented along the $[1,0,1]$ zone axis. The elemental distribution by EDXS in Fig. 10c–f reveals the accumulation of calcium, combined with the depletion of lanthanum in this area. Using Cliff-Lorimer quantification, the composition of the brownmillerite phase was found to be approximately $\text{Ca}_2\text{Co}_{1.5}\text{Fe}_{0.5}\text{O}_5$. Furthermore, some additional areas in the sample, which contained a brownmillerite phase or cobalt oxide, were detected by EDXS in the LCCF membrane.

Additionally, Fig. 11a shows an HRTEM micrograph from the membrane surface, demonstrating the presence of two phases in this area. The phase on the left-hand side exhibited lattice fringes with a separation distance of approximately 7.4 Å, which corresponds to the (020) planes of the brownmillerite phase. The EEL spectra, which were acquired from both phase areas marked in Fig. 11a, showed lanthanum- $\text{M}_{4,5}$, cobalt- $\text{L}_{2,3}$, iron- $\text{L}_{2,3}$, and oxygen-K ionization edges (Fig. 11b and c). The weak intensities of the lanthanum- $\text{M}_{4,5}$ edge in Fig. 11c clearly reveal that the phases had different chemical compositions. Furthermore, unequal chemical environments of the cations in these phases were detected via analysis of the O-K energy-loss near edge structure (ELNES), which is sensitive to cation coordination, valence, and spin-state [8,60]. The O-K ELNES in Fig. 11d is typical for perovskite oxides [38,39]. In contrast, the pattern of the O-K ELNES in Fig. 11e cannot be attributed to a perovskite structure. According to HRTEM and EELS experiments, the phase in the LCCF membrane surface shown in Fig. 11a can be indexed as brownmillerite and perovskite oxides. The presence of lanthanum traces in the brownmillerite phase may be explained by the limited substitution of calcium due to similar ionic sizes [25].

Because the traces of brownmillerite and cobalt oxide were observed in the as-prepared powder and in the sintered ceramic, we assumed that the formation of foreign phases in the LCCF membrane was not due to operation in a CO_2 -containing atmosphere. The non-perovskite phases developed during the synthesis of LCCF materials and sintering of the ceramic, which is a general problem of this type of solid solutions. Nevertheless, Ca-based materials can be considered promising for operation in the presence of CO_2 , as LCCF ceramics exhibit stable functional performance in CO_2 -containing atmospheres and no carbonate formation was observed by different analytical methods.

3.5. Comparison of the oxygen permeation flux through LCCF and LCF perovskite with established MIEC materials

To evaluate whether Ca-containing perovskites are candidate membrane materials, the oxygen permeation flux through LCCF

Table 3

Comparison of oxygen permeation flux through several relevant MIEC materials under CO_2 -free conditions; sweep flow rates: He = $29 \text{ cm}^3 \text{ min}^{-1}$, Ne = $1 \text{ cm}^3 \text{ min}^{-1}$; feed flow rates: $150 \text{ cm}^3 \text{ min}^{-1}$ synthetic air (80 vol.% N_2 , 20 vol.% O_2).

	$J(\text{O}_2)/\text{cm}^3 \text{ min}^{-1} \text{ cm}^{-2}$	
	1073 K	1173 K
$(\text{Ba}_{0.5}\text{Sr}_{0.5})(\text{Co}_{0.8}\text{Fe}_{0.2})\text{O}_{3-\delta}$ ^a	1.48	2.26
$(\text{La}_{0.4}\text{Sr}_{0.6})(\text{Co}_{0.8}\text{Fe}_{0.2})\text{O}_{3-\delta}$ ^a	0.31	0.61
$\text{La}_2\text{NiO}_{4+\delta}$	0.22	0.38
$(\text{La}_{0.6}\text{Ca}_{0.4})(\text{Co}_{0.8}\text{Fe}_{0.2})\text{O}_{3-\delta}$ (LCCF)	0.08	0.27
$(\text{La}_{0.6}\text{Ca}_{0.4})\text{FeO}_{3-\delta}$ (LCF)	0.02	0.16

^a Useable only under CO_2 -free conditions.

and LCF bulk membranes were compared with that of established MIEC materials. Table 3 summarizes the oxygen permeation fluxes of relevant MIEC membranes with equal thicknesses of 1 mm. These experiments were conducted under the same conditions as for our measurement setup. Obviously, the LCCF and LCF membranes exhibited lower oxygen permeation fluxes compared with Ba- and/or Sr-containing materials, as well as $\text{La}_2\text{NiO}_{4+\delta}$. Nevertheless, Ba- and/or Sr-containing membranes cannot be operated in the presence of CO_2 because of the formation of $(\text{Ba,Sr})\text{CO}_3$ [11–16]. The tolerance of $\text{La}_2\text{NiO}_{4+\delta}$ material toward CO_2 is just as desirable as that of our presented LCCF and LCF membranes. In terms of electrical conductivity, however, Ca-containing materials clearly exceeded $\text{La}_2\text{NiO}_{4+\delta}$ [31,61,62]. Thus, we propose that Ca-based perovskites can be considered promising membrane materials for operation in CO_2 -containing atmospheres, especially when high electrical conductivity is required as, for example, with cathode material applications in SOFCs [63,64].

4. Conclusions

$(\text{La}_{1-x}\text{Ca}_x)\text{FeO}_{3-\delta}$ and $(\text{La}_{1-x}\text{Ca}_x)(\text{Co}_{0.8}\text{Fe}_{0.2})\text{O}_{3-\delta}$ ($x=0.4\text{--}0.6$) perovskite systems were fabricated as alternative materials to Ba- and/or Sr-based perovskite for operation in the presence of CO_2 . Because only the first member of the systems with low Ca content ($x=0.4$) consisted mainly of a perovskite phase, these were investigated regarding chemical stability and oxygen ionic conducting properties. The $\text{La}_{0.6}\text{Ca}_{0.4}\text{FeO}_{3-\delta}$ (LCF) perovskite was found to be orthorhombically distorted, adopting a cubic symmetry at temperatures above 1173 K. The lattice symmetry of $\text{La}_{0.6}\text{Ca}_{0.4}\text{Co}_{0.8}\text{Fe}_{0.2}\text{O}_{3-\delta}$ (LCCF) perovskite was reversibly transformed from rhombohedral to cubic above 873 K. Furthermore, *in situ* XRD experiments in the CO_2 -containing atmosphere reveal the high tolerance of both materials toward CO_2 , as expected from the thermodynamic considerations. The bulk and self-supported asymmetrically structured membranes were designed from both materials. Here, the LCF material was found to not be stable at extremely high temperatures because of the formation of a tarnish

layer consisting of Ca₂FeO₄ spinel during sintering at 1523 K. The bulk LCCF membrane exhibited an oxygen permeation flux with a maximal value of 0.43 cm³ min⁻¹ cm⁻² at 1223 K. The flux of 0.66 cm³ min⁻¹ cm⁻² through asymmetric membranes with a dense layer thickness of about 10 μm was found to be two orders of magnitude lower than the value expected from theoretical calculations. The activation energies of oxygen ionic conductivity of bulk and self-supported membranes were determined to be 137 kJ mol⁻¹ and 65 kJ mol⁻¹, respectively. These results point out that oxygen permeation through a bulk membrane is limited by self-diffusion. In contrast, the limiting step for the oxygen permeation performance of asymmetric membranes lies in the surface exchange reaction. Similar behaviors were also observed for the LCF membrane. Additionally, the relatively low oxygen permeation flux through asymmetric membranes can be explained by the accumulation of impurities, like brownmillerite and spinel phases, in the surface layer, as well as by the poor distribution of pore sizes in the porous support. The LCCF bulk membrane showed a constant oxygen permeation performance during long-term operation in the presence of CO₂. No formation of carbonate was detected in the membrane after testing for 100 h at 1173 K and for 60 h at 1123 K. Therefore, both the high tolerance against CO₂ and good inherent phase stability of the LCCF was confirmed. Thus, we propose that Ca-containing perovskites, LCCF, can be considered alternative membrane materials to Ba- and/or Sr-based perovskite for operation in CO₂-containing atmospheres. The synthesis and sintering conditions, however, should be optimized to prevent the formation of non-perovskite phases, which are primarily critical for performance of an asymmetrically structured membrane.

Acknowledgement

The authors acknowledge financial support from the State of Lower Saxony (Germany, NTH bottom-up project, no. 21-71023-25-7/09).

References

- Z. Shao, W. Yang, Y. Cong, H. Dong, J. Tong, G. Xiong, Investigation of the permeation behavior and stability of a Ba_{0.5}Sr_{0.5}Co_{0.8}Fe_{0.2}O_{3-δ} oxygen membrane, *J. Membr. Sci.* 172 (2000) 177–188.
- W. Zhou, R. Ran, Z. Shao, Progress in understanding and development of Ba_{0.5}Sr_{0.5}Co_{0.8}Fe_{0.2}O_{3-δ}-based cathodes for intermediate-temperature solid-oxide fuel cells: a review, *J. Power Sources* 192 (2009) 231–246.
- Y. Teraoka, H. Zhang, S. Furukawa, N. Yamazoe, Oxygen permeation through perovskite oxides, *Chem. Lett.* 11 (1985) 1743–1746.
- J. Yi, H. Lein, T. Grande, S. Yakovlev, H.J.M. Bouwmeester, High-temperature compressive creep behaviour of the perovskite-type oxide Ba_{0.5}Sr_{0.5}Co_{0.8}Fe_{0.2}O_{3-δ}, *Solid State Ionics* 180 (2009) 1564–1568.
- S. McIntosh, J.F. Vente, W.G. Haije, D.H.A. Blank, H.J.M. Bouwmeester, Oxygen stoichiometry and chemical expansion of Ba_{0.5}Sr_{0.5}Co_{0.8}Fe_{0.2}O_{3-δ} measured by in-situ neutron diffraction, *Chem. Mater.* 18 (2006) 2187–2193.
- J. Vente, W. Haije, Z. Rak, Performance of functional perovskite membranes for oxygen production, *J. Membr. Sci.* 276 (2006) 178–184.
- S. Švarcova, K. Wiik, J. Tolchard, H.J.M. Bouwmeester, T. Grande, Structural instability of cubic perovskite Ba_xSr_{1-x}Co_{0.8}Fe_{0.2}O_{3-δ}, *Solid State Ionics* 178 (2008) 1787–1791.
- M. Arnold, T. Gesing, J. Martynczuk, A. Feldhoff, Local charge disproportion in a high-performance perovskite, *Chem. Mater.* 20 (2008) 5858–5881.
- K. Efimov, Q. Xu, A. Feldhoff, TEM study of BSCF perovskite decomposition at intermediate temperatures, *Chem. Mater.* 22 (2010) 5866–5875.
- T. Nagai, W. Ito, T. Sakon, Relationship between cation substitution and stability of perovskite structure in SrCoO_{3-δ}-based mixed conductors, *Solid State Ionics* 177 (2007) 3433–3444.
- M. Arnold, H. Wang, A. Feldhoff, Influence of CO₂ on the oxygen permeation performance and the microstructure of perovskite-type (Ba_{0.5}Sr_{0.5})(Co_{0.8}Fe_{0.2})O_{3-δ} membranes, *J. Membr. Sci.* 293 (2007) 44–52.
- O. Czuprat, M. Arnold, S. Schirmermeister, T. Schiestel, J. Caro, Influence of CO₂ on the oxygen permeation performance of perovskite-type BaCo_xFe_yZr_zO_{3-δ} hollow fiber membranes, *J. Membr. Sci.* 364 (2010) 132–137.
- J. Martynczuk, K. Efimov, L. Robben, A. Feldhoff, Performance of zinc-doped perovskite-type membranes at intermediate temperatures for long term oxygen permeation and under carbon dioxide atmosphere, *J. Membr. Sci.* 344 (2009) 62–70.
- J. Tong, W. Yang, B. Zhu, R. Cai, Investigation of ideal zirconium-doped perovskite-type ceramic membrane materials for oxygen separation, *J. Membr. Sci.* 203 (2002) 175–189.
- J.E. ten Elshof, H.J.M. Bouwmeester, H. Verweij, Oxygen transport through La_{1-x}Sr_xFeO_{3-δ} membranes. II. Permeation in air/CO, CO₂ gradients, *Solid State Ionics* 89 (1996) 81–92.
- S.J. Benson, D. Waller, J.A. Kilner, Degradation of La_{0.6}Sr_{0.4}Fe_{0.8}Co_{0.2}O_{3-δ} in carbon dioxide and water atmospheres, *J. Electrochem. Soc.* 146 (4) (1999) 1305–1309.
- Z. Shao, S.M. Haile, A high-performance cathode for the next generation of solid-oxide fuel cells, *Nature* 431 (2004) 170–173.
- H. Wang, Y. Cong, W. Xang, Investigation on the partial oxidation of methane to syngas in a tubular Ba_{0.5}Sr_{0.5}Co_{0.8}Fe_{0.2}O_{3-δ} membrane reactor, *Catal. Today* 82 (2003) 157–166.
- J. Caro, H. Wang, C. Tablet, A. Kleinert, A. Feldhoff, T. Schiestel, M. Kilgus, P. Kölsch, S. Werth, Evaluation of perovskites in hollow fibre and disk geometry in catalytic membrane reactors and in oxygen separators, *Catal. Today* 118 (2006) 128–135.
- J. Sunarso, S. Baumann, J.M. Serra, W.A. Meulenber, S. Liu, Y.S. Lin, J.C. Diniz da Costa, Mixed ionic-electronic conducting (MIEC) ceramic-based membranes for oxygen separation, *J. Membr. Sci.* 320 (2008) 13–41.
- I. Barin, F. Sauer, G. Patzki, *Thermochemical Data of Pure Substances*, vols. I and II, 3rd ed., VCH, Weinheim, 1995.
- A.N. Shirsat, M. Ali, K.N.G. Kaimal, S.R. Bharadwaj, D. Das, Thermochemistry of La₂O₂CO₃ decomposition, *Thermochim. Acta* 399 (2003) 167–170.
- Y. Watanabe, S. Miyazaki, T. Maruyama, Y. Saito, Dissociation pressure of lanthanum dioxide carbonate, *J. Mater. Sci. Lett.* 5 (1996) 135–136.
- K. Efimov, M. Arnold, J. Martynczuk, A. Feldhoff, Crystalline intermediate phases in the sol-gel-based synthesis of La₂NiO_{4+δ}, *J. Am. Ceram. Soc.* 92 (2008) 876–880.
- R.D. Shannon, Revised effective ionic radii and systematic studies of interatomic distances in halides and chalcogenides, *Acta Crystallogr., Sect. A* 32 (1976) 751–767.
- K.H. Stern, E.L. Weise, *High Temperature Properties and Decomposition of Inorganic Salts. Part 2. Carbonates*, NSDRS, Washington, 1969.
- H. Yokokawa, N. Sakai, T. Kawada, M. Dokiya, Thermodynamic stability of perovskites and related compounds in some alkaline earth-transition metal-oxygen systems, *J. Solid State Chem.* 94 (1991) 106–120.
- H. Yokokawa, N. Sakai, T. Kawada, M. Dokiya, Thermodynamic stabilities of perovskite oxides for electrodes and other electrochemical materials, *Solid State Ionics* 52 (1992) 43–56.
- F.M. Figueiredo, M.R. Soares, V.V. Kharton, E.N. Naumovich, J.C. Waerenborg, J.R. Frade, Properties of CaTi_{1-x}Fe_xO_{3-δ} ceramic membranes, *J. Electroceram.* 13 (2004) 627–636.
- Y. Teraoka, T. Nobunaga, N. Yamazoe, Effect of cation substitution on the oxygen semipermeability of perovskite-type oxides, *Chem. Lett.* 17 (1988) 503–506.
- J.W. Stevenson, T.R. Armstrong, R.D. Carneim, L.R. Pederson, W.J. Weber, Electrochemical properties of mixed conducting perovskites La_{1-x}M_xCo_{1-y}Fe_yO_{3-δ} (M = Sr, Ba, Ca), *J. Electrochem. Soc.* 143 (1996) 2722–2729.
- M. Trunec, J. Cihlar, S. Diethelm, J. Van Herle, Tubular La_{0.7}Ca_{0.3}Fe_{0.85}Co_{0.15}O_{3-δ} perovskite membranes. Part I. Preparation and properties, *J. Am. Ceram. Soc.* 89 (2006) 949–955.
- C.Y. Tsai, A.G. Dixon, Y.H. Ma, W.R. Moser, M.R. Pascucci, Dense perovskite, La_{1-x}A_xFe_{1-y}Co_yO_{3-δ} (A⁺ = Ba, Sr, Ca), membrane synthesis, applications, and characterization, *J. Am. Ceram. Soc.* 81 (1998) 1437–1444.
- S. Diethelm, J. Van Herle, P.H. Middleton, D. Favrat, Oxygen permeation and stability of La_{0.4}Ca_{0.6}Fe_{1-x}Co_xO_{3-δ} (x = 0, 0.25, 0.5) membranes, *J. Power Sources* 118 (2003) 270–275.
- A.N. Nadeev, S.V. Tsybulya, E.Y. Gerasimov, N.A. Kulikovskaya, L.A. Isupova, Structural features of the formation of La_{1-x}Ca_xFeO_{3-δ} (0 ≤ x ≤ 0.7) heterovalent solid solutions, *J. Struct. Chem.* 51 (2010) 891–897.
- K. Watanabe, M. Yuasa, T. Kida, K. Shimanoe, Y. Teraoka, N. Yamazoe, Preparation of oxygen evolution layer/La_{0.6}Ca_{0.4}CoO₃ dense membrane/porous support asymmetric structure for high-performance oxygen permeation, *Solid State Ionics* 179 (2008) 1377–1381.
- K. Watanabe, M. Yuasa, T. Kida, K. Shimanoe, Y. Teraoka, N. Yamazoe, Dense/porous asymmetric-structured oxygen permeable membranes based on La_{0.6}Ca_{0.4}CoO₃ perovskite-type oxide, *Chem. Mater.* 20 (2008) 6965–6973.
- A. Feldhoff, M. Arnold, J. Martynczuk, T.M. Gesing, H. Wang, The sol-gel synthesis of perovskites by an EDTA/citrate complexing method involves nanoscale solid state reactions, *Solid State Sci.* 10 (2008) 689–701.
- A. Feldhoff, J. Martynczuk, H.H. Wang, Advanced Ba_{0.5}Sr_{0.5}Zn_{0.2}Fe_{0.8}O_{3-δ} perovskite-type ceramics as oxygen selective membranes: evaluation of the synthetic process, *Prog. Solid State Chem.* 35 (2007) 339–353.
- H. Wang, C. Tablet, A. Feldhoff, J. Caro, Investigation of phase structure, sintering, and permeability of perovskite-type Ba_{0.5}Sr_{0.5}Co_{0.8}Fe_{0.2}O_{3-δ} membranes, *J. Membr. Sci.* 262 (2005) 20–26.
- J. Martynczuk, M. Arnold, A. Feldhoff, Influence of grain size on the oxygen permeation performance of perovskite-type (Ba_{0.5}Sr_{0.5})(Fe_{0.8}Zn_{0.2})O_{3-δ} membranes, *J. Membr. Sci.* 322 (2008) 375–382.
- V.M. Goldschmidt, *Die Gesetze der Kristallchemie*, *Naturwiss* 14 (1926) 477–485.
- G.J. Redhammer, G. Tippelt, G. Roth, G. Amthauer, Structural variations in the brownmillerite series Ca₂(Fe₂₋₃Al_x)O₅: single-crystal X-ray diffraction at 25 degrees C and high-temperature X-ray powder diffraction (25 degrees C ≤ T ≤ 1000 degrees C), *Am. Mineral.* 89 (2004) 405–420.

- [44] P. Boullay, V. Dorcet, O. Pérez, C. Grygiel, W. Prellier, B. Mercey, M. Hervieu, Structure determination of a brownmillerite $\text{Ca}_2\text{Co}_2\text{O}_5$ thin film by precession electron diffraction, *Phys. Rev.* 79 (2009) 184108.
- [45] G.S. Pawley, Unit cell refinement from powder diffraction scans, *J. Appl. Cryst.* 14 (1981) 357–361.
- [46] H. Fjellvag, E. Gulbrandsen, S. Aasland, A. Olsen, B.C. Hauback, Crystal structure and possible charge ordering in one-dimensional $\text{Ca}_3\text{Co}_2\text{O}_6$, *J. Solid State Chem.* 124 (1996) 190–194.
- [47] H. Falcon, A.E. Goeta, G. Punte, E. Carbonio, Crystal structure refinement and stability of $\text{LaFe}_x\text{Ni}_{1-x}\text{O}_3$ solid solutions, *J. Solid State Chem.* 133 (1997) 379–385.
- [48] M. Ain, J.M. Delrieu, A. Menelle, G. Parette, J. Jegoudez, Orthorhombicity and oxygen uptake by $\text{YBa}_2\text{Cu}_3\text{O}_{6+x}$, *J. Phys. France* 50 (1989) 1455–1461.
- [49] R.H. Mitchell, *Perovskites: Modern and Ancient*, Almaz Press Inc., Ontario, Canada, 2002.
- [50] M.L. Fontaine, J.B. Smith, Y. Larring, R. Bredesen, On the preparation of asymmetric $\text{CaTi}_{0.9}\text{Fe}_{0.1}\text{O}_{3-\delta}$ membranes by tape-casting and co-sintering process, *J. Membr. Sci.* 326 (2009) 310–315.
- [51] A.V. Kovalevsky, V.V. Kharton, F.M.M. Snijkers, J.F.C. Cooymans, J.J. Luyten, F.M.B. Marques, Oxygen transport and stability of asymmetric $\text{SrFe}(\text{Al})\text{O}_{3-\delta}$ - SrAl_2O_4 composite membranes, *J. Membr. Sci.* 301 (2007) 238–244.
- [52] G. Etchegoyen, T. Chartier, P.D. Gallo, An architectural approach to the oxygen permeability of a $\text{La}_{0.6}\text{Sr}_{0.4}\text{Fe}_{0.9}\text{Ga}_{0.1}\text{O}_{3-\delta}$ perovskite membrane, *J. Eur. Ceram. Soc.* 26 (2006) 2807–2815.
- [53] S. Araki, Y. Hoshi, S. Hamakawa, S. Hikazudani, F. Mizukami, Synthesis and characterization of mixed ionic-electronic conducting $\text{Ca}_{0.8}\text{Sr}_{0.2}\text{Ti}_{0.7}\text{Fe}_{0.3}\text{O}_{3-\alpha}$ thin film, *Solid State Ionics* 178 (2008) 1740–1745.
- [54] C. Wagner, Equations for transport in solid oxides and sulfides of transition metals, *Prog. Solid State Chem.* 10 (1975) 3–16.
- [55] S. Carter, A. Selcuk, R.J. Chater, J. Kajda, J.A. Kilner, B.C.H. Steele, Oxygen transport in selected nonstoichiometric perovskite-structure oxide, *Solid State Ionics* 53–56 (1992) 597–605.
- [56] J.A. Lane, J.A. Kilner, Oxygen surface exchange on gadolinia doped ceria, *Solid State Ionics* 136–137 (2000) 927–932.
- [57] K. Yashiro, S. Onuma, A. Kaimai, Y. Nigara, T. Kawada, J. Mizusaki, K. Kawamura, T. Horita, H. Yokokawa, Mass transport properties of $\text{Ce}_{0.9}\text{Gd}_{0.1}\text{O}_{2-\delta}$ at the surface and in the bulk, *Solid State Ionics* 152–153 (2002) 469–476.
- [58] I.V. Khromushin, T.I. Aksenova, Zh.R. Zhotabaev, Mechanism of gas–solid exchange processes for some perovskites, *Solid State Ionics* 162–163 (2003) 37–40.
- [59] S. Yakovlev, C.Y. Yoo, S. Fang, H.J.M. Bouwmeester, Phase transformation and oxygen equilibration kinetics of pure and Zr-doped $\text{Ba}_{0.5}\text{Sr}_{0.5}\text{Co}_{0.8}\text{Fe}_{0.2}\text{O}_{3-\delta}$ perovskite oxide probed by electrical conductivity relaxation, *Appl. Phys. Lett.* 96 (2010) 254101.
- [60] J. Martynczuk, M. Arnold, H. Wang, J. Caro, A. Feldhoff, How $(\text{Ba}_{0.5}\text{Sr}_{0.5})(\text{Fe}_{0.8}\text{Zn}_{0.2})\text{O}_{3-\delta}$ and $(\text{Ba}_{0.5}\text{Sr}_{0.5})(\text{Co}_{0.8}\text{Fe}_{0.2})\text{O}_{3-\delta}$ perovskites form via an EDTA/citric acid complexing method, *Adv. Mater.* 19 (2007) 2134–2140.
- [61] G. Amow, I.J. Davidson, S.J. Skinner, A comparative study of the Ruddlesden-Popper series, $\text{La}_{n+1}\text{Ni}_n\text{O}_{3n+1}$ ($n = 1, 2$ and 3), for solid-oxide fuel-cell cathode applications, *Solid State Ionics* 177 (2006) 1205–1210.
- [62] N. Ortiz-Vitoriano, I. Ruiz de Larramendi, J.I. Ruiz de Larramendi, M.I. Arriortua, T. Rojo, Synthesis and electrochemical performance of $\text{La}_{0.6}\text{Ca}_{0.4}\text{Fe}_{1-x}\text{Ni}_x\text{O}_3$ ($x = 0.1, 0.2, 0.3$) material for solid oxide fuel cell cathode, *J. Power Sources* 192 (2009) 63–69.
- [63] K. Kendall, Progress in solid oxide fuel cell materials, *Int. Mater. Rev.* 2005 (2005) 257–264.
- [64] J. Richter, P. Holtappels, T. Graule, T. Nakamura, L.J. Gauckler, Materials design for perovskite SOFC cathodes, *Monatsh. Chem.* 140 (2009) 985–999.

4 Studies of microstructure and phase stability of perovskites

4.1 Summary

This chapter deals with the investigation of the effect of microstructure on BSCF and SCF membranes and the influence of partial B-site substitution on long-term stability of the well known BSCF material.

In section 4.2 membranes of BSCF and SCF with different grain size distributions were obtained by variation of the dwell times between 2 and 32 hours. The grain growth was found to follow a power law. The grains of SCF exhibited an average grain size from 11.3 to 19.9 μm , whereby the average grain size of BSCF was found to reach from 13.9 to 41.3 μm . The membranes with larger grains showed a reduction of oxygen flux for the SCF system, which may be related to a phase transition to an oxygen ordered $\text{SrCo}_{0.8}\text{Fe}_{0.2}\text{O}_{2.5}$ brownmillerite by-phase, which was identified by TEM. The BSCF membranes exhibited a reduced oxygen flux for smaller grains. With larger grain size the oxygen flux increased, but it was found that it was nearly independent from grain sizes in the regiment between 24 to 42 μm .

Section 4.3 deals with investigations of B-site zirconium substitution to improve the long-time stability of BSCF. The series of $(\text{Ba}_{0.5}\text{Sr}_{0.2})(\text{Co}_{0.8}\text{Fe}_{0.2})_{1-x}\text{Zr}_x\text{O}_{3-\delta}$ ($x = 0.01, 0.03, 0.05, 0.07, \text{ and } 0.09$) was synthesized and it was found using XRD and TEM, that the composition up to $x = 0.03$ consists of a single phase cubic perovskite phase. With higher zirconium content a $(\text{Ba,Sr})\text{ZrO}_3$ secondary phase formed and the oxygen permeation flux decreased considerably. Long-term oxygen permeation measurements and *in-situ* XRD reveal that a relative stabilization compared to undoped BSCF is achieved. However, the overall stability still remains poor.

4.2 Effect of microstructure on oxygen permeation of $\text{Ba}_{0.5}\text{Sr}_{0.5}\text{Co}_{0.8}\text{Fe}_{0.2}\text{O}_{3-\delta}$ and $\text{SrCo}_{0.8}\text{Fe}_{0.2}\text{O}_{3-\delta}$ membranes

Tobias Klande, Olga Ravkina, and Armin Feldhoff

Journal of the European Ceramic Society **33** (2013) 1129-1136

Available online at www.sciencedirect.com

SciVerse ScienceDirect



Journal of the European Ceramic Society 33 (2013) 1129–1136

www.elsevier.com/locate/jeurceramsoc

Effect of microstructure on oxygen permeation of $\text{Ba}_{0.5}\text{Sr}_{0.5}\text{Co}_{0.8}\text{Fe}_{0.2}\text{O}_{3-\delta}$ and $\text{SrCo}_{0.8}\text{Fe}_{0.2}\text{O}_{3-\delta}$ membranes

Tobias Klande*, Olga Ravkina, Armin Feldhoff

Institute of Physical Chemistry and Electrochemistry, Leibniz Universität Hannover, Callinstr. 3a, D-30179 Hannover, Germany

Received 25 July 2012; received in revised form 23 November 2012; accepted 26 November 2012

Available online 27 December 2012

Abstract

The effect of grain size on oxygen permeation properties of $\text{Ba}_{0.5}\text{Sr}_{0.5}\text{Co}_{0.8}\text{Fe}_{0.2}\text{O}_{3-\delta}$ (BSCF) and $\text{SrCo}_{0.8}\text{Fe}_{0.2}\text{O}_{3-\delta}$ (SCF) membranes was investigated by variation of the dwell time. The membrane microstructure was examined by field-emission scanning microscopy (FE-SEM) and then evaluated using a statistical approach. With longer dwell times the grain growth was stimulated and led to grains with a narrower size distribution. The grains of SCF (average size from 11.3 to 19.9 μm) were found to be smaller than those of BSCF (average size from 13.9 to 41.3 μm). The oxygen permeation flux of BSCF membranes was found to be independent of grain size in the range from 24 to 42 μm . However, membranes with smaller grains (13.9 μm) show a decreased oxygen permeation flux. For the SCF membranes a decrease in permeation flux with larger grains was observed for average grain sizes between 11.3 and 19.9 μm . By transmission electron microscopy (TEM) formation of an oxygen ordered $\text{SrCo}_{0.8}\text{Fe}_{0.2}\text{O}_{2.5}$ brownmillerite by-phase could be observed at the oxygen-depleted sweep side of the membrane.
© 2012 Elsevier Ltd. All rights reserved.

Keywords: Microstructure; Grain size; Oxygen permeation; Scanning electron microscopy; Transmission electron microscopy

1. Introduction

The emission of green-house gases from fossil power plants can be reduced by sequestration of CO_2 by oxyfuel combustion.¹ In this process the fuel is directly combusted with pure oxygen and the reaction products, water and CO_2 , can be easily separated from each other by condensation. The required oxygen for this technology can be produced by the use of mixed ionic–electronic conductors (MIECs) as oxygen-transporting membranes (OTMs).² For this application, ceramic membrane materials with good oxygen-ionic and electronic conductivities are advantageous, which are often classic ABO_3 perovskite materials. Other structures such as fluorites or perovskite-related structures like $\text{La}_2\text{NiO}_{4+\delta}$ are known to possess slightly lower oxygen permeation properties.³ Among the perovskite materials $\text{Ba}_{0.5}\text{Sr}_{0.5}\text{Co}_{0.8}\text{Fe}_{0.2}\text{O}_{3-\delta}$ (BSCF) is known to possess the highest stable oxygen permeability under long-term conditions at high temperatures ($T > 1123 \text{ K}$).⁴ To obtain further optimized membranes the focus is on: (i) technical improvements such as

asymmetric membrane design⁵; (ii) optimization of microstructure and processing parameters.⁶ In fact, the influence of microstructure on membrane properties has to be understood but it is discussed controversially throughout a lot of different studies and materials. For $(\text{La}_{0.5}\text{Sr}_{0.5})\text{FeO}_{3-\delta}$, Diethelm et al. reported lower oxygen permeation performance with larger grain size.⁷ This matches with measurements by Kusaba et al. and Etchegoyen et al. who reported analogous results for $\text{La}_{0.1}\text{Sr}_{0.9}\text{Co}_{0.9}\text{Fe}_{0.1}\text{O}_{3-\delta}$ and $\text{La}_{0.6}\text{Sr}_{0.4}\text{Fe}_{0.9}\text{Ga}_{0.1}\text{O}_{3-\delta}$ perovskite material.^{8,9} Watanabe et al. observed this behavior for $\text{Ba}_{0.95}\text{La}_{0.05}\text{FeO}_{3-\delta}$.¹⁰ For the perovskite-related anisotropic oxygen conductor $\text{La}_2\text{NiO}_{4+\delta}$ as well, a decrease of oxygen permeation with larger grains, thus fewer grain boundaries, was reported.¹¹ Also for so called dual-phase membranes a decrease of oxygen flux was found for larger grains for $\text{Ce}_{0.85}\text{Sm}_{0.15}\text{O}_{3-\delta}$ – $\text{Sm}_{0.6}\text{Sr}_{0.4}\text{FeO}_{3-\delta}$.¹² Other groups showed a increase of oxygen flux for larger grains – therefore a negative impact of grain boundaries – for $(\text{Ba}_{0.5}\text{Sr}_{0.5})(\text{Fe}_{0.8}\text{Zn}_{0.2})\text{O}_{3-\delta}$,¹³ $\text{Ca}(\text{Ti}_{0.8}\text{Fe}_{0.2})\text{O}_{3-\delta}$,¹⁴ $\text{LaCoO}_{3-\delta}$,^{15,16} $(\text{La}_{0.6}\text{Sr}_{0.4})(\text{Co}_{0.2}\text{Fe}_{0.8})\text{O}_{3-\delta}$,¹⁷ $\text{La}_{0.3}\text{Sr}_{0.7}\text{CoO}_{3-\delta}$,¹⁸ $\text{Sr}(\text{Co},\text{Fe},\text{Cu},\text{Cr})\text{O}_{3-\delta}$,¹⁹ and $\text{SrFe}(\text{Al})\text{O}_{3-\delta}$ – SrAl_2O_4 composites.²⁰ However, for the system $(\text{Ba}_{1-x}\text{Sr}_x)(\text{Co}_{0.8}\text{Fe}_{0.2})\text{O}_{3-\delta}$ contradicting results were reported. For the end member $\text{SrCo}_{0.8}\text{Fe}_{0.2}\text{O}_{3-\delta}$ larger

* Corresponding author. Tel.: +49 511 762 2943; fax: +49 511 762 19121.
E-mail address: tobias.klande@pci.uni-hannover.de (T. Klande).

oxygen permeation with decreasing grain size was reported.²¹ Grain size of BSCF was reported to have a strong influence,²² small influence²³ or no influence.^{24,25} In this study on BSCF and SCF we prepared different membranes with different microstructure by changing the dwell time during sintering. All samples were investigated using X-ray diffraction (XRD) to ensure phase purity. The microstructure was investigated by field-emission scanning electron microscopy (FE-SEM) and the obtained micrographs were analyzed to obtain the grain sizes. The different membranes were investigated by oxygen permeation measurements to observe the influence of different grain sizes. Transmission electron microscopy (TEM) was used to investigate the microstructure after permeation experiments.

2. Experimental

Powders of $\text{SrCo}_{0.8}\text{Fe}_{0.2}\text{O}_{3-\delta}$ (SCF) and $\text{Ba}_{0.5}\text{Sr}_{0.5}\text{Co}_{0.8}\text{Fe}_{0.2}\text{O}_{3-\delta}$ (BSCF) were prepared via a combined citrate and ethylene-diamine-tetraacetic acid (EDTA) complexing method as described elsewhere.²⁶ Stoichiometric amounts of metal oxides were dissolved in water with subsequent addition of complexing agents and $\text{NH}_3 \cdot (\text{H}_2\text{O})$. The obtained aqueous solution was changed into a gel by continuous stirring and heating. After combustion in a heating mantle, the powders were precalcined at 1173 K in air for 10 h with heating and cooling rates of 2 K min^{-1} . The ground powders were uniaxially pressed into 16 mm green bodies at 150 kN for 20–30 min. The final sintering process was conducted at 1373 K with a heating and cooling rate of 1 K min^{-1} in ambient air atmosphere with different dwell times of 2, 4, 8, 16, and 32 h. The relative densities were measured via the Archimedes method on a Sartorius balance model BP 211D with a resolution of 0.01 mg. X-ray diffraction (XRD) analysis was performed using a Bruker AXS D8 Advance diffractometer equipped with a $\text{Cu K}\alpha$ radiation source. Data sets were recorded in a step-scan mode in the 2θ range of $20^\circ \leq 2\theta \leq 90^\circ$ at an interval of 0.02° . All powders, membranes, and ground membranes were investigated to ensure phase purity. The microstructure of the different membranes was investigated in a JEOL JSM-6700F field-emission instrument at a low excitation voltage of 2 kV. Several micrographs of each membrane were taken and then analyzed using the Image J particle analyzer.²⁷ Effective grain diameters were estimated from measured grain areas in μm^2 by assuming circle-shaped grains. For each membrane between 400 and 500 grains were evaluated. Oxygen permeation was measured in a custom-made high-temperature permeation cell, as described elsewhere.¹³ Both sides of each membrane were carefully polished with 800 mesh emery paper and then sealed on an alumina tube with a gold cermet (Heraeus). The feed side was fed with synthetic air (20 vol.% O_2 /80 vol.% N_2) at a rate of 150 mL min^{-1} , whereas Ne (1.0 mL min^{-1} , 99.995%) and He (29.0 mL min^{-1} , 99.995%) were fed to the sweep side. An Agilent 7890 gas chromatograph with a Carboxen 1000 column was employed to analyze the gas mixture. The absolute flux rate was calculated using neon as an internal standard. A possible O_2 leakage was calculated and subtracted from the

total O_2 flux after the N_2 concentration was measured. TEM investigations were performed at an accelerating voltage of 200 kV on a JEOL JEM-2100 F-UHR field-emission instrument ($C_s = 0.5 \text{ mm}$, $C_c = 1.2 \text{ mm}$). The microscope was operated as a high-resolution TEM (HRTEM) and in selected area electron diffraction (SAED) mode. The preparation method of TEM specimen is described in detail elsewhere.²⁸

3. Results

All produced powders and crushed membranes were investigated by XRD. The post-calcination process at 1223 K was sufficient to form single-phase material. However, to achieve gas-tight membranes higher sintering temperatures of 1373 K were necessary. The XRD analysis confirmed formation of single-phase cubic perovskite structure (s.g. $Pm\bar{3}m$) as can be seen for example in Fig. 1. The cell parameter for BSCF with $a = 3.986 \text{ \AA}$ and for SCF with $a = 3.872 \text{ \AA}$ are in agreement with literature data (ICSD no. 109462 and 79022).^{29,30} The decrease of the cell parameter with decreasing barium content is in accordance with the cation radii of Ba^{2+} (161 pm) and Sr^{2+} (144 pm).³¹

To judge the quality and gas-tightness of the membranes, the relative density was determined by Archimedes method on sintered membranes. Only membranes with low porosity, which means not more than 10% deviation from the theoretical density, were taken into investigation of the permeation properties (Table 1).

In order to increase the grain size of the material, several membranes were sintered with different dwell times. As expected the average grain size increased with increasing time. Fig. 2 shows surface of all BSCF membranes with corresponding grain size distributions. The slope of the cumulative distribution function shows the spreading around the mean value. A steeper curve represents a smaller variation. By the shape of the curve the amount of grains below a certain grain size can be determined.

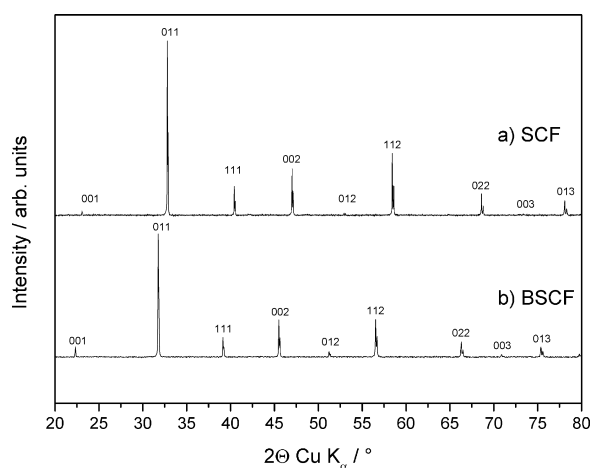


Fig. 1. Room-temperature XRD powder patterns of (a) $\text{SrCo}_{0.8}\text{Fe}_{0.2}\text{O}_{3-\delta}$ (SCF, $a = 3.872 \text{ \AA}$) and (b) $\text{Ba}_{0.5}\text{Sr}_{0.5}\text{Co}_{0.8}\text{Fe}_{0.2}\text{O}_{3-\delta}$ (BSCF, $a = 3.986 \text{ \AA}$). Miller indices are given for cubic symmetry (s.g. $Pm\bar{3}m$).

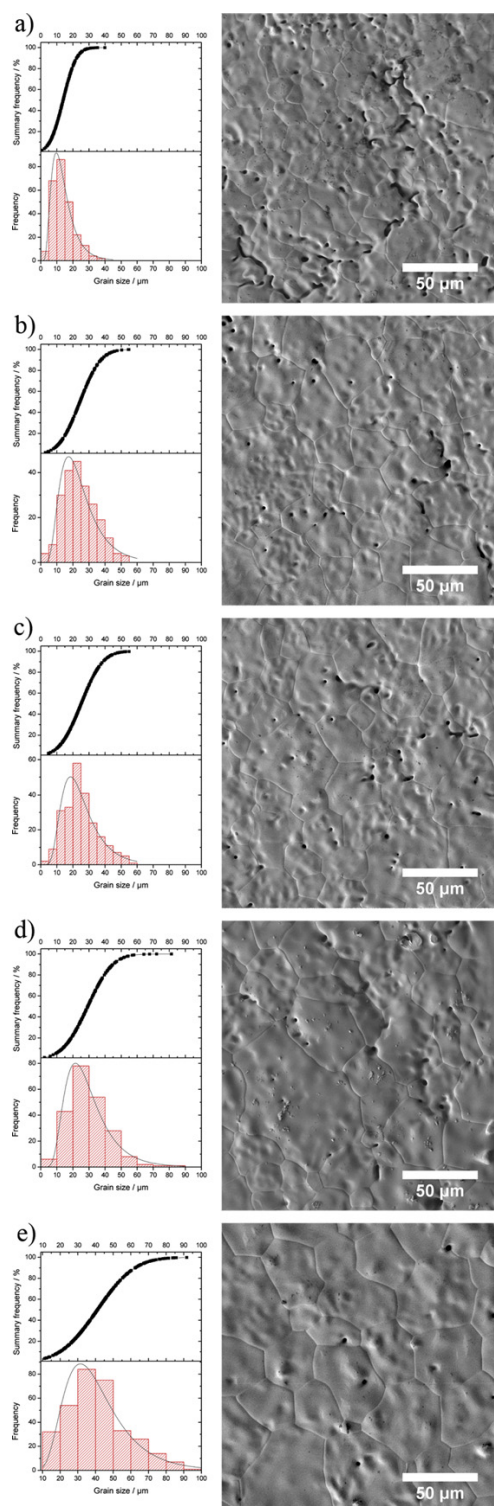


Fig. 2. Cumulative distribution function, log-normal density function, and surface view of $\text{Ba}_{0.5}\text{Sr}_{0.5}\text{Co}_{0.8}\text{Fe}_{0.2}\text{O}_{3-\delta}$ membranes after sintering at 1373 K with different dwell times: (a) 2 h, (b) 4 h, (c) 8 h, (d) 16 h, and (e) 32 h.

Table 1

Overview of samples according to sintering time, density, average grain size, and activation energy.

Sample	Sintering time (h)	Density (% theoretical)	Average grain size (μm)	Act. energy O_2 permeation (kJ mol^{-1})
BSCF 1	2	90.7	13.9	29.7
BSCF 2	4	92.8	24.1	34.9
BSCF 3	8	92.2	25.2	34.8
BSCF 4	16	92.0	29.1	33.5
BSCF 5	32	91.4	41.3	34.5
SCF 1	8	94.2	11.3	46.8
SCF 2	16	94.1	15.1	46.6
SCF 3	32	94.3	19.9	55.8

The obtained grain sizes were plotted as histograms. Then, they were fitted with log-normal distribution density function. For each sintering time more than 400 different grains were analyzed and the spreading correlates to a log-normal distribution.

The average grain size as estimated by SEM micrographs increases from 13.9 to 41.3 μm . The grain size for BSCF sintered for 2 h is in the range of 1–40 μm whereby most of the grains are between 5 and 16 μm . With longer dwell times the growth of bigger grains was stimulated. The membrane sintered for 4 h exhibited grains in the range of 3–55 μm with the majority of grains between 15 and 25 μm . When sintered for 8 h the grain size spans from 5 to 60 μm with a lot of grains between 20 and 30 μm . A dwell time of 16 h leads to a grain size distribution between 6 and 90 μm with many grains between 20 and 40 μm . When sintered for 32 h the grain sizes distribute between 10 and 90 μm with most of the grains are around 30–50 μm . The slope of the cumulative distribution function shows an inhomogeneous distribution of grains for the BSCF 2 h sample. With increasing dwell time the grain size distribution is shifted to larger grains with smaller scatter around the mean value, as can be seen in Fig. 2. The grain size of all BSCF samples plotted as a function of dwell time is shown in Fig. 3. The grain growth follows a

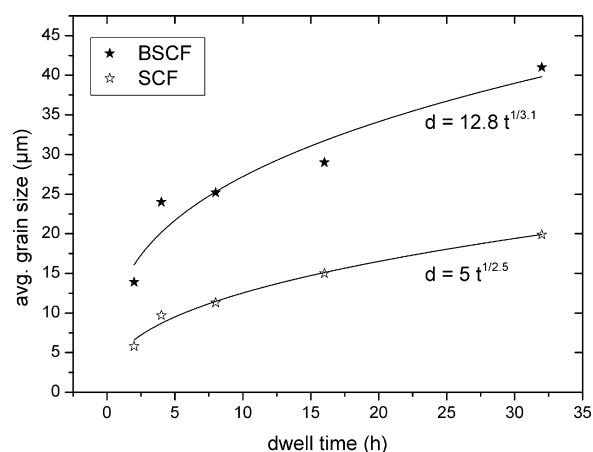


Fig. 3. Dependence of the average grain size on dwell time during sintering at 1373 K for $\text{Ba}_{0.5}\text{Sr}_{0.5}\text{Co}_{0.8}\text{Fe}_{0.2}\text{O}_{3-\delta}$ and $\text{SrCo}_{0.8}\text{Fe}_{0.2}\text{O}_{3-\delta}$. Fitting was performed using the power law $d = kt^{1/n}$.³²

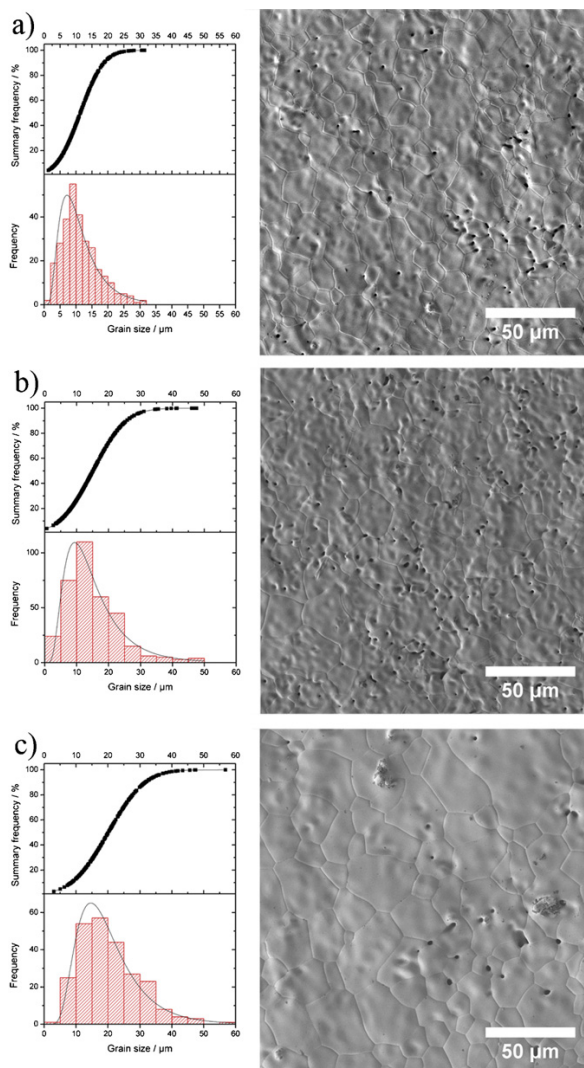


Fig. 4. Cumulative distribution function, log-normal density function, and surface view of $\text{SrCo}_{0.8}\text{Fe}_{0.2}\text{O}_{3-\delta}$ membranes after sintering at 1373 K with different dwell times: (a) 8 h, (b) 16 h, and (c) 32 h.

power law $d = kt^{1/n}$,³² where k is the grain growth constant and n the grain growth exponent. Experimental results show a variation for metals and ceramics for n between 2 and 4.³³ The grain growth constant and the grain growth exponent for BSCF were estimated to be 12.8 and 3.1. The change in porosity was insignificant for the different dwell times.

For SCF analogous behavior was observed with an increase of the grain size from 11.3 to 19.9 μm (Fig. 4). The grain size of SCF sintered for 8 h ranges from 1 to 34 μm with most of the grains between 7 and 11 μm . When sintered for 16 h, grains between 2 and 48 μm with a dominant fraction between 10 and 15 μm were found. For the sample sintered for 32 h the grain size spans from 2 to 58 μm with the majority of grains around 12–18 μm . The variation of grain sizes around the mean value, obtained by cumulative distribution function, behaves

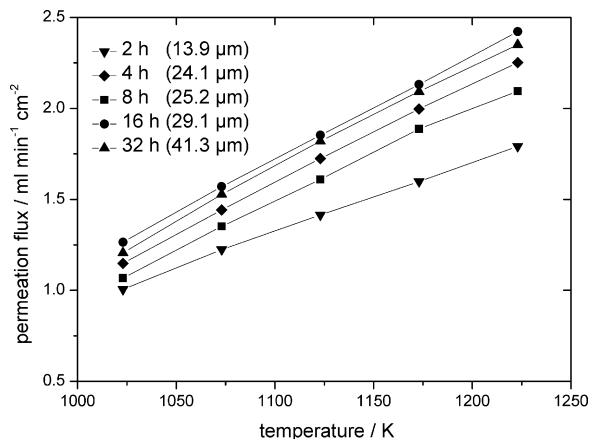


Fig. 5. Oxygen-permeation flux of $\text{Ba}_{0.5}\text{Sr}_{0.5}\text{Co}_{0.8}\text{Fe}_{0.2}\text{O}_{3-\delta}$ membranes after sintering at 1373 K for different dwell times. Average grain sizes are indicated as estimated from Fig. 2.

similarly as reported for BSCF above. However, the grains in the SCF membranes compared to the BSCF membranes were much smaller at same dwell times and temperatures. The grain size increased, as expected, by a power law dependence with dwell time (Fig. 3). The grain growth constant and the grain growth exponent for SCF were estimated to be 5 and 2.5. This is in contrast to the findings by Zhang et al., who reported before, that grain size for SCF does not depend on sintering time at 1327 K.²¹ Sintering times of 2 and 4 h in case of SCF did not lead to gas-tight ceramics, so that these samples were excluded in this study.

The oxygen permeation measurements for the BSCF system are shown in Fig. 5. The membrane sintered for 2 h with an average grain size of 13.9 μm exhibited the lowest permeation flux of 1.6 $\text{mL min}^{-1} \text{cm}^{-2}$ at 1173 K. With further increase of the grain size the permeation rate remained identically at around 2 $\text{mL min}^{-1} \text{cm}^{-2}$. The relative deviation between the oxygen flux of the samples sintered for 4 and 8 h is 5.5%. For the samples sintered for 16 and 32 h it is 1.8%. Both are inside the measurement uncertainty. The deviation of the sample sintered for 2 h compared to the sample sintered for 4 h is 20.1%. The activation energies calculated by Arrhenius representation are around 35 kJ mol^{-1} for membranes sintered between 4 and 32 h. The membrane sintered for 2 h exhibited a slightly decreased activation energy of 29 kJ mol^{-1} . However, this is in accordance with earlier reported values for BSCF membranes of 25–30 kJ mol^{-1} in the temperature range of 973–1173 K²⁴ and 40.9 kJ mol^{-1} in the temperature range of 1048–1223 K.⁴

For SCF the membrane with the smallest grains of 11.3 μm exhibited the highest flux of 1.92 $\text{mL min}^{-1} \text{cm}^{-2}$. However, with increasing grain size the permeation flux decreases (Fig. 6), which is opposite behavior to that of BSCF as described before. The relative deviation between the oxygen permeation fluxes for the samples sintered for 8 and 16 h is 6.8% and for the samples sintered for 16 and 32 h 20.7%. The activation energy for the oxygen permeation estimated by Arrhenius representation was around 46 kJ mol^{-1} for the membranes sintered for 8 and

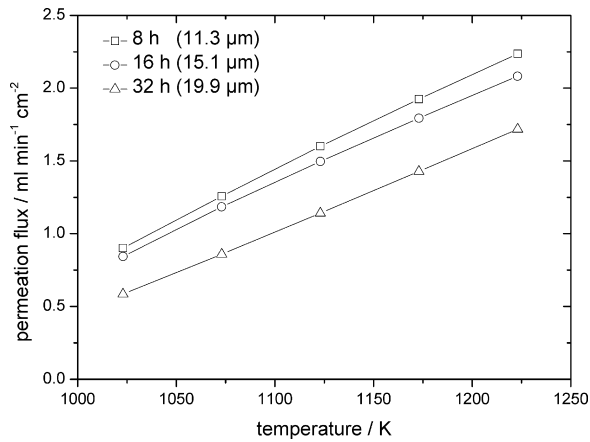


Fig. 6. Oxygen-permeation flux of $\text{SrCo}_{0.8}\text{Fe}_{0.2}\text{O}_{3-\delta}$ after sintering at 1373 K for different dwell times. Average grain sizes are indicated as estimated from Fig. 4. For short dwell times (2 h, 4 h) no dense membranes for oxygen permeation measurements could be obtained.

16 h. The membrane sintered for 32 h exhibited slightly higher activation energy of 55.7 kJ mol^{-1} . Fig. 7a shows a bright-field TEM micrograph of the sweep side of the SCF 32 h membrane. The insets show the sample regions, which were investigated by high-resolution TEM (Fig. 7b–d). The determination of the zone axis for each grain was performed by two-dimensional fast Fourier transformation shown as insets on each corresponding grain. The grain boundaries were atomically thin without any interface phases between orthorhombic brownmillerite grains I and II, as well as between brownmillerite grain II and cubic perovskite grain III.

4. Discussion

Some groups reported about the influence of microstructure on functional properties of oxygen-transporting materials, e.g. BSCF and SCF. It is hard to determine the dominating oxygen-transport paths for materials because they can change with composition. The main mechanisms for oxygen diffusion are bulk and grain boundary diffusion. The diffusion through

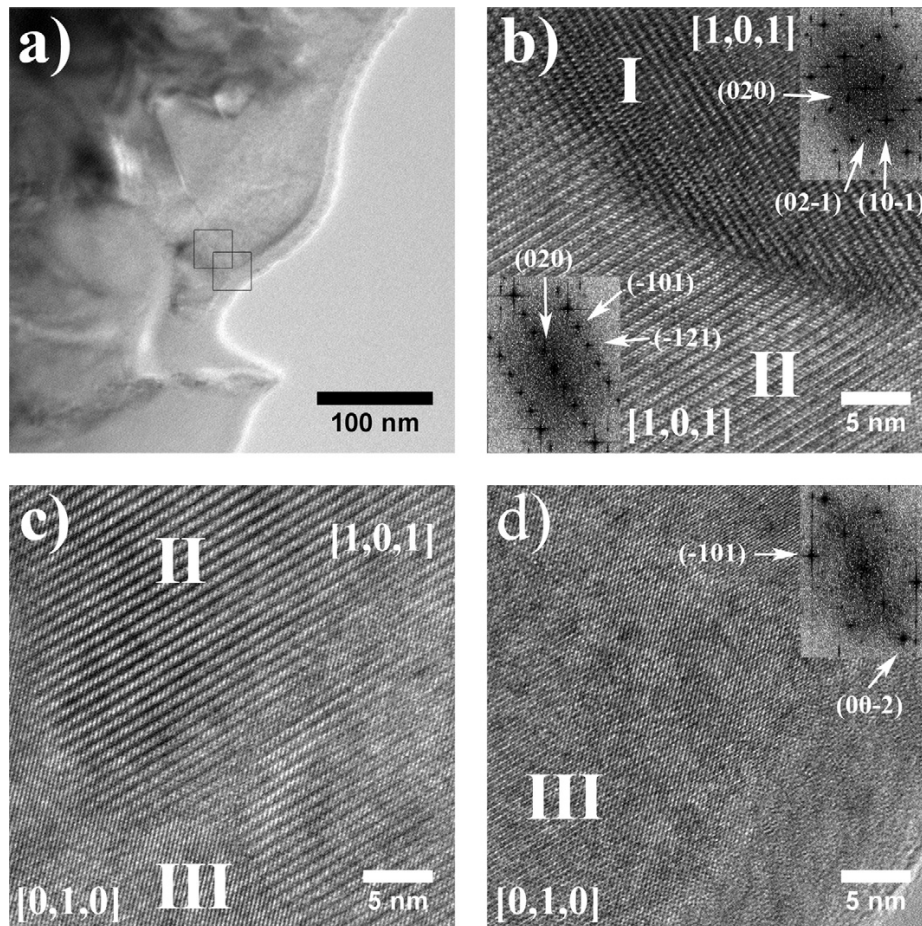


Fig. 7. (a) Bright-field TEM of the sweep side of the $\text{SrCo}_{0.8}\text{Fe}_{0.2}\text{O}_{3-\delta}$ membrane, (b) grain boundary between two brownmillerite grains I and II, which are both viewed along $[1,0,1]$ zone axis, but with different in-plane rotation (c) interface between brownmillerite II and perovskite III and (d) perovskite III viewed along zone axis $[0,1,0]$. Insets showing the two-dimensional fast Fourier transformed of the corresponding grains.

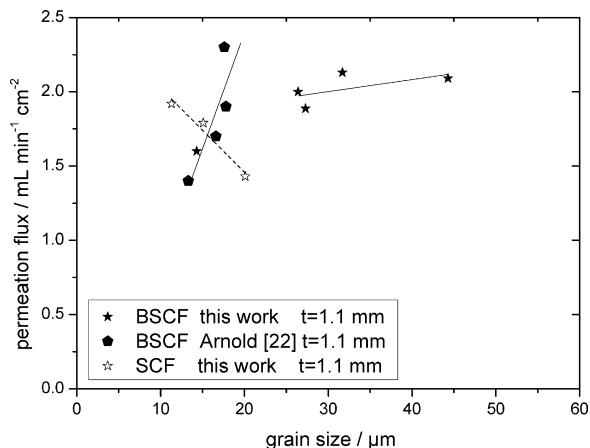


Fig. 8. Dependence of oxygen-permeation flux on the average grain size for $\text{Ba}_{0.5}\text{Sr}_{0.5}\text{Co}_{0.8}\text{Fe}_{0.2}\text{O}_{3-\delta}$ and $\text{SrCo}_{0.8}\text{Fe}_{0.2}\text{O}_{3-\delta}$ at 1173 K. The data points are taken from this work (Figs. 5 and 6) and from Arnold et al.²²

pores may have an additional effect. However, Bauman et al. already showed low influence of porosity up to 15% in samples of BSCF.²⁴

If grain-boundary diffusion is predominant, small grains are favorable. Otherwise, if bulk diffusion is the major contribution, large grains are favorable. The third possibility is no effect in the observed grain size spectrum. Grain growth can be easily induced by increasing the dwell time and sintering temperature for the BSCF and SCF membranes. Furthermore, a possible influence of the microstructure on surface exchange rates has to be kept in mind. By reducing the thickness below a characteristic value the oxygen flux is predominantly controlled by surface exchange reactions. With increasing thickness the ionic transport is governed by a combination of both processes and will be finally controlled predominantly by bulk diffusion for thick membranes. The ratio of grains and grain boundaries therefore affects both surface exchange rates and bulk diffusion coefficients. Which transport mechanism is significant, depends on membrane thickness, temperature, oxygen partial pressure gradients and possibly phase instability and/or demixing.³⁴

In Fig. 8 an overview of our measured data for BSCF and the results of Arnold et al. is given.²² In previous publications Wang et al. observed a slight increase of permeation flux with increasing grain size between 55 and 80 μm ,²³ whereby the work of Baumann et al. showed a small decrease of permeation flux in the range of 10–45 μm ,²⁴ and the result from Salehi et al. indicate no effect on permeation flux in the grain size range of 3–18 μm .²⁵ These results give raise to the assumption that there is no significant contribution of the grain size in the observed grain size regiment. However, according to the data from Arnold et al., who found a strong dependence for small grain sizes, i.e. predominant bulk diffusion, which is in favor of large grains, was observed in the range of 12–18 μm .²² The small grain sizes were achieved by using boron nitride as sintering aid. By HRTEM investigations of the grain boundaries and electron-energy loss spectroscopy of the grains no

boron containing phase could be detected after sintering of the membranes. The results of Arnold et al. are in agreement with our findings for a membrane with an average grain size of 13.9 μm . However, with further increase in the average grain size beyond 24 μm the variation of permeation flux is not significantly changed. A significant influence of larger grains on oxygen permeation in the grain size range of 24.1–41.3 μm could not be observed.

For SCF membranes, the oxygen permeation flux was decreased with larger grain sizes, which is in agreement with results of Zhang et al.²¹ This leads to the assumption that the grain boundaries provide a faster path for oxygen transport. The increase in grain boundaries may affect the surface exchange and diffusion processes. The grain boundaries, which exhibit a higher defect concentration than the bulk material, should promote oxygen transport. Zhang et al. observed this behavior and a decrease of permeation flux on 2 mm thick membranes in the grain size regiment from 4 to 15 μm . Our measurements, which were extended to the range of 11.3–19.9 μm , could confirm this trend (Fig. 8). However, due to the low oxygen partial pressure in the used helium gas ($p(\text{O}_2) \approx 10^{-4}$ atm) a partial formation of a small amount of brownmillerite by-phase at the sweep side of the membrane, which leads to lower oxygen conductivity³⁵ would be another possible explanation. The increase in oxygen permeation by smaller grains may then be additionally attributed to stabilization of an oxygen-disordered phase, as observed for cobalt-substituted bismuth vanadate.³⁶ As shown in our TEM investigations at the sweep side of the SCF membrane sintered for 32 h an orthorhombic brownmillerite phase could be identified (Fig. 7). The XRD patterns taken from the sweep side showed single-phase cubic perovskite material. Also EDXS measurements performed on brownmillerite and perovskite grains give no evidence of difference in chemical composition, which leads to the conclusion that ordering of oxygen between $\text{SrCo}_{0.8}\text{Fe}_{0.2}\text{O}_{3-\delta}$ and $\text{SrCo}_{0.8}\text{Fe}_{0.2}\text{O}_{2.5}$ phases occurs. This is also indicated by Fig. 7c, which shows a sluggish transition between the brownmillerite II and perovskite III. A biphasic reversible transition of brownmillerite to perovskite was also found for $\text{SrCoO}_{3-\delta}$ ($\delta = 0.25\text{--}0.5$) material by Toquin et al. who did electrochemical oxygen intercalation with simultaneous in situ neutron powder diffraction.³⁷ As was reported by Bouwmeester et al.³⁴ and Qiu et al.³⁵ the surface exchange rates play a decisive role in SCF materials. The overall transport kinetics are probably not completely governed by the surface exchange reaction due to relative thick membranes. However, a formation of oxygen ordered by-phases like brownmillerites can cause the observed decrease in permeation flux. This may also explain the increase in activation energy for the sample sintered for 32 h compared to the samples sintered at 8 and 16 h.

5. Conclusions

The microstructural properties of BSCF and SCF membranes, which were sintered for different dwell times, were investigated in order to elucidate a possible influence on the oxygen-transport performance. The distribution of the grain size

was affected by dwell times, whereby a power law dependence of the grain growth with time was observed. The grains of SCF membranes were found to be smaller than the grains of BSCF membranes at same dwell times and sintering temperatures. The oxygen permeation flux of BSCF membranes was found to be independent of grain size in the grain size regiment from 24 to 42 μm . However, membranes with smaller grains (13.9 μm) show a decrease in oxygen permeation flux. It is believed that there is an onset threshold in grain size after that the microstructural influence on the permeation flux becomes insignificant. For the SCF membranes a decrease in permeation flux with larger grains was observed for average grain sizes between 11.3 and 19.9 μm . This behavior was reported earlier by Zhang et al. for average grain sizes between 4 and 15 μm . It may be explained by faster grain-boundary diffusion and/or phase stabilization by smaller grains, which inhibit formation of an oxygen-ordered by-phase.

Acknowledgements

The authors greatly acknowledge financial support from the Chinese-German Centre for Science (GZ676) and the Deutsche Forschungsgemeinschaft (FE 928/4-1) and fruitful discussions with Prof. Jürgen Caro.

References

- Bredesen R, Jordal K, Bolland A. High-temperature membranes in power generation with CO_2 capture. *Chem Eng Process* 2004;**43**: 1129–58.
- Wang HH, Werth S, Schiestel T, Caro J. Perovskite hollow-fiber membranes for the production of oxygen-enriched air. *Angew Chem Int Ed* 2005;**44**:6906–9.
- Sunarso J, Baumann S, Serra JM, Meulenberg WA, Liu S, Lin YS, et al. Mixed ionic–electronic conducting (MIEC) ceramic-based membranes for oxygen separation. *J Membr Sci* 2008;**320**:13–41.
- Shao ZP, Yang WS, Cong Y, Dong H, Tong JH, Xiong GX. Investigation of the permeation behavior and stability of a $\text{Ba}_{0.5}\text{Sr}_{0.5}\text{Co}_{0.8}\text{Fe}_{0.2}\text{O}_{3-\delta}$ oxygen membrane. *J Membr Sci* 2000;**172**:177–88.
- Baumann S, Serra JM, Lobera MP, Escolastico S, Schulze-Kuppers F, Meulenberg WA. Ultrahigh oxygen permeation flux through supported $\text{Ba}_{0.5}\text{Sr}_{0.5}\text{Co}_{0.8}\text{Fe}_{0.2}\text{O}_{3-\delta}$ membranes. *J Membr Sci* 2011;**377**: 198–205.
- Kharton VV, Marques FMB. Mixed ionic–electronic conductors: effects of ceramic microstructure on transport properties. *Curr Opin Solid State Mater Sci* 2002;**6**:261–9.
- Diethelm S, Van Herle J, Sfeir J, Buffat P. Correlation between oxygen transport properties and microstructure in $\text{La}_{0.5}\text{Sr}_{0.5}\text{FeO}_{3-\delta}$. *J Eur Ceram Soc* 2005;**25**:2191–6.
- Kusaba H, Shibata Y, Sasaki K, Teraoka Y. Surface effect on oxygen permeation through dense membrane of mixed-conductive LSCF perovskite-type oxide. *Solid State Ionics* 2006;**177**:2249–53.
- Etchegoyen G, Chartier T, Del-Gallo P. Oxygen permeation in $\text{La}_{0.6}\text{Sr}_{0.4}\text{Fe}_{0.9}\text{Ga}_{0.1}\text{O}_{3-\delta}$ dense membrane: effects of surface microstructure. *J Solid State Electrochem* 2006;**10**:597–603.
- Watanabe K, Ninomiya S, Yuasa M, Kida T, Yamazoe N, Haneda H, et al. Microstructure effect on the oxygen permeation through $\text{Ba}_{0.95}\text{La}_{0.05}\text{FeO}_{3-\delta}$ membranes fabricated by different methods. *J Am Ceram Soc* 2010;**93**:2012–7.
- Klande T, Efimov K, Cusenza S, Becker KD, Feldhoff A. Effect of doping, microstructure, and CO_2 on $\text{La}_2\text{NiO}_{4+\delta}$ -based oxygen-transporting materials. *J Solid State Chem* 2011;**184**:3310–8.
- Li Q, Zhu X, He Y, Cong Y, Yang W. Effects of sintering temperature on properties of dual-phase oxygen permeable membranes. *J Membr Sci* 2011;**367**:134–40.
- Martynczuk J, Arnold M, Feldhoff A. Influence of grain size on the oxygen permeation performance of perovskite-type $(\text{Ba}_{0.5}\text{Sr}_{0.5})(\text{Fe}_{0.8}\text{Zn}_{0.2})\text{O}_{3-\delta}$ membranes. *J Membr Sci* 2008;**322**:375–82.
- Shaula AL, Fuentes RO, Figueiredo FM, Kharton VV, Marques FMB, Frade JR. Grain size effects on oxygen permeation in submicrometric $\text{CaTi}_{0.8}\text{Fe}_{0.2}\text{O}_{3-\delta}$ ceramics obtained by mechanical activation. *J Eur Ceram Soc* 2005;**25**:2613–6.
- Kharton VV, Naumovich EN, Kovalevsky AV, Viskup AP, Figueiredo FM, Bashmakov IA, et al. Mixed electronic and ionic conductivity of $\text{LaCo}(\text{M})\text{O}_3$ (M=Ga, Cr, Fe or Ni), IV. Effect of preparation method on oxygen transport in $\text{LaCoO}_{3-\delta}$. *Solid State Ionics* 2000;**138**: 135–48.
- Kharton VV, Figueiredo FM, Kovalevsky AV, Viskup AP, Naumovich EN, Yaremchenko AA, et al. Processing, microstructure and properties of $\text{LaCoO}_{3-\delta}$ ceramics. *J Eur Ceram Soc* 2001;**21**: 2301–9.
- Pingyong Z, Ran R, Zhihao C, Hongxia G, Zongping S, da Costa JCD, et al. Significant effects of sintering temperature on the performance of $\text{La}_{0.6}\text{Sr}_{0.4}\text{Co}_{0.2}\text{Fe}_{0.8}\text{O}_{3-\delta}$ oxygen selective membranes. *J Membr Sci* 2007;**302**:171–9.
- Kharton VV, Kovalevsky AV, Yaremchenko AA, Figueiredo FM, Naumovich EN, Shaula AL, et al. Surface modification of $\text{La}_{0.3}\text{Sr}_{0.7}\text{CoO}_{3-\delta}$ ceramic membranes. *J Membr Sci* 2002;**195**:277–87.
- Kharton VV, Tikhonovich VN, Li SB, Naumovich EN, Kovalevsky AV, Viskup AP, et al. Ceramic microstructure and oxygen permeability of $\text{SrCo}(\text{Fe},\text{M})\text{O}_{3-\delta}$ (M=Cu or Cr) perovskite membranes. *J Electrochem Soc* 1998;**145**:1363–73.
- Kharton VV, Kovalevsky AV, Yaremchenko AA, Snijders FMM, Coymans JFC, Luyten JJ, et al. Oxygen transport and thermomechanical properties of $\text{SrFe}(\text{Al})\text{O}_{3-\delta}\text{--SrAl}_2\text{O}_4$ composites: microstructural effects. *J Solid State Electrochem* 2006;**10**:663–73.
- Zhang K, Yang YL, Ponnusamy D, Jacobson AJ, Salama K. Effect of microstructure on oxygen permeation in $\text{SrCo}_{0.8}\text{Fe}_{0.2}\text{O}_{3-\delta}$. *J Mater Sci* 1999;**34**:1367–72.
- Arnold M, Martynczuk J, Efimov K, Wang HH, Feldhoff A. Grain boundaries as barrier for oxygen transport in perovskite-type membranes. *J Membr Sci* 2008;**316**:137–44.
- Wang HH, Tablet C, Feldhoff A, Caro J. Investigation of phase structure, sintering, and permeability of perovskite-type $\text{Ba}_{0.5}\text{Sr}_{0.5}\text{Co}_{0.8}\text{Fe}_{0.2}\text{O}_{3-\delta}$ membranes. *J Membr Sci* 2005;**262**:20–6.
- Baumann S, Schulze-Kueppers F, Roitsch S, Betz M, Zwick M, Pfaff EM, et al. Influence of sintering conditions on microstructure and oxygen permeation of $\text{Ba}_{0.5}\text{Sr}_{0.5}\text{Co}_{0.8}\text{Fe}_{0.2}\text{O}_{3-\delta}$ (BSCF) oxygen transport membranes. *J Membr Sci* 2010;**359**:102–9.
- Salehi M, Clemens F, Pfaff EM, Diethelm S, Leach C, Graule T, et al. A case study of the effect of grain size on the oxygen permeation flux of BSCF disk-shaped membrane fabricated by thermoplastic processing. *J Membr Sci* 2011;**382**:186–93.
- Feldhoff A, Martynczuk J, Wang HH. Advanced $\text{Ba}_{0.5}\text{Sr}_{0.5}\text{Zn}_{0.2}\text{Fe}_{0.8}\text{O}_{3-\delta}$ perovskite-type ceramics as oxygen selective membranes: evaluation of the synthetic process. *Prog Solid State Chem* 2007;**35**:339–53.
- Abramoff MD, Magelhaes PJ, Ram SJ. Image processing with Image. *J Biophotonics Int* 2004;**11**:36–42.
- Arnold M, Wang HH, Feldhoff A. In situ study of the reaction sequence in the sol-gel synthesis of a $(\text{Ba}_{0.5}\text{Sr}_{0.5})(\text{Co}_{0.8}\text{Fe}_{0.2})\text{O}_{3-\delta}$ perovskite by X-ray diffraction and transmission electron microscopy. *J Membr Sci* 2007;**293**:3651–5.
- Koster H, Mertins FHB. Powder diffraction of the cubic perovskite $\text{Ba}_{0.5}\text{Sr}_{0.5}\text{Co}_{0.8}\text{Fe}_{0.2}\text{O}_{3-\delta}$. *Powder Diffr* 2003;**18**:56–9.
- Harrison WTA, Lee TH, Yang YL, Scarfe DP, Liu LM, Jacobson J. A neutron diffraction study of two strontium cobalt iron oxides. *Mater Res Bull* 1995;**30**:621–30.
- Shannon RD. Revised effective ionic radii and systematic studies of interatomic distances in halides and chalcogenides. *Acta Crystallogr, Sect A: Found Crystallogr* 1976;**32**:751–67.

32. El-Khozondar R, El-Khozondar H, Gottstein G, Rollet A. Microstructural simulation of grain growth in two-phase polycrystalline materials. *Egypt J Solids* 2006;**72**:35–47.
33. Anderson MP, Srolovitz DJ, Grest GS, Sahni PS. Computer simulation of grain growth. I. Kinetics. *Acta Metall* 1984;**32**:783–91.
34. Bouwmeester HJM, Kruidhof H, Burggraf AJ. Importance of the surface exchange kinetics as rate limiting step in oxygen permeation through mixed-conducting oxides. *Solid State Ionics* 1994;**72**:185–94.
35. Qiu L, Lee TH, Liu LM, Yang YL, Jacobson AJ. Oxygen permeation studies of $\text{SrCo}_{0.8}\text{Fe}_{0.2}\text{O}_{3-\delta}$. *Solid State Ionics* 1995;**76**:321–9.
36. Steil MC, Fouletier J, Kleitz M, Labrune P. BICOVOX: Sintering and grain size dependence of the electrical properties. *J Eur Ceram Soc* 1999;**93**:815–8.
37. Le Toquin R, Paulus W, Cousson A, Prestipino C, Lamberti C. Time-resolved in situ studies of oxygen intercalation into $\text{SrCoO}_{2.5}$, performed by neutron diffraction and X-ray absorption spectroscopy. *J Am Chem Soc* 2006;**128**:13161–74.

4.3 Investigation of Zr-doped BSCF perovskite membrane for oxygen separation in the intermediate temperature range

Olga Ravkina, Tobias Klande, and Armin Feldhoff

Journal of Solid State Chemistry **201** (2013) 101-106



Investigation of Zr-doped BSCF perovskite membrane for oxygen separation in the intermediate temperature range

Olga Ravkina*, Tobias Klande, Armin Feldhoff

Gottfried Wilhelm Leibniz Universität Hannover, Institute of Physical Chemistry and Electrochemistry, Callinstr. 3A, 30167 Hannover, Germany

ARTICLE INFO

Article history:

Received 17 December 2012

Received in revised form

12 February 2013

Accepted 13 February 2013

Available online 26 February 2013

Keywords:

BSCF

Transmission electron microscopy

Oxygen permeation

Mixed ionic electronic conductors

Long-term phase stability

ABSTRACT

The series of $(\text{Ba}_{0.5}\text{Sr}_{0.5})(\text{Co}_{0.8}\text{Fe}_{0.2})_{1-z}\text{Zr}_z\text{O}_{3-\delta}$ ($z=0, 0.01, 0.03, 0.05, 0.07, \text{ and } 0.09$) was synthesized by a sol-gel method. The materials with a zirconium content up to 3 mol% were found to be single phase. Further increase results in formation of a mixed (Ba,Sr)ZrO₃ by-phase, which was found along the grain boundaries and in the grains. With increasing zirconium content the oxygen permeation flux decreases considerably. The effect of the zirconium substitution on the long-term phase stability was investigated by long-term oxygen permeation experiments and X-ray diffraction. A slight stabilization of the oxygen flux of $(\text{Ba}_{0.5}\text{Sr}_{0.5})(\text{Co}_{0.8}\text{Fe}_{0.2})_{0.97}\text{Zr}_{0.03}\text{O}_{3-\delta}$ was found after 180 h at 1023 K. However, all compositions show a decrease in permeation flux with time, but the pure BSCF membrane exhibited the strongest drop after 180 h of operation. The decomposition products of the cubic perovskite phase were found to be a hexagonal $\text{Ba}_{0.5\pm x}\text{Sr}_{0.5\pm x}\text{CoO}_3$ and a rhombohedral $\text{Ba}_{1-x}\text{Sr}_x\text{Co}_{2-y}\text{Fe}_y\text{O}_{5-\delta}$.

© 2013 Elsevier Inc. All rights reserved.

1. Introduction

Mixed ionic electronic conductors (MIECs) offer the advantage of mobile ionic oxygen species and electrons in the same material. Therefore, they can be used as dense oxygen-transporting membranes (OTMs) for the separation of oxygen from ambient air or in integrated systems as solid oxide fuel cell (SOFC) cathodes [1–3]. This field is clearly ruled by oxides with perovskite structure and features the well-known $\text{Ba}_{0.5}\text{Sr}_{0.5}\text{Co}_{0.8}\text{Fe}_{0.2}\text{O}_{3-\delta}$ (BSCF). This material attained a lot of attention since 2000, when Shao et al. demonstrated the very high oxygen permeation flux for a BSCF membrane over a wide temperature range [3], which is mainly attributed to the high amount of mobile oxygen vacancies in the cubic perovskite lattice [4,5]. In fuel cells BSCF exhibits a low polarization resistance of 0.055–0.071 $\Omega\text{ cm}^{-2}$ at 873 K and 0.51–0.60 $\Omega\text{ cm}^{-2}$ at 773 K in a BSCF|electrolyte|BSCF cell [1].

However, Shao et al. and van Veen et al. discovered that a stable oxygen flux is only achieved when the temperature is higher than 1123 K [3,6]. To reach an economic operation of SOFCs, the temperatures should be lowered to the intermediate temperature range (773–1123 K) [7]. The aforementioned instability of BSCF was observed by several groups, which correlate a slow decrease of the oxygen permeation flux in the intermediate temperature range to a phase decomposition into a non-cubic perovskite [8–10]. Shao et al. and

Rebeilleau-Dassonneville et al. observed additional reflections in the X-ray diffraction (XRD) patterns after long-term measurements, which could not be identified [3,8]. Švarcová et al. extended the XRD investigation and described the unknown phase as a hexagonal 2H or 4H polymorph perovskite [9]. However, the composition of the phase was still unclear. Some hints were delivered by basic investigations of the formation route of BSCF by Arnold et al. They showed that the hexagonal $\text{Ba}_{0.75}\text{Sr}_{0.25}\text{CoO}_{3-\delta}$ is an intermediate on the way to the cubic BSCF structure [11,12]. D. Müller et al. investigated the degradation of BSCF with transmission electron microscopy (TEM) techniques. They found foreign phases in the grains, but focused mainly on the grain boundaries, where they identified a hexagonal phase. They proposed decomposition into the two end members, hexagonal $\text{Ba}_{1-x}\text{Sr}_x\text{CoO}_{3-\delta}$ and cubic $\text{Ba}_x\text{Sr}_{1-x}\text{FeO}_{3-\delta}$ and constructed a simple phase diagram [13]. The first detailed study was performed by Efimov et al., who addressed the grain intergrowth phases. They found a hexagonal phase and a lamellar non-cubic perovskite phase, which was identified as a trigonal perovskite. They suggested a hexagonal $\text{Ba}_{0.6}\text{Sr}_{0.4}\text{CoO}_{3-\delta}$ and a trigonal 15R-related $\text{Ba}_{1-x}\text{Sr}_x\text{Co}_{2-y}\text{Fe}_y\text{O}_{5-\delta}$ oxide as main decomposition products with minor amounts of a mixed barium–strontium oxide $\text{Ba}_{0.4}\text{Sr}_{0.6}\text{O}$ and an iron and strontium-enriched cubic perovskite $\text{Ba}_{0.5-x}\text{Sr}_{0.5+x}\text{Co}_{0.8-y}\text{Fe}_{0.2+y}\text{O}_{3-\delta}$ [10]. Further investigations by Liang et al., who used a dead-end membrane reactor geometry with highly pressurized air (1–5 bar) and vacuum extraction found similar results [14]. The degradation was more severe under the strongly oxidizing conditions at the sweep side rather than under the reducing conditions at the permeate side.

* Corresponding author. Fax: +49 511 762 19121.

E-mail address: olga.ravkina@pci.uni-hannover.de (O. Ravkina).

This view is supported by density functional theory (DFT) calculations by Kuklaja et al. [15] who found that a high concentration of oxygen vacancies stabilizes the cubic phase. The formation energies of the vacancies are significantly smaller in the cubic phase than in the hexagonal phase. Following investigations of BSCF by Ph. Müller et al. confirmed the formation of the hexagonal and trigonal decomposition products. They used the convergent beam electron diffraction (CBED) technique to determine the point group of the trigonal $\text{Ba}_{1-x}\text{Sr}_x\text{Co}_{2-y}\text{Fe}_y\text{O}_{5-\delta}$ [16]. This structure is related to the trigonal 15R barium cobaltite series $\text{Ba}_{n+1}\text{Co}_n\text{O}_{3n+3}(\text{Co}_8\text{O}_8)$ as described by Sun et al. [17]. The first member of this series $\text{Ba}_2\text{CoO}_6(\text{Co}_8\text{O}_8)$ was investigated in consideration of using it as new material for SOFCs by different groups [18–20].

Considering Goldschmidt's tolerance factor [21], which offers a rough estimation whether cubic perovskite structure is formed, based on the ionic radii of the used cations and anions, the radius and spin state change of low- and high-spin $\text{Co}^{2+/3+}$ ions is regarded as the main driving force for the observed phase decomposition [10,12,13,22]. An approach proposed by Švarcová et al. was to partially substitute the B-site cations by fixed valent cations, which exhibit an ionic radius close to that of high-spin Co^{2+} (74.5 pm) [9]. This counteracts the radius decrease during the oxidation to low-spin Co^{3+} (54.5 pm). Some groups reported about B-site substitution of BSCF with Y^{3+} (90 pm), Nb^{3+} (72 pm), or Zr^{4+} (72 pm) [23–25]. All ionic radii for six-fold coordination were taken from Shannon et al. [26]. The substitution of BSCF with varying amounts of zirconium performed by Yakovlev et al. was remarkable, because they found a stabilization of the cubic perovskite phase during long-time in-situ annealing using electrical conductivity relaxation (ECR) measurements [25]. The optimum amount of zirconium substitution was discovered to be 3 mol%.

In this paper, we extend the work of Yakovlev et al. and investigate the effect of B-site zirconium substitution on the stability of BSCF membranes using long-term oxygen permeation experiments and XRD. The series of BSCFZ compounds ($\text{Ba}_{0.5}\text{Sr}_{0.5}(\text{Co}_{0.8}\text{Fe}_{0.2})_{1-z}\text{Zr}_z\text{O}_{3-\delta}$ ($z=0, 0.01, 0.03, 0.05, 0.07, \text{ and } 0.09$)) were synthesized using a standard sol-gel route. The membranes were investigated by scanning electron microscopy (SEM). Furthermore, the microstructure of selected samples was investigated by TEM with combined energy dispersive X-ray spectroscopy (EDXS) analysis of grains and grain boundaries. A Jänecke prism for the Ba–Sr–Co–Fe–Zr system was proposed from XRD and EDXS data.

2. Experimental

2.1. Powder and membrane preparation

Powders of BSCFZ stoichiometry were prepared by a sol-gel route using metal nitrates, citric acid, and ethylenediaminetetraacetic acid (EDTA) as described elsewhere [27,28]. Proper amounts of $\text{Ba}(\text{NO}_3)_2$, $\text{Sr}(\text{NO}_3)_2$, $\text{Co}(\text{NO}_3)_2$, $\text{Fe}(\text{NO}_3)_3$, $\text{ZrO}(\text{NO}_3)_2$ were dissolved in de-ionized water under heating and stirring. EDTA and citric acid were then introduced, so that the total ratio of metal nitrates, EDTA and citric acid was equal to 1:1:1.5. The pH value of the solution was adjusted using $\text{NH}_3 \cdot \text{H}_2\text{O}$ to be in the range of 7–9. The transparent reaction solution was then heated at 423 K under constant stirring for several hours. With the evaporation of water, a dark purple gel was obtained. The gel was then precalcined at 673 K to make the primary powder, which was subsequently calcined for 10 h at 1223 K in air in order to remove organic compounds and obtain the powder with the final composition.

The resulting powders were uniaxially pressed at 10–15 kN for 30 min into green bodies. Followed by the calcination of the pellets at 1373 K for 10 h with a heating and cooling rate of 3 K min^{-1} , dense membrane disks were obtained.

2.2. Characterizations of materials

The phase structure of BSCFZ powders and membranes was characterized by X-ray diffraction (XRD, D8 Advance, Bruker-AXS, with Cu K_α radiation). Data sets were collected in step width of 0.02° in the 2θ range from 20° to 80° .

Scanning electron microscopy (SEM) was performed with a JEOL JSM-6700F field-emission instrument at low excitation voltage of 2 kV with secondary electrons. Specimens of membrane cross-sections were prepared using Buehler a Vibromet 2 vibratory polisher to preserve crystallinity to the very surface. In order to visualize different phases in the polished specimens a backscattered-electron channeling contrast imaging of SEM at 5 kV excitation voltage was used. Transmission electron microscopy (TEM) was performed at 200 kV on a JEOL JEM-2100F-UHR field-emission instrument equipped with light-element energy-dispersive X-ray (EDX) detector (INCA 200 TEM, Oxford Instruments). The microscope was operated as scanning TEM (STEM) in high-angle annular dark-field (HAADF) mode.

The oxygen permeation measurements were performed on a dense membrane disk with diameter 16 mm and a thickness of 1 mm in a high-temperature cell according to the method described elsewhere [29,30]. For the long-term oxygen permeation measurements, the reactor temperature was held at 1023 K for more than 180 h. Air was fed at a rate of 150 mL min^{-1} to the feed side, He (29 mL min^{-1}) and Ne (1 mL min^{-1}), which were used to determine the absolute flux rate of the effluents, were fed to the sweep side. The effluents were analyzed by online-coupled gas chromatography on an Agilent 6890 instrument. The gas concentrations in the effluent stream were calculated from a gas chromatograph calibration. The absolute flux rate of the effluents was determined by using neon as an internal standard. The relative leakage of O_2 , which was evaluated by measuring the amount of N_2 in the effluent stream, was subtracted in the calculation of the oxygen permeation flux.

3. Results and discussion

3.1. Characterization of powders and fresh membranes

The XRD powder patterns of all $(\text{Ba}_{0.5}\text{Sr}_{0.5})(\text{Co}_{0.8}\text{Fe}_{0.2})_{1-z}\text{Zr}_z\text{O}_{3-\delta}$ compounds show reflections from cubic perovskite structure (Fig. 1a). However, only the first members of the BSCFZ system with $z \leq 3 \text{ mol}\%$ consisted of single cubic perovskite phase. With the increasing content of zirconium, additional reflections were evident, indicating the formation of an impurity phase. The by-phase was identified to be a cubic $(\text{Ba,Sr})\text{ZrO}_3$ perovskite, which strongest (1 1 0), (2 0 0) and (2 1 1) reflections occur in the powder diffraction pattern of $(\text{Ba}_{0.5}\text{Sr}_{0.5})(\text{Co}_{0.8}\text{Fe}_{0.2})_{1-z}\text{Zr}_z\text{O}_{3-\delta}$ with $z > 3 \text{ mol}\%$. Lattice parameters of the BSCFZ materials are calculated to be 3.98 Å. Because of minimal difference of the cation size of high spin Co^{2+} (74.5 pm) and Zr^{4+} (72 pm) the lattice parameters of BSCFZ materials change only marginally. As can be seen from SEM micrographs of fresh BSCFZ membrane surfaces the by-phase exerts wide influence on the microstructure of the sample (Fig. 1b). Obviously the formation of the by-phase leads to a decrease of the grain size. While the grains on the BSCF, BSCFZ1 and BSCFZ3 membrane surfaces have a similar average diameter of 20–30 μm , the by-phase formation causes a decline of the average grain diameter down to 1–5 μm .

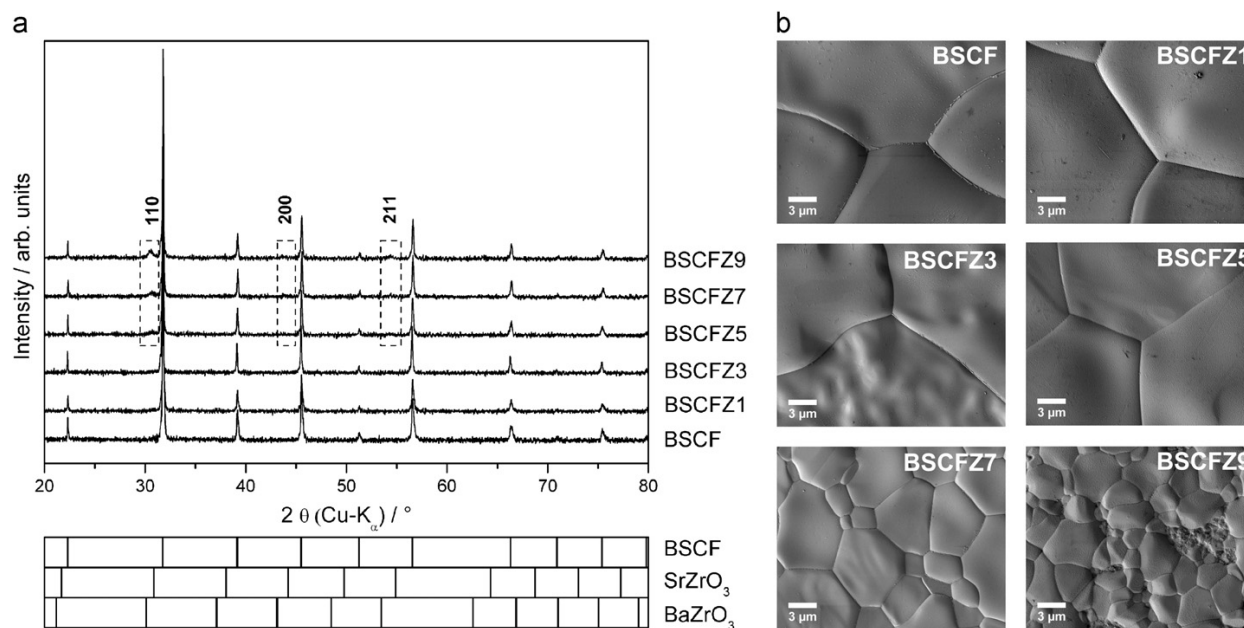


Fig. 1. (a) XRD pattern of BSCFZ powders after calcination for 10 h at 1223 K in air. Major reflections from (Ba,Sr)ZrO₃ by-phase are marked by dashed rectangles (b) SEM micrographs of BSCFZ membrane surfaces after sintering in air at 1373 K for 10 h.

The strongest impact was observed for the BSCFZ9 sample. Because (Ba,Sr)ZrO₃ crystallizes mostly in the grain boundaries, the sintering process and the grain growth could be influenced. The formed by-phase inhibits the material transport through the grain boundaries and obstructs the grain growth of the BSCFZ phase.

Fig. 2 shows EDXS measurements of the BSCFZ, which prove the successful doping with zirconium ions. The increase of zirconium content in the BSCFZ samples can be observed on the increasing intensity of the Zr-L_β-line.

To elucidate these findings, the BSCFZ9 membrane was investigated by TEM. Fig. 3a shows a STEM micrograph of the membrane cross-section. The grain boundaries of the material (2) are decorated with small crystallites with size less than 150 nm. Furthermore, there are some inclusions (3) in the grains itself, although not as numerous as along the boundaries. Elemental distribution by EDXS (Fig. 3b) revealed a strong enrichment of zirconium in these regions. The Zr-L_β-line of the grain boundary by-phase exhibited the strongest intensity, followed by the less zirconium-containing by-phase in the inclusions. Similar results were published by Caro et al. for the BaCo_xFe_yZr_{1-x-y}O_{3-δ} system [31]. The saturation with zirconium ions is reached in the grains and the excess of Zr forms with Ba and Sr cations new zirconium-rich phases, which preferentially crystallize in the grain boundaries. Fig. 2 allows comparison of variations in BSCFZ composition. The Zr-L_β-line for BSCFZ3 material in Fig. 2 corresponds to Zr-L_β-line of the grain in Fig. 3b (BSCFZ9).

A possible explanation for a formation of the by-phase according to the results is the limited miscibility of zirconium ions in the solid solution of BSCF system. Fig. 3c shows a schematic Jänecke prism of BaCoO₃–BaFeO₃–BaZrO₃–SrCoO₃–SrFeO₃–SrZrO₃-compounds. Each of the ternary compounds is located on the corners of the prism. Equilateral triangle areas represent three-component phase diagram. BSCF is located on the side of the triangle with a proportion of 1 of barium and strontium ions. Doping with zirconium can be realized up to 3 mol% (solid line). The dashed line illustrates the miscibility gap in which the system

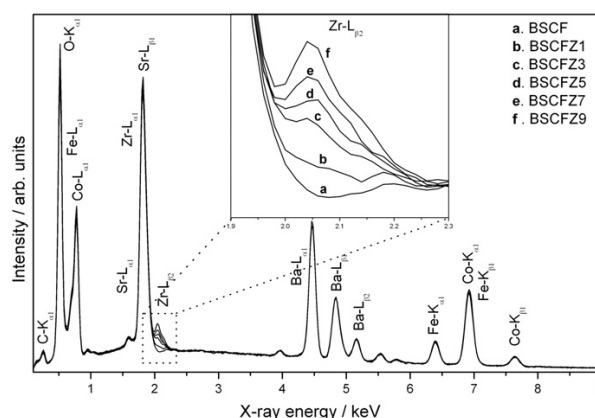


Fig. 2. EDX spectra of the BSCFZ membranes, showing the stronger Zr-L_β-line with increasing content of zirconium. Measurements were made at 10 eV per channel.

demixes to zirconium-rich phases with different compositions. During this demixing process a change of the Ba/Sr ratio, and thus compositional deviation from the shaded triangular plane in Fig. 3c, is also possible.

3.2. Measurements of oxygen permeation through BSCFZ membranes

Measurements of oxygen permeation through gas-tight membranes were carried out in an air/He gradient at temperatures between 1223 K and 1023 K with 50 K steps. To achieve a uniform surface of each membrane, they were polished with polymer-embedded 30 μm diamond lapping film. Fig. 4a shows the results of the oxygen permeation measurements at given conditions for BSCF, BSCFZ3, BSCFZ5, BSCFZ7 and BSCFZ9 membranes. The undoped BSCF membranes demonstrate the highest oxygen permeation flux of 2.1 mL min⁻¹ cm⁻² at 1223 K. This value is

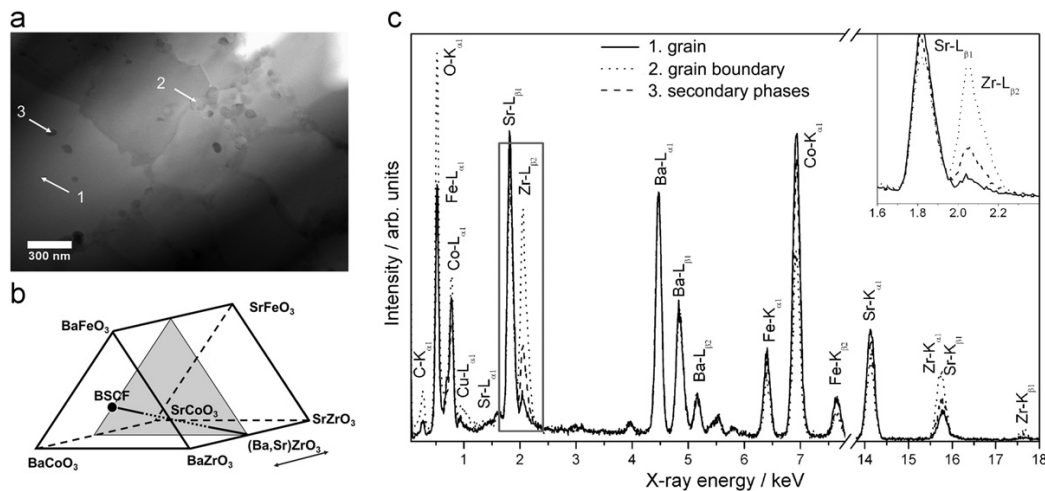


Fig. 3. (a) STEM annular dark-field micrograph of the BSCFZ9 membrane cross-section with labeling areas (1–3) for elemental analysis. (b) EDX spectrum of the selected areas. X-ray lines from C and Cu appear due to a narrow TEM pole piece and do not belong to the specimen. (c) Schematic Jaenecke's prism for Ba–Sr–Co–Fe–Zr oxide system shows the location of BSCF in a quaternary compound system and miscibility gap for more than 3 mol% Zr (dotted line).

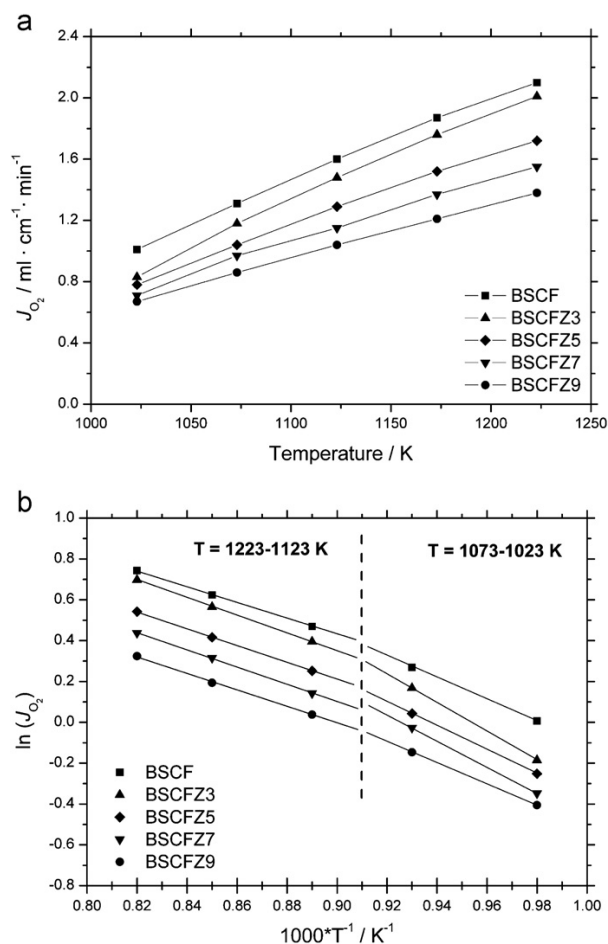


Fig. 4. (a) Oxygen permeation flux through 1 mm thick BSCFZ membranes as function of temperature. Conditions: sweep flow rate: $\text{He} = 29 \text{ mL min}^{-1}$, $\text{Ne} = 1 \text{ mL min}^{-1}$; feed flow rate: 150 mL min^{-1} synthetic air. (b) Arrhenius plot of oxygen permeation flux.

Table 1

Activation energy according to Fig. 3b.

Material	E_a (kJ mol^{-1})	
	1223–1123 K	1073–1023 K
BSCF	31.33	47.85
BSCFZ3	34.61	64.53
BSCFZ5	33.77	58.60
BSCFZ7	33.20	53.77
BSCFZ9	28.26	47.28

comparable to that reported for BSCF by Shao [2]. With increasing Zr^{4+} ion concentration a decline of oxygen permeation can be observed. Because of the higher valence state of Zr^{4+} the oxygen vacancies concentration decreases. Furthermore the enhancement of the metal–oxygen bonding energy leads to the diminishment of the oxygen permeation flux through zirconium-doped materials, because the migration of the oxygen ions is more hindered.

The activation energy of the oxygen ionic conductivity was determined from the temperature dependency of oxygen fluxes by an Arrhenius plot, as given in Fig. 4b. The activation energy of BSCF was determined to be between 31 kJ mol^{-1} and 48 kJ mol^{-1} , which correspond to the value given in the literature [2,32]. The results for BSCFZ are given in Table 1. Nevertheless, it was found, that the activation energies at temperatures between 1073 K and 1023 K are higher, compared to activation energies at elevated temperatures between 1223 K and 1123 K. This may be explained by a greater oxygen vacancy concentration at elevated temperatures. The oxygen content of BSCF decreases with increasing temperatures as was shown by D. Müller et al. using thermo gravimetric analysis (TGA) and Lin et al. using X-ray photoelectron spectroscopy (XPS) [33,34].

3.3. Long-term stability of BSCFZ structure

To investigate the phase stability of the cubic structure in the intermediate temperature range a long-term oxygen permeation experiment was arranged at 1023 K for 180 h. Fig. 5 shows the results of this measurement for BSCFZ membranes. The oxygen permeation flux of BSCF was reduced from $1.0 \text{ mL min}^{-1} \text{ cm}^{-2}$ to

0.44 mL min⁻¹ cm⁻². This result is in a good agreement with the results reported by Shao et al. and Efimov et al. [23,10]. The continuously decreasing oxygen permeation performance can be explained by the formation of secondary phases as reported in literature [10,13–16]. The substitution with zirconium on the *B* site of BSCF should result for one in the lowering of the tolerance factor *t* in the intermediate temperature range, which makes the cubic structure (with *t*=1) more stable at given conditions. Furthermore, the higher charged Zr⁴⁺, compared to Co³⁺, stabilize the neighboring oxygen octahedral and hinder them from twisting. Against the expectations, the zirconium-doped materials did show only a relative stabilization of the oxygen permeation flux at the intermediate temperature. A decline of the oxygen

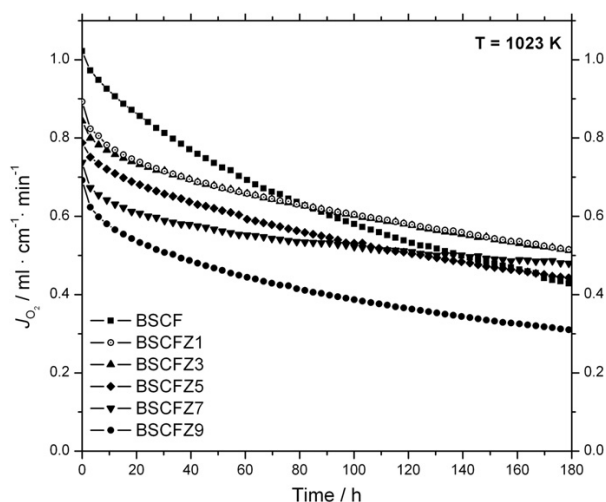


Fig. 5. Long-term oxygen permeation as a function of time at 1023 K. Conditions: sweep flow rate: He=29 mL min⁻¹, Ne=1 mL min⁻¹; feed flow rate: 150 mL min⁻¹ synthetic air. For associated XRD results and SEM micrographs see Fig. 6.

permeation flux was also observed by BSCFZ materials, although in comparison to BSCF the reduction of oxygen permeation flux was not so strong. BSCFZ1 and BSCFZ3 showed the best results in terms of long-term stability and values of the oxygen permeation flux.

Additionally, Fig. 6a shows the XRD patterns of BSCF, BSCFZ3 and BSCFZ7 membrane surfaces after the long-term permeation measurement. The undoped BSCF and BSCFZ9 materials show the degradation. Furthermore, the degradation is most severe under the most oxidizing conditions. The reflections of the hexagonal Ba_{0.5±x}Sr_{0.5±x}CoO_{3-δ} and rhombohedral Ba_{1-x}Sr_xCo_{2-y}Fe_yO_{5-δ} occur with more pronounced intensity on the sweep side in comparison to the permeate side. These results are in good agreement with the result reported by Liang et al. for BSCF dead-end tube membranes [14].

The backscattered-electron channeling contrast images of BSCF and BSCFZ3 membrane cross-sections after the long-term permeation experiment are presented in Fig. 6b. The cubic structure degradation of the BSCF material results in the formation of a hexagonal Ba_{0.5±x}Sr_{0.5±x}CoO_{3-δ}, a trigonal Ba_{1-x}Sr_xCo_{2-y}Fe_yO_{5-δ} and a mixed barium–strontium oxide Ba_{0.5±x}Sr_{0.5±x}O as was observed by in-situ XRD and by TEM EDXS and in previous studies [10]. Furthermore a barium and cobalt depleted cubic perovskite Ba_{0.5-x}Sr_{0.5+x}Co_{0.8-y}Fe_{0.2+y}O_{3-δ} may be proposed [10]. These decomposition products appear mostly, but not exclusively, in the grain boundaries. As recently shown by Ph. Müller et al. the rhombohedral lamellae are formed also near to the hexagonal phase [16], which constitutes a further structural inhomogeneity. The cubic BSCFZ3 structure seems to be more stable at given experimental conditions.

4. Conclusions

We have shown that the partial substitution of *B*-site cations in BSCF by zirconium can be accomplished up to 3 mol% when a single-phase product is desired. The so-obtained oxygen-transporting membrane material possesses an improved phase stability in the

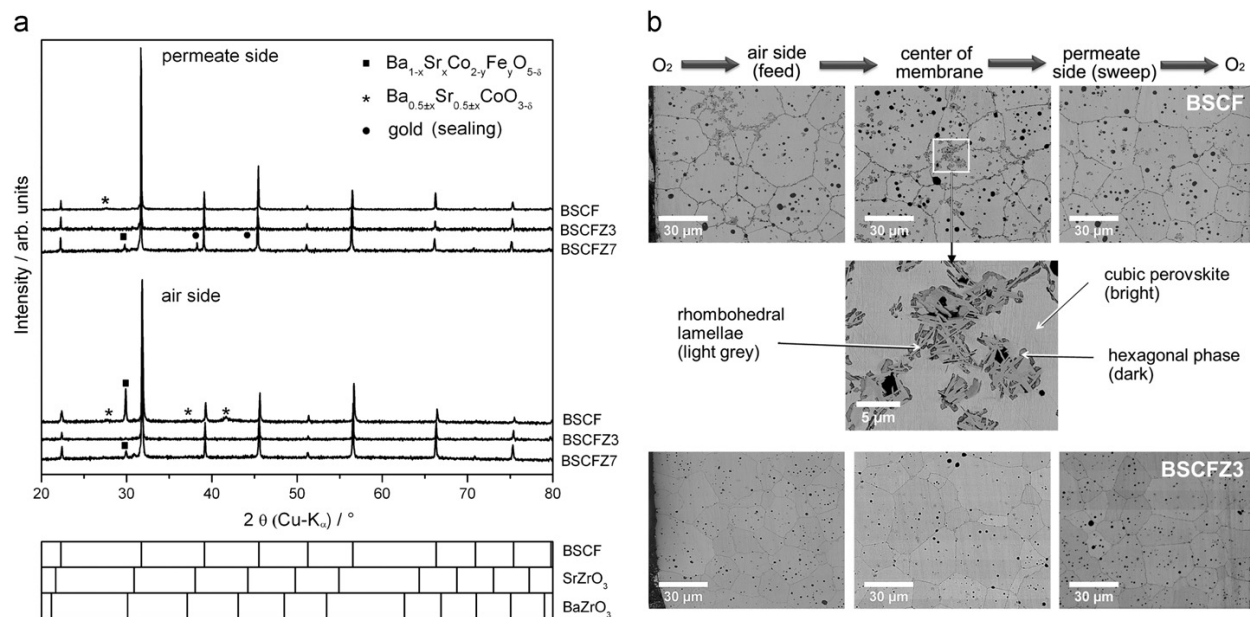


Fig. 6. (a) XRD patterns of the selected BSCFZ membrane surfaces after long-term oxygen permeation at 1230 K for 180 h. (b) Backscattered-electron channeling contrast images of BSCF and BSCFZ3 membrane cross-sections after the long-term permeation experiment.

intermediate temperature range (i.e. 773–1123 K) as compared to the original BSCF perovskite. However, practical application of zirconium-substituted BSCF in the intermediate temperature range seems not to be feasible as the oxygen permeation flux still continuously drops over time. Because of the drawbacks regarding relative stabilization and lower oxygen permeation flux with increasing zirconium content, the BSCFZ materials are not an appropriate alternative for intermediate temperature oxygen-transporting membranes.

Acknowledgments

The authors greatly acknowledge financial support from the Chinese-German Centre for Science (GZ676) and the Deutsche Forschungsgemeinschaft (FE 928/4-1) and fruitful discussions with Prof. Jürgen Caro.

References

- [1] Z.P. Shao, W.S. Yang, Y. Cong, H. Dong, J.H. Tong, G.X.J. Xiong, J. Membr. Sci. 172 (2000) 177.
- [2] J.F. Vente, S. McIntosh, W.G. Hajle, H.J.M. Bouwmeester, J. Solid State Electrochem. 10 (2006) 581.
- [3] Z.P. Shao, S.M. Haile, Nature 431 (2004) 170.
- [4] S. McIntosh, J.F. Vente, W.G. Hajle, D.H.A. Blank, H.J.M. Bouwmeester, Chem. Mater. 18 (2006) 2187.
- [5] R. Kriegel, R. Kircheisen, J. Töpfer, Solid State Ionics 181 (2010) 64.
- [6] A.C. van Veen, M. Rebeilleau, D. Farrusseng, C. Chem. Commun. 1 (2003) 32.
- [7] H. Ullmann, N. Trofimenko, F. Tietz, D. Stöver, A. Ahmad-Khanlou, Solid State Ionics 138 (2000) 79.
- [8] M. Rebeilleau-Dassonneville, S. Rosini, A.C. van Veen, D. Farrusseng, C. Mirodatos, Catal. Today 104 (2005) 131.
- [9] S. Švarcová, K. Wiik, J. Tolchard, H.J.M. Bouwmeester, T. Grande, Solid State Ionics 178 (2008) 1787.
- [10] K. Efimov, Q. Xu, A. Feldhoff, Chem. Mater. 22 (2010) 5866.
- [11] M. Arnold, H.H. Wang, J. Martynczuk, A. Feldhoff, J. Am. Ceram. Soc. 90 (2007) 3651.
- [12] M. Arnold, T.M. Gesing, J. Martynczuk, A. Feldhoff, Chem. Mater. 20 (2008) 5851.
- [13] D.N. Müller, R.A. De Souza, T.E. Weirich, D. Röhrens, J. Mayer, M. Martin, Phys. Chem. Chem. Phys. 12 (2010) 10320.
- [14] F. Liang, H. Jiang, H. Luo, J. Caro, A. Feldhoff, Chem. Mater. 23 (2011) 4765.
- [15] M.M. Kukulja, Y.A. Mastrikov, B. Jansang, E.A. Kotomin, J. Phys. Chem. C 116 (2012) 18605.
- [16] P. Müller, H. Strömer, L. Dieterle, C. Niedrig, E. Ivers-Tiffée, D. Gerthsen, Solid State Ionics 206 (2012) 57.
- [17] J. Sun, M. Yang, G. Li, T. Yang, F. Liao, Y. Wang, M. Xiong, J. Lin, Inorg. Chem. 45 (2006) 9151.
- [18] A. Rolle, N. Preux, G. Ehora, O. Mentré, S. Daviero-Minaud, Solid State Ionics 184 (2011) 31.
- [19] Y. Li, M.W. Xu, J.B. Goodenough, J. Power Sources 209 (2012) 40.
- [20] J.G. Cheng, J.S. Zhou, Z. Hu, M.R. Suchomel, Y.Y. Chin, C.Y. Kuo, H.J. Lin, J.M. Chen, D.W. Pi, C.T. Chen, T. Takami, L.H. Tjeng, J.B. Goodenough, Phys. Rev. B 85 (2012) 94424.
- [21] V.M. Goldschmidt, Die Gesetze der Kristallchemie, Naturwiss 14 (1926) 477.
- [22] A.S. Harvey, F.J. Litterst, Z. Yang, J.L.M. Rupp, A. Infortuna, L.J. Gauckler, Phys. Chem. Chem. Phys. 11 (2009) 3090.
- [23] P. Haworth, S. Smart, J. Glasscock, J.C. Diniz da Costa, Sep. Purif. Technol. 81 (2011) 88.
- [24] S.M. Fang, C.Y. Yoo, H.J.M. Bouwmeester, Solid State Ionics 195 (2011) 1.
- [25] S. Yakovlev, C.Y. Yoo, S. Fang, H.J.M. Bouwmeester, Appl. Phys. Lett. 96 (2010) 254101.
- [26] R.D. Shannon, Acta Cryst. Sect. A 32 (1976) 751.
- [27] A. Feldhoff, M. Arnold, J. Martynczuk, T.M. Gesing, H.H. Wang, Solid State Sciences 10 (2008) 689.
- [28] A. Feldhoff, J. Martynczuk, H.H. Wang, Prog. Solid State Chem 35 (2007) 339.
- [29] H.H. Wang, C. Tablet, A. Feldhoff, J. Caro, J. Membr. Sci. 262 (2005) 20.
- [30] J. Martynczuk, M. Arnold, A. Feldhoff, J. Membr. Sci. 322 (2008) 375.
- [31] J. Caro, H.H. Wang, C. Tablet, A. Kleinert, A. Feldhoff, T. Schiestel, M. Kilgus, P. Kölsch, S. Werth, Catal. Today 118 (2006) 128.
- [32] S. Baumann, F. Schulze-Küppers, S. Roitsch, M. Betz, M. Zwick, E.M. Pfaff, W.A. Meulenber, J. Mayer, D. Stöver, J. Membr. Sci. 359 (2010) 102.
- [33] D.N. Müller, R.A. de Souza, H.-I. Yoo, M. Martin, Chem. Mater. 24 (2012) 269.
- [34] B. Liu, Y. Zhang, L. Tang, Int. J. Hydrogen Energy 34 (2009) 435.

Abbreviations

BSCF	$\text{Ba}_{0.5}\text{Sr}_{0.5}\text{Co}_{0.8}\text{Fe}_{0.2}\text{O}_{3-\delta}$	1.1 Motivation
CA	Citric acid Zitronensäure	1.3.1 Sol-gel process
CCS	Carbon capture and storage Kohlenstoffabscheidung und Lagerung	1.1 Motivation
CO	Carbon monoxide Kohlenstoffmonoxid	1.3.1 Sol-gel process
CO ₂	Carbon dioxide Kohlenstoffdioxid	1.1 Motivation
EDTA	Ethylenediaminetetraacetic acid Ethylendiamintetraessigsäure	1.3.1 Sol-gel process
EDXS	Energy dispersive X-ray spectroscopy Energie-dispersive Röntgenspektroskopie	2.1 Summary
MIEC	Mixed ionic electronic conductor gemischter Ionen- und Elektronenleiter	1.1 Motivation
OCM	Oxidative coupling of methane oxidative Kopplung von Methan	1.1 Motivation
OTM	Oxygen-transporting membrane sauerstofftransportierende Membran	1.1 Motivation
POM	Partial oxidation of methane partielle Oxidation von Methan	1.1 Motivation
SCF	$\text{SrCo}_{0.8}\text{Fe}_{0.2}\text{O}_{3-\delta}$	1.1 Motivation
SEM	Scanning electron microscopy Rasterelektronenmikroskopie	1.5 Integration

SOFC	Solid oxide fuel cell Festoxidbrennstoffzelle	1.1 Motivation
SRU	German advisory council for environmental issues Sachverständigenrat für Umweltfragen	1.1 Motivation
TEM	Transmission electron microscopy Transmissionselektronenmikroskopie	1.5. Integration
UNFCCC	United Nations framework convention on climate change Rahmenübereinkommen der Vereinten Nationen über Klimaänderungen	1.1 Motivation
XRD	X-ray diffraction Röntgendiffraktometrie	1.2.2 Perovskite-related phases

List of Figures

1.1	Possible applications of oxygen-transporting membranes (OTMs). . .	2
1.2	Unit cell of the ABO_3 perovskite.	5
1.3	Overview of the different Ruddlesden-Popper and perovskite phases.	7
1.4	Tetragonal $La_2NiO_{4+\delta}$ with indicated interstitial positions.	8
1.5	Flowchart of the used sol-gel route.	9
1.6	Unit cell of the ABO_3 perovskite and oxygen migration pathway. . .	11
1.7	Oxygen permeation through a dense MIEC oxide membrane with indicated gradient of oxygen partial pressure.	15
1.8	Principle of a oxy-fuel combustion power plant operated in four-end mode.	18
1.9	Ellingham diagram with decomposition temperatures of carbonates under different CO_2 partial pressures.	19
1.10	Principle of a oxy-fuel combustion power plant operated in three-end mode.	20

Scientific publications

Publications included in this thesis (in chronological order)

1. Effect of doping and microstructure on CO₂-stable La₂NiO_{4+δ}-based oxygen-transporting materials,
T. Klande, K. Efimov, S. Cusenza, K.-D. Becker, and A. Feldhoff,
Journal of Solid State Chemistry **184** (2011) 3310-3318.
2. Ca-containing CO₂-tolerant perovskite materials for oxygen separation,
K. Efimov, T. Klande, N. Juditzki, and A. Feldhoff,
Journal of Membrane Science **389** (2012) 205-215.
3. In-situ Mössbauer studies of ⁵⁷Fe-doped Ruddlesden-Popper type lanthanum nickel oxides,
T. Klande, S. Cusenza, P. Gaczyński, K.-D. Becker, L. Dörrer, G. Borchardt, and A. Feldhoff,
Solid State Ionics **222-223** (2012) 8-15.
4. Rapid glycine-nitrate combustion synthesis of the CO₂-stable dual phase membrane 40Mn_{1.5}Co_{1.5}O_{4-δ}-60Ce_{0.9}Pr_{0.1}O_{2-δ} for CO₂ capture via an oxy-fuel process,
H. Luo, H. Jiang, T. Klande, F. Liang, Z. Cao, H. Wang, and J. Caro,
Journal of Membrane Science **423-424** (2012) 450-458.
5. Effect of microstructure on oxygen permeation of Ba_{0.5}Sr_{0.5}Co_{0.8}Fe_{0.2}O_{3-δ} and SrCo_{0.8}Fe_{0.2}O_{3-δ} membranes,
T. Klande, O. Ravkina, and A. Feldhoff,
Journal of the European Ceramic Society **33** (2013) 1129-1136.
6. Effect of A-site lanthanum doping on the CO₂ tolerance of SrCo_{0.8}Fe_{0.2}O_{3-δ} oxygen-transporting membranes,
T. Klande, O. Ravkina, and A. Feldhoff,
Journal of Membrane Science **437** (2013) 122-130.

-
7. Investigation of Zr-doped BSCF perovskite membrane for oxygen separation in the intermediate temperature range,
O. Ravkina, T. Klande, and A. Feldhoff,
Journal of Solid State Chemistry **201** (2013) 101-106.

Publications not included in the thesis

8. Chemical synthesis with inductively heated copper flow reactors,
S. Ceylan, T. Klande, C. Vogt, C. Friese, and A. Kirschning,
Synlett 13 (2010) 2009-2013.
9. CO₂-stable MIEC La₂Ni_{0.9}(M_{0.1})O_{4+δ} membrane materials,
T. Klande, K. Efimov, and A. Feldhoff,
Proceedings of the 12th Conference of the European Ceramic Society - ECerS XII Stockholm, Sweden (2011).
10. Novel cobalt-free, noble metal-free oxygen-permeable 40 Pr_{0.6}Sr_{0.4}FeO_{3-δ} - 60 Ce_{0.9}Pr_{0.1}O_{2-δ} dual-phase membrane,
H. Luo, H. Jiang, T. Klande, Z. Cao, F. Liang, H. Wang, and J. Caro,
Chemistry of Materials 24 (2012) 2148-2154.
11. Effect of CO₂ and SO₂ on oxygen permeation and microstructure of (Pr_{0.9}La_{0.1})₂(Ni_{0.74}Cu_{0.21}Ga_{0.05})O_{4+δ} membranes,
Y. Wei, O. Ravkina, T. Klande, H. Wang, and A. Feldhoff,
Journal of Membrane Science **429** (2013) 147-154.
12. Highly active perovskite electrode for oxygen reduction reaction below 600 °C,
W. Zhou, J. Sunarso, M. Zhao, A. Feldhoff, F. Liang, T. Klande, and Z. Zhu,
Nature, submitted March 2013.

Contributions to conferences

1. Grain boundaries as barriers to the oxygen transport in perovskite-type membranes,
A. Feldhoff, K. Efimov, and T. Klande,
Electroceramics XII, Trondheim, Norway, June 2010, Talk.
2. CO₂-stable MIEC La₂Ni_{0.9}(M_{0.1})O_{4+δ} membrane materials,
T. Klande, K. Efimov, and A. Feldhoff,
12th Conference of the European Ceramic Society: ECerS XII, Stockholm, Sweden, June 2011, Talk.
3. Effect of doping and grain size on oxygen permeation of La₂NiO_{4+δ}-based mixed conducting ceramics,
A. Feldhoff, T. Klande, and K. Efimov,
Solid State Ionics: SSI 18, Warszawa, Poland, July 2011, Talk.
4. CO₂-tolerant La₂Ni_{0.9}(M_{0.1})O_{4+δ} membranes for high-temperature oxygen separation,
A. Feldhoff, T. Klande, and K. Efimov,
European congress on advanced materials and processes: Euromat, Montpellier, France, September 2011, Talk.
5. CO₂-stable La₂NiO_{4+δ}-based oxygen-transporting materials,
T. Klande, K. Efimov, S. Cusenza, K.-D. Becker, and A. Feldhoff,
Diffusion in Solids - Methods, Models, and Materials: Bunsen Colloquium, Hannover, Germany, October 2011, Poster.
6. Ca-based perovskite materials as CO₂-tolerant oxygen-transporting membranes,
A. Feldhoff, T. Klande, N. Juditzki, and K. Efimov,
Diffusion in Solids - Methods, Models, and Materials: Bunsen Colloquium, Hannover, Germany, October 2011, Poster.
7. Effect of doping and microstructure on CO₂-tolerant oxygen transporting ceramic membranes,
A. Feldhoff, T. Klande, K. Efimov, L. Dörrer, G. Borchardt, S. Cusenza, and K.-D. Becker,
Sino-German Symposium: Inorganic membranes for clean energy and clear environment, Hannover, Germany, March 2012, Talk.

-
8. $\text{La}_2\text{NiO}_{4+\delta}$ -based oxygen separating materials: oxygen tracer diffusion and electrical conductivity measurements,
L. Dörrer, G. Borchardt, T. Klande, K. Efimov, A. Feldhoff, and S. Weber,
Sino-German Symposium: Inorganic membranes for clean energy and clear environment, Hannover, Germany, March 2012, Talk.
 9. Investigation of doped Ruddlesden-Popper $\text{La}_2\text{NiO}_{4+\delta}$ and $\text{La}_4\text{Ni}_3\text{O}_{10}$ phases as oxygen-transporting materials,
T. Klande, K.-D. Becker, and A. Feldhoff,
Electroceramics XIII, Enschede, The Netherlands, June 2012, Talk.
 10. Investigation of Zr-doped BSCF perovskite membranes for oxygen separation in the intermediate temperature range,
O. Ravkina, T. Klande, and A. Feldhoff,
Electroceramics XIII, Enschede, The Netherlands, June 2012, Poster.
 11. A high-temperature Mössbauer study of iron-doped Ruddlesden-Popper phases $\text{La}_{n+1}\text{Ni}_n\text{O}_{3n+1}$,
P. Gaczyński, S. Cusenza, T. Klande, A. Feldhoff, and K.-D. Becker,
XXI International Materials Research Congress, Cancún, Mexico, August 2012, Talk.
 12. Ruddlesden-Popper type phases as seen by high-temperature ^{57}Fe Mössbauer spectroscopy,
P. Gaczyński, T. Klande, A. Feldhoff, and K.-D. Becker,
Yucomat 2012, Montenegro, Serbia, September 2012, Talk.
 13. Thermische Dehnung und chemische Stabilität sauerstofftransportierender Oxide,
A. Feldhoff, and T. Klande,
Bruker Anwendertreffen XRD, Lüneburg, Germany, October 2012, Talk.
 14. A high-temperature Mössbauer study of iron-doped Ruddlesden-Popper phases $\text{La}_{n+1}\text{Ni}_n\text{O}_{3n+1}$,
K.-D. Becker, P. Gaczyński, S. Cusenza, T. Klande, and A. Feldhoff,
Materials Research Society: MRS fall meeting, Boston, United States, November 2012, Talk.

Curriculum Vitae

Personal data

Name Tobias Klande
Date of birth 01/21/1983
Place of birth Celle, Germany
Marital status unmarried, no children

Higher education

12/2012 **Submission of doctoral thesis**
Gottfried Wilhelm Leibniz Universität, Hannover, Germany
"Contributions to the development of oxygen-transporting materials as ceramic membranes for gas separation"

2009-2012 **Scientific co-worker**
Gottfried Wilhelm Leibniz Universität, Hannover, Germany
at the group of Prof. Dr. Armin Feldhoff.

2003-2009 **Chemistry degree: Diplom-Chemiker**
Gottfried Wilhelm Leibniz Universität, Hannover, Germany
Diploma thesis: "Bestimmung von Edelmetallen in Katalysatormaterialien"

Military service

2002-2003 **Gunner Leopard 2**
German army base, Celle-Scheunen, Germany.

Education

1995-2002 **Abitur**
Hermann-Billing-Gymnasium, Celle, Germany.

Erklärung zu dieser Dissertation

Hiermit erkläre ich, dass ich die vorliegende Dissertationsschrift selbstständig verfasst und alle benutzten Hilfsmittel und Quellen sowie gegebenenfalls die zu Hilfeleistung herangezogenen Institutionen vollständig angegeben habe.

Diese Dissertation wurde nicht schon als Masterarbeit, Diplomarbeit oder andere Prüfungsarbeit verwendet.

Hannover, den